

Advances in Photochemistry, Volume 27
Edited by Douglas C. Neckers, Günther von Bünau and William S. Jenks
Copyright © 2002 John Wiley & Sons, Inc.
ISBN: 0-471-21451-5

**ADVANCES IN
PHOTOCHEMISTRY**
Volume 27

ADVANCES IN PHOTOCHEMISTRY

Volume 27

Editors

DOUGLAS C. NECKERS

Center for Photochemical Sciences, Bowling Green State University,
Bowling Green, Ohio

GÜNTHER VON BÜNAU

Physikalische Chemie, Universität Siegen, Germany

WILLIAM S. JENKS

Department of Chemistry, Iowa State University, Ames, Iowa



A JOHN WILEY & SONS, INC., PUBLICATION

Copyright © 2002 by John Wiley & Sons, Inc. All rights reserved.

Published by John Wiley & Sons, Inc., Hoboken, New Jersey.

Published simultaneously in Canada.

No part of this publication may be reproduced, stored in a retrieval system, or transmitted in any form or by any means, electronic, mechanical, photocopying, recording, scanning, or otherwise, except as permitted under Section 107 or 108 of the 1976 United States Copyright Act, without either the prior written permission of the Publisher, or authorization through payment of the appropriate per-copy fee to the Copyright Clearance Center, Inc., 222 Rosewood Drive, Danvers, MA 01923, 978-750-8400, fax 978-750-4470, or on the web at www.copyright.com. Requests to the Publisher for permission should be addressed to the Permissions Department, John Wiley & Sons, Inc., 111 River Street, Hoboken, NJ 07030, (201) 748-6011, fax (201) 748-6008, e-mail: permreq@wiley.com.

Limit of Liability/Disclaimer of Warranty: While the publisher and author have used their best efforts in preparing this book, they make no representations or warranties with respect to the accuracy or completeness of the contents of this book and specifically disclaim any implied warranties of merchantability or fitness for a particular purpose. No warranty may be created or extended by sales representatives or written sales materials. The advice and strategies contained herein may not be suitable for your situation. You should consult with a professional where appropriate. Neither the publisher nor author shall be liable for any loss of profit or any other commercial damages, including but not limited to special, incidental, consequential, or other damages.

For general information on our other products and services please contact our Customer Care Department within the U.S. at 877-762-2974, outside the U.S. at 317-572-3993 or fax 317-572-4002.

Wiley also publishes its books in a variety of electronic formats. Some content that appears in print, however, may not be available in electronic format.

Library of Congress Cataloging in Publication Data:

Library of Congress Catalog Card Number: 63-13592

ISBN 0-471-21451-5

Printed in the United States of America

10 9 8 7 6 5 4 3 2 1

CONTRIBUTORS

Gion Calzaferrì

Department of Chemistry and
Biochemistry
University of Bern
Freiestrasse 3, CH-3000 Bern 9
Switzerland

André Devaux

Department of Chemistry and
Biochemistry
University of Bern
Freiestrasse 3, CH-3000 Bern 9
Switzerland

Thomas Fuhrmann

Macromolecular Chemistry and
Molecular Materials
Department of Physics
Kassel University
D-34109 Kassel
Germany

Huub Maas

Department of Chemistry and
Biochemistry
University of Bern
Freiestrasse 3, CH-3000 Bern 9
Switzerland

Silke Megelski

Department of Chemistry and
Biochemistry
University of Bern
Freiestrasse 3, CH-3000 Bern 9
Switzerland

Marc Pauchard

Department of Chemistry and
Biochemistry
University of Bern
Freiestrasse 3, CH-3000 Bern 9
Switzerland

Kevin Peters

Department of Chemistry and
Biochemistry
University of Colorado at Boulder
Campus Box 215
Boulder, CO 80309

Michel Pfenniger

Department of Chemistry and
Biochemistry
University of Bern
Freiestrasse 3, CH-3000 Bern 9
Switzerland

Josef Salbeck

Macromolecular Chemistry and

Molecular Materials

Department of Physics

Kassel University

Heinrich-Plett-Straße 40

D-34109 Kassel

Germany

PREFACE

Volume 1 of *Advances in Photochemistry* appeared in 1963. The stated purpose of the series was to explore the frontiers of photochemistry through the medium of chapters written by pioneers who are experts. The editorial policy has always been to solicit articles from scientists who have strong personal points of view, while encouraging critical discussions and evaluations of existing data. In no sense have the articles been simply literature surveys, although in some cases they may have also fulfilled that purpose.

In the introduction to Volume 1 of this series, the founding editors, J. N. Pitts, G. S. Hammond and W. A. Noyes, Jr. noted developments in a brief span of prior years that were important for progress in photochemistry: flash photolysis, nuclear magnetic resonance, and electron spin resonance. A quarter of a century later, in Volume 14 (1988), the editors noted that since then two developments had been of prime significance: the emergence of the laser from an esoteric possibility to an important light source, and the evolution of computers to microcomputers in common laboratory use of data acquisition. These developments strongly influenced research on the dynamic behavior of the excited state and other transients.

With the increased sophistication in experiment and interpretation since that time, photochemists have made substantial progress in achieving the fundamental objective of photochemistry: elucidation of the detailed history of a molecule that absorbs radiation. The scope of this objective is so broad and the systems to be studied are so many that there is little danger of exhausting the subject. We hope that this series will reflect the frontiers of photochemistry as they develop in the future.

As readers will see from the Senior Editor's Statement on the next page, the Editors of the *Advances* Series are changing with Volume 28. As always we wish to hear from our readers in our attempt to keep the series current and useful.

Bowling Green, Ohio, USA
Siegen, Germany
Ames, Iowa, USA

DOUGLAS C. NECKERS
GÜNTHER VON BÜNAU
WILLIAM S. JENKS

SENIOR EDITOR'S STATEMENT

With this Volume we note a change in Editors. Günther von Büнау, who has recently retired from the University of Siegen has chosen this time to also 'retire' from the Editorial Board of *Advances*. Günther has been a strong contributor to the Series as we have collectively worked to make *Advances* a helpful literature asset. I will really miss working with him and wish him the very best in retirement.

However with change comes opportunity, and we are delighted to welcome Thomas Wolff who will join us with Volume 28 to our editorial triumvirate. Professor Wolff took his degree at the University of Göttingen under the supervision of Albert Weller and Karl-Heinz Grellmann. After joining the group of Günther von Büнау and then finishing his habilitation he became Professor of Physical Chemistry at the University of Siegen. In 1993 he moved to the Technical University of Dresden as a Professor at the Institute of Physical Chemistry. His research interests lay in the region where photochemistry, colloid chemistry, and polymer chemistry meet, that is, macroscopic properties of colloid systems that can be switched via photochemical reactions of solubilized molecules.

In the best of American traditions, we offer Günther our sincere congratulations on a job well done and thank him for his very many excellent contributions to the series.

And to Thomas we say "Welcome on board."

*McMaster Distinguished Research Professor
Center for Photochemical Sciences
Bowling Green State University
Bowling Green, OHIO 43403*

DOUGLAS C. NECKERS

CONTENTS

| | |
|--|------------|
| Supramolecularly Organized Luminescent Dye Molecules in the Channels of Zeolite L | 1 |
| GION CALZAFERRI, HUUB MAAS, MARC PAUCHARD, MICHEL PFENNIGER, SILKE MEGELSKI, AND ANDRE DEVAUX | |
| Proton-Transfer Reactions in Benzophenone/ <i>N,N</i>-Dimethylaniline Photochemistry | 51 |
| KEVIN S. PETERS | |
| Functional Molecular Glasses: Building Blocks for Future Optoelectronics | 83 |
| THOMAS S. FUHRMANN AND JOSEL SALBECK | |
| Index | 167 |
| Cumulative Index, Volumes 1–27 | 177 |

**ADVANCES IN
PHOTOCHEMISTRY**

Volume 27

SUPRAMOLECULARLY ORGANIZED LUMINESCENT DYE MOLECULES IN THE CHANNELS OF ZEOLITE L*

**Gion Calzaferri, Huub Maas, Marc Pauchard, Michel Pfenniger,
Silke Megelski, and André Devaux**

Department of Chemistry and Biochemistry, University of Bern,
CH-3000 Bern 9, Switzerland

CONTENTS

- I. Introduction
- II. The System
 - A. Geometrical Constraints
 - B. Inner- and Outer-Surface of the Zeolite Nanocrystals
 - C. The Dyes
 - D. Three-Dye Antenna
 - E. The Stopcock Principle
- III. Transfer of Electronic Excitation Energy
 - A. Radiationless Energy Transfer

*Dedicated to professor Ernst Schumacher on the occasion of his 75th birthday.

- B. Förster Energy Transfer in Dye Loaded Zeolite L
 - C. Spectral Overlap
- IV. Elegant Experiments for Visual Proof of Energy Transfer and Migration
- A. Energy Transfer
 - B. Intrazeolite Diffusion Monitored by Energy Transfer
 - C. Energy Migration
- V. Conclusions
- Acknowledgments
- References

I. INTRODUCTION

An important aim of photochemistry is to discover or to design structurally organized and functionally integrated artificial systems that are capable of elaborating the energy and information input of photons to perform useful functions such as transformation and storage of solar energy, processing and storage of information, and sensing of the microscopic environment on a molecular level. The complexity and beauty of natural systems have encouraged chemists to study the structure and properties of organized media like molecular crystals, liquid crystals and related regular arrangements, and to mimic some of their functions. Microporous structures containing atoms, clusters, molecules, or complexes provide a source of new materials with exciting properties [1–6]. For this purpose, zeolites are especially appealing crystalline inorganic microporous materials. Some of them occur in nature as a component of the soil. Natural and synthetic zeolites possess a large variety of well-defined internal structures such as uniform cages, cavities, or channels [7–10]. A useful feature of zeolites is their ability to host molecular guests within the intravoid space. Chromophore loaded zeolites have been investigated for different purposes such as interfacial electron transfer, microlasers, second harmonic generation, frequency doubling, and optical bistabilities giving rise to persistent spectral hole burning [11–21]. The role of the zeolite framework is to act as a host for realizing the desired geometrical properties and for stabilizing the incorporated molecules. Incorporation of chromophores into the cavities of zeolites can be achieved in different ways, depending on the used substances and on the desired properties: from the gas phase [22–24], by ion exchange if cations are involved [3, 25–28] by crystallization inclusion [29], or by performing an *in situ* synthesis inside the zeolite cages [30, 31].

Plants are masters of efficiently transforming sunlight into chemical energy. In this process, every plant leaf acts as a photonic antenna in which photonic

energy is absorbed in the form of sunlight and transported by chlorophyll molecules for energy transformation. In natural photosynthesis, light is absorbed by an antenna system of a few hundred chlorophyll molecules arranged in a protein environment. The antenna system allows a fast energy transfer from an electronically excited molecule to unexcited neighbor molecules in a way that the excitation energy reaches the reaction center with high probability. Trapping occurs there. It has been reported that the anisotropic arrangement of chlorophyll molecules is important for efficient energy migration [32, 33]. In natural antenna systems, the formation of aggregates is prevented by fencing the chlorophyll molecules in polypeptide cages [34]. A similar approach is possible by enclosing dyes inside a microporous material and by choosing conditions such that the volume of the cages and channels is able to uptake only monomers but not aggregates.

An artificial photonic antenna system is an organized multicomponent arrangement in which several chromophoric molecular species absorb the incident light and transport the excitation energy (not charges) to a common acceptor component. Imaginative attempts to build an artificial antenna different from ours have been presented in the literature [35]. Multinuclear luminescent metal complexes [36–38], multichromophore cyclodextrins [39], Langmuir–Blodgett films [40–43], dyes in polymer matrices [44–46], and dendrimers [47] have been investigated. Some sensitization processes in silver halide photographic materials [48] and also the spectral sensitization of polycrystalline titanium dioxide films bear in some cases aspects of artificial antenna systems [49–51]. The system reported in [3, 22, 52, 53] is of a bidirectional type, based on zeolite L as a host material, and able to collect and transport excitation over relatively large distances. The light transport is made possible by specifically organized dye molecules that mimic the natural function of chlorophyll. The zeolite L crystals consist of a continuous one-dimensional (1D) tube system. We have filled each individual tube with successive chains of different joint but noninteracting dye molecules. Light shining on the cylinder is first absorbed and the energy is then transported by the dye molecules inside the tubes to the cylinder ends.

A schematic view of the artificial antenna is illustrated in Figure 1.1. The monomeric dye molecules are represented by rectangles. The dye molecule, which has been excited by absorbing an incident photon, transfers its electronic excitation to another one. After a series of such steps, the electronic excitation reaches a trap that we have pictured as shaded rectangles. The energy migration is in competition with spontaneous emission, radiationless decay, and photochemically induced degradation. Very fast energy migration is therefore crucial if a trap should be reached before other processes can take place. These conditions impose not only spectroscopic but also decisive geometrical constraints on the system.

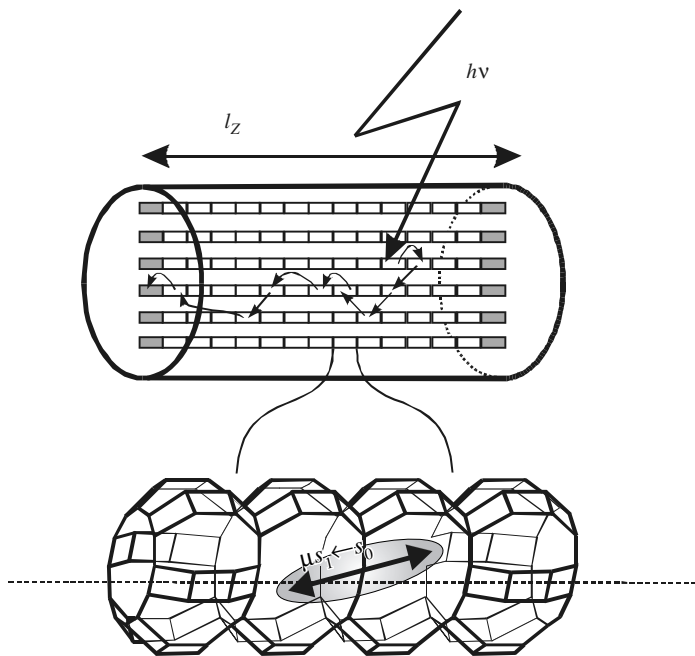


Figure 1.1. Representation of a cylindrical nanocrystal consisting of organized dye molecules acting as donors (empty rectangles) and an acceptor acting as a trap at the front and the back of each channel (shaded rectangles). The enlargement shows a detail of the zeolite L channel with a dye molecule and its electronic transition moment. The orientation of this electronic transition moment with respect to the long axis depends on the length and shape of the molecules [54].

In this chapter, we describe the design and important properties of supramolecularly organized dye molecules in the channels of hexagonal nanocrystals. We focus on zeolite L as a host. The principles, however, hold for other materials as well. As an example, we mention ZSM-12 for which some preliminary results have been reported [55]. We have developed different methods for preparing well-defined dye-zeolite materials, working for cationic dyes, neutral dyes, and combinations of them [3, 22, 25, 52]. The formula and trivial names of some dyes that so far have been inserted in zeolite L are reported in Section II.C. The properties of natural and commercially available zeolites can be influenced dramatically by impurities formed by transition metals, chloride, aluminiumoxide, and others. This fact is not always sufficiently taken care of. In this chapter, we only report results on chemically pure zeolites, the synthesis of which is described in [53].

II. THE SYSTEM

Favorable conditions for realizing a device as illustrated in Figure 1.1 are a high concentration of monomeric dye molecules with high luminescence quantum yield, ideal geometrical arrangement of the chromophores, and an optimal size of the device. Dyes at high concentration have the tendency to form aggregates that in general show very fast radiationless decay [56, 57]. The formation of aggregates can be prevented by fencing dyes inside a microporous material and by choosing conditions such that the volume of the cages and channels is only able to uptake monomers but not aggregates. Linear channels running through microcrystals allow the formation of highly anisotropic dye assemblies. Examples of zeolites bearing such channels large enough to uptake organic dye molecules are reported in Table 1.1. Our investigations have concentrated on zeolite L as a host. The reason for this is that neutral dyes as well as cationic dyes can be inserted into the channels of zeolite L and that synthesis procedures for controlling the morphology of zeolite L crystals in the size regime from 30 to ~ 3000 nm are available [53, 58–62]. Many results obtained on zeolite L are valid for other nanoporous materials as well. In Figure 1.2, we show a scanning electron microscopy (SEM) picture of a zeolite L material with nice morphology. The hexagonal shape of the crystals can easily be recognized. For simplicity, we often describe them as crystals of cylinder morphology.

A space-filling top view and a side view of the zeolite L framework is illustrated in Figure 1.3. The primitive vector \mathbf{c} corresponds to the channel axis while the primitive vectors \mathbf{a} and \mathbf{b} are perpendicular to it, enclosing an angle of 60° .

We distinguish between three types of dye molecules. (1) *Molecules small enough to fit into a single unit cell*. Examples we have investigated so far are

TABLE 1.1 Lattice Constants a , b , and c and Free Opening Diameters \emptyset of Hexagonal Molecular Sieves with Linear Channels (in nm) [8]

| | $a = b$ | c | \emptyset |
|----------------------|---------|------|-------------|
| Mazzite | 1.84 | 0.76 | 0.74 |
| AlPO ₄ -5 | 1.37 | 0.84 | 0.73 |
| Zeolite L | 1.84 | 0.75 | 0.71 |
| Gmelinite | 1.38 | 1.00 | 0.70 |
| Offretite | 1.33 | 0.76 | 0.68 |
| CoAPO-50 | 1.28 | 0.90 | 0.61 |
| Cancrinite | 1.28 | 0.51 | 0.59 |
| VPI-5 | 1.90 | 0.84 | 1.21 |

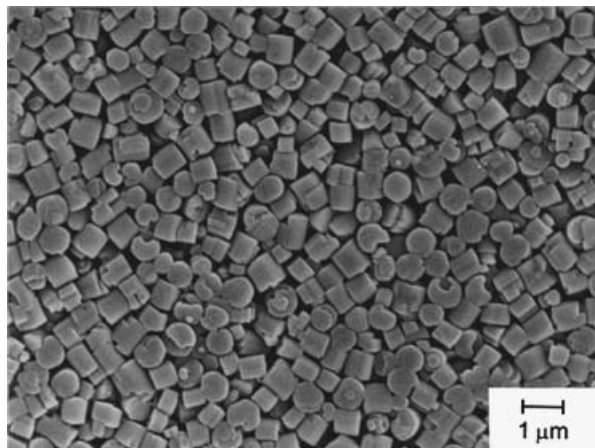


Figure 1.2. Scanning electron microscopy picture of a zeolite L sample [25].

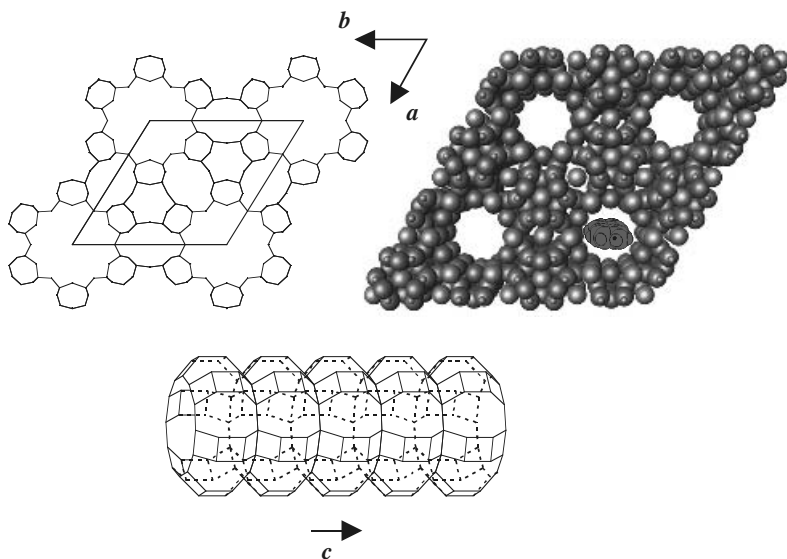


Figure 1.3. Framework of zeolite L. *Upper:* Top view, perpendicular to the c axis, displayed as stick (left) and as van der Waals (right) representation with a dye molecule entering the zeolite channel. *Lower:* Side view of a channel along the c axis, without bridging oxygen atoms.

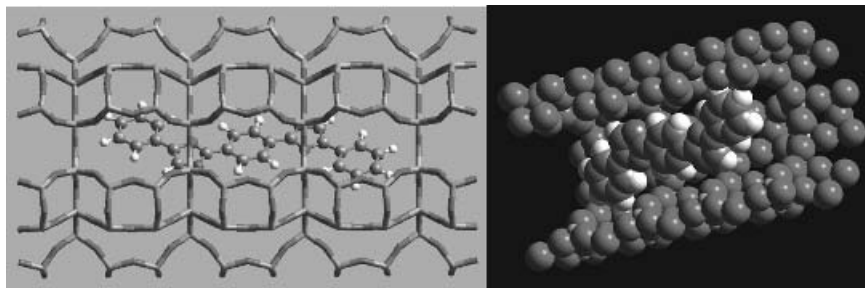


Figure 1.4. Illustration of the length and space-filling POPOP in zeolite L.

biphenyl, hydroxy-TEMPO, fluorenone, and methylviologen (MV^{2+}). Structural details of the latter are known based on vibrational spectroscopy, Rietveld refinement of X-ray data, and molecular modeling. We found that the MV^{2+} lies along the channel wall, and that the angle between the main MV^{2+} axis and the c axis of the zeolite is 27° [25]. (2) *Molecules with a size that makes it hard to guess if they align along the c axis or if they are tilted in the channel.* Oxonine, pyronine, and thionine are molecules of this type, as we will see later. (3) *Molecules that are so large that they have no other choice but to align along the c axis.* Many examples fit into this category. The POPOP illustrated in Figure 1.4 is one of them. It is important to know if molecules can occupy at least part of the same unit cell, so that they can interact via their π -system or if they can “only touch each other” so that their electronic coupling is negligible.

While for molecules of type (1) not only translational but also large amplitude modes can be activated, the latter are severely or even fully restricted for molecules of types (2) and (3). This finding has consequences on their stability and on their luminescence quantum yield, which generally increases. An example that we have investigated, is the very light sensitive DPH, which is dramatically stabilized when inserted into zeolite L, because there is not sufficient space available for trans to cis isomerization [22]. In other cases, a strong increase of stability is observed because reactive molecules that are too large or anions such as hypochlorite have no access because they cannot enter the negatively charged channels [3, 53]. It is not surprising that the fluorescence quantum yield of cationic dyes is not or is only positively affected by the zeolite L framework. More interestingly, the fluorescence quantum yield of neutral dyes also seems to be positively influenced by the zeolite L framework despite the very large ionic strength inside the channels. Only one case of an anionic organic dye in the anionic zeolite L framework has been reported so far, namely, the resorufin, which is also the only case where severe luminescence quenching has been observed [23]. Most results reported here refer to dye loaded zeolite

L material that contains several water molecules per unit cell, see [22]. If the water molecules are completely removed from the main channel, the spectroscopic properties may change.

A. Geometrical Constraints

The geometrical constraints imposed by the host determines the organization of the dyes. We focus on systems consisting of dye molecules in hexagonally arranged linear channels. Materials providing such channels are reported in Table 1.1. We investigate a cylindrical shape as illustrated in Figure 1.5. The primitive vector \mathbf{c} corresponds to the channel axis while the primitive vectors \mathbf{a} and \mathbf{b} are perpendicular to it enclosing an angle of 60° . The channels run parallel to the central axis of the cylinder [62]. The length, and the diameter of the cylinder are l_z , and d_z , respectively. The following concepts and definitions cover situations we found to be important. They refer to systems as illustrated in Figure 1.1.

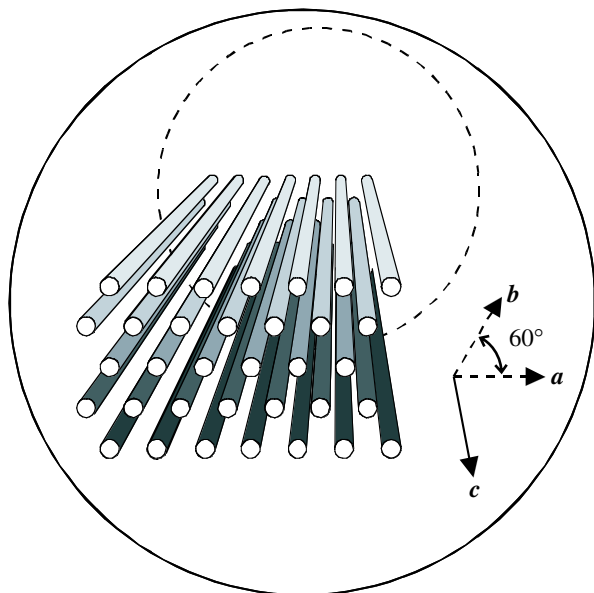


Figure 1.5. Schematic view of some channels in a hexagonal zeolite crystal with cylinder morphology.

1. The number of parallel channels n_{ch} of a hexagonal crystal that can be approximated by a cylinder of diameter d_Z is given by

$$n_{\text{ch}} = \frac{(d_Z/2)^2 \pi}{|\mathbf{a}|^2 \sin(60)} = \frac{\pi}{2\sqrt{3}} \left(\frac{d_Z}{|\mathbf{a}|} \right)^2 \quad (1)$$

which can be approximated for zeolite L as

$$n_{\text{ch}} \simeq 0.268(d_Z)^2 \quad (2)$$

where d_Z is in units of nanometers (nm). This means that a zeolite L of 500-nm diameter gives rise to $\sim 67,000$ parallel channels.

2. The dye molecules are positioned at sites along the linear channels. The length of a site is equal to a number n_s times the length of \mathbf{c} , so that one dye molecule fits into one site. Thus n_s is the number of unit cells that form a site we name the n_s -site. The parameter n_s depends on the size of the dye molecules and on the length of the primitive unit cell. As an example, a dye with a length of ≈ 1.5 nm in zeolite L requires two primitive unit cells, therefore $n_s = 2$ and the sites are called 2-site. The sites form a new (pseudo) Bravais lattice with the primitive vectors \mathbf{a} , \mathbf{b} , and $n_s \cdot \mathbf{c}$ in favorable cases.
3. Different types of sites exist. Those occupied with luminescent dye molecules are marked with small letters. Capital letters are reserved for traps that may or may not be luminescent. Per crystal, the number of sites available for dye molecules is i_{max} and the number of sites available for traps is I_{max} . Equivalent n_s -sites have the same geometrical properties. Dye molecules in equivalent sites i are assumed to be equivalent. The same is valid for traps.
4. In general, only dye molecules with a large electronic transition dipole moment $\mu_{S_1 \leftarrow S_0}$ are considered in this account, which means that the $S_1 \leftarrow S_0$ transition is of $\pi^* \leftarrow \pi$ type.
5. Equivalent n_s -sites i have the same probability p_i to be occupied by a dye molecule. The occupation probability p is equal to the ratio between the occupied and the total number of equivalent sites. The number of unit cells n_{uc} is controlled by the host while n_s is determined by the length of the guest, which means that p relies on purely geometrical (space-filling) reasoning and that the dye concentration per unit volume of a zeolite crystal can be expressed as a function of p as follows:

$$c(p) = \frac{\rho_Z p}{m_Z n_s} \quad (3)$$

where ρ_Z is the density and m_Z is the mass of the zeolite crystal. In cases where cationic dye molecules are inserted by ion exchange, p is proportional to the exchange degree θ , which is defined as the ratio of dye molecules and exchangeable cations. The relation between the exchange degree θ and the occupation probability p is given by [26]

$$p = n_s n_{M^+} \theta \quad (4)$$

where n_{M^+} is the number of exchangeable cations per unit cell. The occupation probability p_I of sites I is treated in an analogous way. Zeolite literature often refers to the equivalent fraction of exchanging species θ_Z [7]. It is defined as the number of inserted cations divided by the total numbers of cations in the zeolite. In simple cases, the relation between the occupation probability and θ_Z is obvious [63]. The occupation probability is more general, however, and more useful for our purpose.

6. Each equivalent site i of a given crystal has the same probability P_i of being occupied by an electronically excited molecule, immediately after irradiation with a Dirac pulse. The excitation probability P_i of site i is the i th element of a vector \mathbf{P} that we call excitation distribution among the sites. We distinguish between the low intensity case in which at maximum one dye molecule per crystal is in an electronically excited state and cases where two or more molecules in a crystal are in the excited state. Where not explicitly mentioned we refer to the low-intensity case.
7. We consider the case where the sites form a Bravais lattice, which means that the position \mathbf{R}_i of an n_s -site i can be expressed by the primitive vectors \mathbf{a} , \mathbf{b} , and $n_s \cdot \mathbf{c}$ of the hexagonal lattice and the integers $n_{a,i}$, $n_{b,i}$, and $n_{c,i}$:

$$\mathbf{R}_i = n_{a,i}\mathbf{a} + n_{b,i}\mathbf{b} + n_{c,i}n_s\mathbf{c} \quad (5)$$

This description is always precise for $n_s = 1$. Because it greatly simplifies the description, we will use it as an approximation for $n_s > 1$, too. Deviations from a more precise statistical treatment are probably small in general because even small crystals consist of a large number of sites so that differences may cancel. It is, however, not yet clear under what conditions this assumption breaks down. Anyhow, in this simplified description sites with equal n_c belong to slabs cut perpendicular to the c axis, which is illustrated in Figure 1.6.

The first slab is situated at the front and the last slab on the back of the cylinder. The total number of slabs n_{sb} depends on the length l_Z of the cylindrical microcrystal.

$$n_{sb} = \frac{l_Z}{n_s |\mathbf{c}|} \quad (6)$$

The thickness of a slab is $n_s \cdot |\mathbf{c}|$.

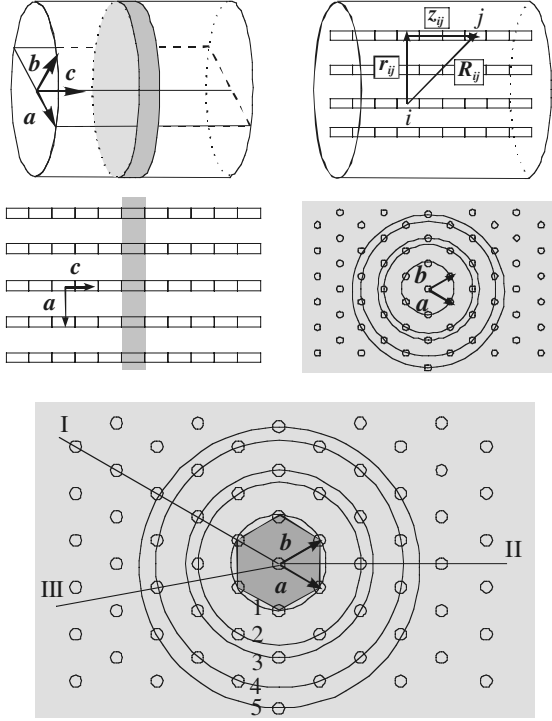


Figure 1.6. Geometrical situation. The sites are marked by rectangles. *Top*: Primitive vectors \mathbf{a} , \mathbf{b} , and \mathbf{c} . Definition of the distances R_{ij} , r_{ij} , and z_{ij} between sites i and j . *Middle, left*: Cut through the center of the hexagonal crystal with cylinder morphology along \mathbf{a} and \mathbf{c} . The sites of the shaded area belong to one slab. *Middle, right*: Cut perpendicular to \mathbf{c} . The channels indicated by circles are arranged on rings around the central channel because of the hexagonal symmetry. *Bottom*: The parameters r_I , r_{II} , and r_{III} are the distances from one channel to the next along lines I, II, and III.

8. The distance r between a channel (n_a, n_b) and the central channel is given by $r = |n_a \mathbf{a} + n_b \mathbf{b}|$. The channels are characterized by the numbers (n_a, n_b) , hence, sites with the same (n_a, n_b) values belong to the same channel. The parameters n_a and n_b are both equal to zero for the central channel, which coincides with the cylinder axis. The possible range of (n_a, n_b) is limited by the condition $|n_a \mathbf{a} + n_b \mathbf{b}| \leq d_z/2$. Because of the hexagonal symmetry, \mathbf{a} and \mathbf{b} have equal lengths and the angle between \mathbf{a} and \mathbf{b} is 60° . The length r of the vector $n_a \mathbf{a} + n_b \mathbf{b}$ is therefore given by

$$r = |\mathbf{a}| \sqrt{(n_a + n_b \cos 60^\circ)^2 + (n_b \sin 60^\circ)^2} = |\mathbf{a}| \sqrt{n_a^2 + n_a n_b + n_b^2} \quad (7)$$

Rings consisting of six channels can be formed, due to the hexagonal symmetry, as illustrated in Figure 1.6. The six channels on one ring all have the same distance from the center (0,0). A transformation can be given to go from one channel on a ring to the other five channels. Two, three, or more six-rings can be located on the same circle but displaced by a certain angle, due to the hexagonal symmetry. The tubes of each of these six-rings, however, behave in the same way. The distances r_I , r_{II} , and r_{III} can be expressed as $r_I = na$, $r_{II} = 3^{0.5}na$, and $r_{III} = (n^2 + n + 1)^{0.5}a$, where $n = 1, 2, 3, \dots$

9. The probability for energy transfer between two sites i and j strongly depends on the vector \mathbf{R}_{ij} , which is characterized by

$$\mathbf{R}_{ij} = (n_{a,i} - n_{a,j})\mathbf{a} + (n_{b,i} - n_{b,j})\mathbf{b} + (n_{c,i} - n_{c,j})n_s\mathbf{c} \quad (8)$$

$$R_{ij} = \sqrt{r_{ij}^2 + z_{ij}^2} \quad (9)$$

where r_{ij} and z_{ij} are the distances between the channels and the slabs to which the two sites belong. They correspond to the distances between the sites parallel and perpendicular to \mathbf{c} , respectively. The parameters R_{ij} , z_{ij} , and r_{ij} are indicated in Figure 1.6.

$$r_{ij} = |\mathbf{a}| \sqrt{(n_{a,i} - n_{a,j})^2 + (n_{a,i} - n_{a,j})(n_{b,i} - n_{b,j}) + (n_{b,j} - n_{b,j})^2} \quad (10)$$

$$z_{ij} = n_s |\mathbf{c}| (n_{c,i} - n_{c,j}) \quad (11)$$

10. In crystals containing more than one type of dye, the definitions, and concepts must be adapted correspondingly.

B. Inner- and Outer-Surface of the Zeolite Nanocrystals

Cationic and neutral dyes have the tendency to adsorb at the inner and at the outer surface of the zeolite crystals. It is to be expected that the affinity of molecules to the coat and the base area differs. The coat and the base area of a good zeolite L material are nicely illustrated on the left and right side, respectively, of Figure 1.7. The number of molecules needed to form a monolayer n_D on a cylinder of surface A_Z is

$$n_D = \frac{A_Z}{A_D} \quad (12)$$

where A_D is the surface required by a dye molecule. It depends not only on its size but also on the specific arrangement of the molecules in the monolayer.

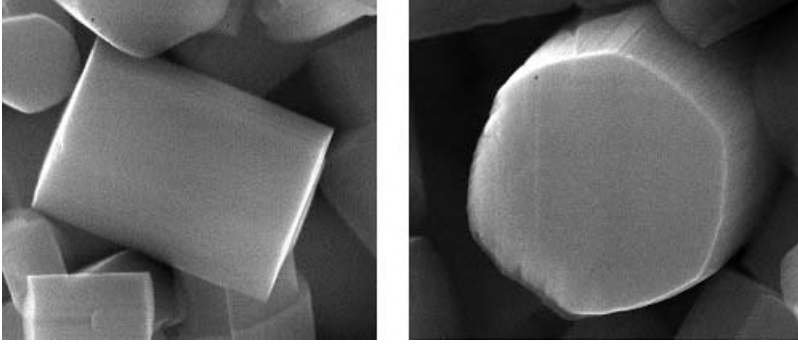


Figure 1.7. Side and top view of zeolite L crystals. The length of the left crystal is ~ 950 nm, the diameter of the right crystal is ~ 850 nm.

It is often useful to express n_D in terms of the volume V_Z and of the density ρ_Z of a zeolite crystal:

$$A_Z = 2\pi(d_Z/2)^2 + \pi d_Z l_Z \quad (13)$$

$$V_Z = \pi(d_Z/2)^2 l_Z = \frac{m_Z}{\rho_Z} \quad (14)$$

where d_Z , l_Z , and m_Z are the diameter, the length, and the mass of the zeolite crystal. This equation leads to the following expression for n_D :

$$n_D = \frac{2}{A_D} \left(\frac{V_Z}{l_Z} + \sqrt{\pi V_Z l_Z} \right) \quad (15)$$

or

$$n_D = \frac{\pi}{A_D} \left(\frac{d_Z^2}{2} + d_Z l_Z \right) \quad (16)$$

We compare n_D with the number of unit cells n_{uc} of the crystal. The number of unit cells per channel is equal to its length divided by the length of the unit cell c . By using Eq. (1), we can write

$$n_{uc} = n_{ch} \frac{l_Z}{|c|} = \frac{\pi}{2\sqrt{3}} \left(\frac{d_Z}{|a|} \right)^2 \frac{l_Z}{|c|} \quad (17)$$

From this follows the ratio of n_{uc} and n_D :

$$\frac{n_{uc}}{n_D} = \frac{d_Z l_Z}{d_Z + 2l_Z} \frac{A_D}{\sqrt{3}|\mathbf{a}|^2|\mathbf{c}|} \quad (18)$$

Applying the values of \mathbf{a} and \mathbf{c} for zeolite L leads to

$$n_{uc} = 0.357d_Z^2 l_Z \quad (19)$$

$$\frac{n_{uc}}{n_D} = 0.227A_D \frac{d_Z l_Z}{d_Z + 2l_Z} \quad (20)$$

where d_Z and l_Z are in units of nanometers (nm). Hence, a zeolite L cylinder of 100-nm length and diameter consists of 2680 channels and 35,700 unit cells, one of 1000-nm length and 600-nm diameter consists of 96,400 channels and 1.28×10^6 unit cells. For a molecule that occupies two unit cells, A_D is in the order of 1.4 nm^2 , which gives a ratio $n_{uc}/2n_D$ of 5.3 for the small crystals and 36.7 for the larger ones. From this, it is clear that the number of molecules that in principle can form a monolayer at the outer surface is in the same order of magnitude as the number of sites inside of the material, despite its high porosity. Obviously, the smaller the crystals, the more important it is to distinguish between molecules at the outer and at the inner surface of the material. Experiments to distinguish between molecules at the inner and outer surface make use of geometrical and electrostatic constraints of the negatively charged zeolite framework. The same principle is used to remove or to destroy unwanted molecules at the outer surface [53].

Because we are studying an anisotropical system where energy transport is possible along the channels and from one channel to another one, it is useful to consider the ratio $R_{ch/site}$ between the number of parallel channels and the number of n_s -sites in a channel:

$$R_{ch/site} = \frac{n_{ch}}{l_Z/(n_s \mathbf{c})} = \frac{\pi}{2\sqrt{3}} \left(\frac{d_Z}{\mathbf{a}} \right)^2 \frac{n_s \mathbf{c}}{l_Z} \quad (21)$$

Applying this to zeolite L gives

$$R_{ch/site} = 0.2n_s \frac{d_Z^2}{l_Z} \quad (22)$$

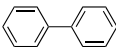
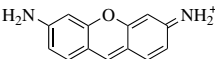
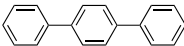
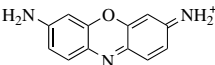
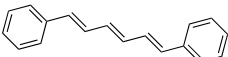
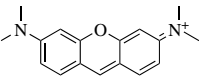
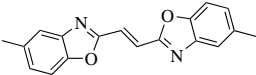
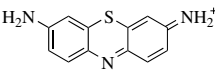
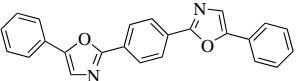
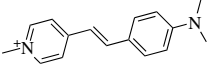
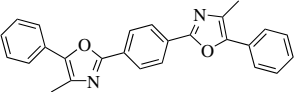
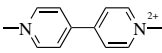
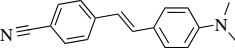
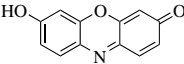
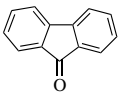
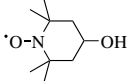
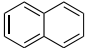
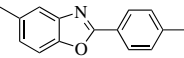
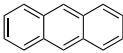
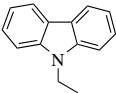
where d_Z and l_Z are in units of nanometers (nm). This means, for example, that $R_{ch/site} = 144$ for a crystal of 1000-nm length and 600-nm diameter and a dye that occupies two unit cells.

C. The Dyes

Representative dyes we have inserted in zeolite L are listed in Table 1.2. Many of them lead to strongly luminescent materials. Some exceptions are fluorenone, MV^{2+} , ResH, and hydroxy-TEMPO.

We distinguish between the four different orientations **1**, **2**, **3**, and **4** of molecules in the channels as explained in Figure 1.8. Molecules with a length of more

TABLE 1.2 Dye Molecules and Abbreviations

| Abbreviation | Molecule | Molecule | Abbreviation |
|-------------------------|---|---|--|
| BP |  |  | Py ⁺ |
| <i>p</i> TP |  |  | Ox ⁺ |
| DPH |  |  | PyGY ⁺ |
| MBOXE |  |  | TH ⁺ |
| POPOP |  |  | DSMI ⁺ |
| DMPOPOP |  |  | MV ²⁺ |
| DSC |  |  | ResH |
| Fluorenone |  |  | Hydroxy-TEMPO |
| Naphtalene ^a |  |  | PBOX |
| Anthracene ^a |  |  | <i>N</i> -Ethyl-carbazole ^a |

^aTaken from [64].

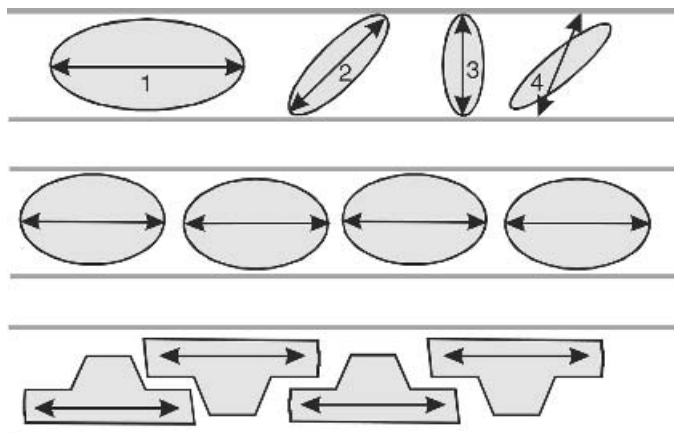


Figure 1.8. Simplified view of different orientations and two arrangements of molecules in the channels of zeolites. *Upper:* Four representative orientations of molecules and their electronic transition moments, indicated by the double arrow. *Middle:* Orientation of large molecules that align parallel to the channel axis and that have no electronic interaction because of their size and shape. *Bottom:* Orientation of large molecules that align parallel to the channel axis and that have some electronic interaction because of their shape.

than two unit cells have no other choice but to align along the channels, see also Figures 1.3 and 1.4. They correspond to case **1** of Figure 1.8, if their first $\pi^* \leftarrow \pi$ electronic transition moment coincides with their long axis. Molecules that are shorter than two unit cells may align as illustrated by the pictures **2** or **3**. Picture **4** indicates that the long axis of the molecule and the transition moment do not coincide. The long molecules **1** will arrange as shown in the middle of Figure 1.8, if their space filling is such that any overlap is prohibited. This means that no orbital interaction occurs and that the material will behave as expected from ordered monomeric molecules of very high concentration in a crystal. More flexible and thinner molecules have the option to arrange as indicated at the bottom of Figure 1.8. In this case, electronic interaction between the molecules occurs with the corresponding consequences.

While DMPOPOP is a case for which orientation **1** and the arrangement in the middle of Figure 1.8 are expected to hold, MV^{2+} is a candidate for orientation **2**, as illustrated in Figure 1.9.

Optical fluorescence microscopy is a powerful and sensitive method for obtaining information about the orientation of luminescent dye molecules in small crystals. In Figure 1.10, we show unpolarized and linearly polarized fluorescence of two perpendicularly lying zeolite L crystals loaded with DSC.

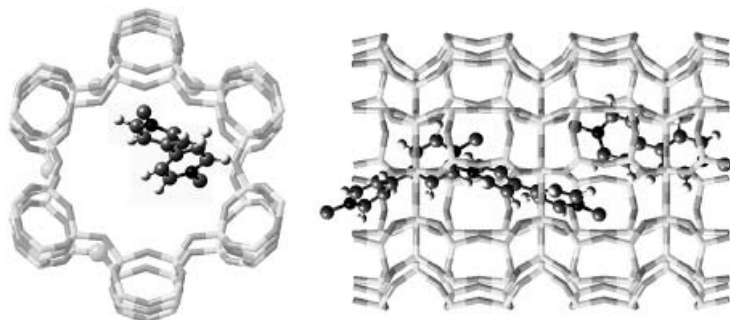


Figure 1.9. Location of MV^{2+} in zeolite L based on X-ray powder diffraction data [25]. *Left:* View along the channel axis showing the position and orientation of a molecule. *Right:* Side view of the channel depicting the arrangement of the molecules.

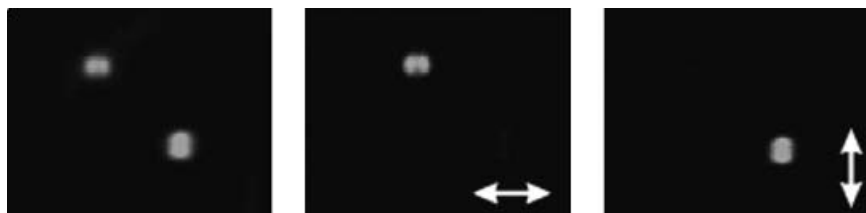


Figure 1.10. Fluorescence microscopy pictures of two 1500-nm long zeolite L crystals containing DSC. Excitation with unpolarized light at 480 nm. *Left:* Unpolarized observation. *Middle* and *right:* Linearly polarized observation. The arrows indicate the polarization direction. (See insert for color representation.)

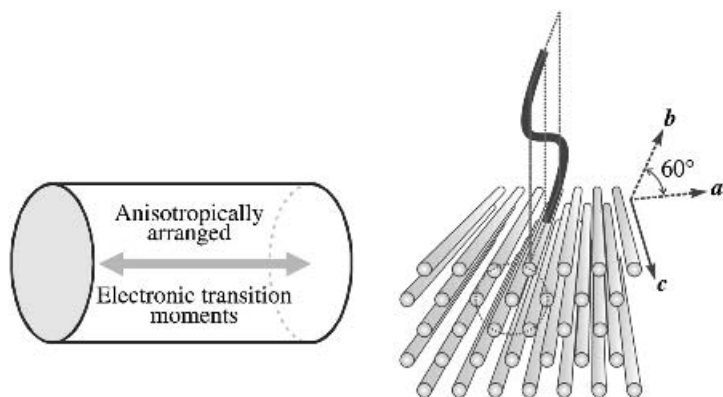


Figure 1.11. Schematic view of a zeolite L crystal loaded with type **1** (Fig. 1.8) dyes with electronic transition moments aligned along the axis of the channels. *Left:* Side view of the morphology, size, and optical anisotropy of the material. *Right:* Front view of a few individual dye-filled channels. The polarization of absorbed and emitted light is indicated.

The exciting light was not polarized. Obviously, the material is optically very anisotropic. Since the atom-to-atom length of DCS is $\sim 15 \text{ \AA}$ and therefore corresponds to almost exactly two unit cells, we conclude that it orients in the channels according to case **1** in Figure 1.8. Other molecules for which we found the same behavior are POPOP, DMPOPOP, DPH, and MBOXE. The optical properties of these materials can be illustrated by means of Figure 1.11 where on the right some individual channels are depicted. Surprisingly, case **4** was observed for Ox^+ loaded zeolite L. We refer to [54] for details.

D. Three-Dye Antenna

We reported the preparation of sophisticated bipolar three-dye photonic antenna materials for light harvesting and transport [22]. The principle is illustrated in Figure 1.12. Zeolite L microcrystals of cylinder morphology are used as host for organizing several thousand dyes as monomers into well-defined zones.

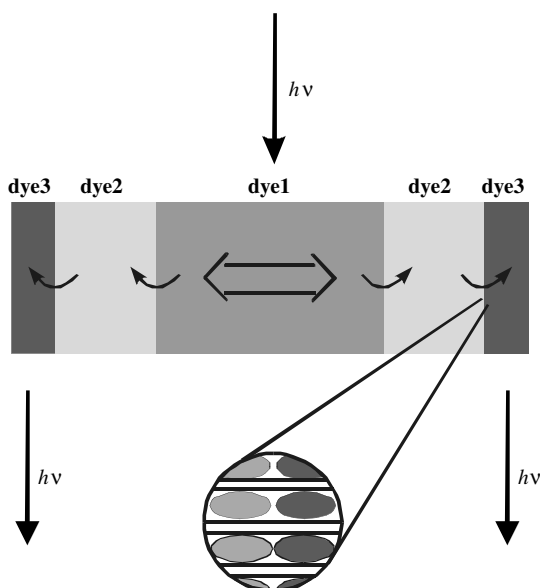


Figure 1.12. Principle of a bipolar three-dye photonic antenna. A crystal is loaded with a blue, a green, and a red emitting dye. After selective excitation of the blue dye in the middle, energy transfer takes place to both ends of the crystal where the red dye fluoresces. (See insert for color representation.)

The enlarged section schematically shows the organization of dye molecules at the domain boundary between dye2 and dye3. The microscopy pictures demonstrate the antenna behavior: They show the red fluorescence of dye3, located at both ends of the crystals, after selective excitation of the blue dye1 in the middle.

The idea that it should be possible to prepare such a sophisticated material emerged from the following qualitative observations, made by means of a standard optical microscope equipped with polarizers and an appropriate set of filters [55]. A side view of a zeolite L crystal of $\sim 1.5 \mu\text{m}$ is illustrated in Figure 1.13. In the first step, we observed in this material the process of insertion of Py^+ and in a second step of Ox^+ into the channels, out of an aqueous suspension of zeolite L crystals containing dissolved Py^+ and Ox^+ , respectively. The zeolite L samples

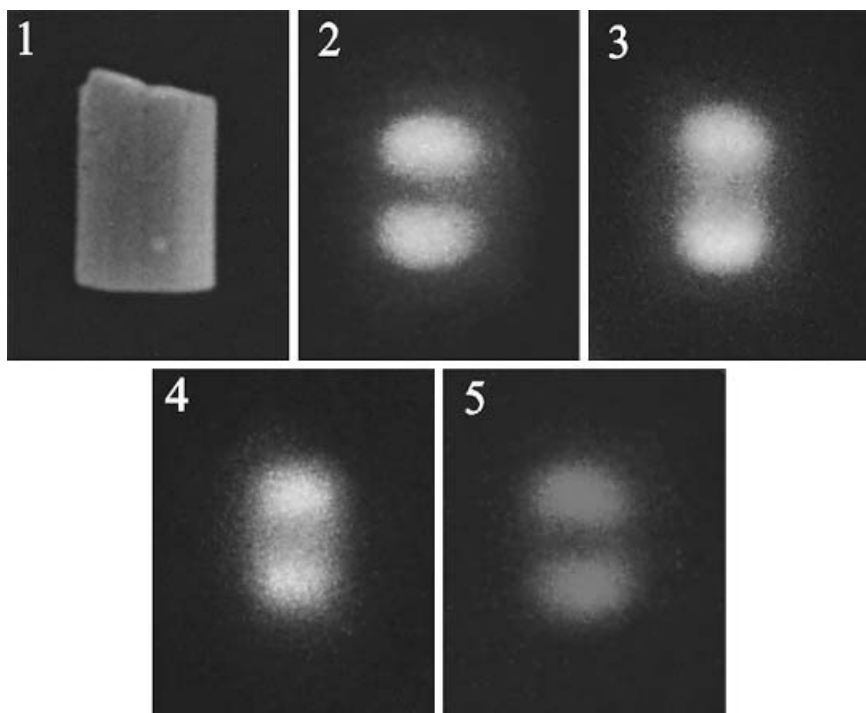


Figure 1.13. (1) Electron microscopy picture of a zeolite L crystal with a length of $\sim 1.5 \mu\text{m}$. (2–5) True color fluorescence microscopy pictures of dye loaded zeolite L crystals. (2–4) Fluorescence after excitation of only Py^+ : (2) after 5-min exchange with Py^+ , (3) after 2 h exchange with Py^+ , (4) after additional 2 h exchange with Ox^+ . (5) The same as 4 but after specific excitation of only Ox^+ . (See insert for color representation.)

2–4 were excited with light of 470–490 nm where only Py^+ absorbs. In **2**, we see how Py^+ penetrates the cylinder from both sides in the direction of the cylinder axis. After an exchange of 5 min under reflux the crystal ends show the typical green fluorescence of Py^+ , while the section in the middle remains dark. The fluorescence is seen over the whole crystal after 2 h exchange, **3**. The dye molecules have moved toward the center now, but the fluorescence at the ends still appears to be more intense. The result after additional exchange with Ox^+ for 2 h is illustrated in **4** and **5**. It leads to crystals, that show the green fluorescence of Py^+ in the center and the fluorescence of Ox^+ at both ends. The yellow color seen in **4** is due to the mixing of the green Py^+ and the red Ox^+ fluorescence. The Ox^+ was not excited directly, but via energy transfer from excited Py^+ molecules. After specific excitation of Ox^+ at 545–580 nm, picture **5**, only the red fluorescence at both ends is visible while the middle part of the zeolite L crystal remains dark. This finding nicely demonstrates that a stacking of Py^+ in the middle and of Ox^+ at both ends of the cylinders is achieved. The electronic absorption and emission spectra of Py^+ and Ox^+ are reported in Figure 1.14. The maxima of the absorption and emission spectra of the dyes inside of the zeolite are slightly shifted to longer wavelengths and they are more structured than those recorded in water.

The general concept of the synthesis of sandwich materials is illustrated in Figure 1.15. In our first report on this [22], we first inserted a neutral dye1 from the gas phase, filling the channels to the desired degree. It was possible to find conditions to insert a cationic dye2 from an aqueous suspension, despite the fact that neutral dyes are usually displaced by water molecules. This process can be well controlled so that a specific desired space is left for the third dye3 to be inserted. It is also possible to insert first a cationic dye and then a neutral one or to use other combinations. The principle can be extended to more than three different dyes.

A nice example that demonstrates the stacking of a neutral and a cationic dye, POPOP and Py^+ , is illustrated in Figure 1.16 on zeolite L crystals of $\sim 2\text{-}\mu\text{m}$ length. We show the luminescent behavior of two selected crystals, which were filled in the middle part by POPOP, and at both ends with a thin layer of Py^+ . The latter is visible in **1**, where Py^+ is excited selectively at 470–490 nm. The characteristic green fluorescence of the Py^+ located at both ends of the crystals is observed. The three other pictures show mainly the luminescence of POPOP on excitation at 330–385 nm. The POPOP fluorescence is strong, because of its much larger concentration, so that the green Py^+ emission can hardly be distinguished. Both **3** and **4** are the same as **2** but observed by means of a polarizer, the direction of which is shown by the arrows. The result is obvious: strong POPOP emission in the direction of the *c* axis, weak emission perpendicular to it. The weak emission at both ends of the crystals in pictures **3** (upper) and **4** (lower) are due to the Py^+ emission, which is nearly perpendicular

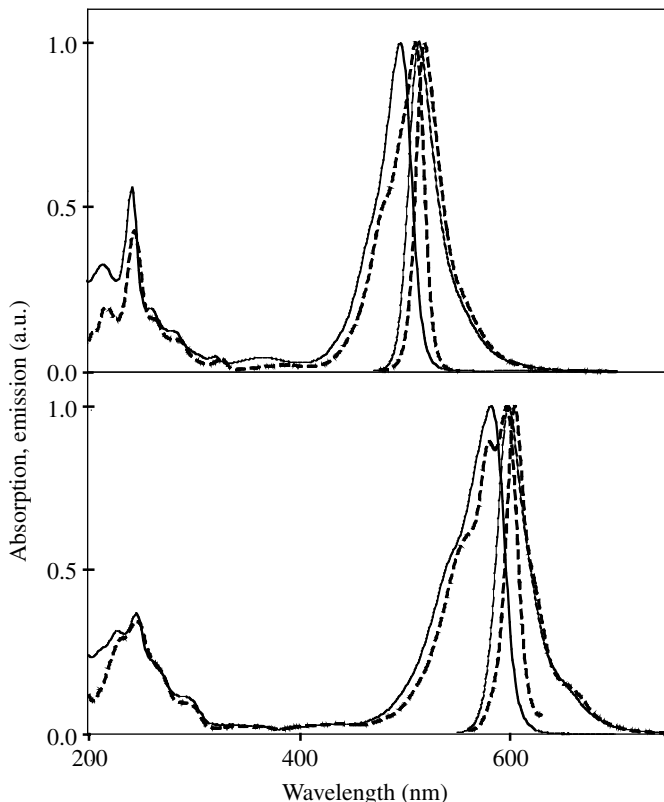


Figure 1.14. Electronic absorption and emission spectra of Py^+ and of Ox^+ in aqueous solution (solid) and in zeolite L (dashed). *Upper:* Py^+ absorption and fluorescence ($\lambda_{\text{ex}} = 460 \text{ nm}$) spectra in aqueous solution and excitation ($\lambda_{\text{em}} = 560 \text{ nm}$) and fluorescence ($\lambda_{\text{ex}} = 460 \text{ nm}$) spectra in zeolite L suspension. *Lower:* Ox^+ absorption and fluorescence ($\lambda_{\text{ex}} = 560 \text{ nm}$) spectra in aqueous solution and excitation ($\lambda_{\text{em}} = 640 \text{ nm}$) and fluorescence ($\lambda_{\text{ex}} = 560 \text{ nm}$) spectra in zeolite L suspension.

to that of the POPOP. Its appearance is mainly due to energy transfer from excited POPOP.

From this, one might assume that the stacking of dye molecules in the channels should always be easily visible by means of optical microscopy, provided that the crystals are large enough. However, this is not the case because special kinetic conditions must hold so that the mean phase boundaries lie perpendicular to the long axis. Other conditions lead to bent mean phase boundaries. The

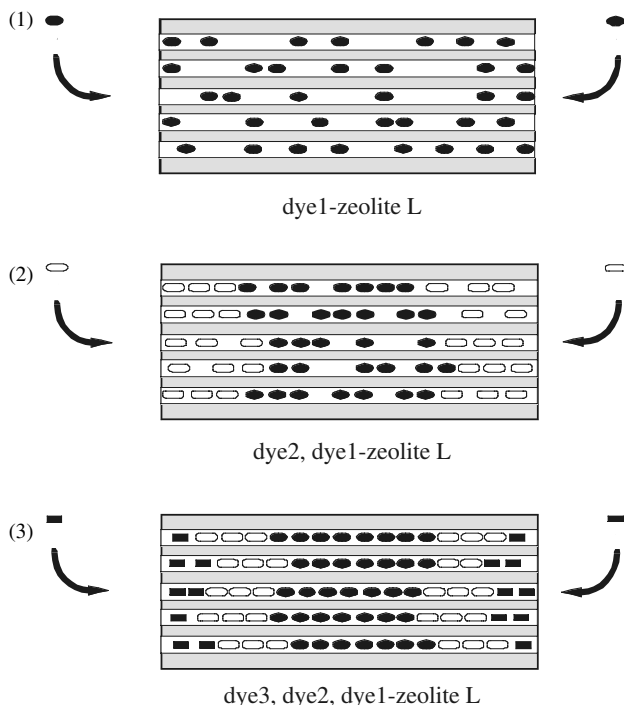


Figure 1.15. Successive insertion of three different dyes into the channels of a zeolite L crystal to form a sandwich material.

two cases are explained in Figure 1.17 for a two dye system, D_1 and D_2 . The upper case is easy to analyze in an optical microscope (see, e.g., Figure 1.16). The lower case is more difficult to detect. The simplest way to obtain the necessary information in this case is to use a thick region with dense filling of D_2 dyes, so that the two D_1 regions appear separated despite of the strong bending of the mean phase boundary.

Figure 1.18 shows fluorescence microscopy images of a bipolar three-dye antenna material with POPOP in the middle, followed by Py^+ and then by Ox^+ . The different color regions that can be observed in this simple experiment are impressive. The red color of the luminescence (1) disappears, when the crystal is observed through a polarizer parallel to the crystal axis while the blue emission disappears when turning the polarizer by 90° . This material is very stable and is easy to handle.

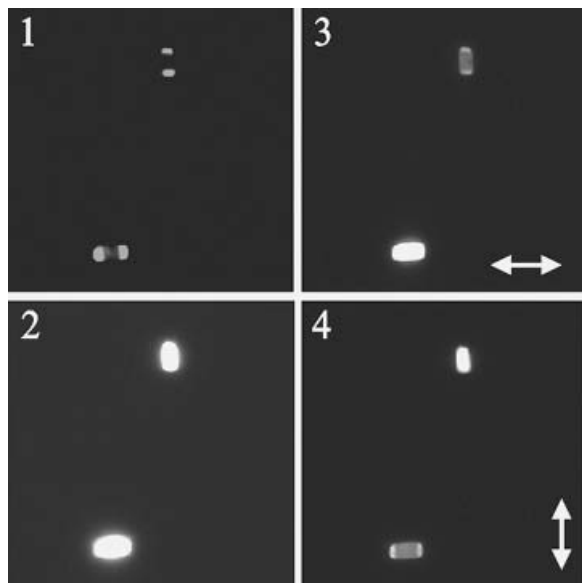


Figure 1.16. True color fluorescence microscopy pictures of Py^+ , POPOP-zeolite L crystals of $\sim 2\text{-}\mu\text{m}$ length. (1) Specific excitation of Py^+ at 470–490 nm. (2) Excitation at 330–385 nm. (3 and 4) Show the same as 2 but after observation with a polarizer. The polarization is indicated by the arrows. (See insert for color representation.)



Figure 1.17. Two kinds of mean phase boundaries of a two dye, D_1 and D_2 , sandwich system. The phase boundaries are sorted according to their distance from the front and back.

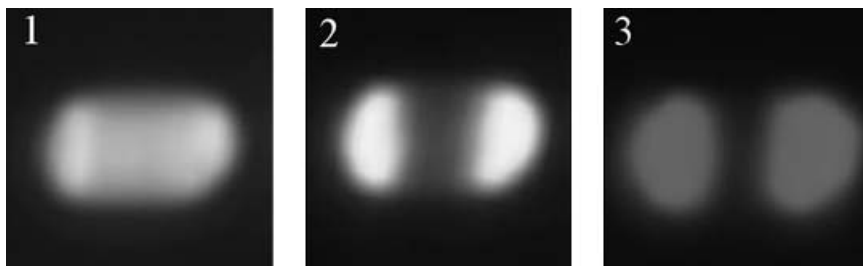


Figure 1.18. Fluorescence microscopy images of an Ox^+ , Py^+ , POPOP-zeolite L crystal of 2000-nm length upon selective excitation of (1) POPOP at 330–385 nm, (2) Py^+ at 470–490 nm, and (3) Ox^+ at 545–580 nm. (See insert for color representation.)

E. The Stopcock Principle

The dye loaded materials described so far exhibit a number of shortcomings. In particular, the stability is unsatisfactory because the dyes can migrate out of the channels resulting in a depletion of the dye loaded zeolite material. Moreover, the task of external trapping of excitation energy or—conversely—of injecting energy at a specific point of the photonic antenna, the realization of a one-directional photonic antenna and the coupling to a specific device are challenging [61].

The stability problem can be solved just by adding a layer of unspecific closure molecules. External trapping and injection of quanta is more demanding. The general approach we are using to solve this problem is to add a “stopcock” as illustrated in Figure 1.19. These closure molecules have an elongated shape consisting of a head and a tail moiety, the tail moiety having a longitudinal extension of more than the dimension of a crystal unit cell along the c axis and the head moiety having a lateral extension that is larger than the channel width and will prevent the head from penetrating into the channel. The channels are therefore terminated in a generally plug-like manner.

Tails can be based on organic and silicon organic backbones. Four types of tails play a role, depending on the desired properties. (1) Nonreactive tails. (2) Tails that can undergo an isomerization after insertion under the influence of irradiation, heat, or a sufficiently small reactive. (3) Reactive tails that can bind to molecules inside of the channels. (4) Luminescent tails, that have the advantage of being protected by the zeolite framework.

The heads of the stopcock molecules must be large enough so that they cannot enter the channels. They should fulfill the stability criteria imposed by a specific application and it should be possible to functionalize them in order to tune the properties of the surface (e.g., the wetting ability, refractive index matching, and

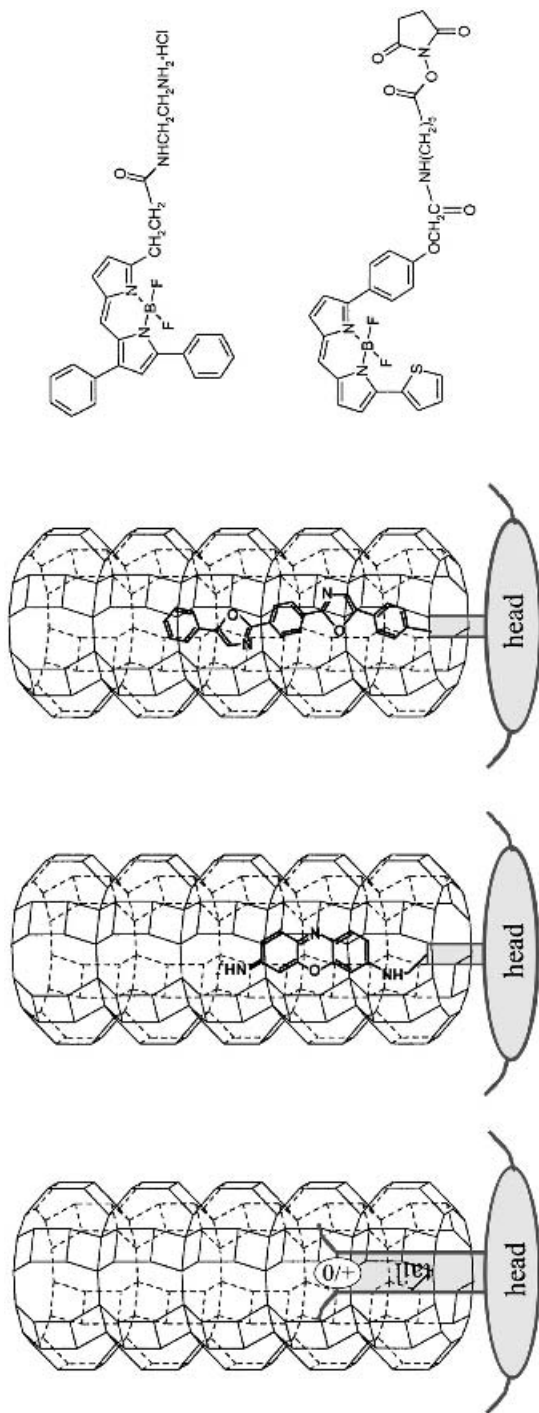


Figure 1.19. *Left:* Typical shape of a head-tail molecule acting as an injector-, acceptor-, or simply as a stopcock. The positive charge is desirable but not necessary for ionic framework hosts. Reactive groups may help to fix the stopcock. *Middle:* Fluorescent molecules that already have been inserted in zeolite L could be modified with an inert head. *Right:* Examples of molecules that could be used as stopcocks with a fluorescent head.

reactivity). Heads can consist of organic, of silicon organic, but also of coordination compounds. In some cases, it is desirable to use heads that bear reactive “arms” so that in an additional step they can interact with each other to form a “monolayer polymer.”

Acceptor-heads should in general be strongly luminescent molecules with a large spectral overlap with the donor molecules located inside of the channels. Since luminescence is quenched by dimerization, the structure must be such that the chromophores do not interact electronically with each other. Nearly all strongly luminescent organic chromophores can be considered since it is always possible to attach inert (e.g., aliphatic) groups so that the head cannot enter the channels. In reality, many of these chromophores will turn out to be less interesting because of stability, shape, toxicity, and so on. A very interesting aspect of the principle discovered by us is that the head can be chosen or functionalized in order to realize the desired properties. The difference of the *donor-heads* with respect to the acceptors is that they must be able to transfer their excitation energy (by a radiationless process, in general dipole–dipole coupling) to acceptors located inside of the channels.

III. TRANSFER OF ELECTRONIC EXCITATION ENERGY

Important transfer and transformation processes of electronic excitation energy that can take place in dye loaded zeolite materials are

Absorption–emission of a photon.

Transformation into chemical energy and the reverse.

Transformation into heat.

Radiationless and radiative transfer to an acceptor.

Stimulated emission.

Upconversion.

Energy-transfer processes in which free photons exist as intermediates are sometimes referred to as “trivial” transfer mechanism. This term is misleading in the sense that such processes (e.g., in combination with internal reflection) can cause very complex and interesting phenomena [61, 65–67]. Radiationless energy-transfer processes have been studied extensively since the pioneering work of Förster [68, 69] and Dexter [70] (see, e.g., [40, 67, 71–73]). Here, we concentrate on the description of one-photon events, specifically with respect to radiationless energy-transfer processes.

A. Radiationless Energy Transfer

Excitation transfer requires some interaction between unexcited and excited molecules M and M^* , respectively. We denote the two molecules under consideration as M and M' . The interaction can then be expressed as occurring between the two configurations MM'^* and M^*M' :

$$\psi_i = \frac{1}{\sqrt{2}} (\psi_{M^*}^{(1)} \psi_{M'}^{(2)} - \psi_{M^*}^{(2)} \psi_{M'}^{(1)}) \quad (23)$$

$$\psi_f = \frac{1}{\sqrt{2}} (\psi_M^{(1)} \psi_{M'^*}^{(2)} - \psi_M^{(2)} \psi_{M'^*}^{(1)}) \quad (24)$$

where i and f denote the initial and final state, respectively, and (1) and (2) refer to electrons. By using H' for the interaction Hamiltonian, the interaction energy β is

$$\beta = u - ex \quad (25)$$

where u denotes the Coulombic interaction and ex the exchange interaction:

$$u = \langle \psi_{M^*}^{(1)} \psi_{M'}^{(2)} | H' | \psi_M^{(1)} \psi_{M'^*}^{(2)} \rangle \quad (26)$$

$$ex = \langle \psi_{M^*}^{(1)} \psi_{M'}^{(2)} | H' | \psi_M^{(2)} \psi_{M'^*}^{(1)} \rangle \quad (27)$$

If more than two electrons should be involved, these expressions can be extended accordingly. The transfer rate k_{el} for electronic excitation energy



can be expressed by means of the Golden Rule as follows:

$$k_{el} = \frac{2\pi}{\hbar} \beta^2 \rho \quad (29)$$

where ρ is the density of states.

We consider situations for which the orbital overlap between M and M' is negligible, this means situations as depicted in the upper and middle part of Figure 1.8, which makes sense because we focus on strongly luminescent materials. In general, orbital overlap causes fast radiationless decay for organic molecules as, for example, observed in dimers [56, 57]. The exchange part ex

vanishes in absence of orbital overlap. In this case, the initial and the final states can be simply expressed as

$$\psi_i = \psi_{M^*} \psi_M \quad (30)$$

$$\psi_f = \psi_M \psi_{M^*} \quad (31)$$

By following the arguments of Förster [74], we distinguish between strong, medium, and weak coupling. Weak interaction means that the interaction energy u is less than the vibrational bandwidth. In this case, energy transfer must be treated as a nonradiative transition between two configurations with continuous energy and the so-called Förster equation as used in the Section III.B can be derived [68–70, 72].

B. Förster Energy Transfer in Dye Loaded Zeolite L

By using the geometrical concepts explained in Section II.A, it is convenient to express the rate constant for energy transfer (ET) from an excited donor i to an acceptor j as follows:

$$k_{ij}^F = \frac{9 \ln(10)}{128 \pi^5 N_A \eta^4} \frac{\phi_i}{\tau_i} J_{ij} G_{ij} p_i p_j \quad (32)$$

$$k_{ij}^F = k_{ij}^{\text{ET}} \quad \text{when sites } i \text{ and } j \text{ are occupied with molecules of different kinds} \quad (33)$$

$$k_{ij}^F = k_{ij}^{\text{EM}} \quad \text{when sites } i \text{ and } j \text{ are occupied with molecules of the same kind} \quad (34)$$

where ϕ_i and τ_i [s] are the fluorescence quantum yield and the intrinsic fluorescence lifetime of the donor, N_A [mol⁻¹] is Avogadro's number, η is the refractive index of the medium, G_{ij} [Å⁻⁶] expresses the geometrical constraints of the sites in the crystal and the relative ordering of the electronic transition moments, p_i and p_j are the occupation probabilities of the sites with excited donors i and acceptors j in the ground state, and J_{ij} [cm³M⁻¹] is the spectral overlap integral between the normalized donor emission and the acceptor absorption spectra. The parameter k_{ij}^{EM} and k_{ij}^{ET} are the rate constants for energy migration from a site i to a site j and energy transfer to a trap J , respectively. Equation (32) relies on nonoverlapping sites and translational symmetry of the sites. It is possible to generalize it by averaging over different site distributions, which is not done here. Expressing G_{ij} as a function of the donor i to acceptor j distance R_{ij} and the relative orientation of the electronic transition moments $(\mu_{S_1 \leftarrow S_0})_i$ and $(\mu_{S_1 \leftarrow S_0})_j$ we write

$$G_{ij} = \frac{\kappa_{ij}^2}{R_{ij}^6} \quad (35)$$

κ_{ij} depends on the angles θ_i , θ_j , and ϕ_{ij} , describing the relative orientation of the electronic transition dipole moments $\mu_{S_1 \leftarrow S_0}$ shown in Figure 1.20(a).

$$\kappa_{ij} = \sin \theta_i \sin \theta_j \cos \phi_{ij} - 2 \cos \theta_i \cos \theta_j \quad (36)$$

Energy transfer between donors and acceptors consisting of different molecules must be distinguished from energy migration that takes place between alike molecules.

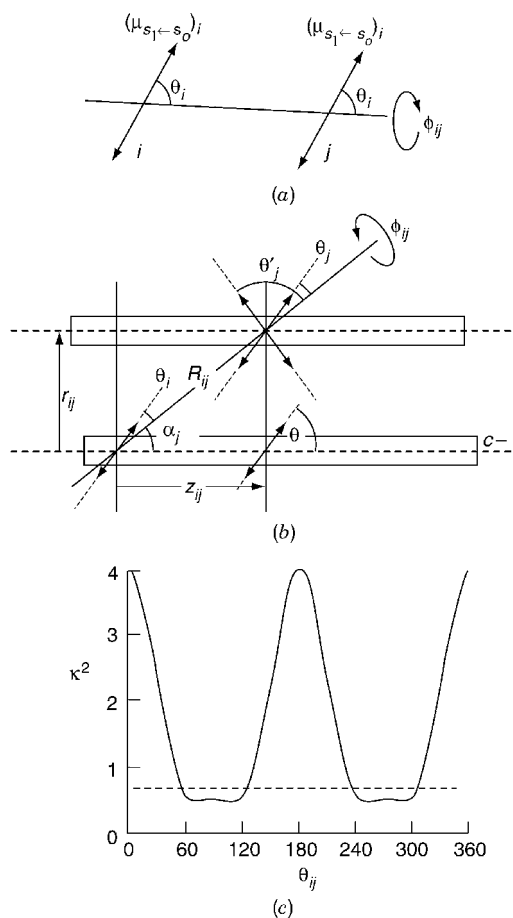


Figure 1.20. (a) Angles θ_i , θ_j , and ϕ_{ij} , describing the relative orientation of the electronic transition dipole moments $\mu_{S_1 \leftarrow S_0}$ between two dye molecules. (b) Relative orientations of the electronic transition dipole moments between two equal dye molecules in the channels of zeolite L. (c) Angular dependence of the orientation factor κ^2 under the anisotropic conditions (b) and averaged over ϕ_{ij} .

We consider a zeolite L crystal that contains alike dye molecules, large enough so that orbital overlap is not possible. This imposes restrictions on the angles between the electronic transition moments we must consider (see Figure 1.20). The two important situations where the electronic transition moments of the molecules are strictly oriented parallel to the channel axis and random orientation have been studied quantitatively in [75]. Here, we consider the angles $\theta - \alpha_{ij}$ and $\pi - \theta + \alpha_{ij}$, which are equally probable. The parameter θ is the angle between the transition moments and the crystal axis, which means that κ_{ij}^2 can be expressed as follows:

$$\kappa_{ij}^2 = [\sin^2(\theta - \alpha_{ij})\cos\phi_{ij} - 2\cos^2(\theta - \alpha_{ij})]^2 \quad (37)$$

The angle α_{ij} is the angle between the site where the excited molecule j is located and any other site i . It can be expressed as

$$\alpha_{ij} = \arccos\left(\frac{z_{ij}}{R_{ij}}\right) \quad (38)$$

where R_{ij} and z_{ij} are given by Eqs. (9) and (11). Averaging over all ϕ_{ij} leads to

$$\kappa_{ij}^2 = \frac{9}{2}\cos^4(\theta - \alpha_{ij}) - \cos^2(\theta - \alpha_{ij}) + \frac{1}{2} \quad (39)$$

The averaging takes into account that each channel is surrounded by six other channels.

Arrangements of densely packed nonoverlapping dye molecules are illustrated in Figure 1.21(a). The molecule in the middle is in its first excited electronic state. It can relax to the ground state either by emitting a photon or by transferring its excitation energy to a molecule in the surrounding. We do not impose any restrictions on the angle ϕ_{ij} , despite the fact that some preferences are to be expected in a hexagonal crystal. Averaging as expressed in Eq. (39) is valid unless crystals containing only very few molecules are investigated. It is interesting to realize that a similarly simple situation can exist for energy transfer between different kinds of molecules, provided they are of similar shape. This situation is shown in Figure 1.21(b). The donor in the middle is in its first electronic excited state. It can either relax to the ground state by emitting a photon or by transferring the excitation energy to a different kind of molecule. This situation can experimentally be realized, for example, by using Py^+ (donor) and Ox^+ (acceptor). Energy migration between alike molecules is another competing process.

We consider a crystal that contains donor molecules in its body and a thin layer of traps at both ends, as illustrated in Figure 1.1. Another way to explain this

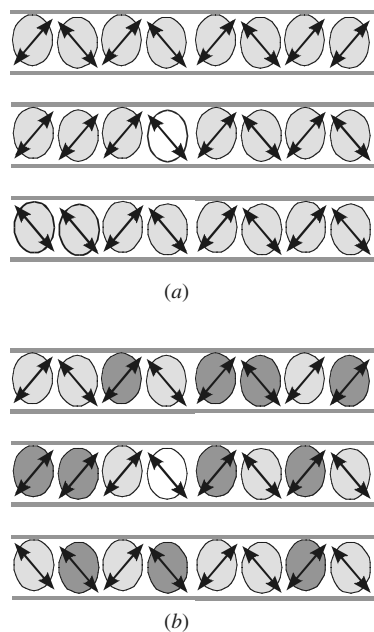


Figure 1.21. (a) Densely packed alike molecules. The white molecule in the middle is in its first electronic excited state. (b) Densely packed donor (darker) and acceptor (lighter) molecules that have the same shape. The white donor in the middle is in its first excited electronic state.

material is shown in Figure 1.22. Somewhere in the bulk a donor is electronically excited by absorbing a photon. We are interested in knowing how fast the excitation energy migrates in the crystal depending on the occupation probability and the characteristics of the dye. We would also like to know how the

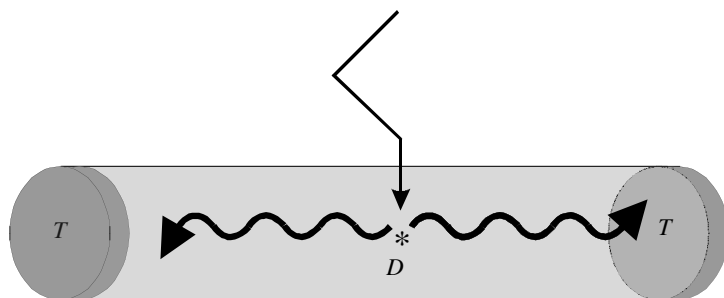


Figure 1.22. Representation of a cylindrical host containing noninteracting donor molecules D and at both ends a layer of traps T .

front-back trapping efficiency depends on these characteristics and on the size of the crystal and we would like to understand the luminescence decay of the donors and of the traps.

We do not know which donor D has been excited. We therefore assume that immediately after irradiation at $t = 0$ all sites i have the same excitation probability $P_i(0)$, while all traps T are in the ground state, hence $P_T(0) = 0$. These probabilities change with time because of energy migration, relaxation processes, and trapping. The excitation probability $P_i(t)$ is governed by the following master equation:

$$\frac{dP_i(t)}{dt} = \sum_j P_j(t)k_{ji}^{\text{EM}} - P_i(t)k_i \quad (40)$$

The sites i are populated by energy migration starting from any other site j with the corresponding rate constants k_{ji}^{EM} . They are depopulated by spontaneous emission, by radiationless decay, by energy migration to all sites $j \neq i$, and by energy transfer to trapping sites J . The depopulation rate of an excited donor i is given by

$$k_i = k_D^F + k_D^{\text{rd}} + k_i^{\text{EM}} + k_i^{\text{ET}} \quad (41)$$

where k_D^F is the intrinsic fluorescence rate constant of the donor and k_D^{rd} is the rate constant of thermal relaxation of the donor including internal conversion and intersystem crossing. The energy migration rate constant k_i^{EM} is obtained by summing up all the individual k_{ij}^{EM} for the energy migration between an excited donor i and surrounding acceptors j :

$$k_i^{\text{EM}} = \sum_{i \neq j} k_{ij}^{\text{EM}} \quad (42)$$

The energy-transfer rate constant k_i^{ET} can be obtained similarly:

$$k_i^{\text{ET}} = \sum_J k_{iJ}^{\text{ET}} \quad (43)$$

The traps are a sink for the electronic excitations of the donors. The donors are considered as the only source for electronic excitation of the traps. The traps, T , can relax by emitting a photon with a rate constant k_T^F or by thermal relaxation k_T^{rd} , which can be expressed as follows:

$$\frac{dP_J(t)}{dt} = \sum_i k_{iJ}^{\text{ET}} P_i(t) - (k_T^F + k_T^{\text{rd}}) P_J(t) \quad (44)$$

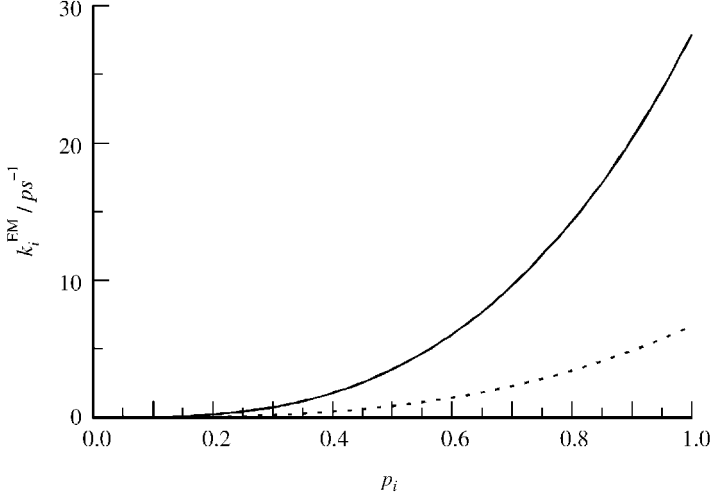


Figure 1.23. Energy migration rate constant k_i^{EM} as a function of the occupation probability p_i for two spectral overlaps (solid: $4.40 \times 10^{-13} \text{ cm}^3/M$ and dashed: $1.05 \times 10^{-13} \text{ cm}^3/M$).

Thus, the time evolution of the excitation probabilities $P_i(t)$ and $P_j(t)$ is described by Eqs. (40) and (44), which allows us to write for time $t + \Delta t$:

$$P_i(t + \Delta t) = P_i(t) + \frac{dP_i(t)}{dt} \Delta t \quad (45)$$

Δt is considered to be small enough so that higher order terms can be neglected. Combining Eqs. (40) and (45) leads to the following homogeneous Markoff chain:

$$P_i(t + \Delta t) = P_i(t)(1 - k_i \Delta t) + \sum_j P_j(t) k_{ji}^{\text{EM}} \cdot \Delta t \quad (46)$$

The Markoff chain that describes the total trapping P_J^0 can be expressed analogously.

$$P_J^0(t + \Delta t) = P_J^0(t) + \sum_i P_i(t) k_{iJ}^{\text{ET}} \Delta t \quad (47)$$

If the fate of the trapped quanta is taken into account, this equation becomes

$$P_J(t + \Delta t) = P_J(t)(1 - (k_T^F + k_T^{\text{rd}})\Delta t) + \sum_i P_i(t) k_{iJ}^{\text{ET}} \Delta t \quad (48)$$

where P_J describes the excitation probability of the traps. The probability that the electronic excitation has reached a trap during the whole time period t after excitation is the trapping probability $P_T(t)$. It is the sum of the trapping P_J^0 of all trapping sites J up to this time.

$$P_T(t) = \sum_J P_J^0(t) \quad (49)$$

The trapping rate dP_T/dt is given by the sum of energy-transfer rates from any site donor i to any trap site J .

$$\frac{dP_T(t)}{dt} = \sum_i \sum_J P_i(t) k_{iJ}^{\text{ET}} \quad (50)$$

The trapping efficiency $P_T(\infty)$ is equal to the sum of the excitation probabilities of all trapping sites J at infinite time after irradiation.

$$P_T(\infty) = \lim_{t \rightarrow \infty} P_T(t) = \lim_{t \rightarrow \infty} \sum_J P_J^0(t) \quad (51)$$

The fluorescence rates of the donors and the traps are given by

$$v_D^F(t) = - \sum_i P_i(t) k_D^F \quad (52)$$

$$v_T^F(t) = - \sum_J P_J(t) k_T^F \quad (53)$$

The average fluorescence rate constants k_D^F and k_T^F are assumed to be the same for all donors and traps, respectively. The integrated fluorescence $FD(t)$ and $FT(t)$ are equal to the probability that the electronic excitation has left the system by donor and trap fluorescence, respectively, at time t after irradiation. The parameter $FD(t)$ is thus equal to the probability that electronic excitation is neither on a site i nor on a site J .

$$FD(t) = 1 - \sum_i P_i(t) - \sum_J P_J(t) \quad (54)$$

By using the same arguments for $FT(t)$, we can write

$$FT(t) = \sum_J P_J(t) \quad (55)$$

We have distinguished between *front trapping*, which refers to traps positioned only on the front side of the cylindrical microcrystals, *front-back trapping*,

which refers to traps on the front and to traps on the back positioned in the slab; *coat trapping*, which refers to traps positioned on the coat of the cylinder; *axial trapping*, which refers to traps located in the central channel; and *point trapping*, which refers to a single trap positioned at the center of the front side [75]. All these trapping types reflect symmetry aspects of the cylinder investigated. Here, we concentrate on front–back trapping $T_{\text{FB}}(t)$, because it is the case for which the best experimental data are available, to date.

Front–Back Trapping. A slab on both sides of the crystal is reserved for traps, as explained in Figures 1.1 and 1.22. Calculation of these trapping types requires knowledge of the excitation distribution \mathbf{Pz} along \mathbf{c} . The excitation distribution \mathbf{Pz} describes the excitation probabilities $P_m(t)$ of whole slabs m . The parameter $P_m(t)$ is equal to the sum of the occupation probabilities of all sites i belonging to slab m . The time evolution of $P_m(t)$ is based on energy migration along \mathbf{c} . The energy-transfer rate constant kz_{mn} from slab m to slab n is assumed to be equal to the sum of the rate constants for energy transfer starting from site $(0,0)$ in slab m to any other site (n_a, n_b) in slab n .

$$kz_{mn} = \sum_{\text{all } (n_a, n_b) \text{ pairs}} k_{mn}[z_{mn}, y(n_a, n_b)] \quad (56)$$

The rate constant kz_{mN} for energy transfer from slab m to a trap containing slab N is calculated analogously, but based on the rate constants k_{mN} . The time evolution of $Pz_m(t)$ and $Pz_N(t)$ are calculated according to Eqs. (46) and (47), respectively.

$$Pz_m(t + \Delta t) = Pz_m(t)(1 - \sum_n kz_{mn}\Delta t) + \sum_n Pz_n(t)kz_{nm}\Delta t \quad (57)$$

$$Pz_N^0(t + \Delta t) = Pz_N^0(t) + \sum_m Pz_m^0(t)kz_{mN}\Delta t \quad (58)$$

$$Pz_N(t + \Delta t) = Pz_N(t)(1 - (k_T^F + k_T^{\text{rd}})\Delta t) + \sum_m Pz_m(t)kz_{mN}\Delta t \quad (59)$$

Both $Pz_m(t)$ and $Pz_N(t)$ express the excitation distribution among the slabs. For front–back trapping, traps are found in the first and the last slab, which we call slabs 0 and m_{max} . Therefore $T_S^{\text{FB}}(t)$ is equal to the sum of the excitation probabilities in both slabs at time t .

$$T_S^{\text{FB}}(t) = Pz_0^0(t) + Pz_{m_{\text{max}}}^0(t) \quad (60)$$

The competition between the trapping and the fluorescence of the donors can be calculated as explained in [75].

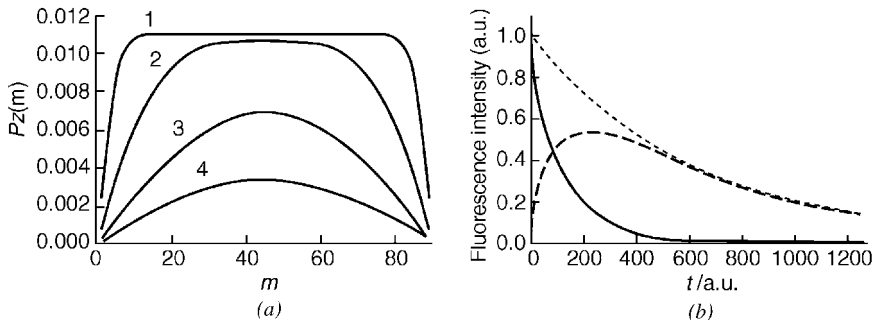


Figure 1.24. (a) Excitation distribution along the channel axis of a zeolite L crystal consisting of 90 slabs under the condition of equal excitation probability at $t = 0$ calculated for front-back trapping. Fluorescence of the donors is assumed. (1) $t = 5$ ps, (2) $t = 10$ ps, (3) $t = 50$ ps, and (4) $t = 100$ ps after irradiation. (b) Luminescence decay of the donors in absence of traps (dotted), in the presence of traps at both ends (solid), and luminescence decay of the acceptors (dashed).

In Figure 1.24(a), we illustrate the influence of trapping and spontaneous emission of the donors on the excitation distribution $Pz(m,t)$ for a row of 90 slabs where the first and the last ones are occupied by traps. Immediately after excitation all slabs have the same excitation probability. The parameter $Pz(m,t)$ is shown after 5, 10, 50, and 100 ps. We observe that the slabs close to the acceptor layers very quickly lose their excitation energy. The trapping rate is proportional to the gradient of $Pz(m,t)$ at the position of the traps. Hence, it depends not only on the remaining excitation probability but also on the excitation distribution. This result is in contrast to the donor fluorescence rate, which depends only on the excitation distribution of the donors, Eq. (52). The fluorescence rate of the traps is proportional to their excitation probability, Eq. (53). We therefore expect a fluorescence decay behavior as illustrated in Figure 1.24(b). The fluorescence decay of the donors becomes much faster in the presence of traps, because of the depopulation due to the irreversible energy transfer to the traps. The fluorescence intensity stemming from the traps initially increases because excited states must first be populated via energy transfer from the donors. It therefore goes through a maximum. Time- and space-resolved luminescence of a photonic dye-zeolite antenna support this physical picture [76].

C. Spectral Overlap

The spectral overlap J_{ij} is an important quantity in radiationless energy transfer and migration, as we have seen in Eq. (32). It is equal to the integral of the corrected and normalized fluorescence intensity $I_i^F(\bar{\nu})$ of the donor multiplied

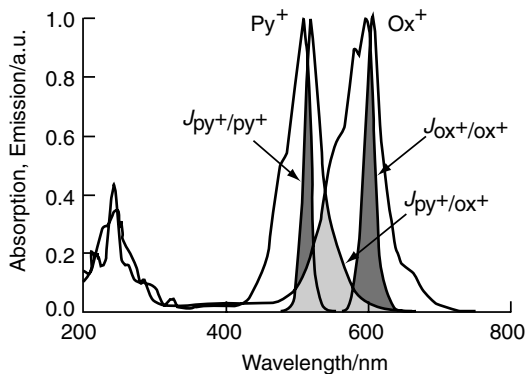


Figure 1.25. Absorption and fluorescence spectra of Py^+ and Ox^+ in zeolite L, measured in an aqueous dispersion. The different spectral overlap regions are shaded.

by the extinction coefficient $\varepsilon_j(\bar{\nu})$ of the acceptor as a function of the wave number $\bar{\nu}$ (it is usually expressed in units of cm^3/M).

$$J_{ij} = \int_0^{\infty} \varepsilon_j(\bar{\nu}) I_i^F(\bar{\nu}) \frac{d\bar{\nu}}{\bar{\nu}^4} \quad (61)$$

The meaning of the spectral overlap is best understood by considering the spectra of the donor (Py^+), acceptor (Ox^+) pair illustrated in Figure 1.25.

It is difficult to measure the oscillator strengths of molecules embedded in a matrix. Despite this, good values of J_{ij} can be determined as a function of the temperature. A procedure we have used to extract the information from excitation spectra was to set the maximum of the excitation spectrum measured at room temperature equal to the extinction coefficient at the absorption maximum in solution. The integrals of the excitation spectra were then normalized to the integral of the corresponding spectrum at room temperature, which is reasonable because the oscillator strength f of a transition $n \leftarrow m$ does not depend on the temperature.

$$f = \frac{8\pi^2 \bar{\nu} c m_e}{3 h e^2} |\vec{\mu}_{nm}^{ed}|^2 \quad (62)$$

where c is the speed of light, m_e is the mass of an electron, h is Planck's constant, and e is the elementary charge. The electronic transition-dipole moment $\vec{\mu}_{nm}^{ed}$ between two wave functions ψ_n and ψ_m is defined as

$$\vec{\mu}_{nm}^{ed} = \langle \psi_n | \vec{\mu}_{ed} | \psi_m \rangle \quad (63)$$

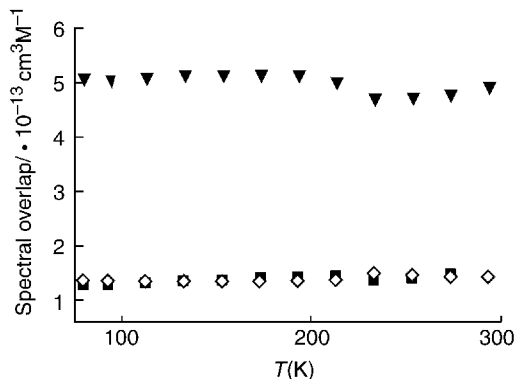


Figure 1.26. Temperature dependence of the spectral overlap of Py⁺/Py⁺ (■), Ox⁺/Ox⁺ (▼), and Py⁺/Ox⁺ (◇) in zeolite L, measured on thin layers coated on quartz plates.

The oscillator strength is a temperature-independent intrinsic property of a molecule. The relation between the molar decadic extinction coefficient ϵ and the oscillator strength f can be expressed as follows:

$$f = 4.32 \times 10^{-9} \int_{\text{band}} \epsilon(\bar{\nu}) d\bar{\nu} \quad (64)$$

A general way to predict the temperature dependence of the spectral overlap is not known. We found that $J_{\text{Py}^+/\text{Py}^+}$, $J_{\text{Ox}^+/\text{Ox}^+}$, and also $J_{\text{Py}^+/\text{Ox}^+}$ do not change significantly in the temperature range from 80 to 300 K (see Fig 1.26). The large difference between the absolute values of the overlap integrals $J_{\text{Py}^+/\text{Py}^+}$, $J_{\text{Ox}^+/\text{Ox}^+}$ is due to a different Stokes shift (140 cm^{-1} for Ox⁺, 560 cm^{-1} for Py⁺). Other cases that show a temperature dependence of the spectral overlap also exist [3].

IV. ELEGANT EXPERIMENTS FOR VISUAL PROOF OF ENERGY TRANSFER AND MIGRATION

Photonic antenna properties of supramolecularly organized dye molecules for light harvesting, transport, and trapping depend critically on their ability to support fast radiationless energy migration and transfer. In this chapter, we present three experiments that beautifully illustrate the exciting capabilities of the dye zeolite material for this purpose. We start with an experiment that we have used many times for classroom demonstration of Förster energy transfer. The second

experiment provides a simple tool to investigate intracrystalline transport of dyes by observing energy transfer from a donor to an acceptor molecule. Very efficient and easily detectable energy migration is illustrated in the third experiment where data of Py^+ loaded and Ox^+ modified zeolites of different lengths are shown.

A. Energy Transfer

The visual proof of energy transfer in this experiment is based on the observation that Py^+ and Ox^+ are incorporated into zeolite L from an aqueous solution with about equal rates. It is therefore possible to control the mean distance between donors D and acceptors A by varying the occupation probability. The main processes are energy transfer and luminescence as illustrated in Figure 1.27. Energy

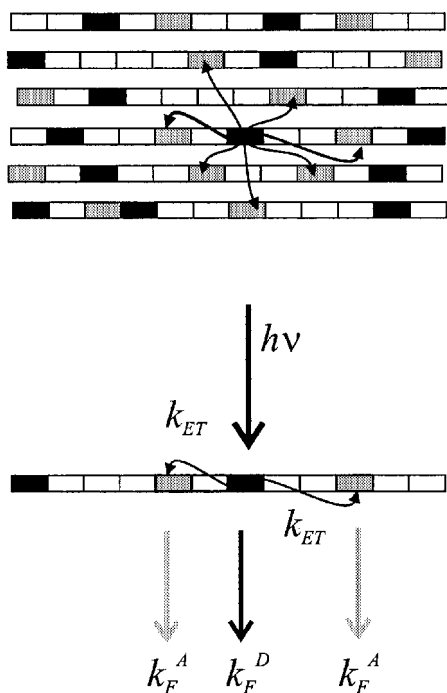


Figure 1.27. Scheme of a few channels of a zeolite L crystal containing acceptor A (gray rectangles) and donor D (black rectangles) molecules. Each rectangle marks a site. The main processes taking place after excitation of a donor are indicated in the lower part. The parameter k_{ET} is the rate constant for energy transfer and k_F^A and k_F^D are the rate constants for fluorescence.

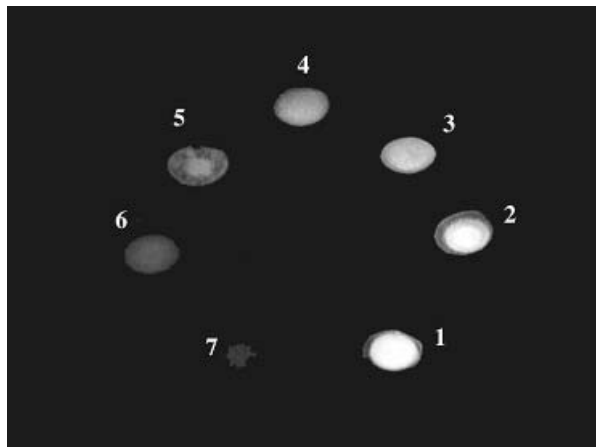


Figure 1.28. Photographic picture of the fluorescence of dye loaded zeolite L layers upon monochromatic irradiation at 485 ± 5 nm and observation through a 500-nm cutoff filter. Both **1** and **7** are references loaded with Py^+ and Ox^+ only and **2–6** contain a 1:1 mixture of Py^+ and Ox^+ of the following concentrations: (**2**) 2.50×10^{-4} M; (**3**) 1.25×10^{-3} M; (**4**), 2.50×10^{-3} M; (**5**) 5.00×10^{-3} M; (**6**) 1.00×10^{-2} M. (See insert for color representation.)

migration between the donor molecules and between the acceptor molecules, which are of similar probability as the energy transfer and radiationless relaxation processes, are not indicated.

The seven luminescent samples shown in Figure 1.28 consist of zeolite L crystals of 300-nm average length filled with different amounts of Py^+ (donor D) and Ox^+ (acceptor A). In all cases, Py^+ was specifically excited at 485 ± 5 nm, where the absorption of Py^+ is strong and that of Ox^+ is very weak, as can be seen from samples **1** and **7**, which are the references. Reference **1** is loaded with 1.25×10^{-3} M Py^+ and **7** is loaded with the same amount of Ox^+ . The other samples contain a 1:1 mixture of Py^+ and Ox^+ of the following concentrations: (**2**) 2.50×10^{-4} M; (**3**), 1.25×10^{-3} M; (**4**) 2.50×10^{-3} M; (**5**) 5.00×10^{-3} M; (**6**) 1.00×10^{-2} M. A rough estimate of the mean donor-to-acceptor distance R_{DA} can be obtained by assuming isotropic conditions and equal concentrations of donor and acceptor:

$$R_{\text{DA}} = \left[\frac{3}{4\pi c_{\text{A}} N_{\text{A}}} \right]^{1/3} \quad (65)$$

N_{A} is the Avogadro number and c_{A} is the concentration of Ox^+ in the zeolite nanocrystal. From this, we obtain the following mean donor–acceptor distances: (**2**) 96 Å; (**3**) 68 Å; (**4**) 54 Å; (**5**) 43 Å; (**6**) 34 Å. The Förster radius for Py^+ to Ox^+ energy transfer in a medium of refractive index of 1.4 is ~ 70 Å, based on the

Py⁺/Ox⁺ spectral overlap, which is $1.5 \times 10^{-13} \text{ cm}^3/M$. In **2**, we mainly observe the green luminescence of Py⁺, which means that energy transfer is unimportant. But the yellow color of **3** is due to a mixture of green and red luminescence, which means that energy transfer is significant in this sample. It becomes more and more important with increasing concentration so that at the end, sample **6**, the red luminescence stemming from excited Ox⁺, is dominant.

The same experiment can be carried out quantitatively. By taking into account radiationless processes, namely, internal conversion k_{IC} , intersystem crossing k_{ISC} , and bimolecular quenching $k_Q[Q]$ with a quencher Q , the time-dependent concentrations of the donor D and the acceptor A in the excited singlet state S_1 , $[D_{S_1}]$ and $[A_{S_1}]$ can be expressed as follows:

$$\frac{d[D_{S_1}]}{dt} = j_{\text{abs}} - (k_{\text{ET}} + k_F^D + k_{\text{IC}}^D + k_{\text{ISC}}^D + k_Q^D[Q])[D_{S_1}] = j_{\text{abs}} - [D_{S_1}] \sum k_d^D \quad (66)$$

$$\frac{d[A_{S_1}]}{dt} = k_{\text{ET}}[D_{S_1}] - (k_F^A + k_{\text{IC}}^A + k_{\text{ISC}}^A + k_Q^A[Q])[A_{S_1}] = k_{\text{ET}}[D_{S_1}] - [A_{S_1}] \sum k_a^A \quad (67)$$

where j_{abs} is the number of photons absorbed per unit time. The fluorescence quantum yield of the donor Φ_F^D and of the acceptor Φ_F^A under stationary conditions is therefore

$$\Phi_F^D = \frac{k_F^D}{\sum k_d^D} \quad (68)$$

$$\Phi_F^A = \frac{k_{\text{ET}}}{\sum k_d^D} \frac{k_F^A}{\sum k_a^A} \quad (69)$$

A quantity that in many cases can easily be measured, even in a heterogeneous system, is the ratio between these two fluorescence quantum yields. We therefore write

$$\frac{\Phi_F^A}{\Phi_F^D} = k_{\text{ET}} \frac{k_F^A}{k_F^D \sum k_a^A} \quad (70)$$

This equation shows that the ratio between the acceptor and donor fluorescence quantum yields is directly proportional to the energy-transfer rate constant k_{ET} . We have shown that this leads to the following linear relation between the fluorescence intensity of the acceptor I_{Ox} and that of the donor I_{Py} , and the occupation probability p_{Ox} of the acceptor [3, 77]:

$$\frac{I_{\text{Ox}}}{I_{\text{Py}}} = Cp_{\text{Ox}} \quad (71)$$

where C is a constant. In Figure 1.29, we show the luminescence spectra measured in an aqueous suspension of similar materials as **2–6** in Figure 1.28.

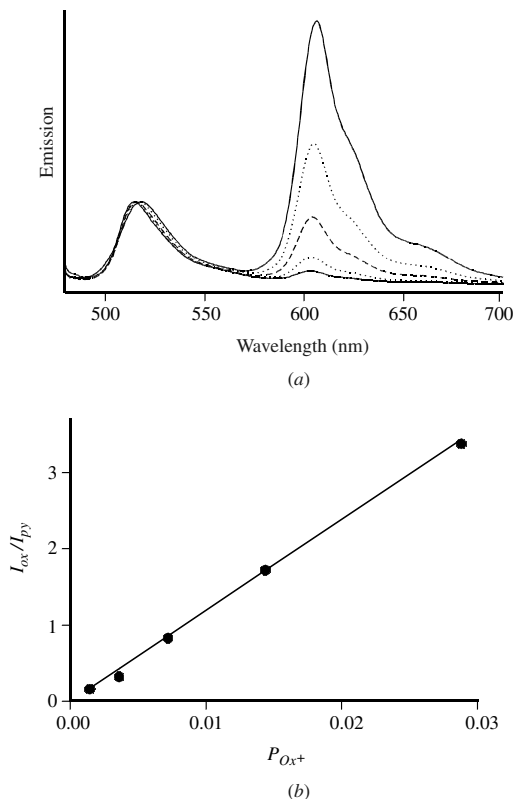


Figure 1.29. Fluorescence of five suspensions with $p_{Ox^-} = 0.0014, 0.0036, 0.0072, 0.0144,$ and 0.0288 after specific excitation of Py^+ at 465 nm for equal p_{Ox^+} and p_{Py^+} . (a) Fluorescence spectra normalized to the same peak height for the Py^+ emission at $\sim 520\text{ nm}$. The intensity of the oxonine emission (peak on the right) increases with increasing p . (b) Ratio of the fluorescence intensity I_{Ox} of Ox^+ and I_{Py} of Py^+ as a function of the loading.

Aqueous suspensions were chosen because this is the easiest way for quantitative measurements. We observe that the acceptor emission is unimportant at low loading and that it becomes dominant at high loading. We also observe that the linear relation between the ratio of the acceptor-to-donor luminescence intensity and the acceptor loading (71) is well fulfilled, with a constant $C = 121$ sites.

B. Intrazeolite Diffusion Monitored by Energy Transfer

The energy transfer between donors Py^+ and acceptors Ox^+ can be used for observing the one dimensional diffusion kinetics of these dyes inside the zeolite

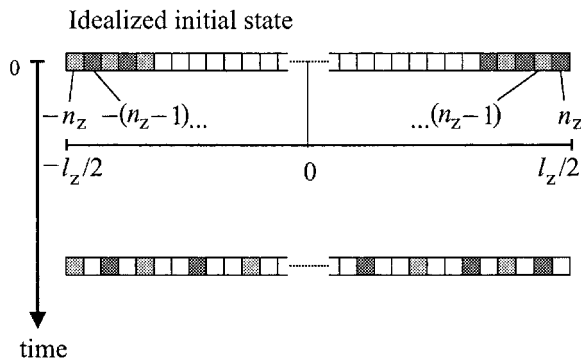


Figure 1.30. Diffusion of dye molecules in the channels of zeolite L. Idealized initial state of a channel and state after diffusion has occurred for some time.

L channels. We assume that in all channels a situation can be prepared as illustrated in Figure 1.30, at the beginning of the experiment. Immediately after all dye molecules have entered the zeolite channels, the maximum energy transfer is observed because the donor-to-acceptor distance is short. The donor-to-acceptor distance increases, and hence the energy-transfer rate decreases, when the molecules diffuse deeper into the channels. From this, the following relation for diffusion kinetics is found under the condition that the initial distributions of the donors and the acceptors are the same, $p_{\text{Py}^+}^0 \approx p_{\text{Ox}^+}^0$, denoted as p^0 . Experimental details can be found in [77].

$$\frac{I_{\text{Ox}^+}}{I_{\text{Py}^+}}(t) = C \frac{(p^0)^2}{\sqrt{8\pi}} \frac{1}{\sqrt{D_0 t}} \quad (72)$$

where C is the same constant as in Eq. (71), t is the time, and D_0 is the dye diffusion coefficient. This finding means that the ratio of the acceptor donor fluorescence intensities is proportional to the inverse square root of time.

Several experimental conditions must be realized for the application of Eq. (72). The donor and acceptor molecules should enter the channels at about the same rate, so that the assumptions made for the initial state are sufficiently well fulfilled. They should not be able to glide past each other once they are inside the channels. The crystals should be so long that molecules entering from both sides do not reach each other in the middle part of the channels during the time of observation. These conditions can be fulfilled for the donor/acceptor pair Py^+/Ox^+ in zeolite L. Moreover, different stages of the diffusion can be observed by means of an optical microscope.

In Figure 1.31, we show fluorescence microscopy images of a sample after 20, 60, and 470-min and 162-h reaction time at 88°C. The images were obtained by

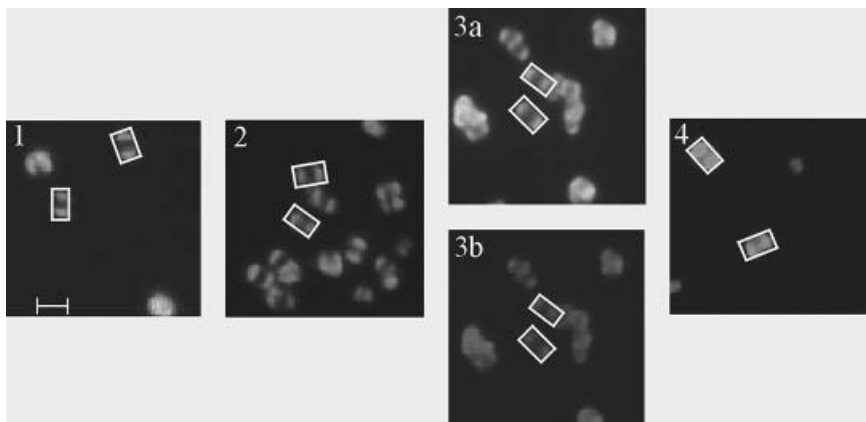


Figure 1.31. Fluorescence microscopy pictures to visualize the diffusion of Ox^+ to Py^+ in zeolite L. The images were taken after (1) 20 min, (2) 60 min, (3) 470 min, and (4) 162 h, respectively. They were obtained by exciting Py^+ at 470–490 nm, with the exception of **3b** where Ox^+ was specifically excited at 545–580 nm. Two crystals of each image are framed. The scale given in **1** corresponds to a length of $1.5 \mu\text{m}$ ($p_{\text{Py}^+} = p_{\text{Ox}^+} = 0.008$). (See insert for color representation.)

specifically exciting Py^+ at 470–490 nm with the exception of **3b** where Ox^+ was excited at 545–580 nm. Two selected crystals are framed to represent what we observed for most crystals. When comparing the images **1**, **2**, **3a**, and **4** (increasing reaction times), we first notice the progress of the insertion (**1** \rightarrow **2**) of the dye molecules and then their diffusion inside the zeolite channels, by considering both the size and the color of the fluorescent spots. The fluorescence of Py^+ appears green and that of Ox^+ deep red, while yellow colors are due to mixtures of red and green. Since Py^+ was excited specifically, the red contribution is due to energy transfer from the excited Py^+ to Ox^+ . We observe two yellow–red spots on both sides of the crystals in image **1**. In image **2**, the spots have extended and, in the middle part, a weak green region appears. While it is hardly visible in **2**, it becomes obvious in **3a**. If Ox^+ is excited specifically, as illustrated in **3b**, its presence in the inner region of the channel can be seen, which also shows that the mean distance between the donor and acceptor molecules is greater in the middle than at the ends of the channels. The green color dominates after the very long reaction time and extends over the whole crystal, as in **4**. The intensity distribution shows that the equilibrium has not yet been reached. Red fluorescence of the same shape is observed if specifically Ox^+ is excited. This means that the distribution of Py^+ and Ox^+ in the crystals is the same or at least similar. The images in Figure 1.31 support the assumptions made that Py^+ and Ox^+ enter the channels of zeolite L at about the same rate.

C. Energy Migration

Now, we show an experiment that illustrates how the photonic antenna principle of Figure 1.1 can be realized. Again Py^+ and Ox^+ were found to be very convenient dyes for this purpose. The channels of zeolite L are first loaded with Py^+ and then modified at both sides with Ox^+ . The latter acts as a luminescent trap that gets excited via radiationless energy transfer from an excited Py^+ . If radiationless relaxation is not considered, Ox^+ can lose its energy only by fluorescence, as it cannot transfer it back to Py^+ because of its lower excitation energy. Fluorescence of excited Py^+ , internal conversion, and intersystem crossing compete with the energy migration and energy transfer. The arrangement shown allows us to investigate the efficiency of energy migration among the Py^+ molecules along the crystals as a function of its lengths. In Figure 1.32, we show the images of some large zeolite L crystals loaded with Py^+ and modified with Ox^+ upon specific excitation of Py^+ at 470–490 nm. Two separate regions of fluorescence can be distinguished. We recall that the resolution of the optical microscope is on the order of one-half of the emitted wavelength. The middle region of the crystals fluoresces green because of the Py^+ . The emission at both ends of the crystals appears yellowish due to the mixing of the green Py^+ and the red Ox^+ emission and Ox^+ is not excited directly but via energy transfer from Py^+ .

We expect that the trapping efficiency increases with decreasing crystal length l_z for otherwise constant parameters, specifically constant p_{Py^+} , because the

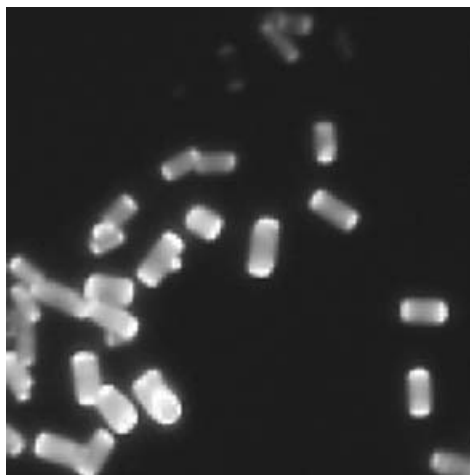


Figure 1.32. True color fluorescence microscopy pictures of Py^+ loaded and Ox^+ modified zeolite L crystals of $\sim 2400\text{-nm}$ length, after excitation of only Py^+ at 470–490 nm. (See insert for color representation.)

excitation energy has to migrate over an increasingly large distance to reach a trap. This result can be tested if materials with different average crystal lengths are available over a significant range. Since we have been able to prepare these materials, experiments with crystals of the following average length were carried out: (1) 300 nm; (2) 500 nm; (3) 850 nm; (4) 1400 nm; and (5) 2400 nm. These crystals were loaded with Py^+ so that the occupation probability was always the same, namely, $p_{\text{Py}^+} = 0.11$. They were then modified with two Ox^+ molecules on average at both ends of the channels. The fluorescence of a thin layer on quartz was measured at room temperature after specific excitation of Py^+ at 460 nm. The fluorescence reported in Figure 1.33 is scaled to the same height at the Py^+ emission maximum, as before. Figure 1.33 shows a very strong increase of the Ox^+

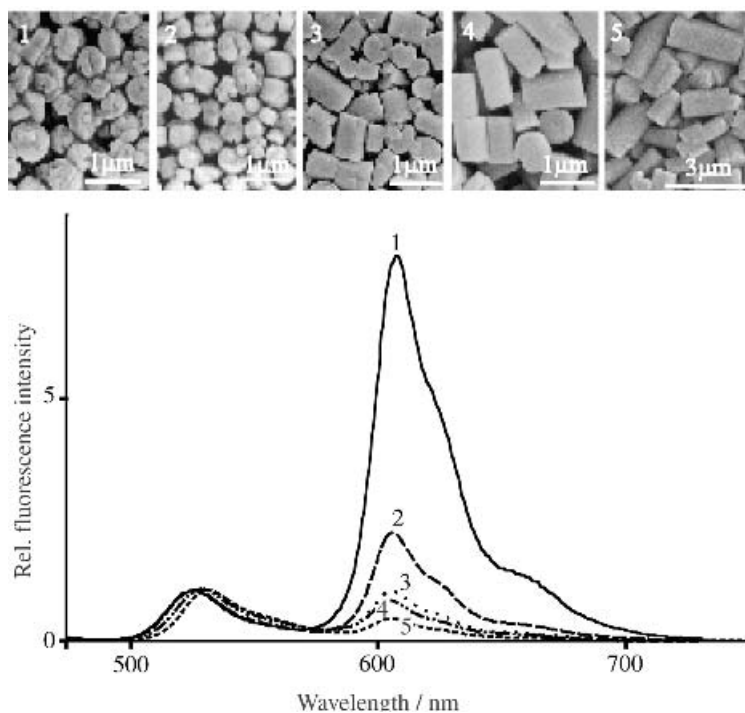


Figure 1.33. *Upper:* electron microscopy (EM) pictures of the investigated zeolite L samples with different crystal length l_z : (1) 300 nm; (2) 500 nm; (3) 850 nm; (4) 1400 nm; (5) 2400 nm. *Lower:* Fluorescence intensity after specific excitation of only Py^+ at 460 nm (scaled to the same height at the maximum of the Py^+ emission) of Py^+ loaded and Ox^+ modified zeolite L crystals with constant Py^+ loading ($p_{\text{Py}^+} = 0.11$) as a function of crystal length. The Ox^+ modification was two molecules at both ends of the channel, on average.

emission with decreasing crystal length l_z . One can calculate that the front-back trapping efficiency increases from 0.33 up to 0.91. This means that in the 300-nm crystals, 90% of the emitted light is due to energy migration along the Py^+ and transfer to the luminescent Ox^+ traps. Interestingly, in these experiments carried out at constant Py^+ loading, there is also a small shift of the Py^+ maximum from 525 nm for the smallest crystals to 530 nm for the largest ones. The maximum of the Ox^+ emission remains at 605 nm. This wavelength shift is most probably due to self-absorption and reemission because the absorption depth increases with increasing crystal size despite the constant p_{Py^+} [53]. The measurements were made on thin dye-loaded zeolite L layers on quartz plates. The pronounced increasing trapping efficiency with decreasing length of zeolite L underlines the interpretation that the antenna behavior is mainly governed by Förster-type energy transfer, supported by some self-absorption and reemission. The latter causes a shift in the maximum of the Py^+ fluorescence spectrum with increased loading, but also with increasing crystal size at constant loading [3]. Some internal reflection may also occur, especially in the larger crystals, where it increases the absorption probability [61].

V. CONCLUSIONS

This chapter shows that zeolite L is a very suitable host for the arrangement of a wide variety of chromophores. The structure of zeolite L is such that the formation of non-fluorescent dimers inside the channels can be prohibited and chromophores can be aligned in a certain direction. We have shown that this host-guest system can be used to make very efficient nanoscale two-directional photonic antenna systems. A broad spectral absorption range can be achieved by using several different cationic and neutral dyes.

It is a challenge to couple the antenna systems to a device (e.g., a semiconductor). It has already been shown that it is possible to prepare organized zeolite monolayers on flat surfaces [78, 79]. For coupling, the interface between the chromophore loaded zeolite L antenna systems and the semiconductor becomes very important. Stopcock molecules are expected to function as a bridge between the chromophores in the zeolite L channels and the device surface, which will open a whole new exciting research area. The first successful experiments with stopcock modified crystals have been reported recently [80].

ACKNOWLEDGMENTS

This research was supported by the Swiss National Science Foundation Project NFP 47 (4047-057481), project NF 2000-053414/98/1 and by the Bundesamt für

Energie, Project 10441. We also thank René Bühler for his help in carrying out the experiments and in preparing the figures. We thank Cindy Hendrikx for measuring and preparing Figure 1.10, and Dr. Stephan Glaus for Figure 1.4.

REFERENCES

1. R. F. Cracknell, K. E. Gubbins, M. Maddox, and D. Nicholson, *Acc. Chem. Res.* **1995**, 28, 281.
2. J. M. Thomas, *Angew. Chem.* **1999**, 111, 3800.
3. G. Calzaferri, D. Brühwiler, S. Megelski, M. Pfenniger, M. Pauchard, B. Hennessy, H. Maas, A. Devaux, and U. Graf, *Solid State Sci.* **2000**, 2, 421.
4. J. P. Langley and J. Hulliger, *Chem. Soc. Rev.* **1999**, 28, 279.
5. A. Douhal, T. Fiebig, M. Chachisvilis, and A. H. Zewail, *J. Phys. Chem. A* **1998**, 102, 1657.
6. Y. S. Park, S. Y. Um, and K. B. Yoon, *J. Am. Chem. Soc.* **1999**, 121, 3193.
7. D. W. Breck, *Zeolite Molecular Sieves*, John Wiley & Sons, Inc., New York, 1974.
8. W. M. Meier, D. H. Olson, and C. Baerlocher, *Atlas of Zeolite Structure Types*, Elsevier, London, 1996.
9. S. L. Suib, *Chem. Rev.* **1993**, 93, 803.
10. F. Schüth, *Chem. Z.* **1995**, 29, 42.
11. G. Calzaferri, M. Lanz, and J. Li, *J. Chem. Soc., Chem. Commun.* **1995**, 1313.
12. K. B. Yoon, Y. S. Park, and J. K. Kochi, *J. Am. Chem. Soc.* **1996**, 118, 12710.
13. U. Vietze, O. Krauss, F. Laeri, G. Ihlein, F. Schüth, B. Limburg, and M. Abraham, *Phys. Rev. Lett.* **1998**, 81, 4628.
14. S. D. Cox, T. E. Gier, G. D. Stucky, and J. Bierlein, *J. Am. Chem. Soc.* **1988**, 110, 2986.
15. L. Werner, J. Caro, G. Finger, and J. Kornatowski, *Zeolites*, **1992**, 12, 658.
16. G. Schulz-Ekloff, in *Advanced Zeolite Science and Applications, Studies in Surface Science and Catalysis*, J. C. Jansen, M. Stöcker, H. G. Karge, and J. Weitkamp, Eds., Elsevier; Amsterdam, 1994, Vol. 85, p. 145.
17. M. Ehrl, F. W. Deeg, C. Bräuchle, O. Franke, A. Sobbi, G. Schulz-Ekloff, and D. Wöhrle, *J. Phys. Chem.* **1994**, 98, 47.
18. R. Hoppe, G. Schulz-Ekloff, D. Wöhrle, C. Kirschhock, and H. Fuess, in *Zeolites and Related Microporous Materials: State of the Art 1994. Studies in Surface Science and Catalysis*, J. Weitkamp, H. G. Karge, H. Pfeifer, W. Hölderich, Eds., Elsevier, Amsterdam, 1994, Vol. 84, pp. 821–827.
19. J. Caro, F. Marlow, and M. Wübbenhorst, *Adv. Mater.* **1994**, 6, 413.
20. D. Wöhrle and G. Schulz-Ekloff, *Adv. Mater.* **1994**, 6, 875.
21. V. Ramamurthy, D. R. Sanderson, and D. F. Eaton, *J. Am. Chem. Soc.* **1993**, 115, 10438.
22. M. Pauchard, A. Devaux, and G. Calzaferri, *Chem. Eur. J.* **2000**, 6, 3456.

23. D. Brühwiler, N. Gfeller, and G. Calzaferri, *J. Phys. Chem. B* **1998**, *102*, 2923.
24. B. R. Müller and G. Calzaferri, *J. Chem. Soc., Faraday Trans.* **1996**, *92*, 1633.
25. B. Hennessy, S. Megelski, C. Marcolli, V. Shklover, C. Bärlocher, and G. Calzaferri, *J. Phys. Chem. B* **1999**, *103*, 3340.
26. G. Calzaferri and N. Gfeller, *J. Phys. Chem.* **1992**, *96*, 3428.
27. F. Binder, G. Calzaferri, and N. Gfeller, *Sol. Energy Mater. Sol. Cells* **1995**, *38*, 175.
28. F. Binder, G. Calzaferri, and N. Gfeller, *Proc. Indian Acad. Sci.* **1995**, *107*, 753.
29. M. Bockstette, D. Wöhrle, I. Braun, and G. Schulz-Ekloff, *Microporous Mesoporous Mater.* **1998**, *23*, 83.
30. P. Lainé, M. Lanz, and G. Calzaferri, *Inorg. Chem.* **1996**, *35*, 3514.
31. D. Brühwiler, R. Seifert, and G. Calzaferri, *J. Phys. Chem. B* **1999**, *103*, 6397.
32. Z. G. Fetisova, A. M. Freiberg, and K. E. Timpmann, *Nature (London)* **1988**, *334*, 633.
33. X. Hu and K. Schulten, *Phys. Today* **1997**, *50*, 28.
34. W. Kühlbrandt and D. N. Wang, *Nature (London)* **1991**, *350*, 130.
35. H. R. Kerp, H. Donker, R. B. M. Koehorst, T. J. Schaafsma, and E. E. van Faassen, *Chem. Phys. Lett.* **1998**, *298*, 302.
36. V. Balzani, S. Campagna, G. Denti, A. Juris, S. Serroni, and M. Venturi, *Sol. Energy Mater. Sol. Cells* **1995**, *38*, 159.
37. V. Balzani, S. Campagna, G. Denti, A. Juris, S. Serroni, and M. Venturi, *Coord. Chem. Rev.* **1994**, *132*, 1.
38. C. V. Kumar and A. Chaudhary, *Microporous Mesoporous Mater.* **1999**, *32*, 75.
39. L. Jullien, J. Canceill, B. Valeur, E. Bardez, and J.-M. Lehn, *Angew. Chem.* **1994**, *106*, 2582.
40. H. Bücher, K. H. Drexhage, M. Fleck, H. Kuhn, D. Möbius, F. P. Schäfer, J. Sondermann, W. Sperling, P. Tillmann, and J. Wiegand, *Mol. Crystals* **1967**, *2*, 199.
41. F. Willig, in *Photochemical Conversion and Storage of Solar Energy*, E. Pelizzetti, and M. Schiavello, Eds., Kluwer Academic Publishers, Dordrecht, 1991, pp. 235–249.
42. N. Tamai, T. Yamazaki, and I. Yamazaki, *J. Phys. Chem.* **1987**, *91*, 841.
43. J. A. Pescatore, Jr., and I. Yamazaki, *J. Phys. Chem.* **1996**, *100*, 13333.
44. B. A. Gregg and U. Resch, *J. Photochem. Photobiol., A: Chem.* **1995**, *87*, 157.
45. S. E. Webber, *Chem. Rev.* **1990**, *90*, 1469.
46. D. M. Watkins and M. A. Fox, *J. Am. Chem. Soc.* **1996**, *118*, 4344.
47. V. Balzani, P. Ceroni, S. Gestermann, M. Gorka, C. Kauffmann, M. Maestri, and F. Vögtle, *ChemPhysChem* **2000**, *4*, 224.
48. D. M. Sturmer and D. W. Heseltine, in *The Theory of the Photographic Process*, T. H. James, Ed., Macmillan Publishing Co., New York, 1977, pp. 194–234.
49. C. A. Bigozzi, R. Argazzi, J. R. Schoonover, G. J. Meyer, and F. Scandola, *Sol. Energy Mater. Sol. Cells* **1995**, *38*, 187.
50. H. Tributsch, *Proc. IPS-10*, Z. W. Tian and Y. Cao, Eds., Intern. Academic Publishers, Beijing, 1993, pp. 235–247.

51. R. Memming and H. Tributsch, *J. Phys. Chem.* **1971**, *75*, 562.
52. N. Gfeller, S. Megelski, and G. Calzaferri, *J. Phys. Chem. B* **1999**, *103*, 1250.
53. S. Megelski and G. Calzaferri, *Adv. Funct. Mater.*, **2001**, *11*, 277.
54. S. Megelski, A. Lieb, M. Pauchard, A. Drechsler, S. Glaus, C. Debus, A. J. Meixner, and G. Calzaferri, *J. Phys. Chem. B* **2001**, *105*, 23.
55. N. Gfeller, S. Megelski, and G. Calzaferri, *J. Phys. Chem. B* **1998**, *102*, 2433.
56. M. Kasha, H. R. Rawls, and M. Ashraf El-Bayoumi, *Pure Appl. Chem.* **1965**, *11*, 371.
57. E. G. McRae and M. Kasha, *J. Chem. Phys.* **1958**, *28*, 721.
58. M. Tsapatsis, T. Okubo, M. Lovallo, and M. E. Davis, *Mater. Res. Soc. Symp. Proc.* **1995**, *371*, 21.
59. S. Ernst and J. Weitkamp, *Catal. Today* **1994**, *19*, 27.
60. P. A. Anderson, A. R. Armstrong, A. Porch, P. P. Edwards, and L. J. Woodall, *J. Phys. Chem. B*, **1997**, *101*, 9892.
61. G. Calzaferri, M. Pauchard, H. Maas, S. Huber, A. Khatyr, T. Schaafsma, *J. Mater. Chem.* **2002**, *12*, 1.
62. T. Ohsuna, Y. Horikawa, and K. Hiraga, *Chem. Mater.* **1998**, *10*, 688.
63. A. Kunzmann, R. Seifert, and G. Calzaferri, *J. Phys. Chem. B* **1999**, *103*, 18.
64. S. Hashimoto, M. Hagiri, N. Matsubara, and S. Tobita, *Phys. Chem. Phys.* **2001**, *3*, 5043.
65. J. S. Batchelder, A. H. Zewail, and T. Cole, *Appl. Opt.* **1979**, *18*, 3090.
66. P. R. Hammond, *J. Chem. Phys.* **1979**, *70*, 3884.
67. G. Juzeliūnas and D. L. Andrews, in *Resonance Energy Transfer*, D. L. Andrews and A. A. Demidov, Eds., John Wiley & Sons, Chichester, UK, 1999, pp. 65–107.
68. T. Förster, *Ann. Phys. (Leipzig)* **1948**, *2*, 55.
69. T. Förster, *Fluoreszenz organischer Verbindungen*, Vandenhoeck & Ruprecht, Göttingen, 1951.
70. D. L. Dexter, *J. Chem. Phys.* **1953**, *21*, 836.
71. K. B. Eisenthal and S. Siegel, *J. Chem. Phys.* **1964**, *41*, 652.
72. H. Kuhn, *J. Chem. Phys.* **1970**, *53*, 101.
73. J. R. Lacowicz, *Principles Fluorescence Spectroscopy*, 2nd ed., Kluwer Academic/Plenum, New York, 1999.
74. T. Förster, in *Comparative Effects of Radiation*, M. Burton et al., Eds., John Wiley & Sons, Inc., New York, 1960, pp. 300–319.
75. N. Gfeller and G. Calzaferri, *J. Phys. Chem. B* **1997**, *101*, 1396.
76. M. Pauchard, S. Huber, R. Méallet-Renault, H. Maas, R. Pansu, and G. Calzaferri, *Angew. Chem. Int. Ed.* **2001**, *40*, 2839.
77. M. Pfenniger and G. Calzaferri, *ChemPhysChem.* **2000**, *1*, 211.
78. P. Lainé, R. Seifert, R. Giovanoli, and G. Calzaferri, *New J. Chem.* **1997**, *21*, 453.
79. K. Ha, Y.-J. Lee, D.-Y. Jung, J. H. Lee, and K. B. Yoon, *Adv. Mater.* **2000**, *12*, 1614.
80. H. Maas and G. Calzaferri, *Angew. Chem. Int. Ed.* **2002**, *41*, 2284.

PROTON-TRANSFER REACTIONS IN BENZOPHENONE/ *N,N*-DIMETHYLANILINE PHOTOCHEMISTRY

Kevin S. Peters

Department of Chemistry and Biochemistry,
University of Colorado, Boulder, CO 80304

CONTENTS

- I. Introduction
- II. Photoreduction of Benzophenone by *N,N*-Dimethylaniline
- III. Theoretical Models for Proton Transfer
 - A. Classical Model
 - B. Semiclassical Model
 - C. Proton Tunneling
 - D. Dogonadze, Kuznetsov, and Levich (DKL) Model
 - E. Borgis–Hynes (BH) Model
 - F. Lee–Hynes (LH) Model
 - G. Comparison of Semiclassical and Quantum Models

- IV. Benzophenone–*N,N*-Dimethylaniline Proton Transfer
 - A. Energetics
 - B. Kinetics
 - C. Application of the BH Model to the Kinetics of Proton Transfer
 - D. Application of the LH Model to the Kinetics of Proton Transfer
- V. Comparison with Other Molecular Systems
- VI. Summary
 - Acknowledgment
 - References

I. INTRODUCTION

Proton transfer is among the most important class of reactions occurring in all of chemistry [1–3]. Given the ubiquity of these processes in nature, it is important that a detailed understanding of the parameters that control the reaction dynamics be achieved. Toward this end, both theory and experiment have worked toward elucidating the nature of the molecular processes that control the dynamics of proton transfer. Surprisingly, during the past few years there has been a major revamping of the models that serve to depict the proton-transfer process. This revamping is having a profound influence in the field of reaction dynamics in organic and biochemistry.

The model that has been extensively employed in interpreting the kinetics of proton transfer, as well as hydrogen atom and hydride transfer, is based on transition state theory [4–6]. This theory assumes a classical transition state defined by a free energy maximum along the proton-transfer reaction coordinate over which the proton passes. However, in the last few years the basic tenant of transition state theory, that the proton passes over the free energy maximum, has been brought into question [7–9]. Recent theoretical studies reveal that when there exists a free energy barrier along the proton-transfer coordinate, instead of the proton surmounting the potential energy barrier the proton tunnels through the potential energy barrier, even at ambient temperature [10–19]. If these proposals are valid, then, given the importance of proton-transfer reactions, a reformulation of the mechanism of proton transfer will have a profound impact on our understanding of the nature of these reaction processes.

Theorists have been addressing the issue of tunneling as the predominant reaction mode in proton-transfer reactions for more than 20 years [10]. However, from an experimental perspective, there have been few significant advances relating to tunneling as a predominant reaction mode in the condensed phase at ambient temperature [20, 21]. In part, this is because design of experiments to test the predictions of the various theoretical formulations has been exceedingly difficult.

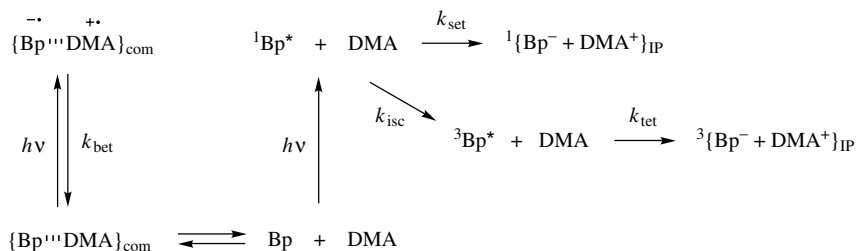
Since the rate for the tunneling of a proton is strongly dependent on barrier width, it is necessary that the molecular systems to be studied constrain the distance of proton transfer. Also, since the various theoretical models make predictions as to how the rate of proton transfer should vary with a change in free energy for reaction as well as how the rate constant should vary with solvent, it is desirable to study molecular systems where both the driving force for the reaction and the solvent can be varied widely.

A molecular system that is ideally suited to the study of the dynamics of proton transfer, in which a wide range of solvents can be employed and the thermodynamic driving force for the reaction can be varied, is the photochemical reduction of benzophenone by *N,N*-dimethylaniline [20, 22–24]. Under the appropriate conditions, the triplet state of benzophenone is reduced by the amine. Fast electron transfer produces a triplet contact radical ion pair and is followed by a proton transfer to produce a triplet radical pair. Since the triplet contact radical ion pair has the structure of a π -stacked complex [20], the distance for proton transfer is constrained by the Coulombic interaction of the complex. By placing substituents at the 4 and 4' positions of the benzophenone, the driving force for proton transfer can be varied by >10 kcal/mol [20]. The proton transfer occurs over a wide variation in solvent polarity so that solvents ranging from cyclohexane to acetonitrile can be utilized. Thus, the study of the kinetics of proton transfer between benzophenone and *N,N*-dimethylaniline provides a molecular system for probing the validity of the various theoretical models pertaining to proton-transfer processes.

The following discussion begins by presenting an in-depth view of the mechanism for the photochemical reduction of benzophenone by *N,N*-dimethylaniline. This discussion is followed by a presentation of the theoretical models describing the parameters controlling the dynamics of proton-transfer processes. A survey of our experimental studies is then presented, followed by a discussion of these results within the context of other proton-transfer studies.

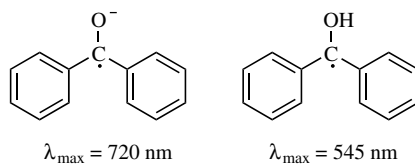
II. PHOTOREDUCTION OF BENZOPHENONE BY *N,N*-DIMETHYLANILINE

The reaction pathways by which the net transfer of a hydrogen atom from an amine to a photoexcited ketone has been extensively examined in the nanosecond [23, 25–30], picosecond [20, 22, 31–33], and femtosecond [24] time domains. The following mechanism, as it pertains to the photochemical reduction of benzophenone (Bp) by *N,N*-dimethylaniline (DMA), is derived from these numerous studies. Only an overview of the mechanism will be presented. The details of the studies leading to the mechanism will not be given; for specifics, the reader is referred to the original literature.



Scheme 2.1

The overall reaction scheme for the electron-transfer process associated with the photochemical reduction of Bp by DMA is presented in Scheme 2.1. Prior to photoexcitation, Bp and DMA in CH_3CN form a Mulliken ground-state charge-transfer (CT) complex, $\{\text{Bp}::\text{DMA}\}_{\text{com}}$ with an equilibrium constant on the order of $K = 0.1$, derived from a Benesi–Hildebrand plot analysis [24]. At high concentrations of DMA ($> 0.5 M$), a charge-transfer band appears to the red (350–400 nm) of the $n-\pi^*$ band of Bp. Thus, irradiation in the range of 370–400 nm selectively excites the charge-transfer band, transforming the ground-state complex $\{\text{Bp}::\text{DMA}\}_{\text{com}}$ into a singlet radical ion pair (IP) species, ${}^1\{\text{Bp}^-::\text{DMA}^+\}_{\text{com}}$. Mataga and co-workers [24] examined the photophysics of the CT complex. Following the 397-nm irradiation of $\{\text{Bp}::\text{DMA}\}_{\text{com}}$, the ${}^1\{\text{Bp}^-::\text{DMA}^+\}_{\text{com}}$ decays by back electron transfer, k_{bet} , to reform the ground-state (CT) complex on the timescale of 85 ps; the dynamics of the decay were obtained from the decay of the Bp radical ion absorbing in the region of 650–800 nm, (Scheme 2.2). The diffusional separation of ${}^1\{\text{Bp}^-::\text{DMA}^+\}_{\text{com}}$ to free radical ions is not observed, even in acetonitrile, as no radical anions of Bp are observed for the time domain beyond 200 ps [24]. Also, no proton transfer occurs following the production of ${}^1\{\text{Bp}^-::\text{DMA}^+\}_{\text{com}}$, as evidenced by the lack of an absorption at 545 nm that would correspond to the ketyl radical of benzophenone (Scheme 2.2). However, it may be that proton transfer does occur to produce a singlet radical pair that then decays by back hydrogen atom transfer on a timescale substantially faster than 85 ps, thus leading to a lack of observation of the ketyl radical.



Scheme 2.2

Before addressing the electron- and proton-transfer processes, the photophysics of Bp is considered. In the absence of DMA, irradiation of BP produces the first excited singlet state, $^1\text{Bp}^*$, whose electronic configuration is $S_1(n\pi^*)$ with an energy of 74 kcal/mol and having an absorption maximum for the $S_n \leftarrow S_1$ transition at 575 nm. The $^1\text{Bp}^*$ state decays in acetonitrile with a unit efficiency of 9 ± 2 ps, to form the triplet state of benzophenone, $^3\text{Bp}^*$, whose electronic configuration is $T_1(n\pi^*)$ with an energy of 69 kcal/mol and having an absorption maximum for the $T_n \leftarrow T_1$ transition at 525 nm [24, 32]. The $^3\text{Bp}^*$ state persists on the millisecond timescale in the absence of quenchers.

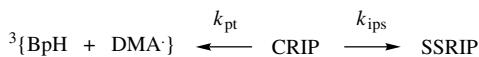
When uncomplexed Bp is irradiated in the presence of DMA, it produces $^1\text{Bp}^* + \text{DMA}$ (Scheme 2.1). The fate of $^1\text{Bp}^*$ is then determined by the concentration of DMA as well as the nature of the solvent; either $^1\text{Bp}^*$ may undergo intersystem crossing, k_{isc} , to form $^3\text{Bp}^*$ or be reduced to the radical ion, Bp^- , by electron transfer from DMA. The kinetics of the singlet electron-transfer process, k_{set} , to produce a singlet radical ion pair $^1\{\text{Bp}^- + \text{DMA}^+\}_{\text{IP}}$ are governed by bimolecular diffusion and thus k_{set} is dependent on the concentration of DMA. At 1 M DMA, Mataga estimates that k_{set} be of the order of $10^{11} \text{M}^{-1} \text{s}^{-1}$ so that at high concentrations, the formation of $^1\{\text{Bp}^- + \text{DMA}^+\}_{\text{IP}}$ is competitive with the formation of $^3\text{Bp}^* + \text{DMA}$, $k_{\text{isc}} = 1.1 \times 10^{11} \text{s}^{-1}$ [24]. The rate constant for the reduction of the triplet state of Bp by DMA, k_{tet} , to form the triplet radical ion pair, $^3\{\text{Bp}^- + \text{DMA}^+\}$, have not been explicitly determined, but are thought to be of the same magnitude as that for k_{set} .

A fundamental question relating to the electron-transfer processes that form $^1\{\text{Bp}^- + \text{DMA}^+\}_{\text{IP}}$ and $^3\{\text{Bp}^- + \text{DMA}^+\}_{\text{IP}}$ is whether the electron transfer occurs at short-range to produce contact radical ion pairs or long-range transfer to produce solvent separated radical ion pairs. This topic has been a subject of extensive discussion and has been reviewed recently for a great variety of electron-transfer systems other than ketones and amines [34]. In our original picosecond studies of the photoreduction of BP by DMA, we theorized that the reduction of $^3\text{Bp}^*$ by DMA in acetonitrile led to the formation of a solvent separated radical ion pair (SSRIP) and that prior to proton transfer the SSRIP must collapse to a contact radical ion pair (CRIP) [23]. This assumption was based on the pioneering work of Weller and co-workers [35–37] who examined the fluorescence quenching of anthracene by a series of electron donors. The lack of exciplex emission in the quenching process in polar solvents lead Weller to propose that the quenching of the excited state of anthracene by electron transfer led to the production of a solvent separated radical IP that would not display exciplex emission. However, recent electron-transfer studies now suggest that for $^3\{\text{Bp}^- + \text{DMA}^+\}_{\text{IP}}$, based on energetic considerations as well as the dynamics of proton transfer, the electron transfer occurs when the two species are in contact, leading to the production of the contact radical ion pair [24]. The energetic argument is based on the driving force for the reaction $^3\text{Bp}^* + \text{DMA} \rightarrow$

$^3\{\text{Bp}^- + \text{DMA}^+\}_{\text{IP}}$ of -9.7 kcal/mol, which is derived from the difference in energies of $^3\text{Bp}^*$ (69 kcal/mol) and $^3\{\text{Bp}^- + \text{DMA}^+\}$ (59.3 kcal/mol), obtained from oxidation and reduction potentials [24]. From both a theoretical and an experimental perspective, when ΔG for electron transfer is no more negative than about -10 kcal/mol in a polar solvent such as acetonitrile, the electron transfer occurs when the two species are in contact and not through long-range electron transfer. Also, as will be shown below, immediately following the production of $^3\{\text{Bp}^- + \text{DMA}^+\}_{\text{IP}}$ in acetonitrile, proton transfer, which can only occur when the two species are in direct contact, commences.

The nature of the radical IP formed in the reduction of the singlet state of Bp to yield $^1\{\text{Bp}^- + \text{DMA}^+\}_{\text{IP}}$ has yet to be firmly established. The ΔG for the reaction $^1\text{Bp}^* + \text{DMA} \rightarrow ^1\{\text{Bp}^- + \text{DMA}^+\}_{\text{IP}}$ is -14.7 kcal/mol. From Gould and Farid's study of the electron-transfer quenching of S_1 for dicyanoanthracenes by alkylbenzenes that occurs when ΔG for the reaction is -15 kcal/mol or more negative only solvent separated radical ion pairs are formed in acetonitrile [38–40]. However, we found that the quenching of the S_1 state of *trans*-stilbene by fumaronitrile through electron transfer, which has a ΔG of -17.5 kcal/mol, forms only contact radical ion pairs in acetonitrile [41,42]. Clearly, energetics arguments alone cannot be used to establish the form of radical IP produced upon electron transfer when the driving force for reaction is large, > -15 kcal/mol. Given the limited number of kinetic studies addressing the issue of the nature of the radical IP formed upon electron transfer as a function of driving force, the nature of the radical IP formed by the quenching of $^1\text{Bp}^*$ by DMA cannot be established employing only energetic arguments.

The fates of the radical ion pairs produced upon electron transfer depends on the nature of their production. As already mentioned, the $^1\{\text{Bp}^-::\text{DMA}^+\}_{\text{com}}$ formed from irradiation of the ground-state CT complex, $\text{Bp}::\text{DMA}$, is suggested by Mataga and co-workers [24] to decay only by k_{bet} , on a timescale of 85 ps. Diffusional separation to solvent separated radical ion pairs or proton transfer within $^1\{\text{Bp}^-::\text{DMA}^+\}_{\text{com}}$ are not kinetically competitive. The triplet CRIP $^3\{\text{Bp}^- + \text{DMA}^+\}_{\text{IP}}$ has two decay pathways that occur on the picosecond timescale. The first process is proton transfer, k_{pt} , to generate a triplet radical pair, $^3\{\text{BpH} + \text{DMA}\cdot\}$ (Scheme 2.3). In acetonitrile, this occurs with a rate constant of k_{pt} of $1.3 \times 10^9 \text{ s}^{-1}$ [43]. The second process leading to the decay of the CRIP is diffusional separation to the SSRIP, k_{ips} , which occurs with a rate constant of $5 \times 10^8 \text{ s}^{-1}$ (Scheme 2.3) [43]. Thus the efficiency of the



Scheme 2.3

proton-transfer process for the CRIP in acetonitrile is 0.72. Back electron transfer within the CRIP does not occur on the picosecond timescale as this process is spin forbidden.

The decay pathways for $^1\{\text{Bp}^- + \text{DMA}^+\}_{\text{IP}}$ have yet to be clearly defined. In order to study the dynamics of $^1\{\text{Bp}^- + \text{DMA}^+\}_{\text{IP}}$, the singlet radical ion pair must be produced in high yield, necessitating the employment of high concentrations of DMA so that $k_{\text{set}} [\text{DMA}]$ becomes competitive with k_{isc} (Scheme 2.1). However, under conditions of high concentrations of DMA, all three radical ion pairs $^1\{\text{Bp}^-::\text{DMA}^+\}_{\text{com}}$, $^3\{\text{Bp}^- + \text{DMA}^+\}_{\text{IP}}$, and $^1\{\text{Bp}^- + \text{DMA}^+\}_{\text{IP}}$ are formed. Since all three radical ion pairs have similar transient absorption spectra, separating out their individual dynamics becomes problematic. However, Mataga and co-workers [24] have undertaken such a study and find that $^1\{\text{Bp}^- + \text{DMA}^+\}_{\text{IP}}$ decays by three pathways: diffusional separation, $k_{\text{ID}} = 9 \times 10^8 \text{ s}^{-1}$; charge recombination to generate ground-state reactants, $k_{\text{CR}} = 5.8 \times 10^8 \text{ s}^{-1}$; and proton transfer to generate the Bp ketyl radical, $k_{\text{pt}} = 6.6 \times 10^8 \text{ s}^{-1}$. Given the complexity of the analysis, care should be exercised when employing the derived values for these kinetic processes.

In the following discussion of proton-transfer processes, we are interested in analyzing the transfer process occurring only within the triplet CRIP, $^3\{\text{Bp}^- + \text{DMA}^+\}_{\text{IP}}$. Therefore it is important that the dynamics of the $^1\{\text{Bp}^-::\text{DMA}^+\}_{\text{com}}$ and $^1\{\text{Bp}^- + \text{DMA}^+\}_{\text{IP}}$ do not contribute to the observed kinetics processes, given the high degree of difficulty in the deconvolution of the dynamical processes associated with the three species. A method for minimizing the contributions from $^1\{\text{Bp}^-::\text{DMA}^+\}_{\text{com}}$ and $^1\{\text{Bp}^- + \text{DMA}^+\}_{\text{IP}}$ to the observed dynamics is to examine the reaction kinetics at low concentrations of DMA so that only $^3\{\text{Bp}^- + \text{DMA}^+\}_{\text{IP}}$ is formed. An example of such an analysis is shown in Figure 2.1, where the decay of the radical anion of benzophenone, Bp^- , is monitored at 680 nm as a function of the concentration of DMA. At high concentrations of DMA (0.8–1.0 *M*), the radical anion appears within 10 ps and then decays in a biexponential fashion, reflecting chemistry that arises from numerous species, which decay through several pathways. When the concentration of DMA is varied over the range of 0.2–0.6 *M*, the appearance of the radical ion occurs on a timescale varying from 30 to 100 ps, which can only come about from the quenching of $^3\text{Bp}^*$, thus only producing $^3\{\text{Bp}^- + \text{DMA}^+\}_{\text{IP}}$. The decay of $^3\{\text{Bp}^- + \text{DMA}^+\}_{\text{IP}}$ is independent of the concentration of DMA over the range of 0.2–0.6 *M*. The derived values for the rate of proton transfer within the triplet CRIP is $k_{\text{pt}} = 1.3 \times 10^9 \text{ s}^{-1}$ and the rate of diffusional separation of the CRIP to form the SSRIP is $k_{\text{ips}} = 5.0 \times 10^8 \text{ s}^{-1}$ (Scheme 2.3). Thus when concentrations of DMA in the range of 0.4 *M* are employed, only the chemistry occurring within $^3\{\text{Bp}^- + \text{DMA}^+\}_{\text{IP}}$ is observed; it is at this concentration that all of our proton-transfer studies are undertaken.

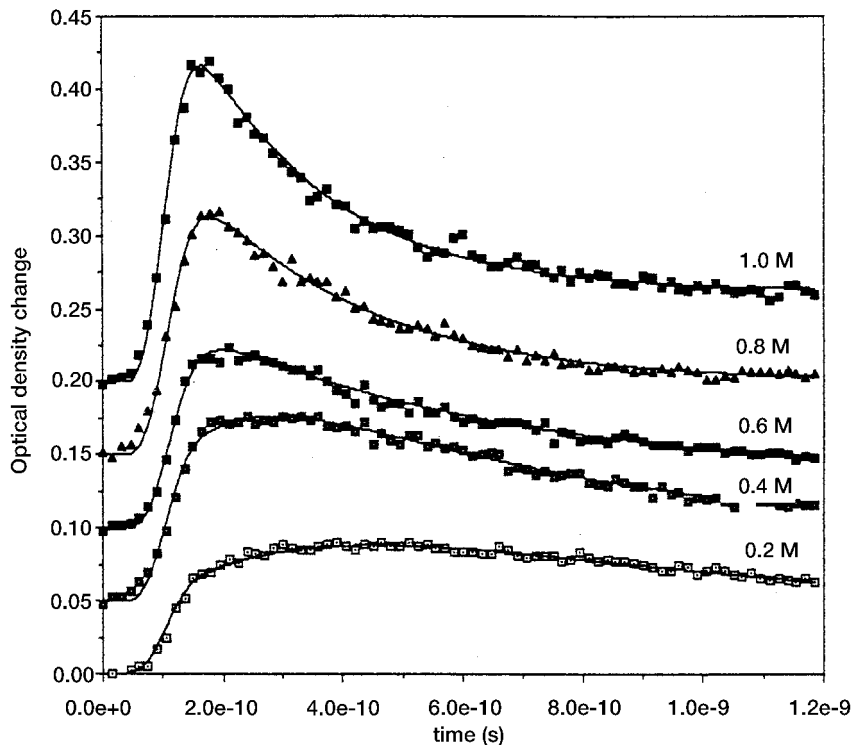


Figure 2.1. Transient absorption at 680 nm following the 355-nm excitation of 0.02 *M* benzophenone in acetonitrile as a function of concentration of *N,N*-dimethylaniline. 1.0 *M*: Fit to a rate of appearance of $6.9 \times 10^{10} \text{ s}^{-1}$, and a biexponential decay with $k_{\text{pt}1} = 2 \times 10^{10} \text{ s}^{-1}$ and $k_{\text{pt}2} = 1.3 \times 10^9 \text{ s}^{-1}$, and a rate of IP diffusional separation of $k_{\text{isp}} = 5.0 \times 10^8 \text{ s}^{-1}$. 0.8 *M*: Fit to a rate of appearance of $6.3 \times 10^{10} \text{ s}^{-1}$ and a biexponential decay with $k_{\text{pt}1} = 1.0 \times 10^{10} \text{ s}^{-1}$ and $k_{\text{pt}2} = 1.3 \times 10^9 \text{ s}^{-1}$, and a rate of IP diffusional separation of $k_{\text{isp}} = 5.0 \times 10^8 \text{ s}^{-1}$. 0.6 *M*: Fit to a rate of appearance of $3.6 \times 10^{10} \text{ s}^{-1}$ and a single exponential decay with $k_{\text{pt}} = 1.3 \times 10^9 \text{ s}^{-1}$, and a rate of IP diffusional separation of $k_{\text{isp}} = 5.0 \times 10^8 \text{ s}^{-1}$. 0.4 *M*: Fit to a rate of appearance of $8.3 \times 10^9 \text{ s}^{-1}$ and a single exponential decay with $k_{\text{pt}} = 1.3 \times 10^9 \text{ s}^{-1}$, and a rate of IP diffusional separation of $k_{\text{isp}} = 5.0 \times 10^8 \text{ s}^{-1}$. 0.2 *M*: Fit to a rate of appearance of $3.2 \times 10^9 \text{ s}^{-1}$ and a single exponential decay with $k_{\text{pt}} = 1.3 \times 10^9 \text{ s}^{-1}$, and a rate of IP diffusional separation of $k_{\text{isp}} = 5.0 \times 10^8 \text{ s}^{-1}$.

III. THEORETICAL MODELS FOR PROTON TRANSFER

A. Classical Model

Since the discovery of the deuterium isotope in 1931 [44], chemists have long recognized that kinetic deuterium isotope effects could be employed as an indicator for reaction mechanism. However, the development of a mechanism is predicated upon analysis of the kinetic isotope effect within the context of a theoretical model. Thus, it was in 1946 that Bigeleisen advanced a theory for the relative reaction velocities of isotopic molecules that was based on the “theory of absolute rate”—that is, transition state theory as formulated by Eyring as well as Evans and Polanyi in 1935 [44, 45]. The rate expression for reaction is given by

$$k = \kappa(C^\ddagger/C_A C_B)(kT/2\pi m^*)^{1/2} 1/\delta \quad (1)$$

where C^\ddagger is the concentration of the activated complex, C_A and C_B are the concentrations of reactants A and B, m^* is the effective mass for the transferring particle in the activated complex, δ the length of the region associated with the transition state, and κ is the transmission coefficient.

In the original formulation of transition state theory, the transmission coefficient κ was assumed to arise from two contributions [45]. The first contribution to κ comes from the supposition that the system will not always pass through the transition state toward the product state with unit efficiency; there is a finite probability that the system will be reflected back toward the reactant state. The second contribution to κ comes from the tunnel effect in the transition state that recognizes that there is a finite probability for reaction for those systems with energies less than that for the transition state. The tunnel effect in the region of the transition state is the result of the wave-particle duality of matter. The wavelength of the reacting particle, λ , that gives rise to the tunnel effect is dependent on the mass of the particle, $\lambda = h/mv$, where v is the velocity of the reacting particle. In this formalism, the transfer of a deuteron contributes less to the tunnel effect relative to the transfer of a proton, given the difference in the mass of the two particles. On a historical note, when Biegeleisen developed the formalism for the kinetic deuterium isotope effect, he recognized the potential importance of the tunneling contribution to the overall rate of reaction. It included the Wigner tunneling correction to transition state theory [45]. However, in subsequent years, the tunnel effect was often neglected in the analysis of the kinetic deuterium isotope effect [5].

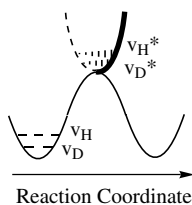
The standard analysis for the kinetic isotope effect that was prevalent in the 1950s and 1960s is based upon our ability to obtain the ratio of the rate constants

for proton–deuteron transfer, k_H/k_D [5]. Ascertaining this ratio greatly simplifies the analysis of the kinetics for proton and deuteron transfer due to the cancellation of terms that leads to the resulting expression

$$k_H/k_D = (C_H^\ddagger C_{AD}/C_D^\ddagger C_{AH})(m_D/m_H)^{1/2} \quad (2)$$

where the C parameters are the concentrations for the reactants and the C^\ddagger parameters are the concentrations for the activated complexes. This particularly pleasing form for the kinetic deuterium isotope effects assumes that the transmission coefficients κ for proton and deuteron transfer are identical, which derives from the assumption that tunneling does not contribute to the overall rate of reaction.

The difference in the rates of proton and deuteron transfer is ascribed to the differences in the zero-points energies of the reactant state and the activated complex (Scheme 2.4) [5]. The difference in the zero-point energies of the reactants, $v_H - v_D$, is normally greater than the difference in the zero-point energies of the transition states, $v_H^* - v_D^*$, given that the force constants for the reactants are generally greater than the force constants for the transition states; this finding is attributed to the breaking of bonds in the transition state, which reduces the force constants for the associated vibrations. The consequences of the shift in zero-point energies upon the interchange of a deuteron for a proton is that the energy of activation is greater for deuteron transfer than for proton transfer. From an extensive analysis of the effect of change in isotope upon zero-point energies, the maximum difference in the energies of activation for the breaking of a C–H bond when compared to a C–D bond, $E_H - E_D$, is of the order of 1.4 kcal/mol [4]. The analysis of the effect of replacement of a deuteron for a proton for the Arrhenius A factor reveals that the ratio of A factors, A_D/A_H , for this model leads to a predicted range of $0.6 < A_D/A_H < 1.4$ [4]. Thus, for the transition state model for proton–deuteron transfer to be valid for a given reaction, assuming the neglect of κ , a necessary condition is that the differences in the energies of activation and the ratio of A factors fall within the above range of values.



Scheme 2.4

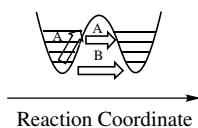
B. Semiclassical Model

There have been numerous kinetic studies of the deuterium isotope effect for proton and hydrogen atom transfer where values for $E_H - E_D$ greatly exceed 1.4 kcal/mol and the ratio of A factors, A_D/A_H , are significantly >1.4 ; values >10 are very common [4]. These observations directly challenge the classical model for proton transfer based upon transition state theory that neglects contributions from κ .

Bell and others have strongly advocated that these deviations from the expected values derived from transition state theory support the proposition that tunneling in the region of the transition state makes a significant contribution to the overall reaction dynamics for proton, as well as hydrogen atom and hydride, transfer [4, 46–49]. There has been a great effort, principally on the part of Bell, to model the tunneling contribution to κ to aid in the analysis of the kinetic deuterium isotope effect. Unfortunately, the tunneling contribution to κ is highly dependent on the shape and dimension of the potential energy surface in the region of the transition state and thus a general analytical formulation cannot be achieved. However, if it is assumed that the potential energy surface in this region can be modeled as an inverted parabola, then simple analytical forms for the kinetic deuterium isotope effect are derived and have been employed in the kinetic analysis. With reasonable potentials, the E_a and A parameters that greatly deviate from the prediction of transition state theory can be rationalized by assuming a varying degree of tunneling contribution to the reaction dynamics. These ideas have found a wide range of application in the field of organic and biochemistry [1, 49].

C. Proton Tunneling

The kinetic model for proton transfer based upon transition state theory that incorporates a tunneling contribution to the overall reaction rate assumes that tunneling occurs near the region of the transition state (pathway *a* in Scheme 2.5). There is, however, another possibility for the reaction path for proton transfer. In lieu of thermally activating the vibration associated with the proton-transfer coordinate to bring it into the region of the transition state, the proton may instead



Scheme 2.5

TABLE 2.1. Tunneling Times as a Function of Distance for a Barrier Height of 14 kcal/mol

| Distance (Å) | $d = 0.5$ | $d = 0.6$ | $d = 0.7$ | $d = 0.8$ |
|--------------|------------------------------------|------------------------------------|------------------------------------|------------------------------------|
| Time | $5 \times 10^{-13} \text{ s}^{-1}$ | $1 \times 10^{-12} \text{ s}^{-1}$ | $4 \times 10^{-12} \text{ s}^{-1}$ | $1 \times 10^{-11} \text{ s}^{-1}$ |

tunnel out of the reactant state and into the product directly, without the transferring coordinate being thermally activated, pathway *b* in Scheme 2.5 [10, 50].

To gain insight into the timescale associated with reaction paths *a* and *b*, a method is required for estimating the time it takes for a proton to tunnel along reaction path *b*. Employing the quasiclassical WKB approximation, Brickmann developed a model for estimating the reaction times associated with the tunneling of a proton along pathway *b* [51]. The rates for proton tunneling are a sensitive function of both the barrier height and width. For a barrier height of 14 kcal/mol and a vibrational frequency of 3000 cm^{-1} for the proton stretch coordinate in the reactant well, the rates of proton tunneling as a function of transfer distance have been determined. The results are presented in Table 2.1.

Typical changes in the distance associated with proton transfer fall in the range of 0.5–0.8 Å. For example, in the hydrogen-bonded complex of O—H···O, the distance separating the two oxygens is on the order of 2.8 Å and the distance of an O—H bond is on the order of 1.0 Å [50]. Therefore, the net transfer distance is 0.8 Å. Thus, the timescale associated with a proton tunneling from the $v = 0$ vibrational level in the reactant state to the $v = 0$ level in the product state will be 10 ps. For a barrier height of 14 kcal/mol, transition state theory predicts a reaction rate on the timescale of 1 ms, which would shorten by one or two orders of magnitude by incorporation of a tunneling contribution in the region of the transition state [4]. However, reaction path *b* will still dominate reaction path *a* by several orders of magnitude. Thus, based on this analysis, the expectation is that if a potential energy barrier exists along the proton-transfer coordinate, the predominant reaction pathway entails the proton tunneling out of the reactant state from the ground vibrational level and into the product state, a process termed nonadiabatic proton transfer. It is this process, nonadiabatic proton transfer, that is the centerpiece of the kinetic theories for proton transfer developed during the past 20 years.

D. Dogonadze, Kuznetsov, and Levich (DKL) Model

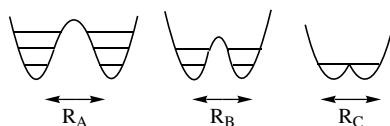
In 1967, Dogonadze, Kuznetsov, and Levich began the development of a theoretical model that would account for the full quantum nature of the transferring proton [10, 18, 52, 53]. In contrast to the model based on transition state theory where the quantum properties of the proton are an ad hoc addition to the model,

the DKL model explicitly recognizes the proton's quantum nature. Also, the dynamical role of the solvent is directly incorporated into the model. As with electron-transfer reactions, the transfer of a proton leads to a change in the charge distribution in the reacting species. This redistribution of charge will be coupled to the reorganization of the solvent and thus the solvent becomes a controlling factor in the dynamics of proton transfer.

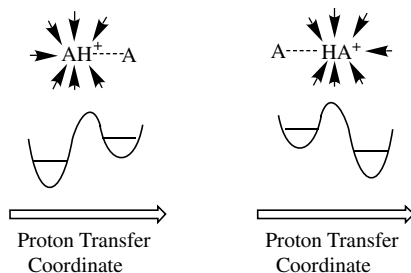
Before discussing the various limits of the DKL model for proton-transfer reactions, the magnitude of the electronic barrier in the proton-transfer coordinate needs to be addressed [10]. If we consider the generic $AH^+ \cdots A$ system, at large internuclear separations the electronic barrier will be large (Scheme 2.6, R_A), and the reacting state will contain a number of bound vibrations associated with the transferring proton. The DKL model allows for the tunneling, a nonadiabatic process, out of each of the vibrational levels associated with the transferring proton in the reactant state into the corresponding product state. As the $A \cdots A$ distance is reduced (Scheme 2.6, R_B), the number of bound vibrations will be reduced, and a further reduction in distance (Scheme 2.6, R_C), will result in an electronic barrier that lies below the zero-point vibration of the transferring proton. In this limit, the transferring proton does not encounter an electronic barrier and thus moves adiabatically from the reactant into the product state. Thus, if the zero-point energy of the vibration associated with the transferring proton lies below the electronic barrier for proton transfer, the reaction falls in the nonadiabatic regime. Conversely, if the zero-point energy of the vibration associated with the transferring proton lies above the electronic barrier for proton transfer, the reaction falls in the adiabatic regime.

The reaction potentials displayed in Scheme 2.6 are those appropriate for the symmetric transfer of a proton in a vacuum, $AH^+ \cdots A \leftrightarrow A \cdots HA^+$. However, when the system is placed in a polar solvent, the effect of the polar solvent upon the stability of the reactant and product state must be taken into account. The reactant and the proton state will have different solvent structures (Scheme 2.7). The effect of having different solvent structures associated with the reactant and product state is to break the symmetry of the potential energy surface associated with the proton-transfer coordinate.

The effect of the solvent upon the breaking of the symmetry of the potential energy surface for proton transfer has a profound consequence for the reaction dynamics for proton transfer. The tunneling of the proton out of the reactant state



Scheme 2.6



Scheme 2.7

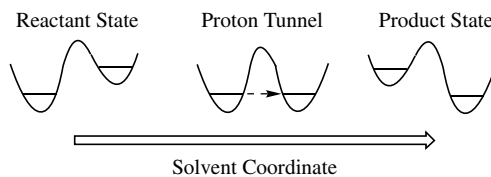
and into the product is only possible when the energy levels of the reactant state match those of the product state so that the transition does not violate the energy conservation principle. Thus, if the solvent does not recognize, the proton cannot transfer nonadiabatically. Therefore, a fundamental coordinate in proton-transfer reactions is the reorganization of the solvent structure to bring the reactant state and the product into resonance so that the proton can be transferred via tunneling. The effect of the solvent on nonadiabatic proton transfer is depicted in Scheme 2.8. A similar scheme is appropriate for adiabatic proton transfer except that when the reactant and product state are brought into resonance, the electronic barrier will drop below the zero-point energy of the vibration associated with the transferring proton. Consequently, in both adiabatic and nonadiabatic proton transfer, the solvent reorganization coordinate is fundamental in determining the dynamics of reaction [10].

The DKL model for nonadiabatic proton transfer at a fixed distance R allows for the tunneling of the proton out of any of the bound vibrations, n , associated with the proton-transfer coordinate, into any of the bound vibrations in the product state, m [10].

$$k = \sum_n \sum_m P_n k_{nm} \quad (3)$$

where

$$k_{nm} = 2\pi(C_{nm}/2)^2 (\pi/h^2 k_B T E_s)^{1/2} \exp(-\Delta G_{nm}^\ddagger/k_B T) \quad (4)$$



Scheme 2.8

and

$$\Delta G_{nm}^\ddagger = (\Delta E + E_s + \Delta E_{nm})^2 / 4E_s \quad (5)$$

The term k_{nm} is the rate constant associated with the proton tunneling out of the n th vibrational level of the reactant state into the m th vibrational level in the product state. The parameter P_n is the Boltzmann population of the n th vibrational energy level, C_{nm} is the proton tunneling probability for the transition out of the n th vibrational level of the reactant state and into m th vibrational energy level of the product state. T is temperature, and k_B is Boltzmann constant. The term ΔE is the energy difference between the solvent equilibrated reactant state and the solvent equilibrated product state, and corresponds to the driving force for the reaction. The difference between the vibrational energy levels in the reactant state and in the product state is ΔE_{nm} , where $\Delta E_{nm} = (n - m)h\nu$ and ν is the vibrational frequency associated with the transferring proton. Finally, E_s reflects the solvent reorganization energy that is associated with the solvent coordinate.

The overall rate constant for proton transfer will reflect the distribution of the reacting species of the distance R between species. As R decreases, the potential energy barrier in the proton-transfer coordinate decreases leading to an increase in the rate of reaction but at a cost of increasing the energy of the reactant and product states at short distances. The DKL model thus defines the rate of proton transfer as [10]

$$k = \int \phi(R)k(R) dR \quad (6)$$

where $k(R)$ is the reaction rate constant from reactant to product at a distance R given by Eq. (3), and $\phi(R)$ is the distribution function for the molecular species over the distance R , a term that is a function of temperature.

E. Borgis–Hynes (BH) Model

In 1989, Borgis and Hynes proposed a theory for nonadiabatic proton transfer that includes all the parameters contained with the DKL model. In addition, they addressed the important issue of low-frequency vibrations serving as promoting modes in proton tunneling [11]. For nonadiabatic proton transfer, the distance dependence of the tunneling coupling, $C(Q)$, has the analytical form [13]

$$C(Q) = C_0 \exp[-\alpha(Q - Q_0)] \quad (7)$$

where Q_0 is the equilibrium distance separating the reactant and product state proton wells. The decay parameter, α , reflects that rate at which the tunneling

either increases or decreases with a decrease or increase in distance. For proton tunneling, the values of α are in the range of 25–35 \AA^{-1} [13]. Thus if a vibration serves to reduce the equilibrium separation of the two proton wells by the amount of just 0.1 \AA , the rate of proton tunneling will be enhanced by a factor of 20, assuming $\alpha = 30 \text{\AA}^{-1}$. For comparison, the decay parameter for the distance dependence of the electronic coupling associated with electron transfer is of the order of 1 \AA^{-1} , so that a decrease in distance of 0.1 \AA^{-1} will lead to just a 10% increase in the rate of electron transfer. Thus, a fundamental difference in the theoretical formalisms for nonadiabatic electron and proton transfer is the importance of a low-frequency promoting mode in the proton-transfer process.

On the basis of a Landau–Zener curve crossing formalism, Borgis and Hynes derived the nonadiabatic rate constant k , which is similar to that expressed by the DKL model but where the tunneling term C_{nm} found in Eq. (4) is significantly modified due to the influence of the low-frequency promoting mode Q , with a frequency ω_Q , on the tunneling rate. The dependence of C_{nm} on Q is given by [13]

$$C_{nm}^2 = C_0^2 \exp(-\alpha \Delta Q_e) \exp[(E_\alpha - E_Q)/h\omega_Q] F[L(E_Q, E_\alpha, \omega_Q)] \quad (8)$$

The energy E_α is a quantum term associated with the proton reaction coordinate coupling to the Q vibration, $E_\alpha = h^2 \alpha^2 / 2m$ and C_0 is the tunneling matrix element for the transfer from the 0th vibrational level in the reactant state to the 0th vibrational level in the product state. The term ΔQ_e is the shift in the oscillator equilibrium position and $F[L(E_Q, E_\alpha, \omega_Q)]$ is a function of a Laguerre polynomial. For a thorough discussion of Eq. (8), see [13].

Also within the Landau–Zener curve crossing formalism, Borgis and Hynes examined the limit where coupling between the reactant and product states is sufficiently large so that the electronic barrier in the proton-transfer coordinate is below the zero-point energy level of the transferring proton that occurs when the A...A internuclear separation is small, leading to the adiabatic limit. The rate expression for adiabatic proton transfer is given by [13]

$$k_{\text{ad}} = (\omega_s / 2\pi) \exp(-\beta \Delta G^\ddagger) \quad (9)$$

where ω_s is the solvent frequency and ΔG^\ddagger is the free energy of activation. If the proton-transfer reaction is adiabatic, that is, it does not occur through proton tunneling, then the A factor will be of the order of 10^{13} s^{-1} or greater.

F. Lee–Hynes (LH) Model

In 1996, Lee and Hynes [54] further expanded the kinetic theory for nonadiabatic proton transfer developed by Borgis and Hynes by including contributions to the

rate constant from the excited vibrations associated with the transferring proton in both the reactant and the product state. The rate constant for the transfer of the proton out of the n_R vibrational level in the reactant state into the m_P vibrational level in the product state is given by

$$k(n_r \rightarrow m_p) = k_{mp,nr}(0)(\pi/2A_2)^{1/2} \exp(-A_1^2/2A_2) \quad (10)$$

where $k_{mp,nr}(0)$, A_1 , and A_2 are defined as

$$\begin{aligned} k_{mp,nr}(0) &= 2(2\pi/h)^2 [C_{mp,nr}(Q)]^2 \exp\{(E_\alpha/h\nu_Q)2 \coth(\beta h\nu_Q/2)\} \\ A_1 &= (2\pi/h)\{\Delta E + E_s + E_Q + E_\alpha + [hm_P\nu_P - hn_R\nu_R] \\ &\quad + 2\Delta Q/|\Delta Q|(E_\alpha E_Q)^{1/2} \coth(\beta h\nu/2)\} \\ A_2 &= 2(2\pi/h)^2 k_B T \{E_s + (E_\alpha + E_Q)(\beta h\nu_Q/2\pi \coth\{\beta h\nu_Q/2\pi\} \\ &\quad + \Delta Q/|\Delta Q|(E_\alpha E_Q)^{1/2}(\beta h\nu_Q)\} \end{aligned}$$

In the above expression, ν_R and ν_P are the frequencies associated with the n th level of reacting proton in the reactant state and the m th level in the product state, and ν_Q is the frequency associated with the low-frequency mode developed in the BH model. The term ΔQ reflects the change in equilibrium distance between the reactant and product states and $C_{mp,nr}(Q)$ is the tunneling matrix element from the n th level in the reactant state to the m th level in the product state. An explicit evaluation of the tunneling matrix element $C_{mp,nr}(Q)$ is obtained within the WKB semiclassical framework and is given by

$$C_{mp,nr}(Q) = (h/4\pi^2)(\omega_R \omega_P)^{1/2} \exp\{-2\pi^2/h\omega^\ddagger [V^\ddagger - 1/2(V_{nr} + V_{mp})]\} \quad (11)$$

where ω^\ddagger is the frequency associated with the inverted parabola of the transition state for the proton-transfer coordinate, V^\ddagger is the energy of the transition state, and V_{nr} and V_{mp} are the energies of the reactant and the product states, which depend on the level of vibrational excitation in the two states.

The key differences in the BH and the LH models are that in the BH model the tunneling term C_0 is independent of the driving force, ΔE , while in the LH model, the tunneling term is dependent on the driving force as expressed in Eq. (11). Also, the LH model allows for excitation of the vibrational mode associated with the proton-transfer coordinate in both the reactant and product state; this is not taken into account in the BH model.

G. Comparison of Semiclassical and Quantum Models

At present, there are two contrasting theories serving to describe the dynamics of proton transfer when an electronic barrier exists in the transfer coordinate. The

reaction path for the semiclassical model envisions thermal activation of the vibration associated with the transfer coordinate that brings the system to the region of the transition state where the proton–deuteron may then tunnel into the product state. The quantum model is based on the assumption that the fluctuation in the solvent structure brings the reactant and product state into resonance subsequent to which the proton–deuteron tunnels into the product state. From an experimental perspective, the question that arises is how to distinguish between these two models.

Two parameters that are accessible to the experimentalist have been the effect of the interchange of a deuteron for a proton upon the dynamics of transfer and the effect of temperature variation upon the kinetics of proton–deuteron transfer [49]. As previously mentioned, the semiclassical model has been employed in the rationalization of kinetic deuterium isotope effects that exceed the factor of 7.0, the maximum predicted by the classical model [5]. However, the full quantum model also allows for the wide range in the kinetic deuterium isotope effect, the range of which overlaps that predicted by the semiclassical model [53]. Thus, the kinetic deuterium isotope effect in and of itself cannot be used to distinguish between the two models.

Variation in temperature has also been employed extensively in the analysis of the dynamics of proton–deuteron transfer. One of the interesting predictions of the semiclassical model is that there is a high-temperature regime where the kinetics of proton transfer is thermally activated and a low-temperature regime where the kinetics for proton transfer is independent of temperature. The Arrhenius behavior in the high-temperature regime is attributed to the thermal activation of the vibration associated with the proton-transfer reaction coordinate while the low-temperature regime reflects proton tunneling, a process that is independent of temperature. Indeed, there have been numerous studies showing both types of kinetic behavior, and it is this observation that has been put forth as validation of the semiclassical model [49]. However, the quantum models also make such a prediction as to the temperature dependence for the kinetic behavior of proton transfer, an example of which is shown for the BH model in Figure 2.2. In the quantum model, the thermally activated component is associated with solvent and vibrational reorganization of the system while the low-temperature component reflects the quantum nature of the proton and the solvent modes. Consequently, the temperature dependence of the dynamics of proton–deuteron transfer cannot unambiguously serve to distinguish the two kinetic models.

There is one experimental parameter that does serve to distinguish between the semiclassical model and the quantum model for nonadiabatic proton transfer. In the semiclassical model, if one assumes that the magnitude of the electronic barrier directly correlates with the thermodynamic driving force, a statement of the Hammond postulate, then as the driving force increases the rate of reaction increases, eventually reaching a maximum rate. The quantum model has a

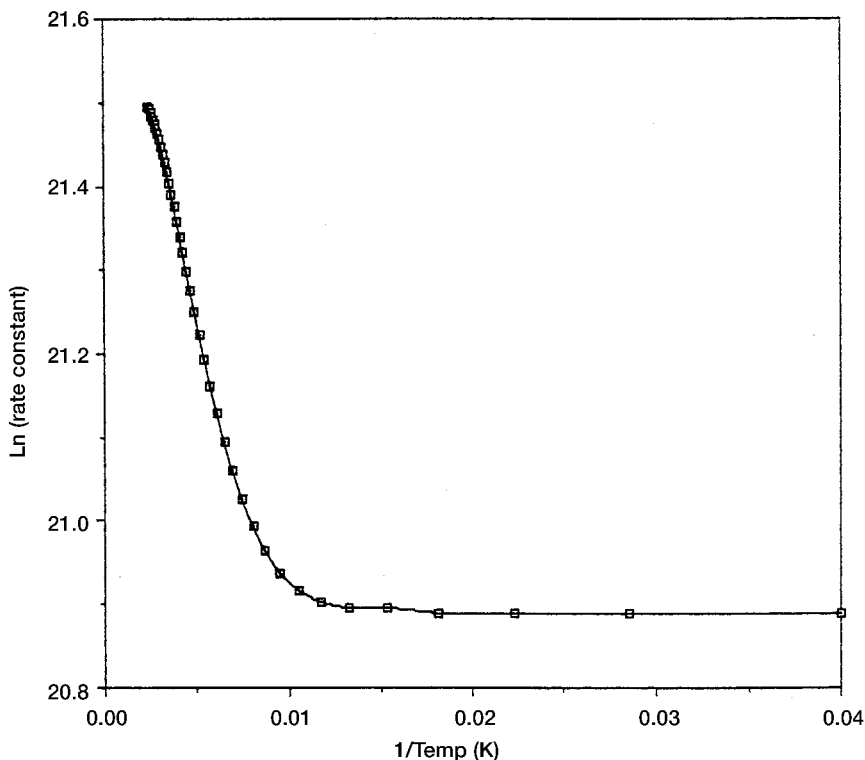


Figure 2.2. Temperature dependence of the rate of proton transfer k_{pt} as a function of temperature for the BH model for proton transfer with $E_\alpha = 1.0$ kcal/mol, $E_Q = 1.0$ kcal/mol, $E_s = 7.0$ kcal/mol, $\Delta Q = 0.1$ Å, and $\omega_Q = 200$ cm^{-1} . The parameter k/C_0^2 adjusted for a maximum rate of 2.1×10^9 s^{-1} . Temperature range 25–415 K.

different prediction for nonadiabatic proton transfer. Given the quadratic nature of the free energy of activation for nonadiabatic proton transfer, Eq. (5), the rate constant for proton transfer will initially increase with an increase in driving force, reaching a maximum value, but then decreases with a further increase in driving force. Thus the kinetics for nonadiabatic proton transfer should manifest a normal region and an inverted region for proton transfer over a wide range in driving force [20]. Within the context of the BH model, graphs of the free-energy dependence for the rate of proton transfer are shown in Figure 2.3. The calculated rate constants have been normalized by the value of the tunneling matrix element, k/C_0^2 . The two graphs differ only in the value of the solvent reorganization energy, E_s . With increasing solvent reorganization energy, the maximum rate

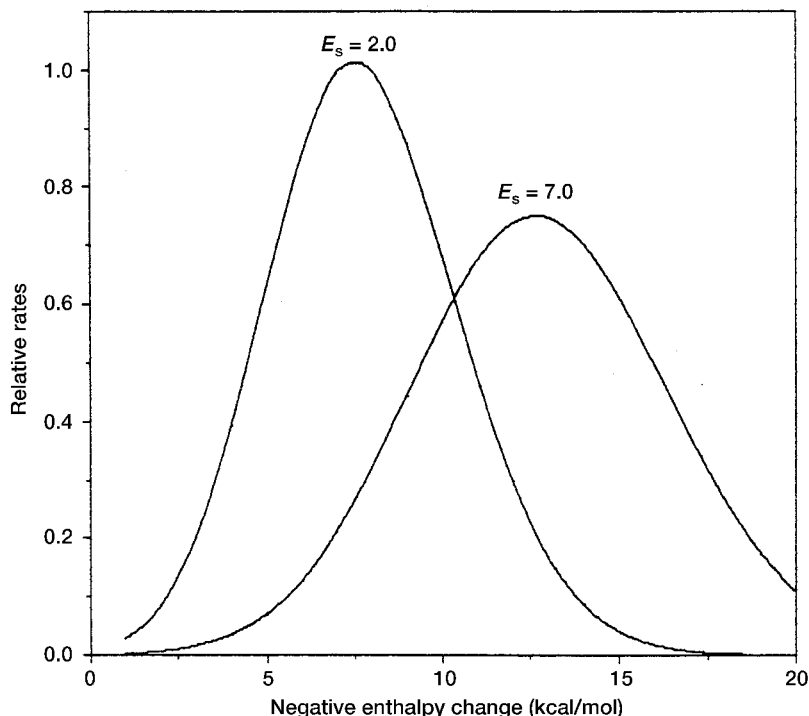


Figure 2.3. The enthalpy dependence ($-\Delta E$, kcal/mol) as a function of the solvent reorganization energy for the rate of proton transfer when $E_x = 1.0$ kcal/mol, $E_Q = 1.0$ kcal/mol, $\Delta Q = 0.1 \text{ \AA}$ and $\omega_Q = 200 \text{ cm}^{-1}$. Rates are normalized to the maximum rate constant for proton transfer. Larger graph: $E_s = 2.0$ kcal/mol. Smaller graph: $E_s = 7.0$ kcal/mol.

constant for a given solvent reorganization energy shifts to a larger negative free energy change and the maximum amplitude is reduced in magnitude, which is attributed to the $E_s^{-1/2}$ in Eq. (4). Thus, the BH model predicts an inverted region for proton transfer; similar behavior is found for the LH model. The basis of this kinetic behavior is directly analogous to that observed in nonadiabatic electron transfer. If an inverted region is observed for the dynamics of proton transfer and if the maximum rate of proton transfer is found to be a function of the solvent reorganization energy, E_s , this would strongly support the full quantum model for nonadiabatic proton transfer.

On a cautionary note, if there is strong electronic coupling between the reactant and product states that serves to reduce the electronic barrier in the proton-transfer coordinate below the zero-point energy of the transferring vibration, then

the quantum model would fall into the adiabatic regime whose rate equation has the analytical form given by Eq. (9). In the adiabatic regime, the rate of proton transfer is predicted to increase with an increase in thermodynamic driving force, eventually reaching a maximum rate that is controlled by solvent dynamics. An inverted region is not anticipated for adiabatic proton transfer [13]. Therefore, the semiclassical model and the quantum adiabatic model have similar predictions for the functional form of the dependence of the rate of proton transfer with driving force. Thus this kinetic behavior cannot be used to distinguish between the two models. Only the existence of an inverted region serves to support the nonadiabatic proton-transfer model.

IV. BENZOPHENONE-*N,N*-DIMETHYLANILINE PROTON TRANSFER

A. Energetics

In the ensuing discussion, the energy dependence of the rate constants for proton transfer within a variety of substituted benzophenone-*N,N*-dimethylaniline contact radical ion pairs is examined; only the data for the nitrile solvents are discussed. This functional relationship is examined within the context of theories for non-adiabatic proton transfer. Finally, these results are viewed from the perspective of other proton-transfer studies that examine the energy dependence of the rate constants.

The enthalpy changes associated with proton transfer in the various 4,4'-substituted benzophenone contact radical ion pairs as a function of solvent have been estimated by employing a variety of thermochemical data [20]. The effect of substituents upon the stability of the radical IP were derived from the study of Arnold and co-workers [55] of the reduction potentials for a variety of 4,4'-substituted benzophenones. The effect of substituents upon the stability of the ketyl radical were estimated from the kinetic data obtained by Creary for the thermal rearrangement of 2-aryl-3,3-dimethylmethylenecyclopropanes, where the mechanism for the isomerization assumes a biradical intermediate [56]. The solvent dependence for the energetics of proton transfer were based upon the studies of Gould et al. [38]. The details of the analysis can be found in the original literature [20] and only the results are herein given in Table 2.2.

B. Kinetics

The rate constants for proton transfer as a function of substituent and solvent are given in Table 2.3 [43]. All experiments involved the 355-nm irradiation of various benzophenones in the presence of 0.4 *M* *N,N*-dimethylaniline.

TABLE 2.2. Solvent Dependence of the Substituent Effects upon Enthalpy Change for Proton Transfer^a

| 4 | 4' | CH ₃ CN | C ₂ H ₅ CN | C ₃ H ₇ CN | C ₄ H ₉ CN |
|-------------------|-------------------|--------------------|----------------------------------|----------------------------------|----------------------------------|
| CH ₃ O | CH ₃ O | -7.4 | -8.0 | -8.2 | -8.4 |
| CH ₃ | CH ₃ | -5.0 | -5.5 | -5.7 | -5.9 |
| CH ₃ O | H | -5.0 | -5.5 | -5.7 | -5.9 |
| CH ₃ | H | -3.7 | -4.2 | -4.4 | -4.6 |
| H | H | -2.7 | -3.2 | -3.4 | -3.6 |
| F | H | -2.1 | -2.6 | -2.8 | -3.0 |
| Cl | H | -0.9 | -1.4 | -1.6 | -1.8 |

^aAll values are in kilocalories per mole (kcal/mol). Acetonitrile = CH₃CN, propanenitrile = C₂H₅CN, butanenitrile = C₃H₇CN, pentanenitrile = C₄H₉CN.

C. Application of the BH Model to the Kinetics of Proton Transfer

In applying the BH model to the analysis of the observed correlation between rate constants and driving force, given the great number of parameters contained within the model, it is not possible to obtain a unique fit between the model and the experimental data [43]. Since the value of the tunneling matrix element C_0 and the magnitude of the change in the displacement in the promoting mode Q , ΔQ_e , are unknown, only a reduced rate for proton transfer $k/C_0^2 \exp(-\alpha Q_e)$ is determined. Furthermore, the frequency of the promoting mode Q is assumed to be 200 cm^{-1} and the value of the E_α and E_Q terms are estimated to be 1 kcal/mol based upon the work of Borgis and Hynes [13]. Thus, the only parameter that is varied in modeling the kinetic data for proton transfer in butanenitrile is the solvent reorganization energy, whose optimum value is found to be $E_s = 1.5 \text{ kcal/mol}$. The correlation between experimental data and the BH model is shown in

TABLE 2.3. Solvent Dependence of the Substituent Effects upon Rate Constants for Proton Transfer^a

| 4 | 4' | CH ₃ CN | C ₂ H ₅ CN | C ₃ H ₇ CN | C ₄ H ₉ CN |
|-------------------|-------------------|--------------------|----------------------------------|----------------------------------|----------------------------------|
| CH ₃ O | CH ₃ O | 3.9×10^9 | 4.3×10^9 | 3.2×10^9 | 2.7×10^9 |
| CH ₃ | CH ₃ | 2.9 | 4.1 | 4.3 | 3.8 |
| CH ₃ O | H | 2.9 | 4.0 | 4.0 | 3.6 |
| CH ₃ | H | 2.3 | 3.8 | 4.3 | 4.2 |
| H | H | 1.3 | 2.9 | 3.9 | 4.2 |
| F | H | 1.0 | 2.6 | 3.9 | 4.1 |
| Cl | H | 0.7 | 1.8 | 2.9 | 3.1 |

^aAll values are in reciprocal seconds (s^{-1}). Acetonitrile = CH₃CN, propanenitrile = C₂H₅CN, butanenitrile = C₃H₇CN, pentanenitrile = C₄H₉CN, benzene = C₆H₆.

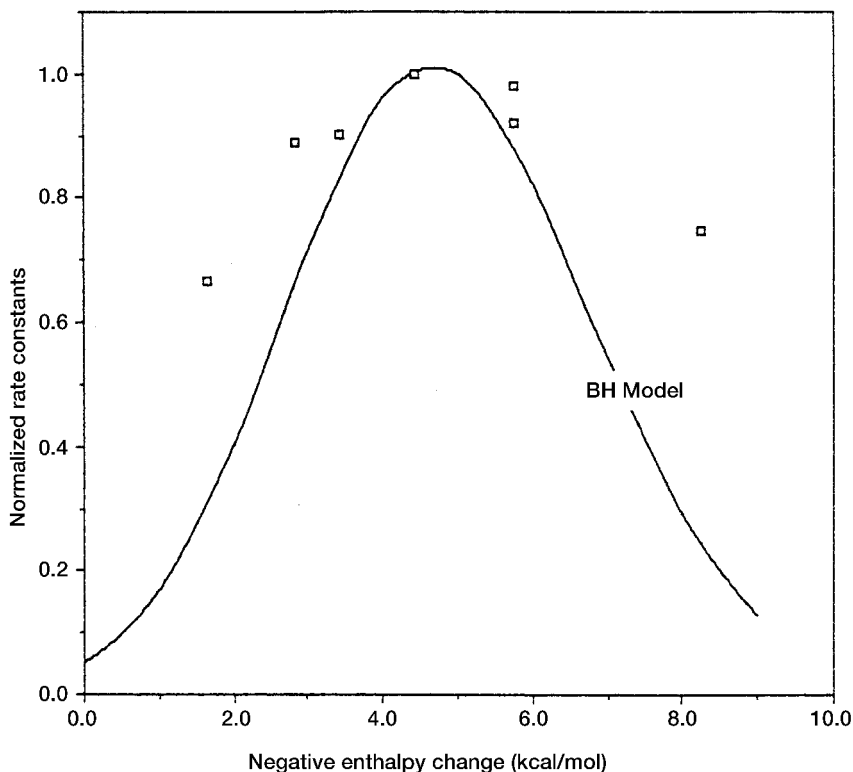


Figure 2.4. The normalized rate constants for proton transfer as a function of the negative enthalpy change ($-\Delta E$ kcal/mol) for the solvent butanenitrile. Experimental data = squares. The BH model = solid curve with $E_s = 1.5$ kcal/mol, $E_x = 1.0$ kcal/mol, $\omega_Q = 200$ cm^{-1} , and $T = 298$ K.

Figure 2.4, where the experimental rate constants have been normalized to the maximum rate of proton transfer and the maximum rate constant obtained from the BH model is scaled to the maximum experimental rate constant.

As evidenced by the correlation of the BH model with the experimental data, Figure 2.4, the model is only in qualitative accord with the experiment. Clearly, the BH model cannot account for the breadth in the correlation of the rate constants for proton transfer with driving force. The origin of the discrepancy may lie in the single-mode nature of the BH model, which allows only for vibrational excitation in the low-frequency promoting mode. Excitation in the reactant and product modes of the vibration associated with the transferring proton is not taken into account in the BH model. Therefore, the discrepancy between experiment

and the BH model may point to the importance of vibrational excitation in the proton-transfer mode.

D. Application of the LH Model to Kinetics of Proton Transfer

In applying the LH model to the above set of kinetic data, the vibrational frequencies associated with the transferring proton in the reactant and product states must be specified to determine $C_{mp,nr}(Q)$ in Eq. (11). The C–H stretching frequency in the reactant state is set to 2700 cm^{-1} and the O–H stretching frequency in the product state is set to 3100 cm^{-1} . The numbers were derived from AM1 calculations. The transition state frequency ω^\ddagger is set to 2500 cm^{-1} based on the work of

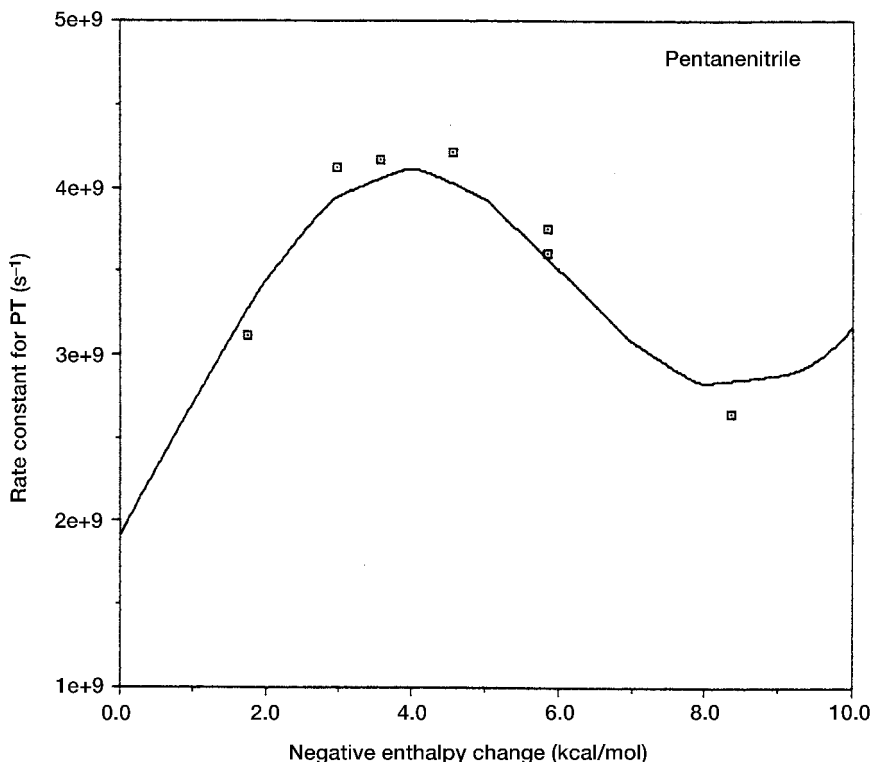


Figure 2.5. The rate constants for proton transfer as a function of the negative enthalpy change for the solvent pentanenitrile. Experimental data = squares; LH model = solid curve with $E_s = 7.0\text{ kcal/mol}$, $V^\ddagger = 17.5\text{ kcal/mol}$, $\omega_Q = 200\text{ cm}^{-1}$, $\omega_R = 2700\text{ cm}^{-1}$, $\omega_P = 3100\text{ cm}^{-1}$, $\omega^\ddagger = 2500\text{ cm}^{-1}$, $E_x = 1.0$, and $E_Q = 0.0\text{ kcal/mol}$.

Lee and Hynes [54]. The only parameter contained within the expression for the tunneling matrix element $C_{mp,nr}(Q)$, which serves as a fitting parameter, is the barrier height, V^\ddagger . In addition, since the magnitude of the change in ΔQ_e is unknown, both ΔQ_e and its associated energy E_Q are set to zero while the value of E_α is set to 1 kcal/mol. Consequently, only two parameters remain to be specified, the solvent reorganization energy, E_s , and the value of the low-frequency promoting mode, Q .

In the fitting of the kinetic data for the solvent pentanenitrile, it was assumed that the low-frequency promoting mode Q has a value of 200 cm^{-1} for ω_Q , which is associated with the modulation of the intermolecular distance within the contact radical IP, thus leaving only two fitting parameters, the barrier height, V^\ddagger , and the solvent reorganization energy. The optimum values for the two fitting parameters are $V^\ddagger = 17.5\text{ kcal/mol}$ and $E_s = 7.0\text{ kcal/mol}$ (Fig. 2.5). It is evident that the LH model yields a far superior fit to the kinetic data relative to the BH model.

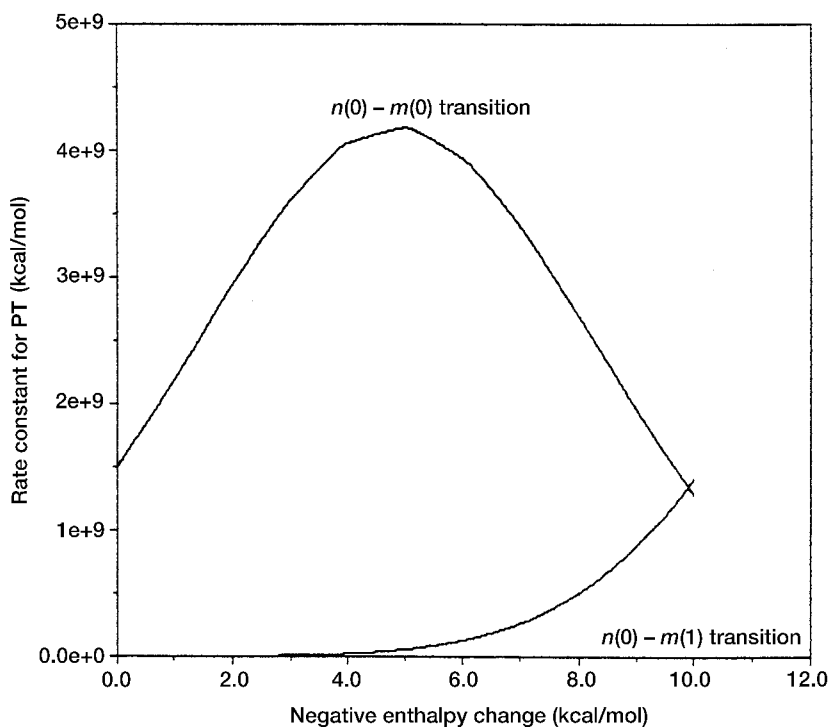


Figure 2.6. The individual transitions within the LH model of $n(0) \rightarrow m(0)$ and $n(0) \rightarrow m(1)$ for the parameters specified in Figure 2.5.

The role of excited vibrations in determining the overall reaction rate can be assessed by examining the contributions of the individual $n(0) \rightarrow m(0)$ and the $n(0) \rightarrow m(1)$ transitions to the overall rate constants as a function of driving force, the results of which are shown in Figure 2.6. At a large driving force, > -7.0 kcal/mol, formation of the product state with one quantum of vibration in the O—H stretching mode begins to make a significant contribution to the overall rate constant. It is the participation of vibrationally excited product modes that gives rise to the breadth in the correlation of the rate constant for proton transfer with driving force that could not be accommodated within the BH model.

The fit of the LH model to the remaining kinetic data for the nitrile solvents employed only two fitting parameters, the low-frequency promoting mode, ω_Q , and the solvent reorganization energy, E_s . A factor determining the magnitude of

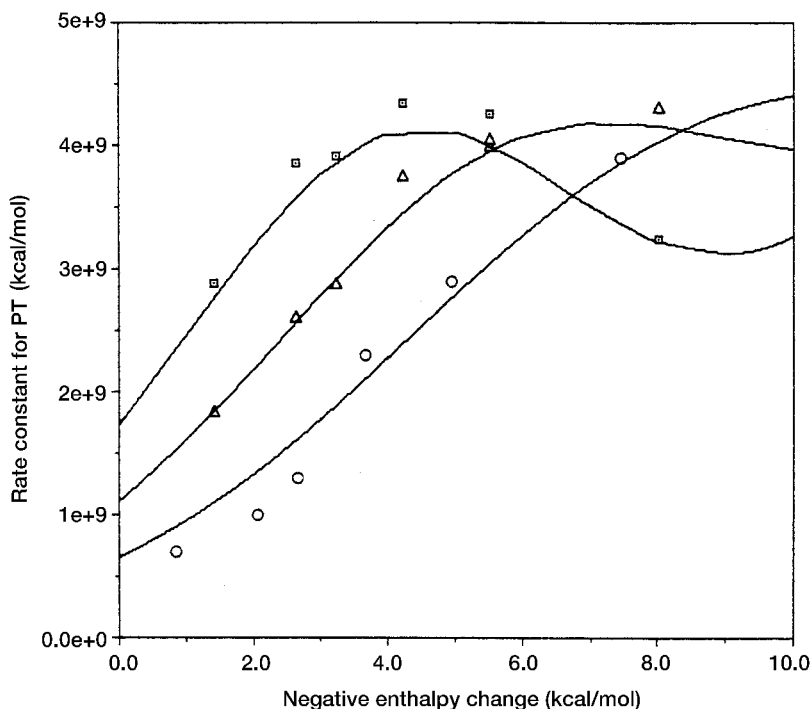


Figure 2.7. The rate constants for proton transfer as a function of the negative enthalpy change for the three nitrile solvents as a function of E_s and ω_Q with the remaining parameters held constant as specified in Figure 2.5. Butanenitrile = squares with $E_s = 8.0$ kcal/mol and $\omega_Q = 195$ cm^{-1} . Propanenitrile = triangles with $E_s = 12.0$ kcal/mol and $\omega_Q = 179$ cm^{-1} . Acetonitrile = circles with $E_s = 17.0$ kcal/mol and $\omega_Q = 164$ cm^{-1} .

the low-frequency promoting mode is the dielectric constant of the medium, as the interaction within the contact radical IP is Coulombic in nature. Therefore, as the solvent polarity increases it is anticipated that value of ω_Q will decrease. Also, the solvent reorganization energy should correlate with the solvent polarity so that the value of E_s should increase with increasing polarity. During the fitting of the parameters, the magnitude of the electronic barrier height, V^\ddagger , is assumed to remain constant throughout the series of nitrile solvents.

With V^\ddagger set to 17.5 kcal/mol, the fit of the LH model to the remaining three solvent systems is shown in Figure 2.7. The derived values are as follows: butanenitrile ($E_s = 8.0$ kcal/mol and $\omega_Q = 195$ cm^{-1}), propanenitrile ($E_s = 12.0$ kcal/mol and $\omega_Q = 179$ cm^{-1}) and acetonitrile ($E_s = 17.0$ kcal/mol and $\omega_Q = 164$ cm^{-1}). Clearly, the LH model gives an excellent account of the solvent dependence of the rate of proton transfer as a function of enthalpy change for proton transfer. Consistent with expectation [57, 58], the derived values for the solvent reorganization energy fitting parameters for the four nitrile solvents indeed correlate with the solvent polarity E_T (30) (Fig. 2.8).

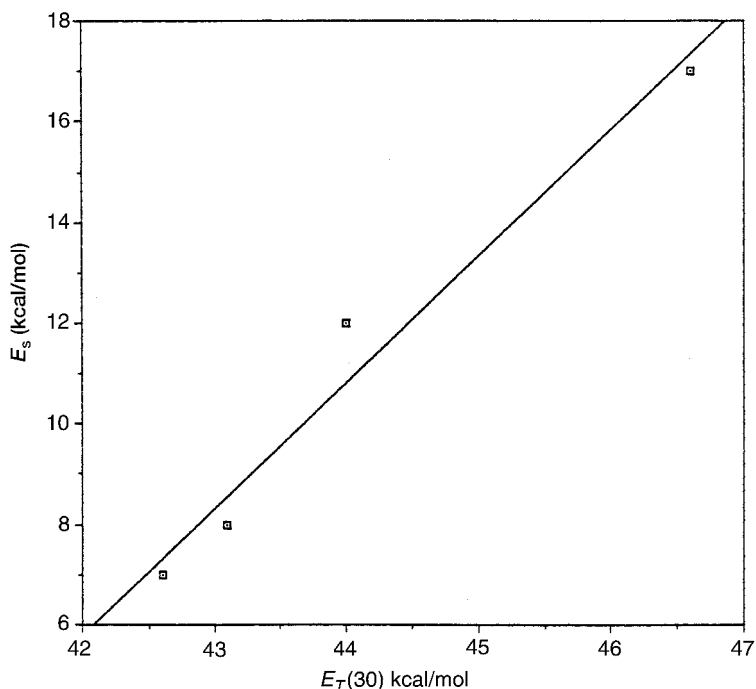


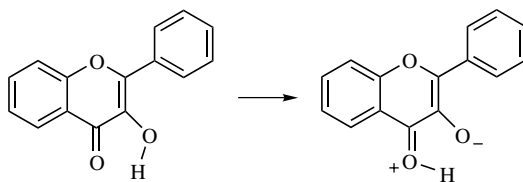
Figure 2.8. The solvent reorganization energies E_s for proton transfer as a function of E_T (30) for the nitrile solvents.

In summary, although the BH model predicts an inverted region for the kinetics of proton in the nonadiabatic regime, the BH model is only in qualitative accord with the data derived from the proton transfer within the benzophenone-*N,N*-dimethylaniline contact radical ion pairs. The failure of the model lies in its 1D nature as it does not take into account the degrees of freedom for the vibrations associated with the proton-transfer mode. By incorporating these vibrations into the BH model, the LH model provides an excellent account of the parameters serving to control the kinetics of nonadiabatic proton transfer. A more rigorous test for the LH model will come when the kinetic deuterium isotope effects for benzophenone-*N,N*-dimethylaniline contact radical ions are examined as well as the temperature dependence of these processes are measured.

V. COMPARISON WITH OTHER MOLECULAR SYSTEMS

In recent years, there have been numerous studies examining the dynamics of proton transfer within the context of recently developed theoretical models. Reactions in the gas phase, in the solution phase, and in matrices have been examined [59–72]. Few of these studies, however, have addressed the issue of how the rate of proton transfer correlates with the thermodynamic driving force, which is an important correlation for discerning the validity of the various theoretical models. However, there have been two series of investigations by Kelley and co-workers [70, 71], and by Pines et al. [65, 66] that have sought to elucidate the role of solvent dynamics on the rate of proton transfer.

Kelley and co-workers [70, 71] measured the dynamics of the excited-state intramolecular proton transfer in 3-hydroxyflavone and a series of its derivatives as a function of solvent (Scheme 2.9). The energy changes associated with the processes examined are of the order of 3 kcal/mol or less. The model they employed in the analysis of the reaction dynamics was based upon a tunneling reaction path. Interestingly, they find little or no deuterium kinetic isotope effect, which would appear to be inconsistent with tunneling theories. For 3-hydroxyflavone, they suggest the lack of an isotope effect is due to a very large

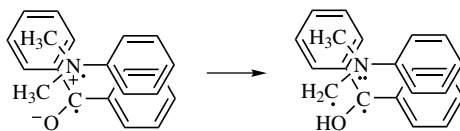


Scheme 2.9

reactant–product electronic coupling, presumably leading to an adiabatic reaction, Eq. (9). A small deuterium kinetic isotope effect was observed in the excited-state intramolecular proton-transfer reactions of 4'-*N,N*-dimethylamino-3-hydroxyflavone and 4'-*N,N*-diethylamino-3-hydroxyflavone, which was attributed to a concomitant phenyl or amine torsion with the proton transfer. There is no clear evidence for nonadiabatic proton transfer in these systems.

Pines et al. [65, 66] examined the energy dependence for the intrinsic rate of proton transfer for several naphthol photoacids–carboxylic base pairs in water. The free energy change for this series of reactions spanned > 14 kcal/mol. The maximum rate of proton transfer approaches a value of $2 \times 10^{11} \text{ s}^{-1}$, which is the magnitude of the slow component of the water reorientation time. No inverted region for proton transfer is observed. This kinetic behavior is in accord with the adiabatic model for proton transfer, Eq. (9), where the dynamics of the solvent become rate limiting. This finding would suggest that in this bimolecular transfer system, the electronic coupling between the reactants and products is large, thus reducing the electronic barrier in the proton-transfer coordinate below the zero-point energy of the vibration associated with the proton-transfer mode (Scheme 2.6, R_C) [13].

An interesting question then arises as to why the dynamics of proton transfer for the benzophenone–*N,N*-dimethylaniline contact radical IP falls within the nonadiabatic regime while that for the naphthol photoacids–carboxylic base pairs in water falls in the adiabatic regime given that both systems are intermolecular. For the benzophenone–*N,N*-dimethylaniline contact radical IP, the presumed structure of the complex is that of a π -stacked system that constrains the distance between the two heavy atoms involved in the proton transfer, C and O, to a distance of $\sim 3.3 \text{ \AA}$ (Scheme 2.10) [20]. Conversely, for the naphthol photoacids–carboxylic base pairs no such constraints are imposed so that there can be close approach of the two heavy atoms. The distance associated with the cross-over between nonadiabatic and adiabatic proton transfer has yet to be clearly defined and will be system specific. However, from model calculations, distances in excess of 2.5 \AA appear to lead to the realm of nonadiabatic proton transfer. Thus, a factor determining whether a bimolecular proton-transfer process falls within the adiabatic or nonadiabatic regimes lies in the rate expression Eq. (6) where $\phi(R)$, the distribution function for molecular species with distance, and $k(R)$, the rate constant as a function of distance, determine the mode of transfer.



Scheme 2.10

VI. SUMMARY

In recent years, there have been many significant advances in our models for the dynamics for proton transfer. However, only a limited number of experimental studies have served to probe the validity of these models for bimolecular systems. The proton-transfer process within the benzophenone–*N,N*-dimethylaniline contact radical IP appears to be the first molecular system that clearly illustrates non-adiabatic proton transfer at ambient temperatures in the condensed phase. The studies of Pines and Fleming on naphthol photoacids–carboxylic base pairs appear to provide evidence for adiabatic proton transfer. Clearly, from an experimental perspective, the examination of the predictions of the various theoretical models is still in the very early stages of development.

ACKNOWLEDGMENT

This work has been supported by the National Science Foundation, CHE 9816540.

REFERENCES

1. R. P. Bell, *The Proton in Chemistry*, Chapman & Hall, London, 1973.
2. A. Fresht, *Enzyme Structure and Mechanism*, W. H. Freeman, New York, 1985.
3. R. D. Gandour and R. L. Schowen, *Transition States of Biochemical Processes*, Plenum Publishing, New York, 1978.
4. R. P. Bell, *The Tunnel Effect in Chemistry*, Chapman & Hall, London, 1980.
5. F. H. Westheimer, *Chem. Rev.* **1961**, *61*, 265.
6. S. Scheiner, *Acc. Chem. Res.* **1985**, *18*, 174.
7. B. C. Garrett, D. G. Truhlar, A. F. Wagner, and T. Dunning, *J. Chem. Phys.* **1983**, *78*, 4400.
8. V. K. Babamow and R. A. Marcus, *J. Chem. Phys.* **1981**, *74*, 1790.
9. D. G. Truhlar and B. C. Garrett, *Acc. Chem. Res.* **1980**, *14*, 440.
10. A. M. Kuznetsov, *Charge Transfer in Physics, Chemistry and Biology*, Gordon & Breach, Luxembourg, 1995, p. 622.
11. D. C. Borgis, S. Lee, and J. T. Hynes, *Chem. Phys. Letts.* **1989**, *162*, 19.
12. D. Borgis and J. T. Hynes, *J. Chem. Phys.* **1991**, *94*, 3619.
13. D. Borgis and J. T. Hynes, *J. Phys Chem.* **1996**, *100*, 1118.

14. R. I. Cukier and M. Morillo, *J. Chem. Phys.* **1989**, *91*, 857.
15. M. Morillo and R. I. Cukier, *J. Chem. Phys.* **1990**, *92*, 4833.
16. D. Li and G. A. Voth, *J. Phys. Chem.* **1991**, *95*, 10425.
17. J. Lobaugh and G. A. Voth, *J. Chem. Phys.* **1994**, *100*, 3039.
18. A. M. Kuznetsov and J. Ulstrup, *Can. J. Chem.* **1999**, *77*, 1085.
19. D. Antoniou and S. D. Schwartz, *Proc. Natl. Acad. Sci. U.S.A.* **1997**, *94*, 12360.
20. K. S. Peters, A. Cashin, and P. Timbers, *J. Am. Chem. Soc.* **2000**, *122*, 107.
21. K. S. Peters and A. Cashin, *J. Phys. Chem. A* **2000**, *104*, 4833.
22. J. Dreyer and K. S. Peters, *J. Phys. Chem.* **1996**, *100*, 19412.
23. J. D. Simon and K. S. Peters, *J. Am. Chem. Soc.* **1983**, *105*, 4875.
24. H. Miyasaka, T. Nagata, M. Kiri, and N. Mataga, *J. Phys. Chem.* **1992**, *96*, 8060.
25. S. G. Cohen, A. Parola, J. George, and H. Parsons, *Chem. Rev.* **1973**, *73*, 141.
26. S. Inbar, H. Linschitz, and S. G. Cohen, *J. Am. Chem. Soc.* **1980**, *102*, 1419.
27. S. Inbar, H. Linschitz, and S. G. Cohen, *J. Am. Chem. Soc.* **1981**, *103*, 1048.
28. D. Griller, J. A. Howard, P. R. Marriott, and J. C. Scaiano, *J. Am. Chem. Soc.* **1981**, *103*, 619.
29. R. F. Bartholomew, R. S. Davidson, P. F. Lambeth, J. F. McKellar, and P. H. Tuner, *J. Chem. Soc. Perkin Trans 2* **1972**, 577.
30. K. Bhattacharyya and P. K. Das, *J. Phys. Chem.* **1986**, *90*, 3987.
31. L. E. Manring and K. S. Peters, *J. Am. Chem. Soc.* **1985**, *107*, 6452.
32. K. S. Peters and J. Lee, *J. Phys. Chem.* **1993**, *97*, 3761.
33. C. Devadoss and R. W. Fessenden, *J. Phys. Chem.* **1990**, *94*, 4540.
34. K. S. Peters, *Advances in Electron Transfer Chemistry*, Vol. 4, JAI Press, 1994, pp. 27–52.
35. A. Weller, *Pure Appl. Chem.* **1982**, *54*, 1885.
36. H. Knibbe, D. Rehm, and A. Weller, *Ber. Bunsenges. Phys. Chem.* **1968**, *72*, 257.
37. D. Rehm and A. Weller, *Israel J. Chem.* **1970**, *8*, 259.
38. I. R. Gould, D. Noukakis, L. G. Omez-Jahn, R. H. Young, J. L. Goodman, and S. Farid, *Chem. Phys.* **1993**, *176*, 439.
39. I. R. Gould and S. Farid, *Acc. Chem. Res.* **1996**, *29*, 522.
40. I. R. Gould, L. J. Mueller, and S. Farid, *Z. Physik. Chem.* **1991**, *170*, 143.
41. K. S. Peters and J. Lee, *J. Phys. Chem.* **1992**, *96*, 8941.
42. K. S. Peters and J. Lee, *J. Am. Chem. Soc.* **1993**, *115*, 3643.
43. K. S. Peters and G. Kim, *J. Phys. Chem. A* **2001**, *105*, 4177.
44. J. Bigeleisen and M. G. Mayer, *J. Chem. Phys.* **1947**, *15*, 261.
45. J. Bigeleisen, *J. Chem. Phys.* **1949**, *17*, 675.
46. W. J. Albery, *Annu. Rev. Phys. Chem.* **1980**, *31*, 227.
47. Y. Kim, D. G. Truhlar, and M. M. Kreevoy, *J. Am. Chem. Soc.* **1991**, *113*, 7837.
48. Y. Kim and M. M. Kreevoy, *J. Am. Chem. Soc.* **1992**, *114*, 7116.

49. A. Kohen and J. P. Klinman, *Acc. Chem. Res.* **1998**, *31*, 397.
50. L. I. Krishtalik, *Biochim. Biophys. Acta* **2000**, *1458*, 6.
51. J. Brickmann, *The Hydrogen Bond-Recent Developments in Theory and Experiments*, North-Holland Publishing, Amsterdam, 1976.
52. E. D. German, A. M. Kuznetsov, and R. R. Dogonadze, *J. Chem. Soc. Faraday Trans. 2* **1980**, *76*, 1128.
53. E. D. German and A. M. Kuznetsov, *J. Chem. Soc. Faraday Trans. 1* **1981**, *77*, 397.
54. S. Lee and J. T. Hynes, *J. Chim. Phys.* **1996**, *93*, 1783.
55. W. J. Leigh, D. R. Arnold, R. W. R. Humphreys, and P. C. Wong, *Can. J. Chem.* **1980**, *58*, 2537.
56. X. Creary, *J. Org. Chem.* **1980**, *45*, 280.
57. M. L. Horng, J. A. Gardecki, A. Papazyan, and M. Maroncelli, *J. Phys. Chem.* **1995**, *99*, 17311.
58. L. Reynolds, J. A. Gardecki, S. J. V. Frankland, M. L. Horng, and M. Maroncelli, *J. Phys. Chem.* **1996**, *100*, 10337.
59. P. F. Barbara, P. K. Walsh, and L. E. Brus, *J. Phys. Chem.* **1989**, *93*, 29.
60. M. Lawrence, C. Marzacco, C. Morton, C. Schwab, and A. M. Halpern, *J. Phys. Chem.* **1991**, *95*, 10294.
61. L. M. Tolbert and S. M. Nesselroth, *J. Phys. Chem.* **1991**, *95*, 10331.
62. R. S. Moog and M. Maroncelli, *J. Phys. Chem.* **1991**, *95*, 10359.
63. G. W. Robinson, *J. Phys. Chem.* **1991**, *95*, 10386.
64. N. Shida, J. Almlof, and P. F. Barbara, *J. Phys. Chem.* **1991**, *95*, 10457.
65. E. Pines and G. R. Fleming, *Chem. Phys.* **1994**, *183*, 393.
66. E. Pines, B. Magnes, M. J. Lang, and G. R. Fleming, *Chem. Phys. Letts.* **1997**, *281*, 413.
67. A. H. Zewail, *J. Phys. Chem.* **1996**, *100*, 12701.
68. M. F. Hineman, G. A. Bruker, D. F. Kelley, and E. R. Bernstein, *J. Chem. Phys.* **1990**, *92*, 805.
69. J. A. Syage, *J. Phys. Chem.* **1995**, *99*, 5772.
70. G. A. Brucker, T. C. Swinney, and D. F. Kelley, *J. Phys. Chem.* **1991**, *95*, 3190.
71. T. C. Swinney and D. F. Kelley, *J. Chem. Phys.* **1993**, *99*, 211.
72. F. Parsapour and D. F. Kelley, *J. Phys. Chem.* **1996**, *100*, 2791.

FUNCTIONAL MOLECULAR GLASSES: BUILDING BLOCKS FOR FUTURE OPTOELECTRONICS

Thomas Fuhrmann and Josef Salbeck

Macromolecular Chemistry and Molecular Materials, Department of Physics,
Kassel University, D-34109 Kassel, Germany

CONTENTS

- I. Introduction: Molecular Materials for Optoelectronics
- II. What is a Low-Molecular Glass?
- III. Structural Concepts for Molecular Glasses
 - A. Class I: Chelate Complexes
 - B. Class II: Twin Molecules
 - C. Class III: Starburst Molecules with C_3 Symmetry
 - 1. Triarylamine Center
 - 2. Benzene Center
 - D. Class IV: Spiro Molecules
 - E. Class V: Tetrahedral Molecules
 - F. Class VI: Other Molecules

- IV. Optical Properties: Absorption and Emission
 - A. Molecular Glasses as Fluorescent Emitters:
From the Blue into the Red
 - 1. Oxadiazoles
 - 2. Oligophenyls
 - 3. Arylamines
 - 4. DPVBi and Derivatives
 - 5. Oligophenylenevinylenes
 - 6. Alq₃
 - 7. Stilbeneamines
 - 8. Oligothiophenes
 - B. Doped Systems for Color Conversion
 - 1. Blue and Green Dopants
 - 2. Yellow and Red Dopants
 - C. Phosphorescent Emitters
 - D. Creating White Light
 - E. Creating Polarized Light
 - V. Amplified Spontaneous Emission and Lasing
 - A. Gain Narrowing in Organic Waveguides
 - B. Laser Resonators
 - VI. Electrical Excitation: Multilayer Structures for Organic Electroluminescent Devices
 - A. The Basic Structure of Organic Light Emitting Diodes
 - B. Redox Potential and Charge Injection Properties
 - 1. Energy Level for Hole Injection
 - 2. Electron Injection
 - 3. Bipolar Molecular Glasses
 - C. Charge Transport
 - 1. Hole Mobilities
 - 2. Electron Mobilities
 - VII. From Light to Current: Application of Molecular Glasses in Solar Cells
 - A. Dye-Sensitized Solar Cells
 - B. Heterojunction Solar Cells
 - VIII. Further Applications: Photochromic and Photorefractive Materials
 - A. Photochromics
 - B. Azo Reorientation and Surface Gratings
 - C. Photorefractives
 - D. Lithographic Resist Materials
 - IX. Conclusion
- References

I. INTRODUCTION: MOLECULAR MATERIALS FOR OPTOELECTRONICS

In modern microelectronics and optoelectronics, there are signs that the way is paved for the application of new organic materials evolving from the art of molecular design and synthetic chemistry. The possibility of introducing various functionalities into molecules—which is the strong point of organic synthesis—offers a broader range of optical and electrical properties than for traditional semiconductors. Especially important—and this will be the key of this chapter—is the combination of different properties to multifunctional materials. Thus, we are talking about the photophysical and photochemical properties of molecular materials, but always in connection with their electrochemical and thermal features, since only the appropriate combination of these properties leads to advanced organic semiconductor devices for real-life applications.

The industrial interest in this area is driven for two reasons: The first one is the steady miniaturization of semiconductor devices down to sizes for which the bulk properties of inorganic semiconductors reach their limit and molecular approaches become important. The second is the need for materials for the increasing low-cost consumer market that is dominated by identifier tags, plastic chip cards, and displays for cellular phones that are all driven by small electronic or optoelectronic circuits. The materials for these applications should be cheap, easy to make, and, last but not least, be environment-friendly, combustible, or better yet biodegradable.

One prominent example of the application of organic materials in optoelectronics is currently making its way from academic research to industrial development: The organic light emitting diode (OLED). It has the potential of following in the success of organic photoconductors in xerography and the introduction of liquid-crystal displays as the third largest scale application of organic optoelectronic materials. The state-of-the-art OLED does not have a simple structure. It consists of a multilayer system made of different functional thin films. Materials optimized for their use as electrodes, charge injection, charge transport, charge barrier, and light emission are employed, which lead to up to seven or more layers. Typically, the layers are prepared by vacuum vapor deposition. A rough scheme of a device preparation line is depicted in Figure 3.1. Following the pretreatment of the substrate, the organic materials and metal electrodes are deposited sequentially in different chambers at high vacuum of $\sim 10^{-7}$ mbar. Usually, effusion cells or molybdenum or tantalum crucibles that are temperature controlled by resistance heating are used. Details of the device structure and the working principle of an OLED will be described in a later chapter.

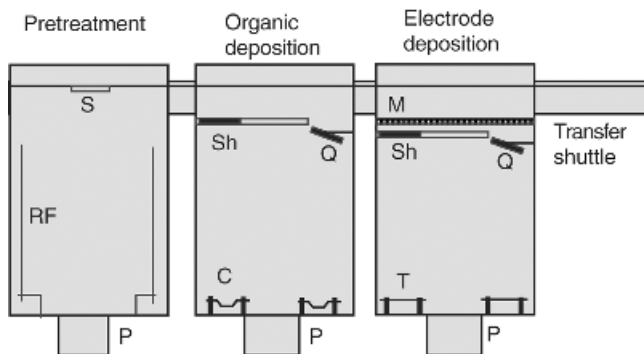


Figure 3.1. Multichamber deposition system for organic light emitting diodes (S: sample, RF: O₂ plasma generator, P: vacuum pump, Sh: shutter, Q: quartz microbalance, C: crucibles, M: mask for electrode patterning, T: tungsten wires for metal deposition).

It is quite obvious that for multilayer structures, low molecular mass materials are in principle more suitable than polymers. Historically, in the development of organic electroluminescence, low molecular mass materials and polymers form the two opposing (but also sometimes converging) approaches toward optoelectronic organic materials. Thin films of polymers are normally processed by spin-coating from solution, thus the problem occurs that orthogonal solvents are needed in order to avoid resolving underlying layers while coating the next ones. There are some strategies, however, to circumvent this problem, for example, by applying soluble precursors that are converted into the final insoluble form by posttreatment of the coated film [e.g., the precursor route to poly(phenylene-vinylene)[1]], or the use of photosensitized cross-linkers such as oxetane groups [2]. But they introduce other difficulties since solvent molecules and residues that have been split off have to be removed, and unreacted sites may act as charge traps or photon quenchers. Thus, the cleanest way to produce impurity-free films is without doubt the direct evaporation of highly purified low molecular materials. The lack of dependence on molecular weight distributions allows a good separation from byproducts by sublimation or chromatographical methods, as well as reliable physical characterization of the materials. The only crucial issue is their ability to form morphologically stable films, but if this is ensured, low molecular functional materials comprise a large box of building blocks that we may combine to a manifold of organic optoelectronic devices.

Morphological stability means that all materials, regardless of their chromophores and whether they are used because of their photophysical, photochemical, or redox properties, should be able to form stable glasses (or alternatively single

crystals, but this will be beyond the scope of this chapter). Thus, we organize this chapter as follows: In Section II, the concept of a molecular glass is presented as a prerequisite and common feature of all photo- and electrofunctional materials treated in this chapter. In Section III, we discuss the general molecular design rules with which chromophores may be fused together in order to yield amorphous glasses rather than crystalline materials. In the following sections, we present all the different kinds of building blocks to which these concepts have been applied: We will find chromophores that are luminescent, electroactive, photo-reactive, and many others in our box.

II. WHAT IS A LOW-MOLECULAR GLASS?

The main morphological advantage of glasses is the absence of grain boundaries in the materials. For the performance of optoelectronic films, it is absolutely necessary that grain boundaries are avoided since they deteriorate the electrical as well as the optical properties due to scattering. Morphologically homogenous films that are not subjected to this problem may consist of single crystals, liquid crystalline monodomains, or amorphous materials. The physical condition that stabilizes the amorphous state of a material against the formation of polycrystallites is the presence of a glass-transition. Below the glass-transition temperature T_g , the molecular motions are frozen, thus preventing ordering into the thermodynamically more stable crystalline form. For the purpose of this chapter, we will not make any distinction between glasses in the true sense of the word, that is, obtained from supercooling a liquid and amorphous films obtained by other methods such as vacuum evaporation, since for almost all materials a glass transition can be measured by calorimetric methods. Not all glasses are isotropic: Liquid crystalline phases are also able to undergo glass transitions, however, they will not be covered here in detail. But one has to keep in mind that even in vapor-deposited or spin-coated films, the preparation process may lead to anisotropic states.

The glass transition as a kinetic process is in principle a function of the time-scale of the experiment, therefore some conventions have to be made for the definition of T_g . Usually, it is defined as the temperature for which the viscosity η of a supercooled liquid is equal to 10^{12} Pa s. The decrease in viscosity upon cooling is accompanied by a discontinuity in the second-order thermodynamic variables such as the heat capacity C_p , the thermal expansion coefficient α , and the compressibility κ . Thus, a frequently used method of determining T_g is by measuring the temperature dependence of C_p by differential scanning calorimetry (DSC) at heating rates of ~ 10 K/min. The glass transition is then indicated by a step in $C_p(T)$. Figure 3.2 shows results of typical calorimetric experiments.

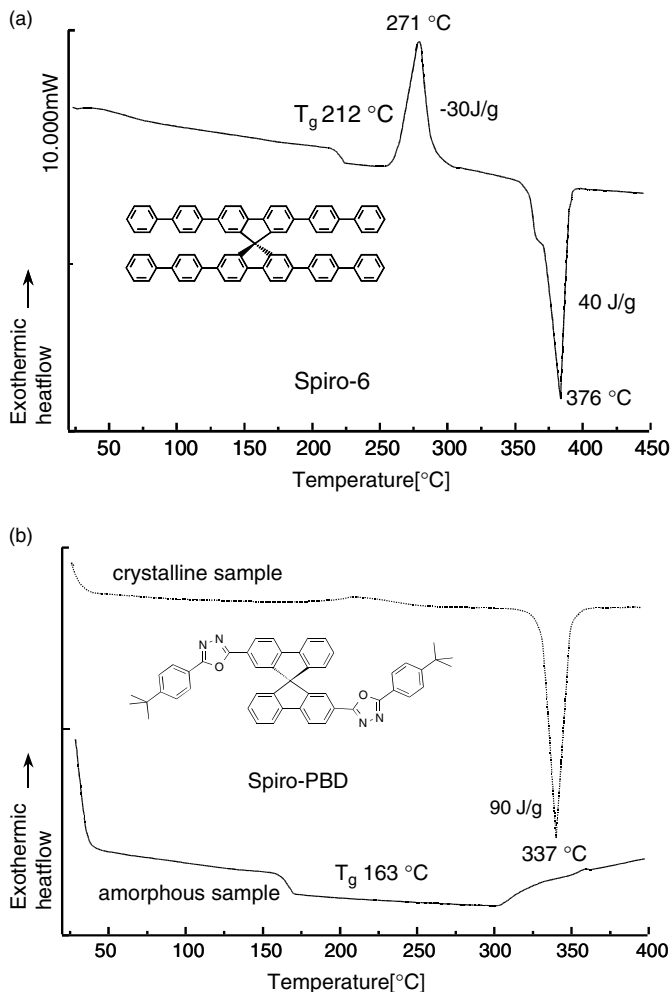


Figure 3.2. Differential calorimetric curves for the molecular glasses (a) Spiro-sexiphenyl (second heating curve) and (b) Spiro-PBD (first and second heating curve). The glass transition is indicated by a characteristic step, the melting point by an endothermic peak. In (a) recrystallization occurs above T_g , which can be seen by an exothermic peak. The material in (b) forms a stable amorphous glass without recrystallization. The melting point from the first heating curve of a crystalline sample (dotted line) disappears in the second heating cycle (solid line). Only the glass transition is visible.

Usually, the materials are crystalline or semicrystalline after the purification procedure, thus a melting peak occurs in the first heating curve. Upon cooling, the material is vitrified, which is indicated by a step in C_p . In the second heating curve, after the endothermal step at T_g , it can be seen whether the material has a low or high tendency toward crystallization. In the latter case, exothermal recrystallization and subsequent melting can be detected (Fig. 3.2a). If the glass is kinetically stable, no recrystallization occurs, and only the step at T_g is visible (Fig. 3.2b).

For ultrathin films, it should also be mentioned that T_g is strongly subjected to interface effects, thus it may be higher or lower than in the bulk material [3]. This finding can be attributed to the interplay between surface and geometric confinement effects. Due to attractive interactions at interfaces, the molecular dynamics may be slowed down, resulting in an increase of T_g , whereas the confinement to a small layer may lead to an increase in the “free volume,” resulting in a decrease of T_g [4].

It would be an advantage to have a detailed understanding of the glass transition in order to get an idea of the structural and dynamic features that are important for photophysical deactivation pathways or solid-state photochemical reactions in molecular glasses. Unfortunately, the formation of a glass is one of the least understood problems in solid-state science. At least three different theories have been developed for a description of the glass transition that we can sketch only briefly in this context: the free volume theory, a thermodynamic approach, and the mode coupling theory.

The free volume theory [5] is based on the assumption that a fixed molecular volume as well as a “free volume” can be assigned to every molecule. Motion of molecules is possible at sufficiently high free volumes in the surrounding. With a linear thermal expansion behavior of the free volume, the empirical temperature dependence of viscosity (see below) can be derived. Indeed, a large fraction of the glassy solid can be considered as empty and capable of incorporating gas and solvent molecules. As a good test for the local free volume, isomerizable molecules like azo dyes have been incorporated into molecular glasses by Moriwaki et al. [6]. The authors investigated the thermal cis–trans back-isomerization of 4-dimethylaminoazobenzene in the molecular glass *m*-MTDATA (**23**) with respect to polystyrene as a host matrix and concluded that the free volume in *m*-MTDATA is smaller than in polystyrene.

The thermodynamic theories [7,8] deny the pure kinetic nature of the glass transition and link it directly to thermodynamic quantities like the configurational entropy of the material. Some recent results suggest a correlation between kinetic quantities and thermodynamic parameters [9]. Also recently, this theory was successfully merged with a potential landscape approach [10]. The thermodynamic approach is interesting since it reflects the different configurations that are allowed not only for the whole ensemble but also for the internal conformations

of one molecule. Almost all molecules that are treated in this chapter can be considered as rigid blocks with only a few links allowing rotational motion. For example, the rotational potential via a biphenyl bond exhibits four minima corresponding to phenyl–phenyl torsions of $\sim 30^\circ$ with energy barriers of 5–10 kJ/mol. For large substituents and highly branched structures, entanglement features also become important.

The mode coupling theory [11] has emerged from the hydrodynamics of liquids. This theory is able to explain the splitting of molecular mobility into relaxation modes that are frozen at the glass transition and molecular motion that is still possible below T_g .

It is useful to compare the glass-forming behavior of small molecules with other glass formers like polymers or inorganic glasses, which can be done by plotting the logarithmic viscosity ($\log \eta$) against the inverse temperature (Angell plot, Fig. 3.3) Based on this plot, the glass-forming materials can be divided into strong glass formers that exhibit an Arrhenius-like linear behavior and fragile glass formers with a steeper change of viscosity while approaching T_g . In the latter case, a Vogel–Fulcher–Tammann relation

$$\eta/\eta_0 = \exp[DT_0/(T - T_0)]$$

or slightly different power laws have been found to be applicable for the viscosity (η) in the temperature (T) range above T_g .

Generally, molecular glasses belong to the most fragile glasses, but details on the vitrification have been investigated for only a few model compounds. The most prominent examples are *o*-terphenyl (OTP) with a T_g of -29°C [12], and the isomeric 1,3,5-trinaphthylbenzenes (TNB) [13, 14] with $T_g = 81^\circ\text{C}$ for 1,3,5-tri- α -naphthylbenzene [15]. The introduction of interactions like hydrogen bonds moves the materials to the less fragile regime. In this case, T_g is enhanced, as Naito [16] demonstrated with nonpolymeric, polyhydrogen-bonded molecules that exhibit T_g values at $\sim 200^\circ\text{C}$.

A unified understanding of the viscosity behavior is lacking at present and subject of detailed discussions [17, 18]. The same statement holds for the diffusion that is important in our context, since the diffusion of oxygen into the molecular films is harmful for many photophysical and photochemical processes. However, it has been shown that in the viscous regime, the typical Stokes–Einstein relation between diffusion constant and viscosity is not valid and has to be replaced by an expression like

$$D \propto \eta^{-\xi}$$

with a temperature-independent coupling parameter ξ . Unfortunately, because of the long timescale of diffusion in the vitreous state, data regarding the diffusion

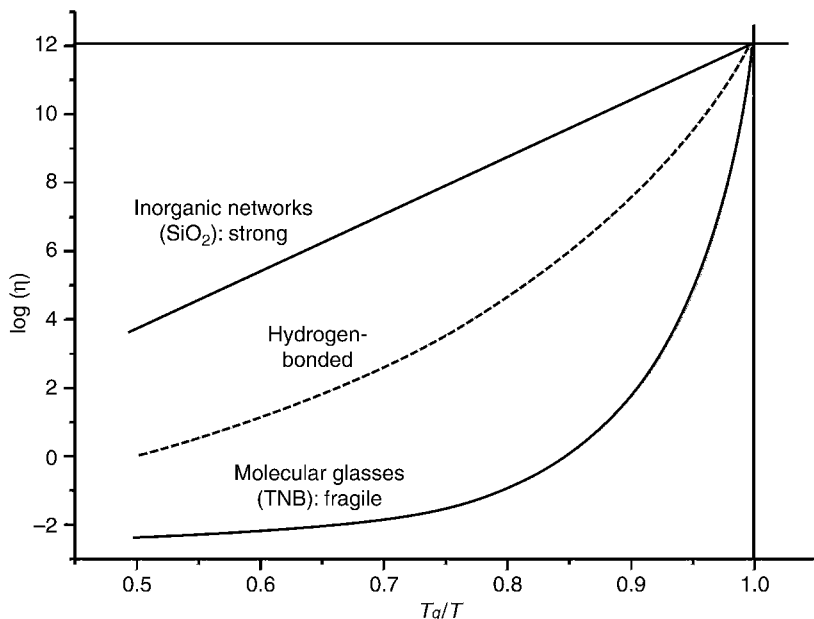


Figure 3.3. Angell plot for the classification of glass formers. The logarithmic viscosity is plotted against the inverse temperature. Above the glass transition, strong glass formers such as inorganic glasses show an Arrhenius behavior, while low molecular glasses obey a Vogel–Fulcher–Tammann law (fragile glasses). In this plot, polymers and hydrogen-bonded networks can be found between the two extremes.

of tracer molecules below T_g are rare. Around T_g , the diffusion coefficient of a dye, 2,2'-bis(4,4'-dimethylthiolan-3-one) in OTP and TNB was measured by forced Rayleigh scattering to be in the order of magnitude of $\sim 10^{-15}$ cm²/s [19].

The importance of the glass transition for device performance that justifies our brief digression into the theory of glasses can be seen clearly in some experiments on the thermal stability of devices. All devices made of the materials presented here are operated in the glassy state. It is therefore necessary that T_g lies well above room temperature. The dynamic nature of the glass transition means that even below T_g motion is possible. Diffusion and crystallization occur, but on a longer timescale. Even at 40 K below T_g , substantial relaxation processes can be found. Some measurements have been made on pharmaceutical products based on molecular glasses for which it is interesting to note that similar requirements have to be fulfilled as for optoelectronic materials. For a range of molecular glasses including indomethacin [20], various benzodiazepines [21] and paracetamol [22], relaxation processes have been determined below T_g . The

authors concluded that storing temperatures of $T_g - 50$ K are necessary in order to achieve the required shelf life. For a fulvene with $T_g = 84^\circ\text{C}$ Alig et al. [23] observed simultaneous ageing and crystallization at $T_g - 40$ K. The best evidence for recrystallization can be seen with the classical hole transport material *N,N'*-diphenyl-*N,N'*-bis(3-methylphenyl)-(1, 1'-biphenyl)-4, 4'-diamine (TPD, **6**). The T_g is $\sim 60^\circ\text{C}$, but for a vacuum evaporated film, crystallization was observed after a few hours at 25°C [24, 25]. The breakdown of the performance of a light emitting diode when one of its components reaches T_g is demonstrated in Figure 3.4 (after [26]). TPD with $T_g = 63^\circ\text{C}$ (**6**, triangles) was replaced by a spiro-linked

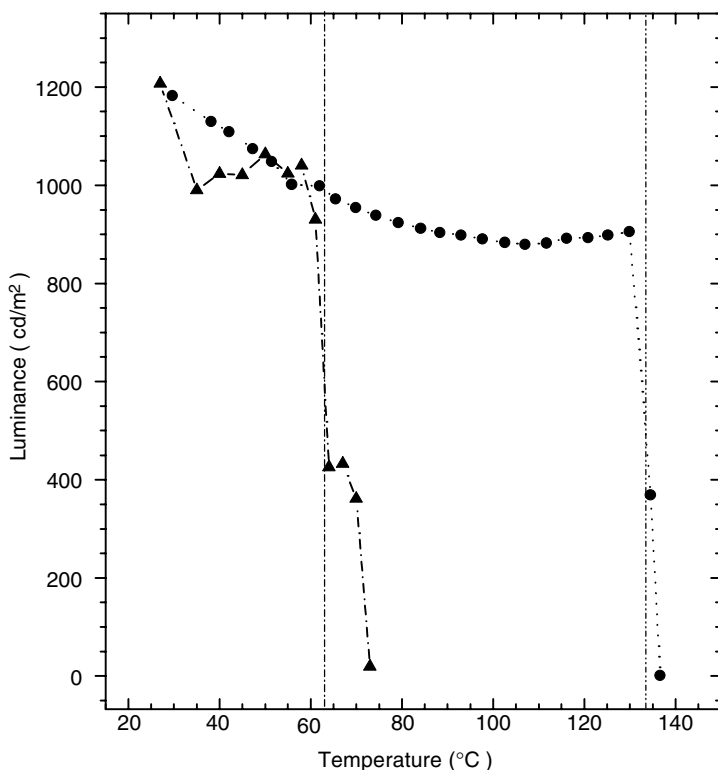


Figure 3.4. Breakdown of device performance at T_g : The luminance for a constant current density of 25 mA/cm^2 is plotted for two light emitting diodes that were made with hole transport materials of different T_g . Triangles: 75-nm TPD/65 nm Alq_3 ; Circles: 75-nm Spiro-TAD/65 nm Alq_3 . The dotted lines mark the respective T_g values: TPD 63°C , Spiro-TAD 133°C . At these temperatures, the materials become soft, which results in a steep decrease in the efficiency.

compound (Spiro-TAD, **36a**, circles) with similar electronic properties but higher T_g (133°C, solid line). It can clearly be seen that the device performance decreases substantially when the temperature reaches T_g in each case.

III. STRUCTURAL CONCEPTS FOR MOLECULAR GLASSES

According to Naito and Miura [27] who examined the relations between thermal properties and thermodynamic parameters, morphologically stable molecular glasses require a high T_g , a low maximum crystal-growth velocity, and a high temperature of maximum crystal growth. They derived a molecular design rule for suitable dyes that are predicted to be large, symmetric, rigid, and dense. Similar concepts have been developed by Wirth [28].

In this section, we present the most important molecular families that have been designed by various groups in order to fulfill these requirements. We will group the materials in different classes by symmetry according to their molecular core. A variety of functional dyes have been linked to each of the cores, the properties and applications of which will be discussed in Section IV.

A. Class I: Chelate Complexes

An important class of molecular glasses is based on metal–chelate complexes (Fig. 3.5). One of the most widely used materials because of its excellent luminescent, electron transporting, and film-forming properties is tris(8-quinolinolato) aluminium, commonly referred to as Alq_3 (**1**). The compound Alq_3 is one of the typical examples for amorphous films that can be prepared by vacuum vapor deposition. The glass transition temperatures reported by several authors are 170 [29], 172 [30], 175°C [27]. Remember that two geometric isomers can be formulated for Alq_3 , the meridional (*mer*) and the facial (*fac*) form [31, 32], which may even be interconverted to each other at high temperatures. The presence of both forms in amorphous films stabilizes the glassy state and prevents crystallization. Approaches toward a further entropic stabilization of the glass involve the substitution of the chelate ligands [33] as well as the preparation of blends [34]. The use of the 4-methyl-8-quinolinolato ligand turned out to be especially successful [35]. A problem in the use of these types of complexes, however, is hydrolysis when traces of moisture are present [30]. At longer exposure to solvent vapors, crystallization occurs in the form of dendrimeric or needle-shaped crystallites [36].

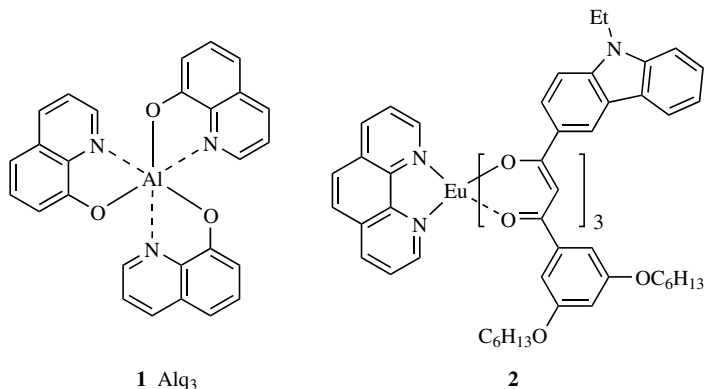


Figure 3.5. Glass-forming metal complexes.

A broad range of metal centers have been used for the complexation of functional ligands, including beryllium [37], zinc, transition metals such as iridium [38], and the lanthanide metals introduced by Kido [39], especially europium and terbium. Common ligands are phenanthroline (phen), bathophenanthroline (bath), 2-phenylpyridine (ppy), acetylacetonate (acac), dibenzoylmethanate (dbm), and 11 thenoyltrifluoroacetate (TTFA). A frequently used complex is the volatile $\text{Eu}(\text{TTFA})_3(\text{phen})$, **66** [40].

In general, these complexes tend to crystallize and require the use of a stabilizing matrix. By incorporating larger ligands, the glass-forming tendency is increased, one example being the europium complex **2** with $T_g = 65^\circ\text{C}$, which was reported recently by Robinson et al. [41].

B. Class II: Twin Molecules

One rather straightforward way to get glass-forming functional molecules is the connection of dyes to “dimeric” twin molecules (Fig. 3.6). In the simplest case, if the electronic structure of each half is to be maintained, the connection is made by an alkyl spacer. Care must be taken that not too much flexibility is introduced, which may reduce T_g . Thus, short spacers like methylene linkages are best suitable. One example is 1,1-bis(di-4-tolylaminophenyl)cyclohexane (**3**), which was used in the first high-efficiency bilayer light-emitting diode by Tang and Van Slyke [42].

Flexible and semiflexible chains for the connection of carbazole units have been used by Braun et al. [43, 44]. However, it can clearly be seen that introducing longer alkyl spacers lowers the T_g . In addition to carbazoles, the

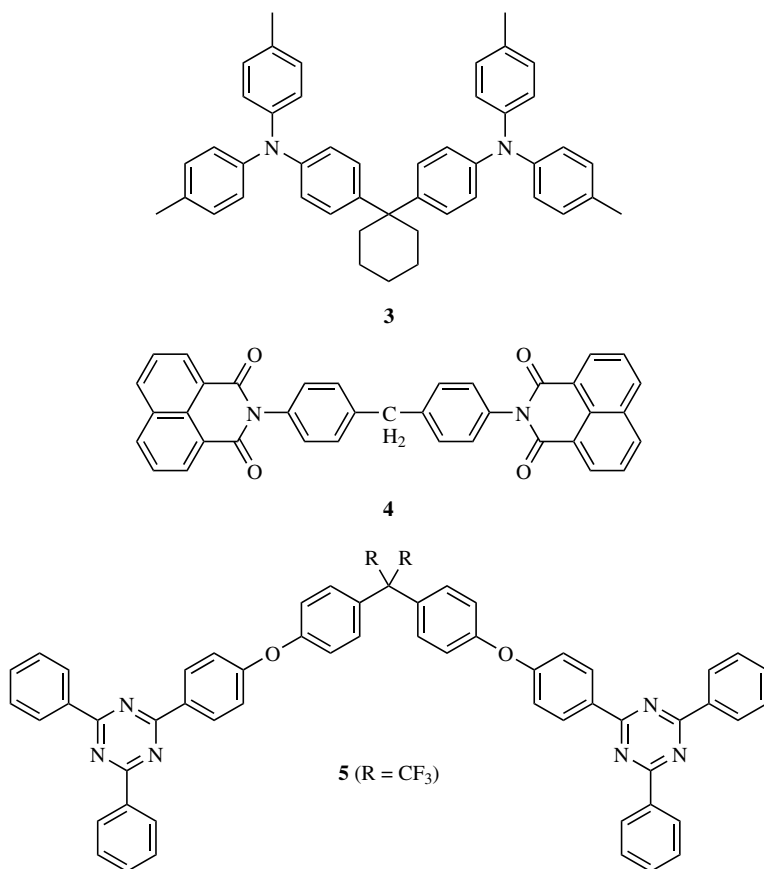


Figure 3.6. Twin molecules connected by alkyl bridges.

authors investigated phenothiazine naphthalimide, and pyrene molecules linked by aliphatic spacers as well. A high T_g of 170°C was obtained for 4,4'-bis(1,8-naphthalimido)diphenylmethane (NI-ME, **4**) with a C1 spacer.

Another example of a dimeric, alkyl-linked molecule is **5**. Here, two triazine ethers are coupled by a central methylene unit [45].

Direct linkage of aromatic halves by a biphenyl bond is also possible, which leads to a large family of molecular glasses. The twist angle of this linkage is $\sim 30^\circ$, which couples the halves electronically. However, the extent of this coupling depends on the nature of the chromophore halves. Most compounds of this family are based on the common diaminobiphenyl core (Fig. 3.7). The classical

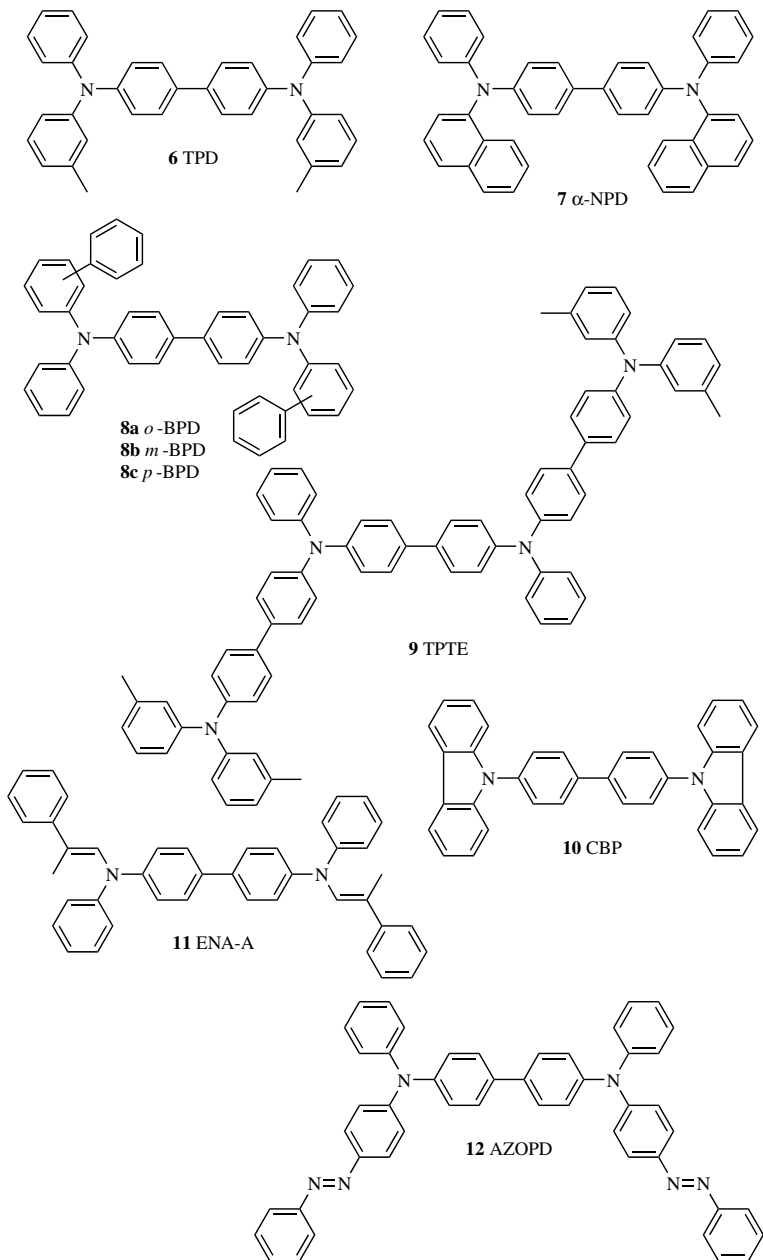


Figure 3.7. The compound TPD and related molecular glasses based on diaminobiphenyl.

example is the hole transporting dye TPD (**6**) [46]. The T_g of TPD is relatively low ($T_g = 60^\circ\text{C}$), but can be increased by proceeding to derivatives with bulkier groups. For example, N,N' -bis(1-naphthyl)- N,N' -diphenyl-4,4'-diamine (α -NPD, **7**) [47], with a T_g of 95°C and the isomeric N,N' -bis(biphenyl)- N,N' -diphenyl-4,4'-diamines (*o*-, *m*-, *p*-BPD, **8**) [48] are derived from TPD. α -NPD has now replaced TPD in many applications. The concept of coupling aryl amino groups via biphenyl bonds was extended to linear oligomers such as TPTE (**9**) with $T_g = 130^\circ\text{C}$ [49]. Other aryl amine chromophores linked by biphenyl bonds include the TPD-derived carbazole **10** [50], enamines like ENA-A, **11** [51], and azo chromophores such as N,N' -bis[4-(phenylazo)phenyl]- N,N' -diphenyl-4,4'-diamine (AZOPD, **12**) [52]. Compounds **11** and **12** exhibit glass transition temperatures of 22 and 101°C , respectively.

Instead of linking phenyl units, thiophene or other heterocycles may be used (Fig. 3.8). In the BMA-*n*T series **13** by Shirota and co-workers [53–55], the aryl amino groups are connected by one, two, three or four thiophene groups. The glass transition temperatures increase in the series from 86, 90, 93, to 98°C . In the corresponding BMB-*n*T (**14**) series, the amine was replaced by dimesityl-boryl moieties [56]. The glass transition temperatures are with 107°C for BMB-2T and 115°C for BMB-3T higher than for the amino derivatives. Other structures involving 13 oligothiophene moieties are the pyrene bearing quaterthiophenes **15** ($T_g = 65^\circ\text{C}$) [57] and **16** [58] with a central thienyl-*S,S*-dioxide unit.

Twin molecules consisting of oxadiazoles have been made by coupling smaller oxadiazoles such as OXD-7 (**17**) which was introduced by Saito and Tsutsui [59] to dimers (**18**). The glass-forming capability was improved with an increase in T_g from 77°C (OXD-7) to 186°C (dimer) [60, 61].

Instead of replacing phenyl rings by heterocycles in order to get altered electronic properties, perfluorated rings may also be used as building units. One example for a perfluorated dimer is **19** with $T_g = 133^\circ\text{C}$ [62, 63].

In order to round-off our overview on the symmetric compounds of this class, we add the stilbene-like molecules TTPAE (**20**) ($T_g = 111^\circ\text{C}$) [27], the bis-(styryl)anthracene (BSA, **21**) [64], and DPVBi (**22**) [65] (Fig. 3.9). Compounds **20** and **21** are characterized by a rigid structure leading to a large electronic delocalization through the center of the molecules. Compound **22** is more flexible due to the biphenyl bond. The outer phenyl rings are twisted by steric repulsion, leading to a nonplanar structure of the stilbene units.

In principle, dimeric molecules may also be made out of different halves leading to asymmetric compounds. Different substituted arylamines have been coupled by Thompson et al. [66]. True bipolar compounds with a different electronic character in each half will be discussed in Section VI in the context of their redox properties. Despite their polar character, the tendency toward crystallization can be low, and amorphous films are obtained.

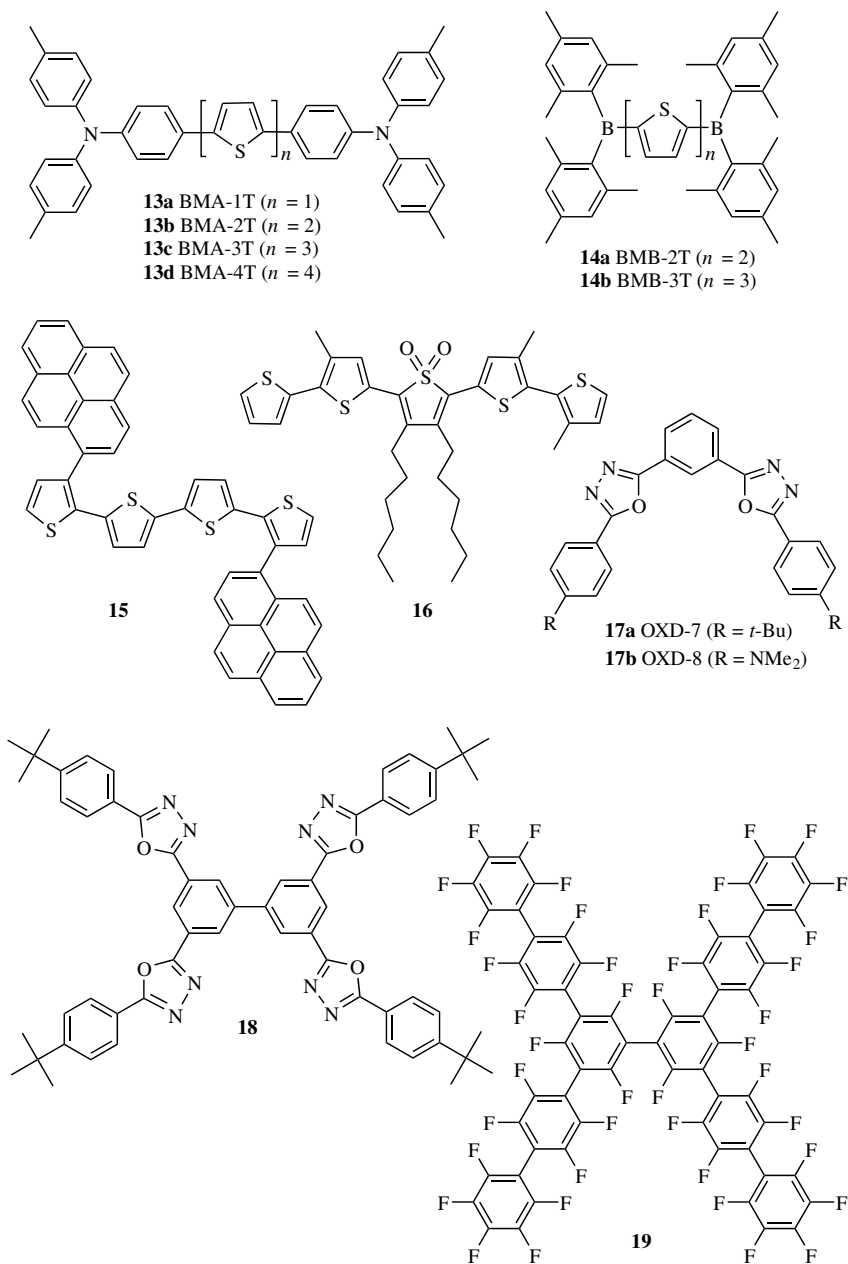
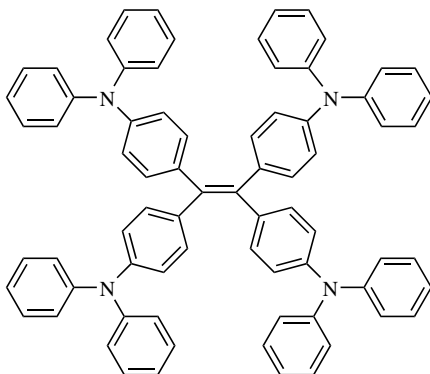
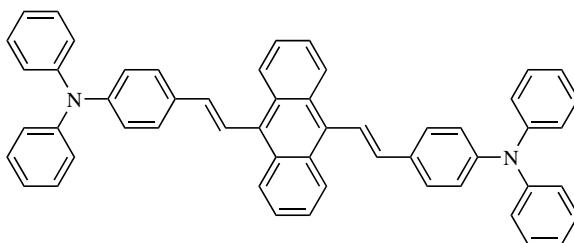
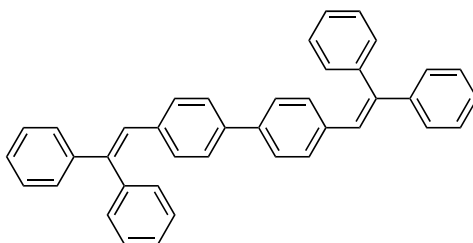


Figure 3.8. Symmetric molecular glasses consisting of thiophenes, oxadiazoles, and perfluorinated aryl rings.

**20 TTPAE****21 BSA****22 DPVBi****Figure 3.9.** Stilbene-like molecular glasses.

C. Class III: Starburst Molecules with C_3 Symmetry

A very productive strategy for the synthesis of glass-forming materials is the use of highly branched rigid structures. As a suitable center for “starburst” molecules with a threefold symmetry, triarylamine or benzene are used most frequently. Due to the large number of starburst molecules described in the literature, we divide this class into two subgroups, compounds based on the triarylamine and the benzene centers.

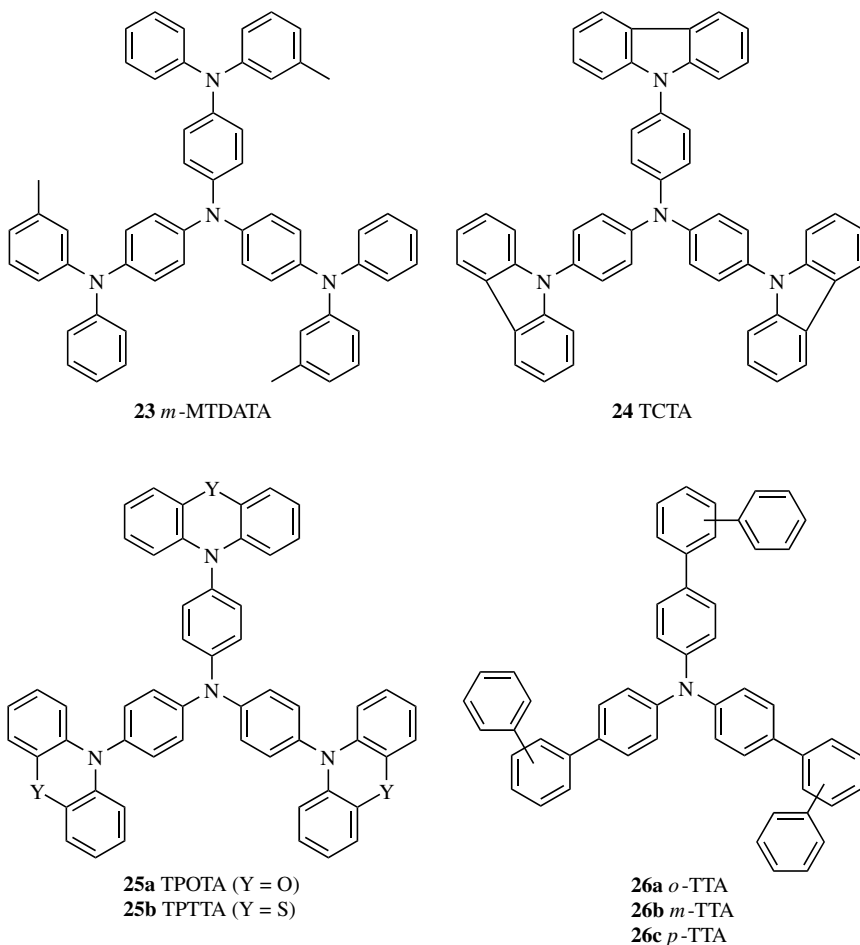


Figure 3.10. Molecular glasses based on a triarylamine core.

1. Triarylamine Center. Since many of the materials have been developed as charge transporting materials, the triarylamine moiety is favored as a branching center for starburst molecules (Fig. 3.10). The classical example is 4,4',4''-tris(3-methylphenylamino)triphenylamine (*m*-MTDATA, **23**) [67], which is used by many research groups as hole injection material for electroluminescent devices. Its T_g is 75°C, and it can be stored for > 10 years without crystallization. Other substituents that have been combined with the triarylamine core include carbazoles (TCTA, **24** [68]), phenoxazines (**25a**), and phenothiazines (**25b**) [69] and oxadiazoles (**71**, Fig. 3.30) [70], or just larger oligophenyl branches (**26**) [71]. The effect on the flexibility and the glass transition can be significant: Compared with *m*-MTDATA, the T_g of TCTA ($T_g = 150^\circ\text{C}$) is increased by 75°C. The glass transition temperatures of TPOTA (**25a**) and TPTTA (**25b**) are reported to be 145 and 141°C, respectively. Compound **71** shows a glass transition at 137°C with no evidence of crystallization.

2. Benzene Center. If a benzene core is 1,3,5-substituted by three amine groups, materials with hole transporting character such as *p*-DPA-TDAB (**27a**) and MTBDAB (**28**) are obtained (Fig. 3.11). Both materials are highly branched and show no recrystallization upon heating from the glassy state. Their glass transition temperatures are 107 and 134°C, respectively. Smaller molecules with lower T_g have been made by substituents like alkyl [72], aryl [73], or halogen [74] groups instead of the outer diarylamino moieties. Another possibility for getting derivatives of this group is by replacing the central benzene ring by 1,3,5-triazine [75].

Corresponding electron-transport materials have been made by replacing the amino substituents in the first shell by oxadiazole groups (**29**) [70, 61] or phenylquinoxalines (**30**) [60]. As in the case of the amines, dendrimer-shaped structures are obtained by repeating the substitution pattern in a second shell (**31**) [76]. The T_g was increased from 142°C in **29** to 222°C in **31**.

The T_g can be raised even further if additional phenyl rings are inserted into the branches of these compounds (Fig. 3.12). Based on this concept, starburst molecules with 1,3,5-triphenylbenzene (**32**) and 1,3,5-triethynylbenzene cores have been reported [77–79]. The T_g of **32** compared with **31** is increased by 23°C.

Other modifications like the insertion of thiophene [80] rings, the use of fluorene moieties [81] (**33**), and perfluorination [62] have also been made. Compound **34** is a structural isomer to **19** with a different arrangement of the 10 rings. It has a lower tendency of crystallization than **19**, but its T_g is similar (135°C).

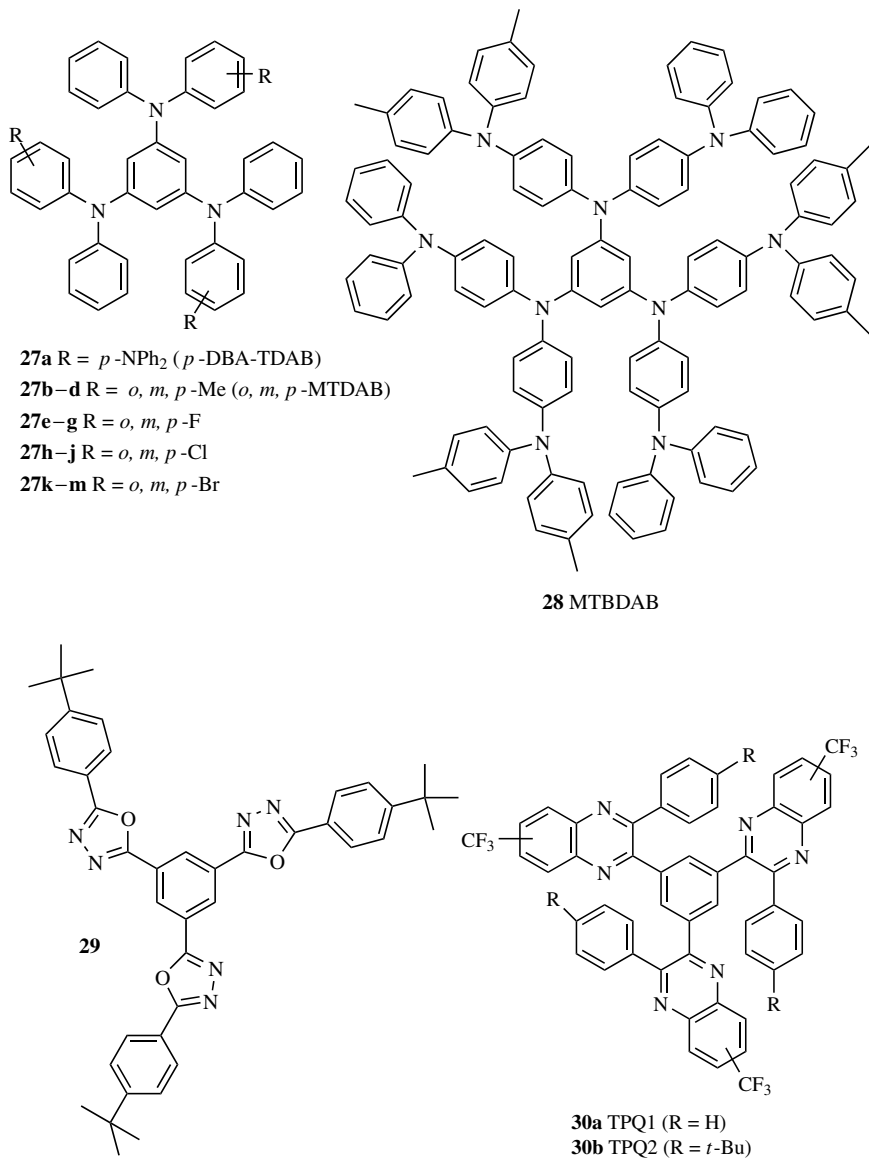


Figure 3.11. Molecular glasses based on a 1,3,5-substituted benzene core.

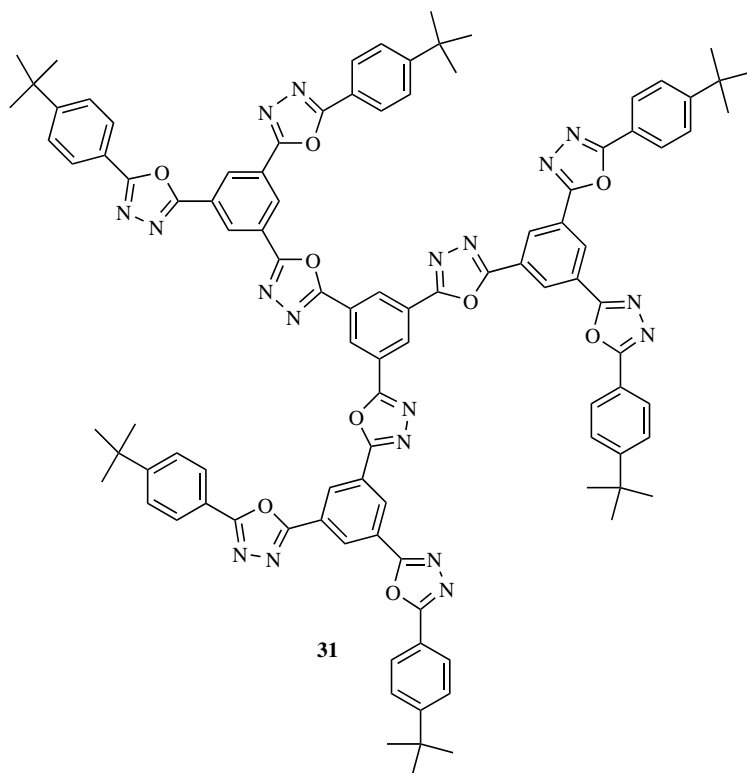


Figure 3.11 (Continued)

D. Class IV: Spiro Molecules

A very promising approach for improving the morphological stability of chromophores while retaining their functionality is linking two chromophores via a spiro center (Fig. 3.13). The chromophores are forced into a perpendicular arrangement by this linkage, resulting in a weak interaction of the molecular halves. Most spiro compounds are based on spirobifluorene as the central unit. If the core is symmetrically substituted (e.g., four equal substituents in the 2,2',7,7'-positions of spirobifluorene), the characteristic D_{2d} symmetry with a fourfold improper rotation axis (S_4) results. Examples include the spiro-oligophenyls (35) diarylamino substituted spirobifluorenes (36), and the corresponding carbazole (37) [82], or Spiro-DPVBi (38) [83]. In the series of the spiro-oligophenyls,

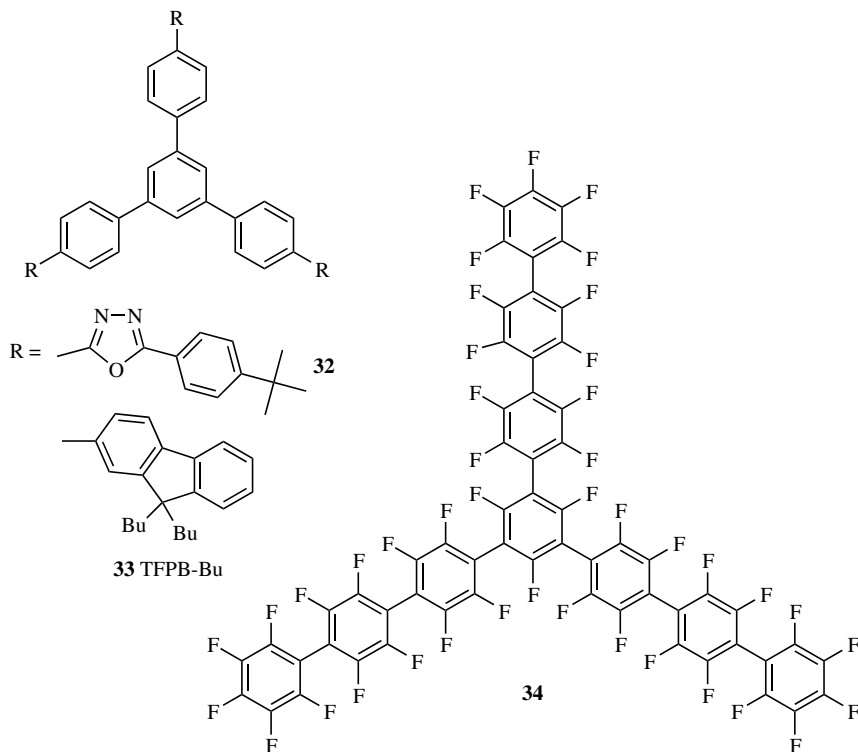
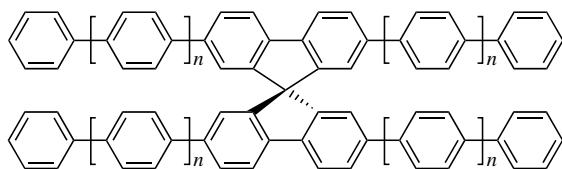


Figure 3.12. Molecular glasses based on a 1,3,5-substituted benzene core.

the T_g is increasing with increasing chain length in the order 184°C (spiro-quaterphenyl, **35a**) $< 212^\circ\text{C}$ (spiro-sexiphenyl, **35b**) $< 243^\circ\text{C}$ (spiro-octiphenyl, **35c**). For the arylamines, the glass transition temperatures are lower. The T_g of (**36a**) is 133°C , whereas the flexible methoxy groups in **36b** lowers T_g somewhat to 121°C . The glass transition of Spiro-DPVBi (**38**) lies in the same range ($T_g = 130^\circ\text{C}$).

In order to obtain asymmetric spiro compounds, there are two different possibilities. First, one can connect two different chromophores via a common spiro center. The thiophene compounds **39a** and **39b** are one example [84, 85]. Second, one can connect two equal but asymmetric chromophores. Based on this principle are Spiro-PBD (**40**), spiro-bridged bis(phenanthrolines) (**41**) [86], and the branched compounds Octo1 (**42a**) and Octo2 (**42b**) [87]. Because of their symmetry, these molecules are chiral. The glass transition temperatures of **40** and **42b** are reported to be 163 and 236°C , respectively [88]. Unfortunately, reports on the thermal properties of **39** and **41** are lacking.

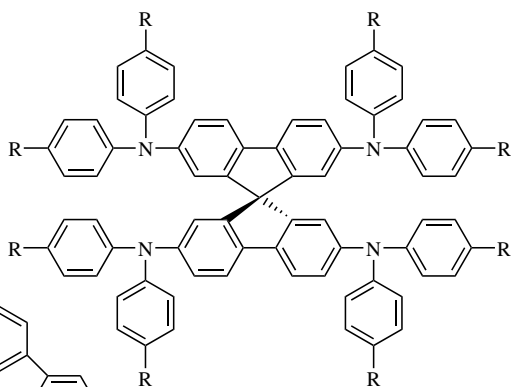


35a Spiro-4 ϕ ($n = 0$)

35b Spiro-6 ϕ ($n = 1$)

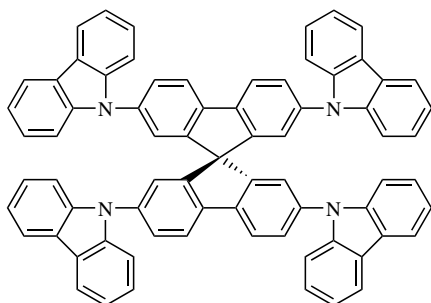
35c Spiro-8 ϕ ($n = 2$)

35d Spiro-10 ϕ ($n = 3$)

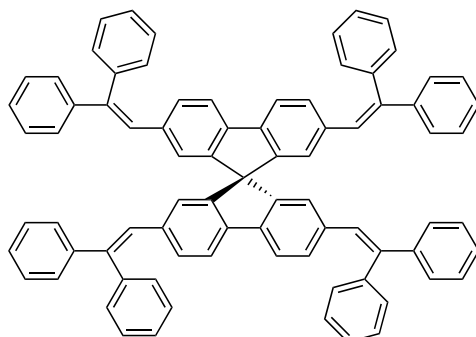


36a Spiro-TAD ($R = H$)

36b Spiro-MeOTAD ($R = OMe$)

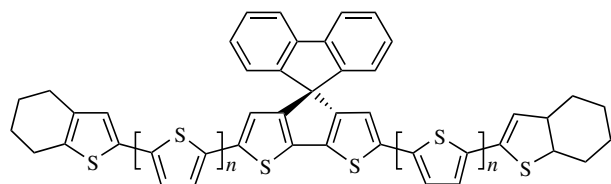
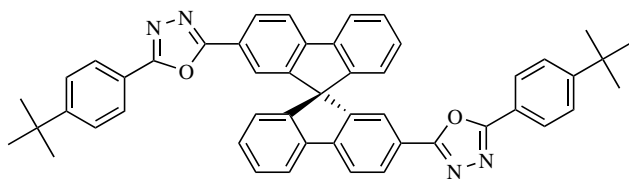
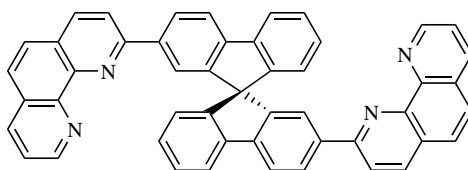


37 Spiro-Carb



38 Spiro-DPVBi

Figure 3.13. Molecular glasses based on a spiro linkage.

**39a** ($n = 0$)**39b** ($n = 1$)**40** Spiro-PBD**41****Figure 3.13** (Continued)

The spiro concept was extended toward higher generations of dendrimer-like molecules (Fig. 3.14) 4-Spiro² (**43**), 4-Spiro³ (**44**) [89]. By multiple spiro linkages, chromophores of different chain length (biphenyl, sexiphenyl, deciphenyl) are connected orthogonally. Only a few bonds are subjected to rotation in these rather rigid molecules. T_g is high, 273°C for 4-Spiro². These types of molecules are interesting for realizing “photon funnels” with cascaded energy-transfer toward the molecular center [90].

One of the great advantages of using spiro compounds is—in addition to the stability of the glassy state—the significant improvement of the solubility which is very well illustrated in the series of the spiro-oligothiophenes. The solubility of the higher homologues with 8 and 10 phenyl rings in each chain is still in the order of 10 g/L, while the parent compounds octi- and deciphenyl are hardly soluble at all [91].

E. Class V: Tetrahedral Molecules

Molecules with tetrahedral symmetry can be realized with adamantane cores or tetrasubstituted sp^3 centers (Fig. 3.15). Braun et al. [92] synthesized some adamantane glasses with glass transition temperatures of 116°C for 1,3,5,7-tetrakis (biphenyl-4-carboxyloxy)adamantane (**45a**) and 118°C for 1,3,5,7-tetrakis (4-iodobenzoyloxy)adamantane (**45b**), respectively. It is interesting to note that if the direction of the ester linkage is reversed (esters of adamantanetetracarboxylic acid), T_g is lowered by ~ 30 K.

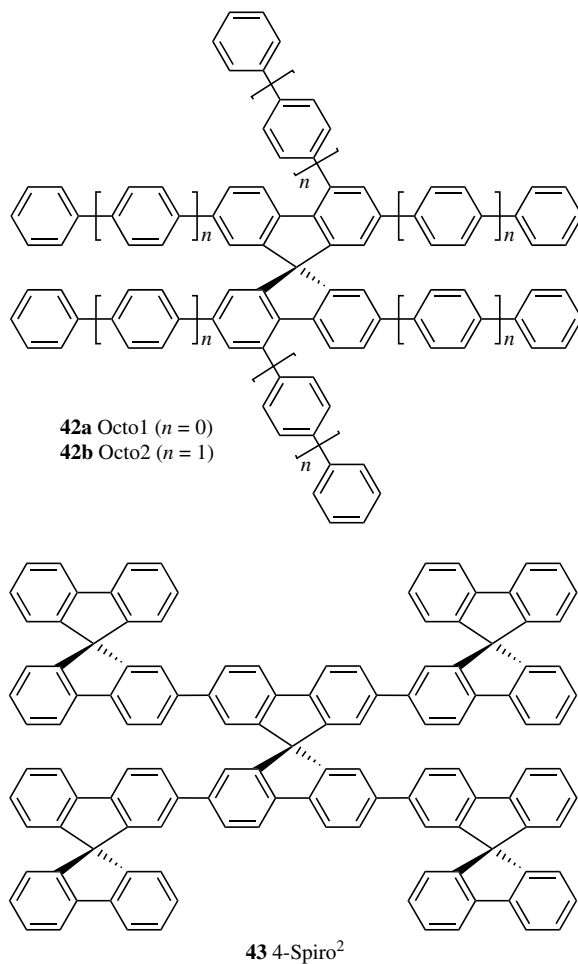
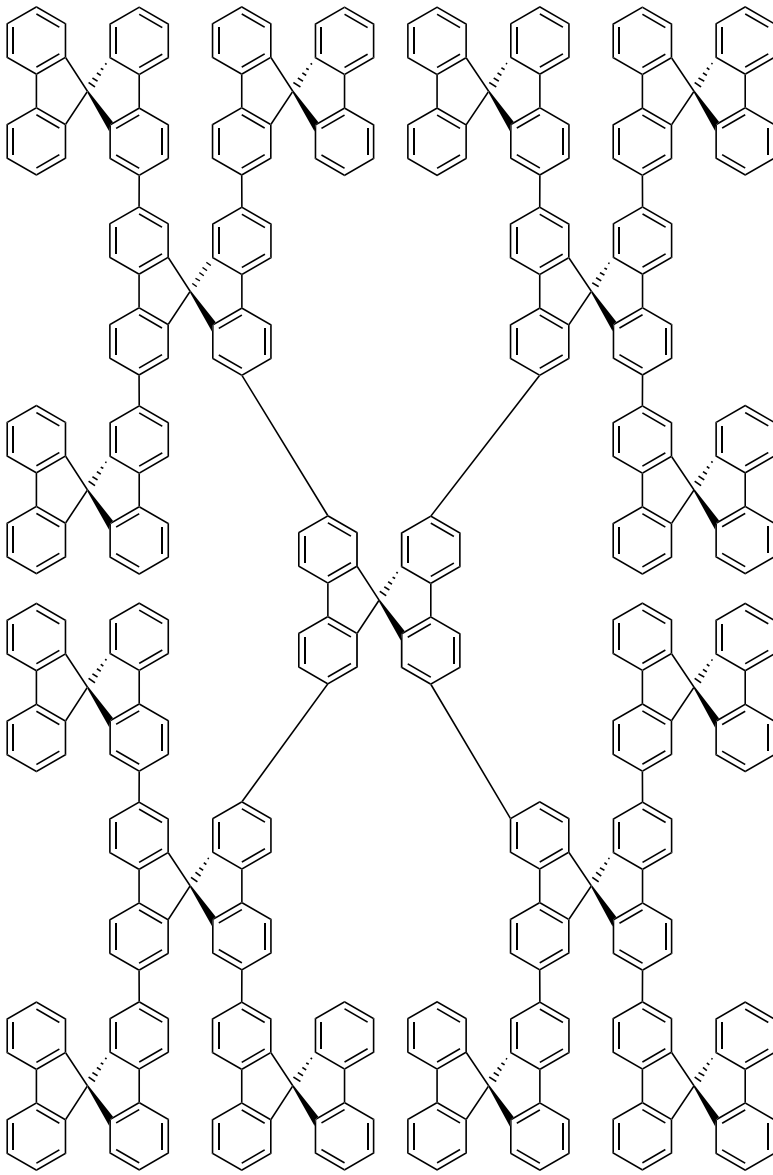


Figure 3.14. Higher generations of spiro-linked glasses.



44 4-Spiro³

Figure 3.14 (Continued)

Bazan and co-workers [93] coupled four branches of stilbene chromophores to a central C atom, leading to tetrastilbenylmethane [C(STB)₄, **46a**]; tetrakis(4-*tert*-butylstyrylstilbenyl)methane [C(*t*-BuSSB)₄, **46b**], and the higher homologue tetrakis{4-[4'-(4''-*tert*-butylstyryl)styryl]stilbenyl}methane [C(4R-*t*-Bu)₄, **46c**]. For **46b**, T_g is 190°C, and for **46c** it is as high as 230°C. Tetrakis(4,4'-2,2-diphenyl-vinyl)-1,1'-biphenyl)methane [C(DPVBi)₄, **47a**] and the cyano derivative **47b** exhibit the glass transition at 142 and 174°C, respectively. Similar compounds to **46a** and **46b** have also been synthesized with silicon and adamantane as the tetrahedral center.

F. Class VI: Other Molecules

Other structural motifs for designing molecular glasses have been exploited (Fig. 3.16). Some of them are based on five-membered rings as the central part of the molecule, like 1,2,4-triazoles (**48**) [94] or the electron-transporting material NAPOXA (**49**) [95]. Pentaphenylcyclopentane (**50**) exhibits a T_g of 57°C [27]. Braun et al. [96] synthesized some fulvenes with T_g ranging from 74 to 120°C (**51**).

Shirota and co-workers [97] showed that arylaldehyde (**52a**) and arylketone hydrazones (**52b**), which find applications in electrophotography, exhibit glass-forming properties. The glass transition temperatures are relatively low (50°C for DPH, **52a**). Indolocarbazoles (**53**) may serve as rigid linking units for molecular glasses leading to high- T_g compounds [98]. Some functional dyes such as merocyanines (**54**) also can be prepared in the glassy state [99–101]. Despite their high

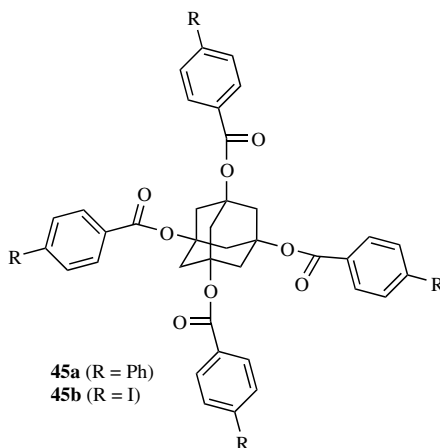


Figure 3.15. Tetrahedral molecular glasses.

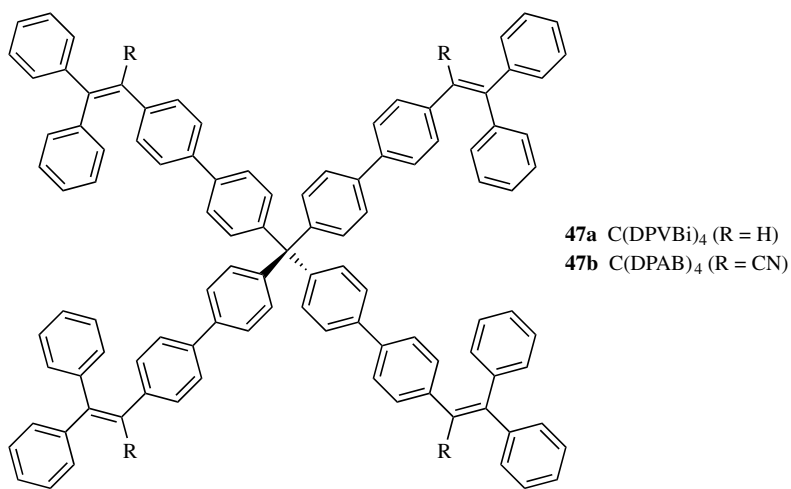
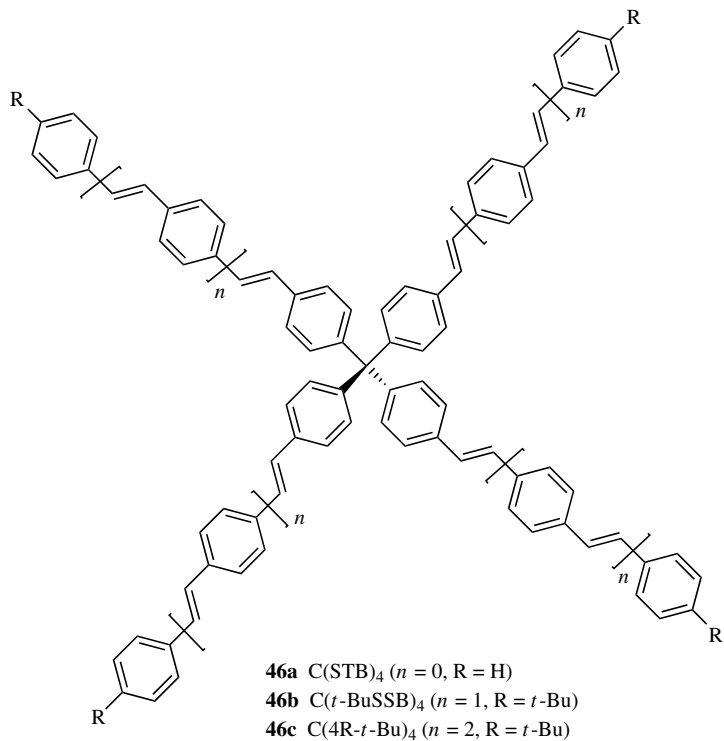


Figure 3.15 (Continued)

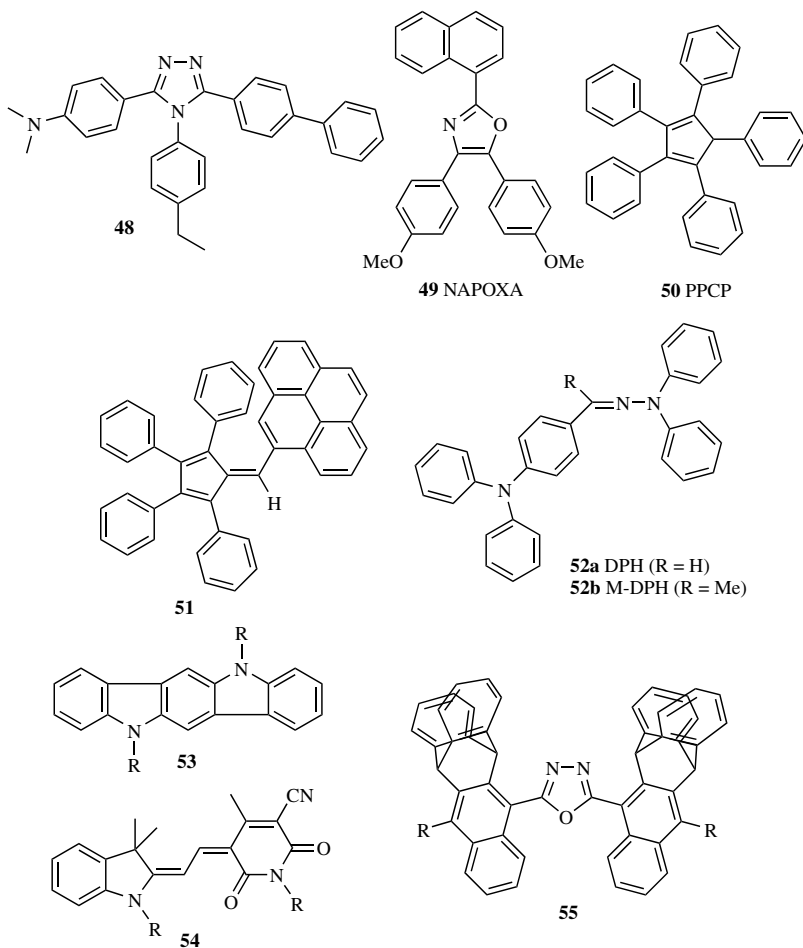


Figure 3.16. Other types of molecular glasses.

dipole moments, good film casting properties are obtained for the indoline–dimethine–dioxypyridine (IDOP) dyes **54**. One problem for these materials is their low thermal stability.

Other structural concepts evolved, one of them being triptycenes (**55**). Here, additional wings are introduced into the molecules by Diels–Alder type reactions. The glass-forming properties are improved by the propeller-like rigid structure [89]. We end our overview of the different classes of molecular glasses with these materials and note that the number of published structures is growing every year. More details on the different materials can be found in one of the recent chemical reviews [102–104].

IV. OPTICAL PROPERTIES: ABSORPTION AND EMISSION

For the light-emitting applications of molecular glasses like light-emitting diodes and lasers, the optical properties in the vitreous solid state are of utmost importance. Due to the close packing in the solid state leading to strong intermolecular interaction and quenching effects, the photophysical and photochemical properties may differ strongly from the behavior in dilute solution. A limited class of chromophores have proven to be useful, but they can be found in almost any combination with one of the design strategies for molecular glasses described in Section III.

One of the main tasks for display applications is the combination of materials of different colors to produce white light and full-color devices. For that reason, separate strategies aim at the development of blue-, green-, and red-emitting materials with suitable color coordinates.

A. Molecular Glasses as Fluorescent Emitters: From the Blue into the Red

1. Oxadiazoles. On the ultraviolet (UV) end of the visible spectrum, we find the diaryloxadiazoles. Typical emission maxima are located at ~ 370 nm, with absorption bands at ~ 300 – 330 nm. Since 2-(4'-biphenyl)-5-(4''-tert-butyl-2,3,4-oxadiazole) (*t*-Bu-PBD) was successfully applied in OLEDs by Adachi et al. [105, 106], morphologically stable derivatives of this parent compound have been investigated widely. The applications, however, are dominated by the electron transporting and hole blocking properties of oxadiazoles (see Section VI), and very rarely the emission properties are used. In multilayer devices comprising oxadiazoles, usually other layers with fluorophores emitting at longer wavelengths act as emission layers. In these devices, oxadiazoles are used effectively as exciton barriers. The excited states of chromophores can be interpreted as Frenkel excitons in terms of semiconductor physics, and exciton diffusion corresponds to resonant energy transfer. This means that a layer with higher photoexcitation energy can be used as an exciton barrier since exciton transfer does not proceed upward in energy. The emission maximum wavelengths may thus serve as a measure of exciton energy [107]. For a vacuum-deposited film of *t*-Bu-PBD, the maximum of the photoluminescence spectrum is at 390 nm. For the meta-coupled OXD-7 (**17a**), the emission occurs at even lower wavelengths (374 nm), whereas the emission maximum for dimethylamino-substituted derivative OXD-8 (**17b**) is shifted ~ 100 -nm bathochromically (470 nm), according to the electron-donating function of the amino group. This bipolar compound is one

of the few examples of using oxadiazoles as emitting materials [59]. The starburst compound **29** emits at the same wavelength as **17a**, which shows the effective interruption of the conjugation by the meta substitution of the central core.

A detailed study of the electronic structure and optical properties was published for the spiro derivative of *t*-Bu-PBD, Spiro-PBD (**40**) [108]. The vibronic structure of the lowest energy absorption band is well resolved, in solution as well as in the amorphous film. The 0–0 transition is at 351 nm (3.53 eV), the 0–1 and 0–2 vibronic bands that have a higher oscillator strength, are at 336 nm (3.69 eV) and 318 nm (3.90 eV), respectively. The fluorescence spectrum of this compound is symmetrical to the absorption spectrum with a Stokes shift of 43 nm.

The quantum yields in the amorphous state are low, and much lower than in the crystalline state, presumably because of the larger molecular degrees of freedom that favor nonradiative deactivation pathways. Naito et al. [109] reported quantum yields for different oxadiazoles in amorphous films, ranging from 2% for **17a** and **29** to 16% for a methoxy-substituted starburst oxadiazole. For **17b**, the quantum yield in the amorphous film is still one-third of the value in the crystalline form (10 vs. 30%).

2. Oligophenyls. The oligophenyls are excellent blue emitters since they exhibit high-fluorescence quantum yields and the color can be tuned by extending the oligophenyl chain, but only to a certain extent (Davydov rule [110]). With an increasing number of phenyl rings, the extinction coefficient increases and the fluorescence lifetime decreases [111]. Oligophenyls exhibit a large Stokes shift. Typical data measured in solution are for *p*-terphenyl $\lambda_{\text{abs}} = 280$ nm, $\lambda_{\text{em}} = 340$ nm; for *p*-quaterphenyl $\lambda_{\text{abs}} = 300$ nm, $\lambda_{\text{em}} = 370$ nm; *p*-quinquephenyl $\lambda_{\text{abs}} = 310$ nm, $\lambda_{\text{em}} = 390$ nm; and *p*-sexiphenyl $\lambda_{\text{abs}} = 320$ nm, $\lambda_{\text{em}} = 393$ nm [112]. Unfortunately, the higher homologues are quite insoluble. There are some strategies of synthesizing soluble derivatives, for example, by alkyl substitution [113–115], ladder-type ring condensation [116], or applying the spiro concept as mentioned in Section III.D. The chromophore is changed, however, to some extent in the various approaches by altering the torsional angle of two adjacent phenyl rings [117]. If the chromophores are substituted with alkyl chains, steric repulsion increases the angle from 23° in unhindered oligophenyls to > 45°. On the contrary, in ladder-type oligomers the phenyl rings are forced in-plane. In spiro compounds such as **43**, or starburst molecules containing fluorene like **33**, the planarization occurs at alternating biphenyl units, leaving some bonds unchanged. Since the equilibrium geometries of the ground and excited state differ, the modifications of the oligophenyl chain have a considerable influence on the photophysical properties, namely, on the Stokes shift.

As an example, for spiro-oligophenyls in the series **35a–d** with 4, 6, 8, and 10 phenyl rings in the chromophore, the absorption maxima are 332, 342, 344, and 344 nm in dichloromethane, respectively. The first fluorescence maxima increase

steadily in the order 359, 385, 395, and 402 nm. The emission spectra exhibit a clearer vibrational fine structure than the absorption spectra. For spiro-sexiphenyl, **35b**, a detailed analysis shows that the vibrational splitting of 0.20 eV corresponds to a phenyl breathing mode in the Raman spectrum [108]. If for spiro-sexiphenyl the outer biphenyl moieties are fixed parallel as in 4-Spiro² (**43**), the absorption maximum is shifted from 346 to 353 nm (amorphous films) and the fluorescence maximum from 420 to 429 nm, maintaining the Stokes shift. The corresponding spectra are shown in Figure 3.17. The absorption signal at 310 nm in the spectrum of **43** can be attributed to the terminal fluorene moieties. The quantum yields for the fluorescence in the amorphous film are 38% for **35b** and as high as $70 \pm 10\%$ for **43** [89].

The fluorescence lifetime was determined to be 1124 ps for **35a**, 785 ps for **35b**, and 831 ps for **43** in dichloromethane, whereas in the corresponding amorphous films a nonexponential decay with shorter time constants was observed [118, 119]. These lifetimes are similar to the parent oligophenyls but different from fluorene (10 ns) [120, 121]. When applying oligophenyls as luminescent films, however, we must consider that photooxidation may occur if molecular oxygen is present [122, 123]. The proposed pathway for the decomposition is

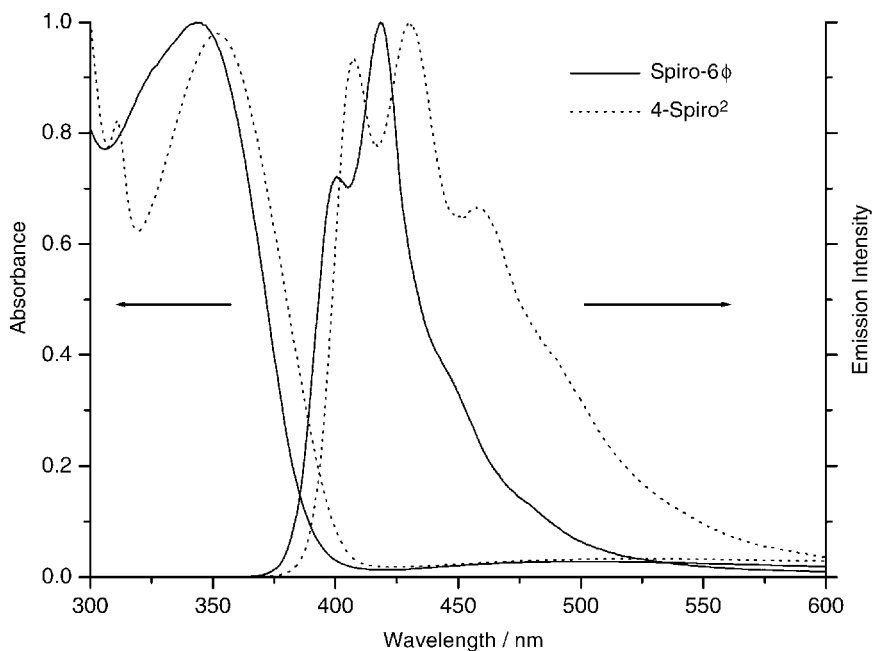


Figure 3.17. Absorption and emission spectra of two blue emitting molecular glasses, Spiro-sexiphenyl (Spiro-6 ϕ) and 4-Spiro² in the solid state.

based on the attack of singlet oxygen that is formed by spin transfer from the excited molecules. Endo- or exo-peroxides are formed that may open to carbonyl compounds. This mechanism is supported by the infrared (IR) spectroscopic detection of carbonyl groups after irradiation in the presence of oxygen.

3. Arylamines. Arylamines are not frequently used as emitter, with the exception of some light emitting diodes using the hole transporting layer as the emission layer. However, the quantum yields are low, and the materials are subjected to photodegradation. The absorption and emission properties of some representative arylamines are as follows: **6** (TPD) absorbs at 362 nm and emits at 448 nm with a reported quantum yield of 6% in the amorphous film [109]. Other authors, however, reported $35 \pm 3\%$ for the quantum yield, measured by different techniques [124, 125]. Contributions from excimer emission exist [126], as it is also the case for **3**, for which Naito et al. [109] report a emission wavelength of 443 nm with a quantum yield of 2%. Effects on electric fields on the emission behavior of **3** and **6** are reported [127]. For the spiro compound **36a** (Spiro-TAD), we measured the solid-state absorption band at 382 nm and the main emission at 405 nm. Compound **23** (*m*-MTDATA) emits at 430 nm and the corresponding carbazole **24** (TCTA) at 400 nm [68]. Compound **26c** (*p*-TTA) emits at 435 nm [128]. All these values are taken for amorphous films.

Bipolar arylamines coupled with oxadiazoles have also been used as emitters with emission colors between blue and green (**70**, $\lambda = 487$ nm) [129].

4. DPVBi and Derivatives. A good blue emitter is 4,4'-bis(2,2'-diphenylethynyl)-biphenyl (DPVBi, **22**), which was presented by Hosokawa et al. [130]. Compound **22** and its high T_g derivatives like the corresponding spiro-compound **38**, and C(DPVBi)₄, **47a**, absorb at ~ 330 nm and emit at ~ 466 nm [83, 93], exhibiting a large Stokes shift. The quantum efficiency for these compounds is strongly increased in the amorphous film compared to solution, a feature that is attributed by Wang et al. [93] to conformationally controlled radiationless transitions that are typical for trans-stilbenes [131]. Whereas the fluorescence in solution is barely detectable by eye, the solid film fluoresces strongly. The corresponding cyano derivative **47b** shows a broad excimer emission at ~ 519 nm.

5. Oligophenylenevinylenes. Since poly(phenylenevinylenes) have been applied for organic electroluminescence [132], the corresponding oligo(phenylenevinylene units) have been incorporated into molecular glasses. The dependence of the absorption and emission wavelengths on chain length was shown by Müllen et al. [133] for a series of soluble oligo(phenylenevinylenes). The absorption bands increase from 340 nm (3 phenyl rings) to 406 nm (7 phenyl rings), and the fluorescence maxima from 420 nm to 527 nm. As in the case of the oligophenyls, the fluorescence bands are more structured than the absorption bands. The

Stokes shift decreases with larger chain length (from 0.29 to 0.16 eV) [134]. For one of the oligophenylenevinylenes, it was demonstrated that the presence of metal electrodes, even if evaporated in submonolayers, strongly quenches the photoluminescence of molecular dye layers [135].

For the distyrylbenzene carbon-centered tetramer **46b**, the fluorescence spectrum in the solid film differs from the spectra in solution or in a polymer matrix due to excimer formation [93]. A concentration of 5% in a polystyrene matrix is sufficient for a distinct broadening of the emission. For the higher homologue **46c**, a fluorescence maximum of 472 nm was measured in freshly prepared films. If the film is thermally annealed, the spectrum shifts to 511 nm, probably due to intermolecular arrangement that favors excimer formation.

6. Alq₃. Probably the currently most widely used amorphous green emitting material is the complex Alq₃ (**1**) since its first application for light emitting diodes was demonstrated in the historical paper of Tang and Van Slyke [42]. Its absorption maximum in the amorphous state is at 390 nm, and its emission band is at 530 nm. Detailed studies on the vibrational fine structures of the electronic transitions have been made recently [136, 137], allowing a comparison between the different crystal modifications and amorphous films containing *mer* and *fac* isomers, respectively. It was concluded that the *mer* form of Alq₃ is strongly preferred.

For vacuum sublimed thin films, Grabuzov et al. [138] reported a photoluminescence quantum efficiency of $32 \pm 2\%$. In the same paper, data on the absorption coefficient at the maximum, $\alpha = (4.4 \pm 0.1) \times 10^4 \text{ cm}^{-1}$, and the refractive index at 633 nm ($n = 1.73 \pm 0.05$) can be found. Other reported values for the photoluminescence quantum efficiency that can be found in the literature are $30 \pm 5\%$ [124] and $25 \pm 5\%$ [139]. Naito et al. [109] reported a quantum yield of 5% in the amorphous film compared to 35% in the crystalline state. The fluorescence lifetime is reported to be biexponential with $\tau = 3.4$ and 8.4 ns, which is much shorter than in the crystal (17.0 ns). In the amorphous state, the larger free volume allows more vibrations and rotations to take place, which favors nonradiative decay.

The absorption and emission bands of the 4-methyl derivative of Alq₃, abbreviated as Almq₃, are slightly blue-shifted but the quantum yield is higher ($42 \pm 3\%$). A systematic study on the influence of methyl substituents on the photophysical properties of Alq₃ complexes confirms the observation of a high quantum yield in Almq₃ [33].

The importance of Alq₃ and its derivatives for applications is increased by the possibility of doping, so numerous dyes for red emission, which will be presented below, have been developed as dopants for Alq₃.

Other metal complexes have also been found to emit in the green spectral region, for example, beryllium complexes [140].

7. Stilbeneamines. The functionalization of stilbenes with arylamino groups leads to materials that emit in the green-to-yellow spectral region. For example, 9,10-bis(4-(*N,N*-diphenylamino)styryl)-anthracene (BSA, **21**) absorbs at 429 nm and emits at 585 nm [141]. Compound **21** and other derivatives of bistyrylanthracene have been successfully applied in yellow emitting OLEDs [64]. Tetra(triphenylamino)ethylene (TTPAE, **20**) emits at 539 nm [109]. The latter compound exhibits a large quantum yield of 25% in the amorphous film, but does not show fluorescence in solution.

A green emitting chromophore consisting of three distyrylbenzene groups around a central nitrogen core was used as the emissive center in several dendrimers [142].

8. Oligothiophenes. Incorporating an increasing number of thiophene rings into molecular glasses allows a wide tunability of the optical properties. For the unsubstituted α -polythiophenes, denoted usually as H-T_{*n*}-H, the absorption wavelengths reach from 302 (*n* = 2) to 432 nm (*n* = 6) (in CHCl₃) [143], the corresponding emission wavelengths are from 362 to 510 nm (in dioxane/acetonitrile) [144]. In **13** and **14**, the thiophene chains are extended by attaching functional groups at both sides. By using triphenylamine as the capping group, the colors obtained were light blue (BMA-1T, **13a**: $\lambda_{\text{max}} = 397$ nm, $\lambda_{\text{em}} = 456$ nm), yellowish green (BMA-2T, **13b**: $\lambda_{\text{max}} = 423$ nm, $\lambda_{\text{em}} = 491$ nm), yellow (BMA-3T, **13c**: $\lambda_{\text{max}} = 440$ nm, $\lambda_{\text{em}} = 516$ nm), and orange (BMA-4T, **13d**: $\lambda_{\text{max}} = 453$ nm, $\lambda_{\text{em}} = 532$ nm) [55]. By using di(mesityl)boron as the end group, blue emitting molecular glasses result for *n* = 2 and 3 (BMB-2T, **14a**: $\lambda_{\text{max}} = 402$ nm, $\lambda_{\text{em}} = 440$ nm; BMB-3T, **14b**: $\lambda_{\text{max}} = 437$ nm, $\lambda_{\text{em}} = 488$ nm) [55]. Bipolar compounds **68** and **69** given by the combination of these two substitution patterns exhibit green fluorescence [145].

The pyrene bearing quaterthiophene **15** has two absorption bands that can be attributed to the pyrene and quaterthiophene unit, but only one emission at 552 nm, indicating that Förster transfer from pyrene to quaterthiophene is very efficient [146]. For oligothiophenes containing *S,S*-dioxides, the emission is shifted to the red with good solid-state quantum efficiencies [147]. For **16**, the absorption maximum is at 461 nm and the emission is at 600 nm with 37% quantum efficiency. For spiro-bridged oligothiophenes, absorption and emission are bathochromically shifted with respect to the unbridged oligothiophenes: **39a** absorbs at 431 nm and emits at 484–511 nm, **39b** absorbs at 472 nm and emits at 536 nm with a shoulder at 570 nm, respectively [84].

B. Doped Systems for Color Conversion

As stated above, the use of molecular glasses offers the possibility of doping the amorphous films with a variety of dopants that shift the emission energy to longer

wavelengths by Förster transfer. When using dopants, the concentrations are usually in the range of 1% in order to avoid phase separation and crystallization as well as concentration quenching effects. Because of solvatochromism, the emitting behavior depends on the imbedding matrix. Very often, exciplex formation occurs [106], which shifts the emission to longer wavelengths than expected from the pure dye spectra. Such exciplexes are not only observed in binary mixtures but also at the interface of two layers of molecular materials with strong intermolecular interactions between the excited state of the emitting material and the other component. The most common dopants are displayed in Figure 3.18.

1. Blue and Green Dopants. Commonly used dopants for emission in the blue-green region are quinacridones (e.g., **56**) and coumarines (e.g., **57**) [148]. Pentaphenylcyclopentadiene (**50**) is a molecular glass by itself but is also used as a dopant, with a blue emission ($\lambda_{\text{em}} = 467 \text{ nm}$) [106]. Perylene (**58**) and its derivatives are also used very frequently, covering a spectral range from blue for the unsubstituted perylene ($\lambda_{\text{em}} = 473 \text{ nm}$) to red for N-aryl substituted perylenetetracarboxydiimids (**59**). Structurally similar to the perylene derivatives are the corresponding naphthalene compounds such as naphthalenetetracarboxydiimids, **60**, but the emission bands are blue-shifted.

2. Yellow and Red Dopants. In contrast to inorganic semiconductors, for molecular glasses it is more difficult to design a red or near-IR emitting material than a blue emitting one. Up to now, no morphologically stable red emitting molecular glass has been proven to fulfill all the demands for applications. Instead, red dopants are used for converting the emission of a green dye, mostly Alq₃, into red. One problem, however, is the large spectral distance that has to be surmounted. Emission wavelengths $>600 \text{ nm}$ are difficult to achieve because of the weak overlap between the fluorescence band of the host and the absorption band of the dopant, on which the efficiency of Förster transfer depends. Very often, luminescence contributions from the host are observed.

The dyes used most frequently as dopants are rubrene (**61**) and the dicyanomethylene dyes (**62**). Rubrene is able to convert the Alq₃ fluorescence to yellow (570 nm), DCM 4-dicyanomethylene-2-methyl-6-(*p*-dimethylaminostyryl)-4*H*-pyran, (**62a**) and its derivatives, **62b–d** [149] to orange (600 nm). The quantum efficiencies are enhanced strongly to values near 100% upon doping with the dyes. For rubrene in Alq₃, a quantum efficiency of $95 \pm 5\%$ was reported [139].

The emission of the Alq₃:DCM system appears orange and not red as the spectrum of the pure DCM dye because of a nonideal overlap of the energy states for Förster transfer. A purer red emission can be obtained in a three-component system with both rubrene (**62**) and DCM2 (**62b**) as dopants. The energy transfer occurs in two steps via rubrene to DCM2 [150]. Here, the emission of DCM2 is at

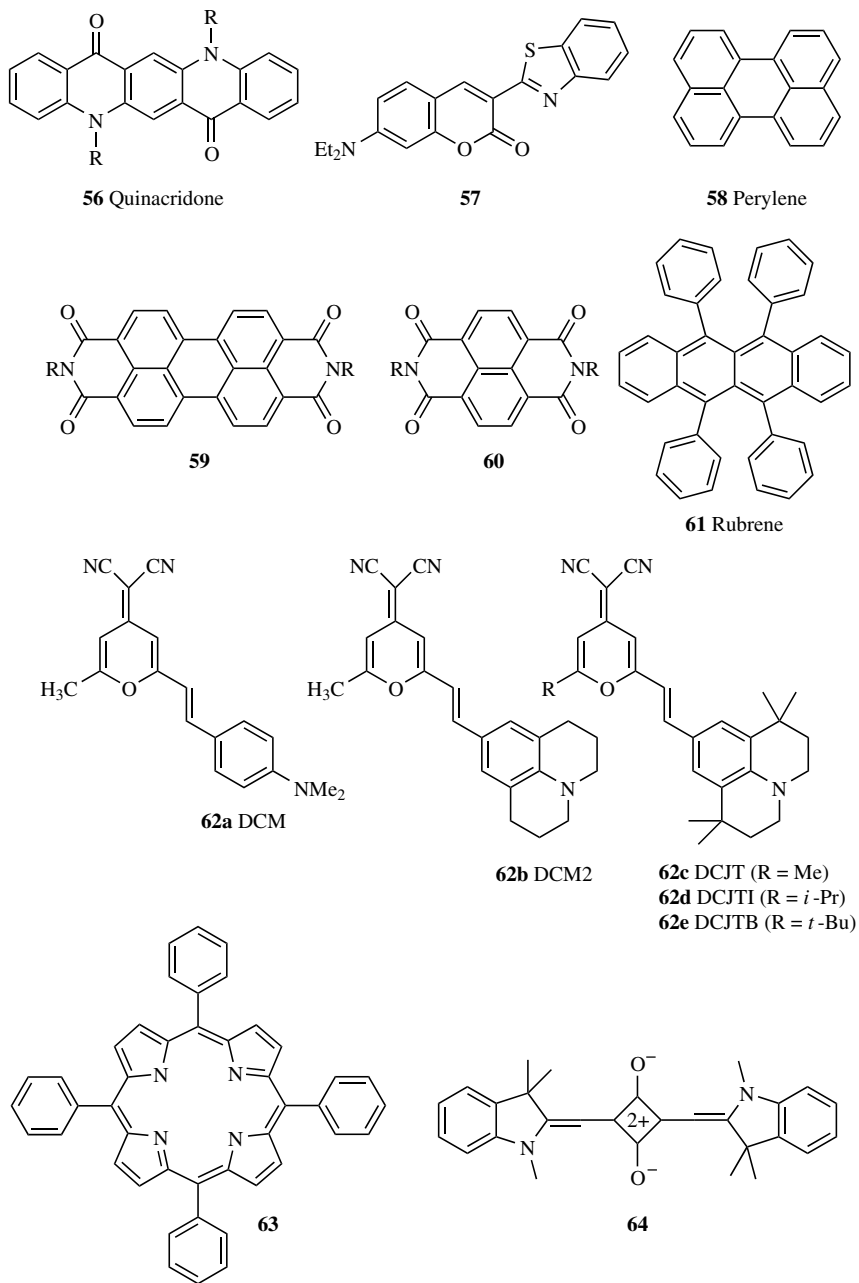


Figure 3.18. Dopants for shifting the emission wavelength.

644 nm, which corresponds to the pure DCM2 emission without any contributions of Alq₃ and rubrene.

Another class of red dopants, tetraphenylporphyrins (**63**), offer a direct energy transfer from blue to red [151]. The absorption bands comprise the sharp porphyrin “Soret” band at 418 nm and the weaker Q bands at 512 and 550 nm. The photoluminescence shows two sharp transitions at 653 and 714 nm and can be induced from a blue emitting host by Förster transfer to the Soret band and internal conversion to the Q bands.

A similar sharp red emission exhibit squarylium dyes like the squarylium cyanine dye **64**, which emits ~650 nm [152]. Unfortunately, the Stokes shift is rather small, which leads to high reabsorption. A number of other red emitting dyes have been exploited as well [153–156].

Cyanine dyes are in principle capable of shifting the emission into the near-IR region [157], however, their ionic character makes it difficult to dope them into films by vacuum vapor evaporation. Other materials investigated for IR emission are complexes based on rare earth ions (Nd³⁺, Er³⁺), which are also used in inorganic amplifiers and lasers [158].

C. Phosphorescent Emitters

The emitter materials discussed up to now are all fluorescent emitters, the excited state being a singlet state. For photoluminescence applications, this is the preferred state since it can be populated directly. In electroluminescence, the situation is a little bit different since the excited states (excitons) are created by recombination of electrons and holes. If one assumes that the formation rate constants for singlet and triplet states are equal, spin statistics predict that the ratio of singlet to triplet excitons are 1 : 3, giving a maximum internal quantum yield of electroluminescence of 25%. Recent reports show that the ratio of singlet excitons may be higher, though [159]. The expected value was confirmed for Alq₃ as host material, with a reported singlet fraction of $22 \pm 3\%$ [160]. In order to increase the luminescence quantum yield by using triplet excitons for emission, phosphorescent emitters are preferred [161] (Fig. 3.19).

The classical example of emitters with transitions between states of different multiplicity are the lanthanide complexes. In europium complexes, the ⁵D₀ to ⁷F₂ transition at 614 nm, which is allowed by spin-orbit coupling, makes these materials excellent red emitters [39, 162]. The excitation of the central ion involves energy transfer from the triplet state of the ligand [163]. The europium complex used most frequently today for red emission is the volatile complex Eu(TTFA)₃(phen) (**65**) [40], which is not a molecular glass by itself but can be coevaporated with a stabilizing glass in high concentration (1 : 2 weight ratio).

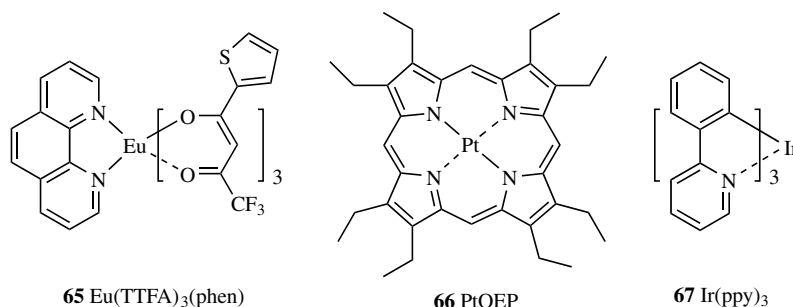


Figure 3.19. Phosphorescent materials.

Baldo et al. [164] used the platinum complex of 2,3,7,8,12,13,17,18-octaethyl-21*H*,23*H*-porphine (PtOEP, **66**) as efficient phosphorescent material. This complex absorbs at 530 nm and exhibits weak fluorescence at 580 nm but strong phosphorescence from the triplet state at 650 nm. Triplet transfer from a host like Alq₃ was assumed to follow the Dexter mechanism. Dexter-type excitation transfer is a short-range process involving the exchange of electrons. In contrast to Förster transfer, triplet exciton transfer is allowed.

Another efficient material introduced by the same group is the green emitting *fac*-tris(2-phenylpyridine)iridium [Ir(ppy)₃, **67**] [38]. A suitable host for this phosphorescent emitter is CBP (**10**). The triplet lifetime is rather short, the experimentally determined value being 500 ns in the CBP matrix. Another iridium complex was shown to emit in the red with high efficiency due to the short phosphorescence lifetime in comparison with PtOEP [165].

Not all the phosphorescent molecular glasses are metal complexes. For the phenoxazine **25a**, it was reported that the phosphorescence intensity may exceed the fluorescence intensity, but only at low temperatures [166].

Phenylquinoxalines (**30**) turned out to be both fluorescent and phosphorescent emitters [167, 168]. By using these molecules as host, singlet excitons as well as triplet excitons can be transferred by long-range interactions to phosphorescent dopant molecules such as **66**.

D. Creating White Light

Doping of an emissive host with a dye emitting at longer wavelengths also offers the possibility of fine-tuning the dopant concentration in order to obtain mixed colors. White light emission is preferred for various display applications. The color of the luminescence can be defined best in the Commission Internationale de l'Éclairage (CIE) chromaticity diagram in which the color coordinates are

defined as follows: The emission spectrum is weighted by the three given color matching functions for the color perception of a standard observer, and integrated, giving the tristimulus values x , y , and z with the normalization $x + y + z = 1$. In the diagram, usually given two-dimensionally by x and y , the white point is defined by the coordinates $x = y = z = 1/3$. If an emitting host is doped, the color coordinates follow a trajectory in the diagram with increasing dopant concentration, which is displayed in Fig. 3.20 for some electroluminescent devices based on molecular glasses as hosts [26]. By using spiro-quaterphenyl **35a** doped with **61** as the emitting system, the white point is crossed for a dopant concentration of 0.58 wt%.

In other white light devices, blue, green and red emitters are combined. Kido et al. [169, 170] designed multilayer systems using **6** (TPD) for blue, metal-chelate complexes for green and red emission, respectively. Similar devices have been developed by other groups, using Förster transfer or exciton confinement for the creation of the three primary colors [171, 172]. Exciplex emission was

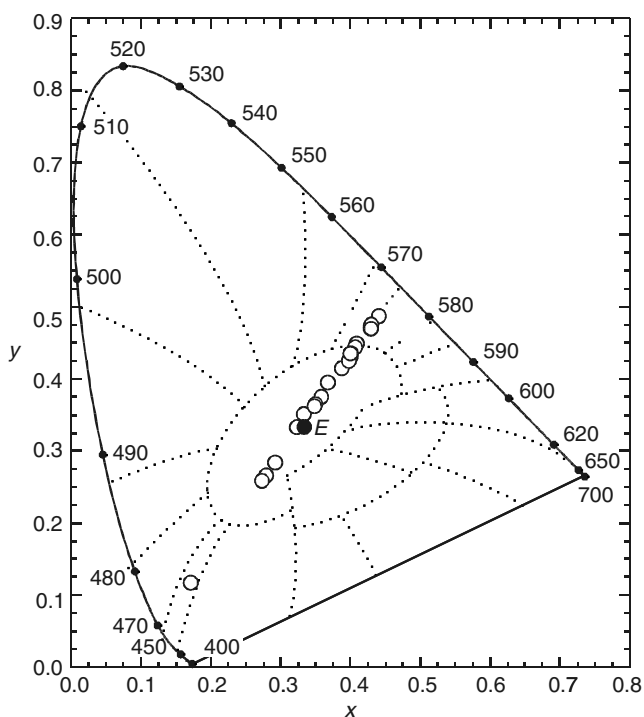


Figure 3.20. The CIE color diagram for electroluminescent devices, consisting of anode/Spiro-TAD/Spiro-quaterphenyl: Rubrene/Alq₃/cathode with different concentrations of rubrene. The spectrum shifts from blue to yellow, crossing the white point (E).

found to be useful as one component of white light emission in some reports [173, 174]. One-component materials capable of emitting white light that are based on zinc complexes have also been presented [175].

E. Creating Polarized Light

In some applications, polarized light is useful. For accomplishing the emission of polarized light without external polarizer sheets, the material has to be anisotropic. For molecular glasses, unless they are in the crystalline state, this is possible if the molecules are chiral and/or form chiral (e.g., liquid crystalline) superstructures. Indeed, for cholesteric molecular glasses with $T_g \sim 70^\circ\text{C}$, doped with an oligofluorene emitter, circularly polarized light was generated upon photoexcitation [176].

V. AMPLIFIED SPONTANEOUS EMISSION AND LASING

Since the early work on dye lasers in the 1970s it is known that organic dyes are ideal candidates for stimulated emission and lasing because of their quite large Stokes shift. The Franck–Condon favored absorption and emission vibronic states form a four-level system that allows population inversion for the fluorescence transition by optical pumping. If a Förster energy-transfer cascade is inserted, the situation is even better since optical reabsorption is suppressed by the larger separation of absorption and emission wavelengths as described above. With the development of light-emitting semiconducting polymers and molecular glasses, organic solid-state lasers came into focus, especially for the electrical excitation mode. Up to now, a lot of work has been done on lasing in semiconducting polymers, initiated by a few key publications [177, 178] and, very recently, the first example of an electrically driven organic crystal laser was presented [179]. The design principles are quite general and are also valid for spin coated or vacuum sublimed films of molecular glasses on which we focus in this chapter.

A. Gain Narrowing in Organic Waveguides

The key prerequisite for optical amplification via stimulated emission is that the emitted photons propagate through the gain medium long enough to initiate further stimulated transitions. This condition can be expressed as

$$g(\lambda) \cdot l > 1$$

$g(\lambda)$ being the wavelength-dependent overall gain coefficient and l the geometric path length (pump length). The pump length dependence of the emitted intensity is given by

$$I_{\text{out}}(\lambda) \propto \exp[g(\lambda) \cdot l] - 1$$

Large path lengths are easy to accomplish in the simplest structure achievable with molecular glasses: the thin-film waveguide. If a thin film of a molecular glass—whose refractive index n_2 is usually higher than the substrate $n_3 \approx 1.52$ (glass) and air $n_1 = 1$ —is evaporated or spin-coated on a substrate, an asymmetric slab waveguide is formed. At propagation angles θ_2 (defined relative to the film normal) larger than the angle of total internal reflection, a discrete number of optical modes exists that are confined into the film and characterized by an effective index

$$n_{\text{eff}} = n_2 \cos \theta_2$$

The effective index represents the dimensionless in-plane component of the propagation vector of the mode (the propagation vectors are in units of $2\pi/\lambda$, λ being the vacuum wavelength). The optical modes can be characterized as transversal electric (TE, the electric field is polarized in-plane) and transversal magnetic (TM, the magnetic field is polarized in-plane). For asymmetric slab waveguides, a minimum thickness (cutoff) exists for each mode to appear [180], which is illustrated in Figure 3.21. The effective indices n_{eff} of the TE and TM modes are plotted against the film thickness t for the optical modes at the fluorescence wavelength (420 nm) for the molecular glass **35b** (spiro-sexiphenyl). At $t = 250$ nm, for example, two TE and two TM modes can propagate. The corresponding intensity distribution of the electric fields is displayed in Fig. 3.22 for the TE modes. In principle, they give the lateral distribution of the coupling efficiency by which an excited dipole can couple to the respective mode, according to Fermi's Golden Rule [181].

Optical amplification experiments for thin films of this material are reported in [182]. Spin coated films were irradiated with a pulsed nitrogen laser at 337 nm. The emission light that was scattered out at an angle of 45° was detected. At low irradiation intensities the normal fluorescence spectrum appears, whereas at a pump intensity threshold of $\sim 4 \mu\text{J}/\text{cm}^2$, the spectrum begins to collapse into one narrow line at 419 nm (Fig. 3.23). This line corresponds to the 0–1 vibronic transition that is amplified, in contrast to the smaller homologue, spiro-quaterphenyl **35a**, where the 0–0 transition dominates. The line widths are as low as 2.9 nm for **35b** and 2.2 nm for **35a**, respectively. This line narrowing due to optical gain in a waveguide is commonly referred to as amplified spontaneous emission (ASE) [183].

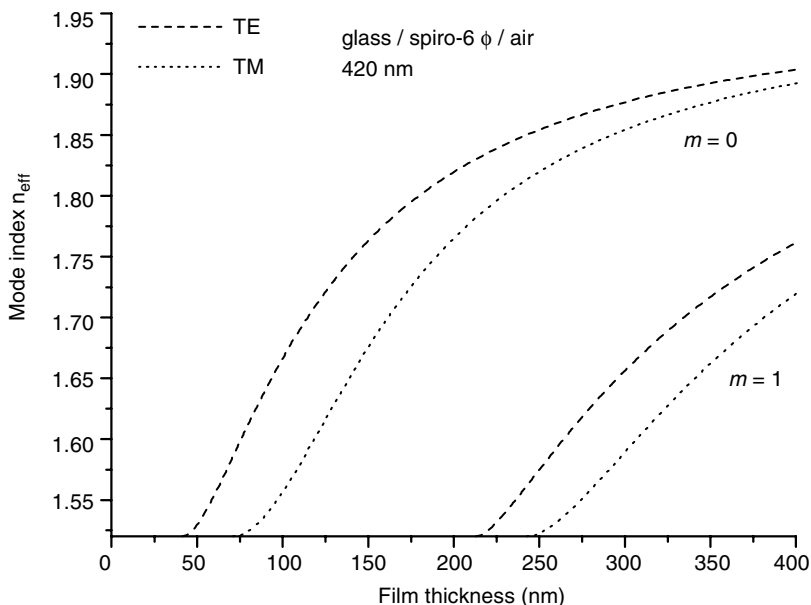


Figure 3.21. Effective index of TE and TM optical modes in a thin film of spiro-sexiphenyl on a glass substrate at the amplified spontaneous emission (ASE) wavelength. Note the different cutoff thicknesses that determine the number of possible modes for a certain film thickness.

The influence of the waveguide structure on the threshold of line narrowing can be deduced from the following observations: First, no gain narrowing can be observed for film thicknesses of ~ 30 nm, which is below the cutoff thickness for the first mode. Second, if a high-index substrate is used, no narrowing occurs. Third, the lowest threshold is at film thicknesses of ~ 100 nm. At this thickness, only one mode for each polarization exists, so the optical energy does not have to be divided into different competing modes [184].

The higher branched derivatives of the spiro compounds, **43** and **44** also exhibit spectral narrowing under pulsed excitation, with emission lines at 428 and 443 nm, and line widths of 3.2 and 3.9 nm, respectively (Fig. 3.24). For the same film thickness, the threshold is lower for 4-Spiro² than for spiro-sexiphenyl despite the lower absorption, which is attributed to the higher luminescence quantum yield.

Other low-molecular systems that have been investigated in waveguiding films are the guest–host system Alq₃:DCM (see below for the emission in true resonators), arylamines, and oligothiophenes. TPD (**6**) shows an emission peak in thin films at 418 nm when pumped with 35-ps pulses at 347 nm [185]. The

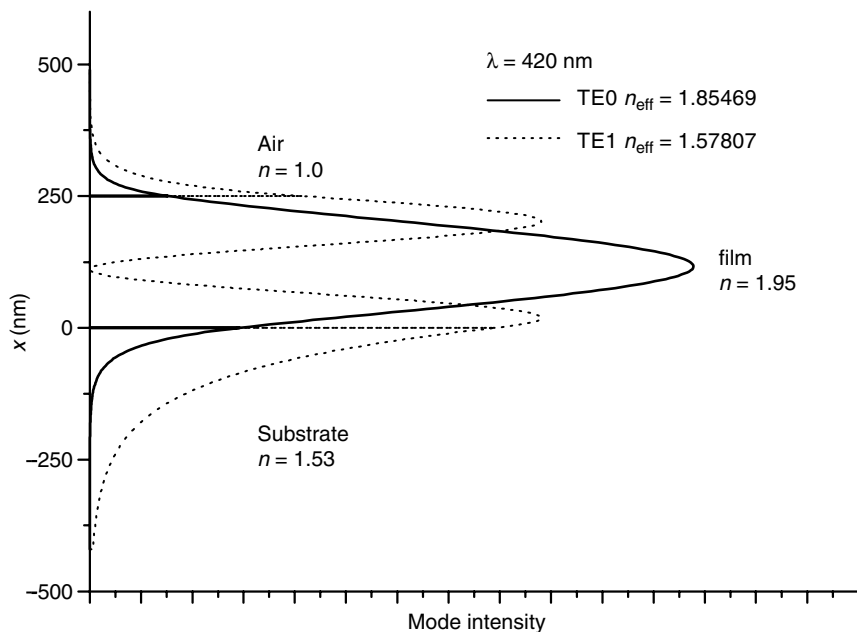


Figure 3.22. Optical mode intensity profile for the first two TE modes of the film in Figure 3.6 at a film thickness of 250 nm.

quinquethiophene-*S,S*-dioxide **16** has a gain peak at 616 nm with an excitation threshold of $960 \mu\text{J}/\text{cm}^2$ [186].

Some low-molecular dyes also have been investigated in inactive polymer matrices. For stilbene compounds in polystyrene, peak wavelengths in the green spectral region are obtained, with net optical gain coefficients of $g = 15\text{--}20 \text{ cm}^{-1}$ [187].

All these waveguiding films lack one important feature that would be necessary for true lasing: They do not have a resonator for optical feedback that would lock the optical modes traveling in the gain direction. The thin-film waveguide confines the optical modes in one direction (in the vertical), but in the other two dimensions the modes have translational and rotational symmetry. The incorporation of resonator structures into the thin films in order to get true organic solid-state lasers will be described next.

B. Laser Resonators

Since one of the most investigated systems for the incorporation of laser resonators is the Förster-transfer couple $\text{Alq}_3 : \text{DCM}$ [188, 189], we will discuss this as a representative example for low molecular glass lasers.

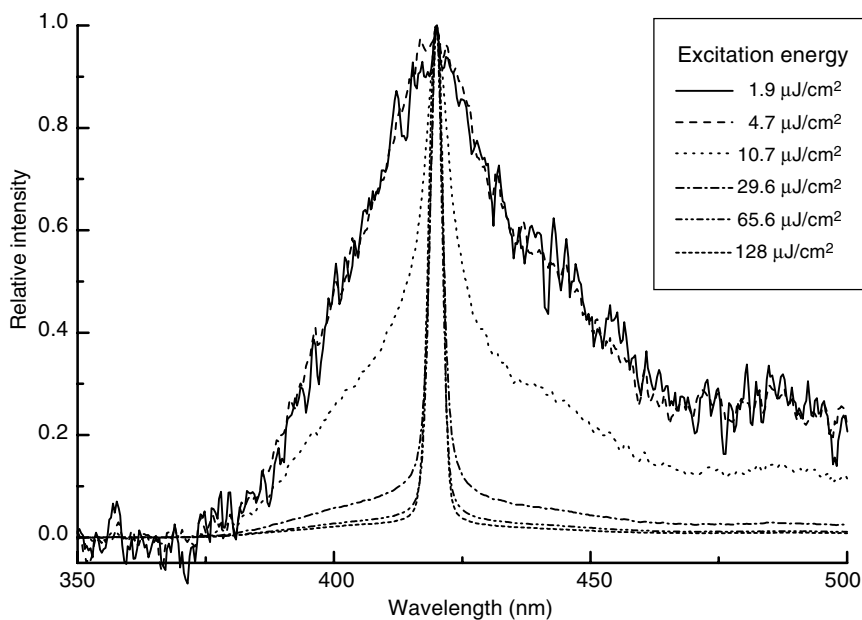


Figure 3.23. ASE of a 50-nm film of spiro-sexiphenyl. At pump intensities $\sim 10 \mu\text{J}/\text{cm}^2$, the normal fluorescence spectrum collapses to a narrow line.

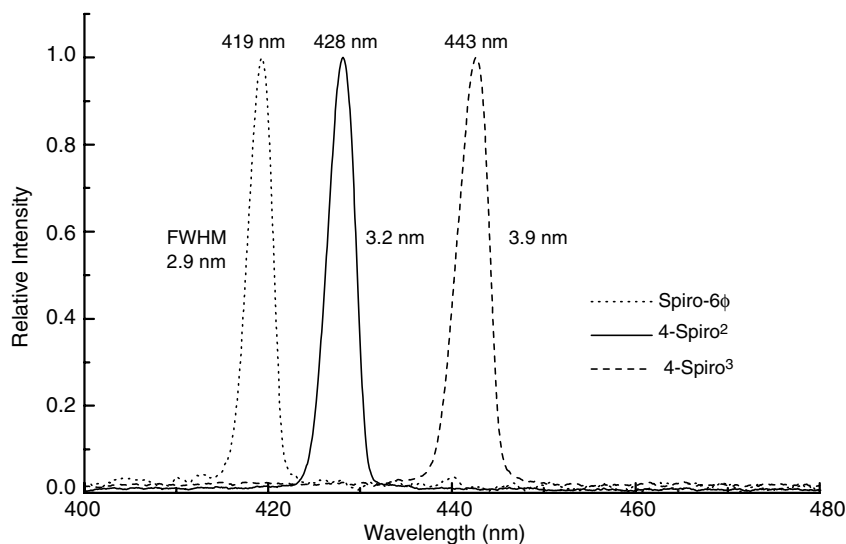


Figure 3.24. ASE lines of different blue emitting spiro compounds. The line widths are ~ 3 nm.

The easiest way to construct a resonator is just cleaving the edges of the substrate, forming parallel reflecting facets. Cleaving one of the edges is also useful for ASE measurements since the amplified modes can be coupled out directly at the facet without scattering into the film normal. This feature is important for the interpretation of gain measurements as was pointed out by McGehee et al. [183]. Parallel facets have been made by Kozlov et al. [190] by using (100) oriented indium phosphide as substrate. In their early paper, they used two configurations: They evaporated (I) a 300-nm thick film of 2.5% DCM doped in Alq_3 and (II) a 50-nm thick film of Alq_3 :DCM sandwiched between two 125-nm thick Alq_3 layers. In both cases, $2\ \mu\text{m}$ of SiO_2 was used as a cladding layer on the substrate side. They obtained lasing at the 645-nm line with thresholds of 3 and $1\ \mu\text{J}/\text{cm}^2$ for configurations (I) and (II), respectively. Because of the better optical confinement in (II), the output energy for given pump energies was higher in this case. A fine structure of the emission spectrum showing the distinct cavity modes was measured for a $500\text{-}\mu\text{m}$ long cavity, thus proving the transition from ASE to true lasing. The reflectivity of the facets with 7% are quite low, though, so other resonators have been applied (Fig. 3.25).

One class of laser resonators is based on circular structures like spheres, disks, and rings. In these structures, the optical modes form closed circular loops and

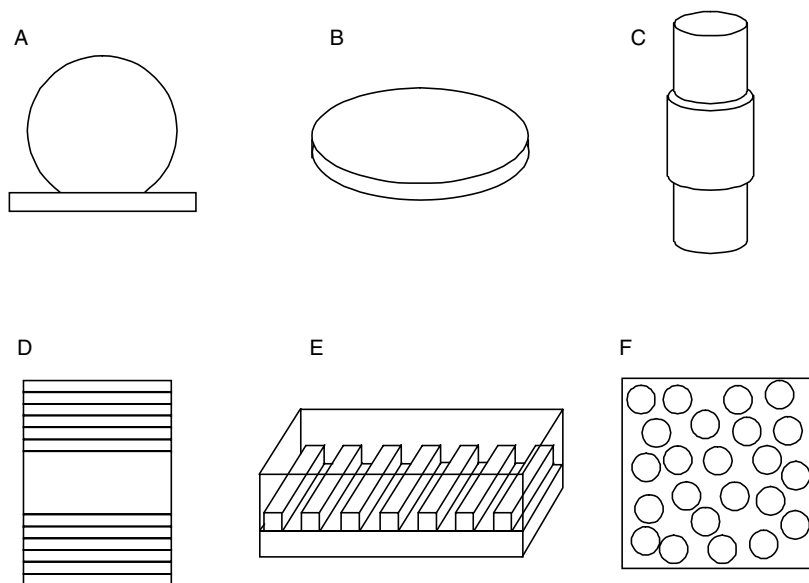


Figure 3.25. Laser resonators applicable to molecular glasses: A = microdroplet, B = microdisk, C = ring laser, D = vertical cavity distributed bragg laser, E = distributed feedback laser, F = random laser.

are thus called whispering gallery modes. Berggren et al. [91] presented the application of these structures to Förster-transfer type molecular films, using **62b** (DCM2) as guest and **1** (Alq₃) and **49** (NAPOXA) as host materials. They prepared a variety of devices, including microdisk arrays with a 3- μm disk diameter and 20- μm spacing, ring lasers made by dip-coating a 125 μm silica fiber into a dye solution, and organic droplets on Teflon substrates. They all exhibit sharp laser lines, the line spacing being consistent with the calculated mode spectrum.

A different approach is the distributed bragg reflector (DBR) and distributed feedback (DFB) laser. In DBR lasers, reflection is provided by a dielectric mirror in the form of a surface relief or refractive index grating rather than by facets or metallic mirrors. In DFB lasers, the grating extends over the whole active area, providing optical feedback by coupling the forward and backward traveling waves through the grating [192]. Such lasers are characterized by low threshold and selective laser lines. In context with organic laser materials, it is interesting to note that the first DFB laser was made completely out of organic materials [193] and the concept was later applied to inorganic semiconductors. The necessary condition for feedback is

$$\Lambda = m \frac{\lambda_0}{2n_{\text{eff}}}$$

in which Λ denotes the grating period, λ_0 the lasing wavelength, and n_{eff} the effective refractive index of a corresponding waveguide mode. The number m denotes the order of the feedback: For $m = 1$, mode coupling occurs only within the film between waveguide modes (edge emitting), for $m = 2$, a beam is also coupled out perpendicular to the plane (surface and edge emitting). The feedback can be achieved both by a variation of the refractive index as well as by a variation of the optical gain with the appropriate period.

The system Alq₃ : DCM was successfully incorporated into a DFB structure by different research groups and optically pumped [194, 195]. The materials were deposited on embossed flexible substrates with grating periods for second- and third-order coupling (400–600 nm). By varying the film thickness, the wavelength of the lasers can be tuned over 44 nm [196].

The gratings can also be made *in situ* by holographic irradiation as was demonstrated for low molecular stilbenes in a polystyrene matrix [197]. Here, the spatial modulation of gain dominates over the refractive index modulation in its contribution to optical feedback. The principles of holographic irradiation will be described in Section VIII, which discusses photosensitive materials.

The DFB grating concept was extended to higher dimensions. Two-dimensional (2D) gratings can be made in a variety of forms, from the simple overlapping of two orthogonal gratings up to concentric rings, or more complicated structures. In modern theory, they can be treated as 2D photonic crystals.

Meier et al. reported the use of molecular guest–host systems in structures like honeycomb, square, or triangular lattices that are defined by photolithography [198] or replica molding [199]. The emitted light is strongly directional giving interesting symmetric far-field patterns.

Vertical emission can also be achieved by the application of dielectric Bragg mirrors layers, which is in principle the DBR structure applied to the direction of the film normal. Such microcavities have been shown to alter the (electro)luminescence spectrum of devices as well as the angular radiation characteristics [200–204]. Normally, the angular dependence of the emission from a thin film follows Lambert's law [205].

$$I(\theta) = I_0 \cos \theta$$

allowing only a fraction of $1/(4n^2)$ of the generated photons to be coupled out via the upper surface, or twice this value if the rear surface acts like an ideal mirror. In a microcavity, a much stronger directionality can be observed, and the external efficiency can be much higher. In the structures derived from OLEDs, usually one mirror is made of a metal layer that serves as the electrode, the other is a stack of alternating layers with a thickness of $\lambda/4$ and high refractive index contrast (e.g., $\text{SiO}_2/\text{TiO}_2$). As emitting layers for (electrically driven) microcavities, Alq_3 with or without dopants such as quinacridones and europium complexes have been used [206–209]. Still below the lasing threshold, the spectral full width at half-maximum (FWHM) can be as low as 10 nm and the spatial (angular) FWHM, which is 60° for a Lambertian radiator, becomes $<30^\circ$.

The lasing threshold was reached by optical pumping. For a 500-nm thick Alq_3 :DCM layer sandwiched between a dielectric mirror with 99.5% reflectivity and a silver mirror with 91% reflectivity, lasing occurs at a pump intensity threshold of $340 \mu\text{J}/\text{cm}^2$ at 337 nm [210]. The high-resolution spectrum shows a bandwidth of 0.06 ± 0.03 nm. By varying the thickness of the organic layer between 450 and 520 nm, the peak wavelength was tuned from 598 to 635 nm.

The intriguing properties of devices made by the combination of a film-forming dye and an optical microstructure turn up in the discovery of strong coupling between excited states and photon modes in microcavities, creating Rabi-split polariton modes [211]. They occur in materials with narrow absorption bands (e.g., porphyrins and cyanine dyes) and may pave the way to new laser types and fundamental insights into the interaction of matter and light.

One final type of laser resonator, which is also applicable for molecular glasses, should be mentioned: The “random” laser, based on coherent backscattering in an amplifying medium [212, 213]. In these structures, strongly scattering nanoparticles like TiO_2 colloids are randomly dispersed in the amorphous films leading to self-contained optical paths and thus to the localization of optical modes. Since disordered structures are much easier to produce than ordered

lattices, it is to be expected that random lasers will gain more interest in the future.

All systems presented in this section show lasing only in the optical pumping mode. There is much interest in electrically pumped devices, but for molecular glasses the difficulties in achieving high excitation densities and low absorption due to charge carriers and electrodes have yet to be overcome. This problem and the related semiconducting polymer lasers that are based on the same principles will not be covered here, but are treated in recent reviews [214–216].

VI. ELECTRICAL EXCITATION: MULTILAYER STRUCTURES FOR ORGANIC ELECTROLUMINESCENT DEVICES

Of all applications, OLEDs have the largest impact on the development of new molecular materials [217, 218]. An immense number of material combinations have been proposed for multilayer OLEDs by the groups working in this field. In Section III, we already encountered emissive materials that have been used for controlling the color of OLEDs if implemented as an emission layer in such a structure. But the true challenge is achieving the multifunctionality that the materials have to fulfill in order to obtain an optimized OLED. Light emission is only one feature, the ability of charge injection and transport being the other issues that have to be considered. The energy levels must be aligned carefully in order to make electrical injection possible, and charge has to be conducted easily in order to avoid large ohmic resistances. Thus, in this section we focus on the electrical properties of the chromophores used as layers in OLEDs.

A. The Basic Structure of Organic Light Emitting Diodes

First, let us consider the basic structure of OLEDs (Fig. 3.26). Not less than seven layers are used in a state-of-the-art device based on low-molecular materials. The structure is derived from a five-layer concept (three organic layers and two electrodes) by Adachi et al. [105], who extended the original bilayer device of Tang and Van Slyke [42]. The central layer is the emitting layer consisting of one of the fluorescent or phosphorescent materials discussed in Section IV. Here, the excited states (excitons) are not formed by photoexcitation but by the recombination of an electron-depleted molecule—a radical cation with a “hole” in the highest occupied molecular orbital (HOMO)—and an excess charge carrying radical anion having an additional electron in the lowest unoccupied molecular orbital

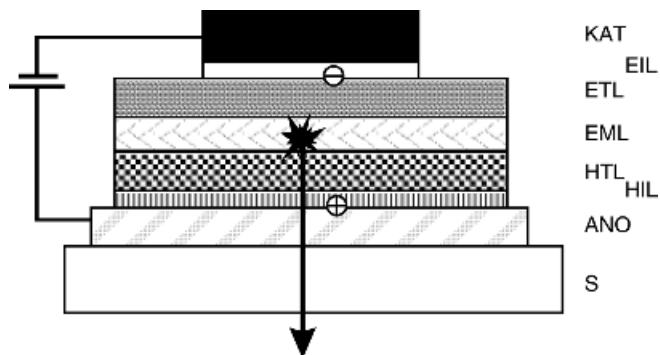
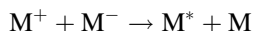
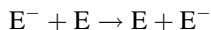


Figure 3.26. Structure of an OLED. S = substrate (glass), ANO = anode (e.g., ITO = indium–tin–oxide), HIL = hole injection layer (e.g., Cu–phthalocyanine), HTL = hole transport layer, EML = emission layer, ETL = electron transport layer, EIL = electron injection layer (e.g., LiF), KAT = cathode (e.g., Ag:Mg, Al). The light that is generated by the recombination of holes and electrons is coupled out via the transparent anode.

(LUMO), according to the following mechanism



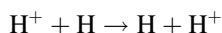
The electrons for the radical anions are injected by the cathode, consisting of a metal with a low work function. Usually, calcium, a coevaporated magnesium–silver alloy with a ratio Mg/Ag of 10 : 1, or aluminum are used. The corresponding work functions are 2.9, 3.7, and 4.3 eV, respectively. The injection of the electrons can be facilitated by an additional layer of lithium fluoride [219]. Since lithium fluoride is an insulator, the mechanism for the improvement of electron injection in electrodes such as LiF/Al is still a subject of discussion. Explanations comprise electron tunneling, the quenching of interfacial reactions, and the dissociation of LiF toward metallic lithium, which reduces the barrier height toward the electron transport layer [220, 221]. The electrons are transported through the electron-transport layer on the LUMO level via hopping transport that is in principle a mutual solid-state redox reaction



and are transferred to the emitter molecules M.

On the substrate side, the same process occurs for the holes, but on a different energy level. The holes are injected by a high work function metal or semiconductor like the transparent ITO, which consists of a nonstoichiometric composite

of 10–20% SnO₂ and 80–90% In₂O₃. The work function of ITO depends strongly on the surface treatment and lies in the range of 4.4–5.2 eV [222, 223]. As in the case of the cathode, hole injection can be improved by an additional layer of, for example, copper phthalocyanine [47] or polyethylenedioxythiophene (PEDOT), doped with polystyrenesulfonic acid (PSS) [224]. The holes are injected into the hole transport layer and proceed by hopping on the HOMO level toward the emission layer.



The zone of recombination can be very small as was shown by Aminaka et al. [225] by doping only a thin layer (5 nm) in the device by a red emission material. By observing the ratio of host and dopant emission, the authors were able to show that the recombination zone of the device was as thin as 10 nm. The emitted light is usually coupled out at the substrate side through the transparent anode. As a rule, the electroluminescence spectrum does not differ much from the photoluminescence spectrum.

Very often, two of the functional layers are replaced by one, using a material with combined emission and electron- or hole-transport capabilities. In addition, the charge-transport layers serve also as blocking layers for the carriers of opposite charge, which helps to confine the zone of recombination into the central area of the device and avoids loss of charges and quenching of the excitons at the electrode interfaces. The control of the recombination zone therefore requires a subtle balance between injection, charge-transport, and charge-blocking kinetics, which is a great challenge for material and device design. The energy level diagram of the OLED, summarizing the charge injection, transport, and recombination processes, is shown in Figure 3.27.

B. Redox Potential and Charge Injection Properties

As can be seen from the energy level structure diagram, the relative position of the HOMO and LUMO levels are not less important than the energy gap between them, since they control the possibility of charge injection. At this point, however, note, that a MO scheme is often used for illustration, but more properly the total energy states of the molecules and their radical cations and anions that may be subjected to electronic rearrangement have to be considered. Bearing this in mind, the measured values of redox potentials can be translated into the molecular orbital picture.

Whereas the work function of the electrodes is measured by photoelectron spectroscopy, the organic materials are usually characterized by cyclic voltammetry [226]. The values can be extrapolated to the gas phase by choosing an

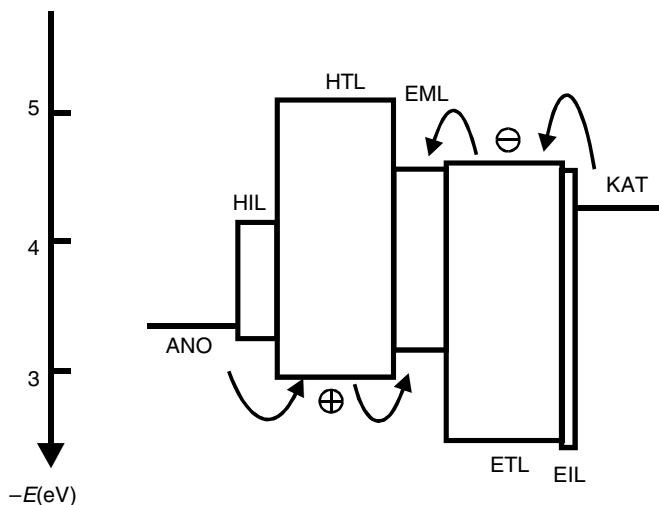


Figure 3.27. Energy level scheme of the device in Figure 3.26, consisting of the electrode work functions and the molecular HOMOs and LUMOs. The relative energy level of HOMOs and LUMOs can be determined by cyclic voltammetry and optical spectroscopy. Note the hole blocking character of the electron-transport layer. This feature is important since holes that proceed via the HOMO levels have much higher mobilities than electrons proceeding via the LUMO levels.

appropriate reference and neglecting the influence of the polarity of the solvent in which the measurements are taken. In addition, the formation of interfacial potentials due to the formation of dipole layers in the solid-state device [227] is neglected. Making these assumptions, the energy levels obtained by cyclic voltammetry can be compared with the electrode work functions. It is more reliable, though, to compare the redox properties of different materials relative to each other.

Cyclovoltammetric measurements [228] are usually performed in acetonitrile, dichloromethane, or tetrahydrofuran (THF) solution with a conducting organic salt such as tetrabutylammonium hexafluorophosphate (TBAHFP). As (pseudo-) reference electrode, Ag/Ag^+ (0.01 Mol/L in acetonitrile) or Ag/AgCl are used. For calibration, an internal reference, ferrocene Fc/Fc^+ (+0.35 V vs. Ag/AgCl) or cobaltocene $\text{CoCp}_2/\text{CoCp}_2^+$ (−0.94 V vs. Ag/AgCl) is added. The ionization energy of ferrocene is assumed to be 4.8 eV, thus linking the electrochemical potential to the work function scale of the electrodes [229]. The energy of the MOs is the negative value, that is,

$$\varepsilon(\text{MO}) = -(4.8 \text{ eV} + E_{1/2})$$

$E_{1/2}$ being the reversible half-wave potential of the electron-transfer reaction with respect to ferrocene. The suggested offset value, however, differs somewhat from group to group.

1. Energy Levels for Hole Injection. For the hole conductor TPD (**6**), measurements are available from different groups that allow a direct comparison of different experimental setups. The ionization potential that corresponds to the HOMO level under the assumptions mentioned above was measured by photoelectron spectroscopy to be 5.34 eV [230]. Anderson et al. [231] identified the onset of the photoelectron spectrum with the ionization potential and the first peak with the HOMO energy, and reported separate values of 5.38 and 5.73 eV, respectively. The cyclic voltammetric data reveal a first oxidation wave at 0.34 V vs. Fc/Fc⁺ in acetonitrile [232], and 0.48 V vs. Ag/0.01 Ag⁺ in dichloromethane [102], respectively. The oxidation proceeds by two successive one-electron oxidations, the second one being located at 0.47 V vs. Fc/Fc⁺.

The different hole injection and transport materials can be compared relative to TPD. The spiro derivative Spiro-TAD (**36a**) has a lower first oxidation potential that can be explained by the better resonance stabilization of the radical cation [87]. The material exhibits two successive one-electron oxidations (0.23 and 0.38 V vs. Fc/Fc⁺) and one subsequent formal two-electron oxidation (0.58 V) to the tetracation (Fig. 3.28).

The starburst triarylamine *m*-MTDATA (**23**) and its derivatives have even lower oxidation potentials [102], making them well suited for the injection of holes. For *m*-MTDATA, a value of 0.06 V vs. Ag/0.01 Ag⁺ is reported. By photoelectron spectroscopy, the low ionization potentials for *m*-MTDATA and for *p*-DPA-TDAB (0.23 V vs. Ag/0.01 Ag⁺) were confirmed. The values are 5.0 ± 0.1 eV and 5.15 ± 0.05 eV, respectively [233]. Equally low is the ionization potential of TPTE (**9**) with 4.96 V [230].

It is interesting to compare the biphenylamine substituted compounds with the corresponding carbazoles, phenoxazines, and phenothiazines. For the triarylamine-based structures, the carbazole **24** has the highest oxidation potential (0.69 V vs. Ag/0.01 Ag⁺) [102], followed by the phenoxazine **25a** (0.46 V vs. Ag/0.01 Ag⁺) [166]. A similar observation was made for the corresponding derivatives of **36a**: the phenothiazine (0.27 V vs. Fc/Fc⁺) and the phenoxazine (0.29 V vs. Fc/Fc⁺) have higher oxidation potentials than the parent compound. The carbazole **37** has an even higher oxidation potential, but in this case the oxidation is not reversible [234]. The redox properties of carbazoles are not fully understood yet. In some devices, a carbazole such as CBP (**10**) was used as an interface layer on the cathode side, suggesting a lower barrier for electron injection [50].

If an increasing number of thiophene rings are inserted into the TPD structure, as in the BMA-*n*T series **13a–d**, the oxidation potential does not change with

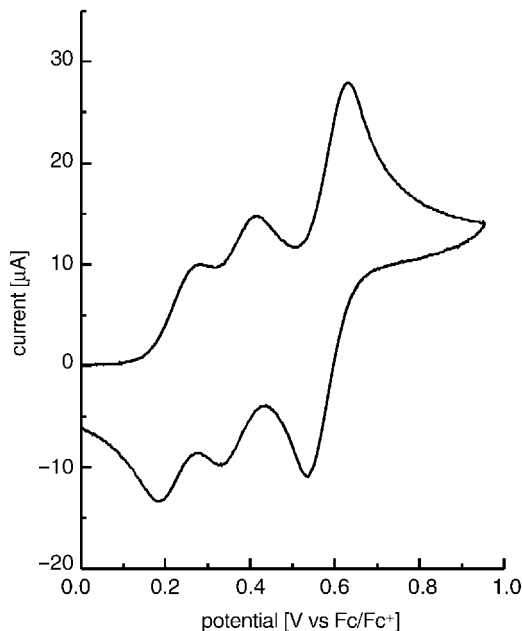


Figure 3.28. Cyclic voltammogram for the hole transporting material Spiro-TAD (36a). The oxidation proceeds in two one-electron and one formal two-electron wave. Solvent: Dichloromethane/TBAHFP 0.1 M, Scan rate 100 mV/s.

increasing conjugation length (0.39–0.35 V vs. Ag/0.01 Ag⁺). Because the absorption and emission bands are significantly shifted, obviously the electron affinity is increased instead. Interestingly, depending on the number of thiophene rings, the materials can be oxidized up to the tetracation (for $n = 4$) [53, 54].

2. Electron Injection. Whereas the energy levels for hole injection from the ITO electrode can be adjusted rather easily, the electron injection side is more crucial since the LUMO levels usually lie much higher than the work function of the electrode materials. For Alq₃ as one of the most typical electron-transport materials, the reduction potential is reported to be -2.01 V vs. Ag/0.01 Ag⁺ [102] and -2.30 V vs. Fc/Fc⁺ [231]. In the latter paper, the electron affinity was calculated to be 3.17 eV, based on the comparison of photoelectron and UV spectroscopic data. The oxidation potential was also determined by cyclic voltammetry (0.73 V vs. Fc/Fc⁺). The ionization energy of Alq₃, determined as the onset in the photoelectron spectrum, is 5.7 eV, the HOMO as the first resolvable peak is supposed to lie a little bit lower, at 6.34 eV [235, 236]. These data for reduction and oxidation mean that for electron injection in Alq₃, a still high

barrier of ~ 0.6 – 1.1 eV, depending on the cathode material, has to be surmounted, whereas it has fairly good blocking properties for holes, which usually proceed at energy levels of 4.6 – 5.3 eV below vacuum level. Newer results reveal, however, that the cationic species of Alq_3 , formed by the injection of holes in the electron-transport layer, is not stable and is suspected to be the main cause of device degradation [237].

Compared to Alq_3 , the oxadiazoles have a lower tendency toward reduction and thus a higher barrier for electron injection. Spiro-PBD (**140**), for example, can accept four electrons, the first electron transfer (merged wave for two electrons) taking place at -2.46 eV vs. Fc/Fc^+ (Fig. 3.29) [87]. The oxadiazoles **17a**, **18**, and **29** exhibit reversible reduction waves at -2.39 and -2.18 eV and an irreversible reduction, respectively [238]. Since the HOMO–LUMO gap is >1 eV larger than for Alq_3 , the hole blocking properties are better for the oxadiazoles.

Other electron-transport materials for which electrochemical data are available comprise phenylquinoxalines **30** with -1.78 V vs. Fc/Fc^+ [60] and twin-type 1,3,5-triazine ethers **5** with -2.2 V vs. Fc/Fc^+ [45]. For thiophene-bridged dimesitylboron compounds BMB-*n*T (**14**), -1.76 V vs. Ag^+/Ag (-1.9 V vs.

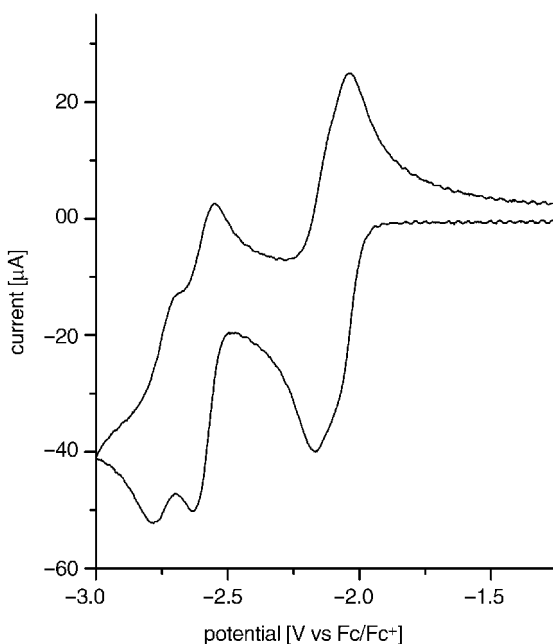


Figure 3.29. Cyclic voltammogram for the electron transporting material Spiro-PBD (**40**). The first reduction is a merged wave with an overall transfer of two electrons. Solvent: THF/TBAHFP 0.1 M, Scan rate 100 mV/s.

Fc/Fc⁺) have been obtained, irrespective of the number of bridging thiophene rings [56]. Naito et al. [239] compared a variety of other electron-transport materials by their ionization potential and electron affinity measured by different methods. For example, some bis(styrylanthracenes) similar to **21** but with electron-withdrawing groups exhibit higher electron affinities than Alq₃. The per-fluorinated compounds **19** and **34** showed irreversible electroreductions [62].

Electrochemical data for the solid state are rare, but one example comprises reduction potential measurements of oligo(*p*-phenylene-vinylenes) with a convergence limit of -2.18 V vs. Fc/Fc⁺ for long chains. In contrast to the solution measurements, all solid-state voltammograms exhibit a strong hysteresis [240].

3. Bipolar Molecular Glasses. Recently, bipolar molecular glasses have been described that allow both injection of holes and electrons (Fig. 3.30). 2-{4-[bis(4-methylphenyl)amino]phenyl}-5-(dimesitylboryl)thiophene (PhAMB-1T, **68**) and 2-{4-[bis(9,9-dimethylfluorenyl)amino]phenyl}-5-(dimesitylboryl)thiophene (FIAMB-1T, **69**) show oxidation potentials of 0.62 and 0.58 V, and reduction potentials of -2.13 and -2.01 V vs. Ag/0.01 Ag⁺, respectively [145]. Oxidation as well as reduction leads to stable radical ions. With the conversion rules given above, the HOMO and LUMO levels can be estimated to be approximately at -5.3 and -2.8 eV. In comparison, for the bipolar compound **70**, consisting of triarylamine and oxadiazole moieties, the values are -5.5 and -2.7 eV [129]. However, in this case no data on the stability of the radical ions are available.

C. Charge Transport

Good hole or electron injection properties do not necessarily mean good transport properties and vice versa. Charge injection is governed by the energetic structure of the molecules, charge transport by the electron-transfer kinetics between a radical ion and a neutral molecule. The charge-transport properties of organic glasses have attracted interest very early since the transport materials are good candidates for electrophotography (xerography). Ordered structures favor the overlap of the electron system of neighboring molecules, thus facilitating electron transfer. This means that the charge mobilities usually decrease in the order molecular crystal [241–244] > liquid crystalline glass [245] > amorphous glass. Thus, for amorphous glasses the task is to find materials with sufficiently high mobilities.

Usually, in amorphous molecular materials, charge transport is described by a disorder formalism that assumes a Gaussian distribution of energetic states of the molecules between which the charges jump [246]. The mobility is then given by

$$\mu = \mu_0 \exp \left[- \left(\frac{2\sigma}{3kT} \right)^2 \right] \exp \left[C \left(\frac{\sigma^2}{(kT)^2} - \Sigma^2 \right) E^{1/2} \right]$$

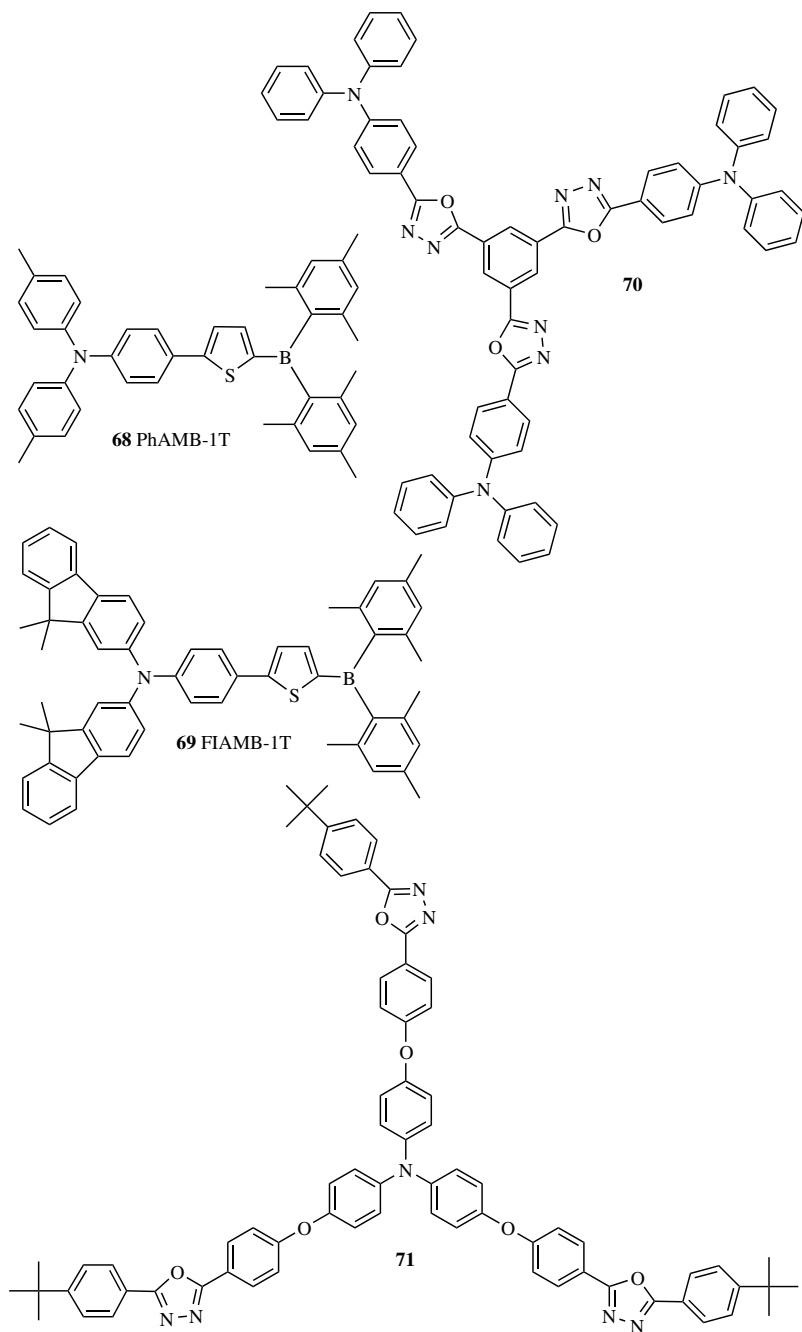


Figure 3.30. Some bipolar molecular glasses.

which expresses the experimentally observed electric field (E) and temperature (T) dependence:

$$\log \mu \propto T^{-2}$$

$$\log \mu \propto E^{1/2}$$

μ_0 is a prefactor mobility (zero field, infinite temperature), C is an empirical constant of $2.9 \times 10^{-4} (\text{cm/V})^{1/2}$, σ and Σ express the energetic (diagonal) and positional disorder (off-diagonal), respectively. Other approaches also exist, one of them being based on the Marcus theory of charge transfer [247, 248].

Experimentally, the charge mobilities are obtained by time-of-flight-measurements or by characterizing field-effect-transistor devices made of the materials. In time-of flight experiments, the mobility μ is directly given by

$$\mu = \frac{d}{Et}$$

where d is the sample thickness, E is the applied electric field, and t is the transit time. In transistor measurements, it can be calculated from the current-gate voltage relation [249].

Most of the early experimental work [250] has been done on molecular materials imbedded in a polymer matrix at concentrations of 10–80%, so a comparison of the intrinsic properties of the materials is not easy. Another obstacle is the dependence of the charge mobilities on the preparation technology (purity, morphology). However, some data are available for true one-component molecular glasses, a selection of which will be presented in the following sections.

1. Hole Mobilities. For TPD (**6**), the hole mobility was measured by Heun and Borsenberger [251] at fields between 40 and 400 kV/cm and in a wide temperature range from 213 up to 345 K. For high field and ambient temperature, the mobility is in the range of $10^{-3} \text{ cm}^2/\text{Vs}$ with $\mu_0 = 3.0 \times 10^{-2} \text{ cm}^2/\text{Vs}$, $\sigma = 0.077 \text{ eV}$, and $\Sigma = 1.6$. For α -NPD (**7**), the mobility is in the same range, but the prefactor mobility is higher ($\mu_0 = 3.5 \times 10^{-1} \text{ cm}^2/\text{Vs}$) [252–254]. Spiro-TAD **36a** shows a hole mobility of $3 \times 10^{-4} \text{ cm}^2/\text{Vs}$ at 200 kV/cm ($\mu_0 = 1.6 \times 10^{-2} \text{ cm}^2/\text{Vs}$, $\sigma = 0.08 \text{ eV}$, $\Sigma = 2.3$) [255], which is lower than for TPD. In a model study on bis(ditolylaminostyryl)benzene, Borsenberger et al. [256] showed that the diagonal disorder can be divided into a dipolar and a van der Waals component, the latter one being higher for this compound than for other triarylaminines.

The starburst arylamine *m*-MTDATA (**23**) exhibits a rather low mobility of $3 \times 10^{-5} \text{ cm}^2/\text{Vs}$ at 100 kV/cm, but *o*-MTDAB (**27b**), *p*-BPD (**8c**), and tris-[4-

(5-phenyl-2-thienyl)phenyl]amine show values exceeding 10^{-3} cm²/Vs, the latter one even 10^{-2} cm²/Vs [102, 257]. For the three isomers **8a–c**, it was demonstrated that the lower mobility of the meta-substituted isomer can be attributed to a larger energetic disorder, the prefactor mobilities all being in the same range. Other materials that approach 10^{-2} cm²/Vs are the enamine derivatives of biphenyl diamine (**11**: $\mu_0 = 2.2 \times 10^{-1}$ cm²/Vs, $\sigma = 0.077$ eV, $\Sigma = 1.0$) [258]. On the other hand, materials like, for example, **52**, and other diphenylhydrazones, the oligothiophene derivatives, **13**, and the large molecule MTBDAB (**28**), exhibit rather low hole mobilities (10^{-5} cm²/Vs) [259, 260].

For materials with small energetic disorder, but large Σ , the mobility may decrease with increasing fields that was demonstrated first for the molecular glass *o*-TTA (**26a**) ($\mu_0 = 9.7 \times 10^{-3}$ cm²/Vs, $\sigma = 0.059$ eV, $\Sigma = 2.4$), measured at room temperature [71].

2. Electron Mobilities. The electron mobilities of good electron transport materials are about two orders of magnitude lower than typical hole mobilities of good hole transport materials. Thus, it is much more difficult to find good electron-transport material for a balanced charge injection in an OLED. The first time-of-flight measurements on Alq₃, have been made by Kepler et al. [261]. They found an electron mobility of 1.4×10^{-6} cm²/Vs at 400 kV/cm, accompanied by a low hole mobility of 2×10^{-8} cm²/Vs at room temperature.

The electron mobility of oxadiazoles have been measured in a polymer matrix, values of 10^{-7} up to 10^{-5} cm²/Vs have been obtained [262, 263]. These values are exceeded by starburst phenylquinoxalines (**30**) that approach 10^{-4} cm²/Vs at 10^6 V/cm [264]. Other material classes that are very interesting candidates for electron-transport layers comprise naphthalene-, **60**, and perylenetetracarboxylic diimides, **59** [265], as well as bathophenanthroline [266] with reported electron mobilities of 10^{-3} and 4.2×10^{-4} cm²/Vs, respectively.

Mobility data on bipolar charge-transport materials are still rare. Some bipolar molecules with balanced mobilities have been developed [267], but the mobilities are low (10^{-6} – 10^{-8} cm²/Vs). Up to now, no low molecular material is known that exhibits both high electron and hole conductivity in the amorphous state, but it is believed that it will be only a matter of time. One alternative approach, however, is to use blends of hole and electron transporting materials [268].

One final aspect on charge transport in molecular glasses should be mentioned: The hole or electron current depends not only on the mobility but also on the number of charge carriers. The latter can be increased just as in inorganic semiconductors by chemical doping with electron donors or acceptors. This kind of doping must not be confused with dye doping with respect to Förster transfer as described above. For example, doping a hole-transport material with a strong electron acceptor such as perfluorinated tetracyanoquinodimethane (F₄-TCNQ) can improve the electrical properties of devices substantially [269].

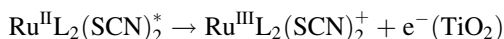
VII. FROM LIGHT TO CURRENT: APPLICATION OF MOLECULAR GLASSES IN SOLAR CELLS

The conversion of light to electric current in photovoltaic devices is the direct inversion of the electroluminescent process in OLEDs, thus it is not surprising that the same molecular glasses as described above have also been used for the realization of solar cells. There are at least two different types of approaches, however, that shall be described now.

A. Dye-Sensitized Solar Cells

Due to its direct relation to Section VI, we begin with a cell in which mainly the hole transporting properties of molecular glasses are used: the solid-state dye sensitized cell.

The dye-sensitized solar cell, commonly referred to as the Grätzel cell, is based on the photoinduced electron transfer from a dye to mesoporous TiO₂ [270]. The network of connected TiO₂ nanoparticles forms a large surface area being active for light absorption and electron transfer. As the active dye ruthenium dyes such as Ru^{II}L₂(SCN)₂, where L = 4,4'-dicarboxy-2,2'-bipyridyl ligands, are well suitable because of the good adhesion of the carboxy groups to the TiO₂ surface. If the dye is excited, electrons are injected into the conducting band of TiO₂, leaving a ruthenium (III) species.



The electrons are collected by an F-doped SnO₂ electrode and the electrical circuit is closed via a gold electrode by a mediator that transports the charges needed for the back-reduction of the dye (electrons from the gold electrode to the LUMO of the dye, or in an equivalent picture, holes from the dye to the gold electrode). The original cell suffers from the use of a liquid electrolyte containing the redox system I₂/I₃⁻ as mediator, which causes some problems due to leakage and solvent evaporation if not sealed properly.

Thus all solid-state variations of this cell have been developed by replacing the liquid electrolyte by hole transporting molecular glasses [271–273]. In the paper by Bach et al. [272], the tetramethoxy derivative of Spiro-TAD (**36b**) was used, with Ru^{II}L₂(SCN)₂ as the sensitizing dye. The structure and energy level diagram of this cell is displayed in Figures 3.31 and 3.32. The internal photon-to-electron-conversion efficiency (IPCE) was determined to be 5%, which is still lower than for comparable liquid cells. However, an IPCE of 33% was measured by doping the hole-transport material with N(PhBr)₃SbCl₆ and Li[(CF₃SO₂)₂N], which increases the charge-carrier concentration by partial oxidation. The overall

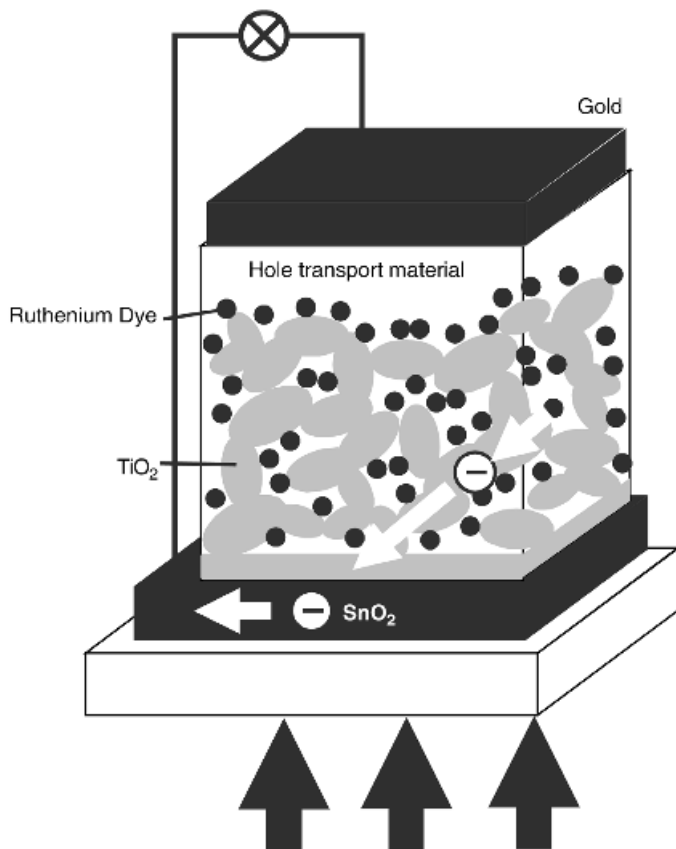


Figure 3.31. Organic solar cell with the molecular glass Spiro-MeOTAD as the solid-state electrolyte. The photosensitive ruthenium dye is attached as a monolayer to TiO_2 nanoparticles, thus forming a large active area for photoinduced electron transfer.

efficiency of the cell was 0.74% at a white-light irradiation with 9.4 mW/cm^2 . Under full sunlight (air mass 1.5, 100 mW/cm^2), short-circuit photocurrents of 3.18 mA/cm^2 have been achieved.

B. Heterojunction Solar Cells

The second type of solar cell is based on a *pn*-heterojunction in analogy to semiconductor devices [274]. Excitons generated by light, diffuse and dissociate at the interface between a hole and an electron-conducting material. The optimum layer thickness was calculated to be ~ 1.5 times the exciton diffusion length [275].

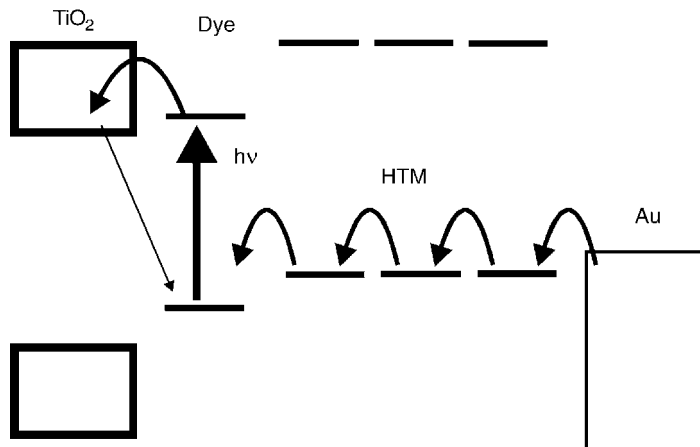


Figure 3.32. Energy level scheme of the device in Figure 3.31. Photoinduced electron transfer takes place from the photoexcited ruthenium dye into the TiO₂ conduction band. The recombination directly back to the dye has to be suppressed. Instead, the current is directed through the circuit to the counterelectrode and the hole conductor that brings the electrons back via hopping transport. HTM: hole transport material.

Most of the devices described up to now are based on materials that tend to crystallize [phthalocyanines, porphyrins and perylenetetracarboxydiimids, (**59**)] [276, 277], or form liquid crystalline phases [278, 279]. With respect to amorphous glasses, light sensitive donor-acceptor type molecules, for example, the p-type triaryl amines tris[4-methylphenyl(4-nitrophenyl)amino]triphenylamine and tris[5-(dimesitylboryl)thiophen-2-yl]triphenylamine have been combined with an n-type material in a double-layer heterostructure [280]. The cells respond to visible light from 400 to 800 nm with overall efficiencies of 0.1%.

A very interesting approach is the combination of charge-transfer donor-acceptor sites in one molecule as it was demonstrated for compounds consisting of oligophenylenevinylene and C₆₀ moieties [281, 282]. By microphase separation, a bicontinuous network is formed for the charge transport. The efficiencies are, however, quite low (0.01–0.03%).

VIII. FURTHER APPLICATIONS: PHOTOCROMIC AND PHOTOREFRACTIVE MATERIALS

A. Photochromics

Photochromic dyes can also be found among the various chromophores that have been implemented in molecular glasses. The free volume available in the amor-

phous solid allows photochemical reactions like the molecular rearrangements on which the photochromic systems are based. By irradiation with light, the absorption spectrum of the thin films as well as the refractive index is changed, which allows the application of molecular glasses for information storage and for sensor and switching devices. A large number of photochromic systems are known [283], which may all be used for the design of photochromic glasses: azo dyes [284] and stilbenes [285], diarylethenes [286], spiroopyran–merocyanines [287], fulgides [288], dihydroazulene–vinylheptafulvenes [289], dihydroindolizines [290], spiroperimidin–chinoximines [291]. These systems are only a representative selection of possible materials. For azo dyes, some special mechanism occurs, thus we will treat them in a separate section.

With respect to molecular glasses, the photochromism of dithienylethene has been investigated by some groups. The first report was published by Kawai et al. [292] using 1,2-bis[5-(4-*tert*-butylphenyl)-2,4-dimethylthiophen-3-yl]-3,3,4,4,5,5-hexafluorocyclopentene (**72**), which has a T_g of 68°C. By irradiation with UV light, the system undergoes ring closure, the closed form being stable unless bleached by visible light (Fig. 3.33). The absorption bands of the open form **72a** are 280 nm, and of the closed form **72b** 380 and 580 nm, respectively. The switching is reversible to a degree of 80% when starting from a film of the closed form, but is only 41% when starting from a film of the open form. This finding is attributed to the fact that for the open form two conformers are possible, only one of which can react easily in the solid state without the need of rotational motion of bulky groups. The refractive index changes in the film were measured by a prism coupler method and are $\Delta n = 0.04$ when starting from the closed form and $\Delta n = 0.01$ when starting from the open form.

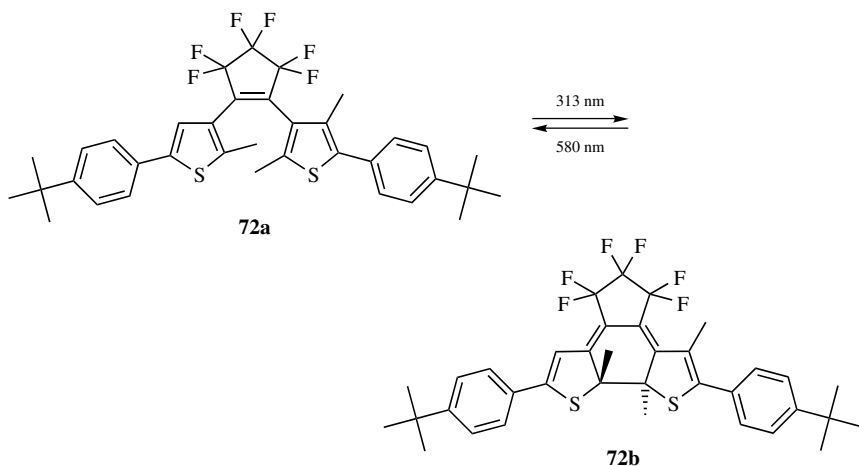


Figure 3.33. Photochromism of diarylethenes.

Other dithienylethenes have been synthesized and investigated for their photochromic properties by replacing the *tert*-butyl group by bis(*p*-methylphenyl) amine, thus raising the glass transition temperatures [293, 294].

B. Azo Reorientation and Surface Gratings

Azo dyes exhibit the special feature that the photochromic forms, the *trans* and *cis* isomers, can be converted to each other by irradiation at the same wavelength, thus forming photostationary states. This is due to the strong overlap of the absorption bands, especially for the $\pi\pi^*$ band at ~ 450 nm, which means that in addition to the normal photochromism that can be detected in amorphous molecular glasses containing azo dye moieties [295–297], a special mechanism may take place under irradiation with polarized light [52]. Under polarized light, the photoselection principle holds [298], which states that the probability for excitation depends on the angle between the molecular transition moment and the polarization direction. The molecules with originally randomly distributed orientations undergo photoisomerization cycles with some rotational diffusion until they adapt an orientation perpendicular to the polarization direction of the light [299] (Fig. 3.34). If a spatial pattern of light polarization is applied to a thin film of a molecular azo glass, a birefringence grating is formed [300]. The orientational grating also alters the surface stress of the sample, finally leading to a corrugated surface grating that has been detected recently in the case of polymers [301–303]. Figure 3.35 shows the holographic setup that is used for

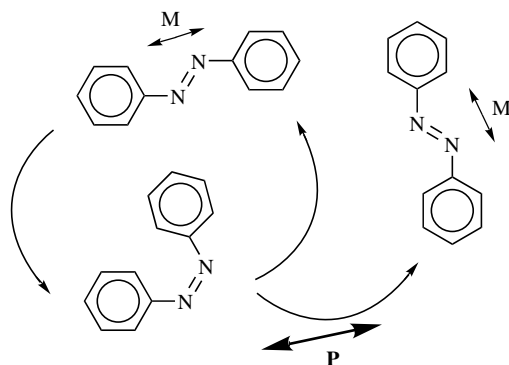


Figure 3.34. Photochromism of azo dyes under irradiation with polarized light. In an amorphous matrix, *trans*–*cis* isomerizations are coupled to rotational diffusion. After many isomerization cycles, the molecules are trapped in an orientation with the transition moment M perpendicular to the polarization direction of the light P .

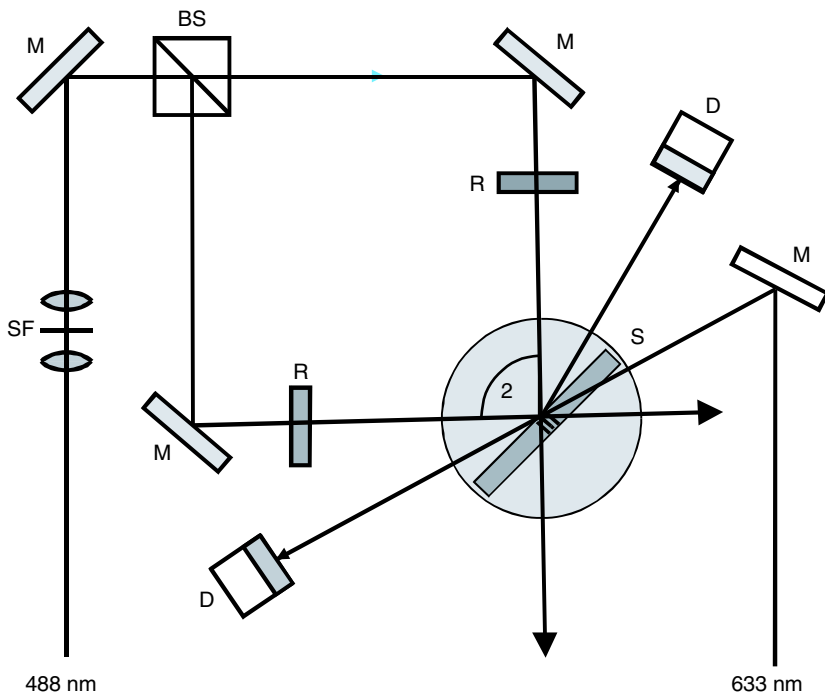


Figure 3.35. Holographic setup for the generation of corrugated surface gratings in azo molecular glasses. The gratings are written at 488 nm and read out at 633 nm. The polarization pattern is defined by choosing an appropriate retarder *R* (half and quarter wave plates), the grating constant by varying the crossing angle of the two beams. *S*: Sample, *SF*: Spatial filter, *BS*: Beam splitter, *M*: Mirror, *D*: Detector.

the writing of such a polarization pattern. The polarizations of the two writing beams can be adjusted to be orthogonally polarized, either linearly or circularly, depending on the phase-shifting elements used (Fig. 3.36).

Originally, this recording principle based on photoinduced birefringence was applied for liquid crystalline and amorphous polymers [304, 305]. Later, it led to the development of appropriate functionalized molecular glasses [52]. For the molecular glass *N,N'*-bis(phenyl)-*N,N'*-bis[(4-phenylazo)-phenyl]benzidine (AZOPD, **12**), imaging of a test pattern and the formation of surface gratings have been demonstrated (Fig. 3.37 [306]). The possible applications of thin films of these azo dye glasses lie not only in the area of optical recording but also in the construction of optical waveguides with implemented grating couplers or distributed feedback gratings [307].

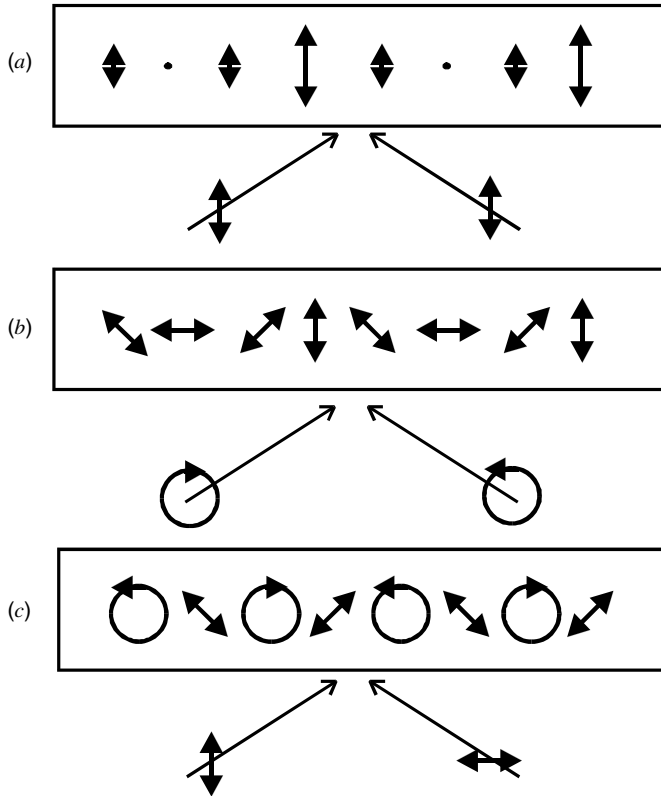


Figure 3.36. Different types of holographic gratings. (a) Both writing beams have the same polarization: intensity grating. (b) The writing beams are left and right circularly polarized: linear polarization grating. (c) The writing beams are s and p polarized: mixed-polarization grating.

C. Photorefractives

In addition to photochromic systems, other approaches exist for the development of materials for optical recording and real-time image processing. For example, one alternative way for data storage may be the use of molecular glasses as phase-change materials: Locally heating the glass induces recrystallization and changes the reflectance properties [308]. The approach on which we will focus in this section is the use of photorefractive composite systems. The principle of photorefractivity is based on the photogeneration of space charges that induces reorientation of the molecules by the electrooptic effect (Fig. 3.38). For testing

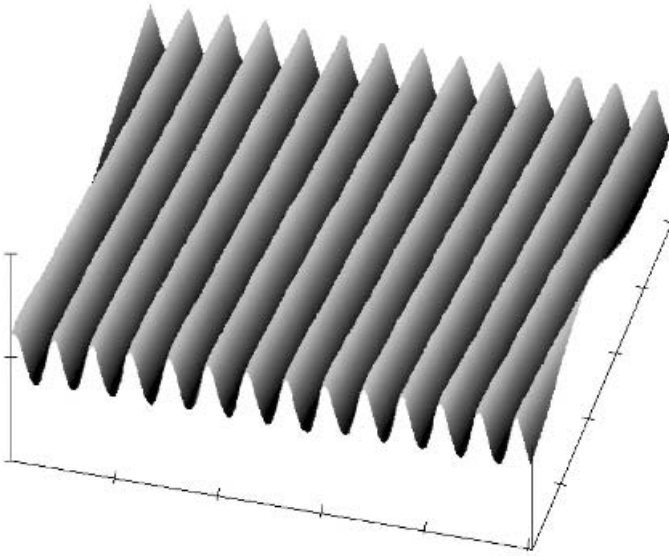


Figure 3.37. Atomic force microscopy of a corrugated surface grating written into a molecular azo glass.

photorefractive materials, a holographic experiment similar to the setup in Figure 3.35 can be used, but with the difference that no retardation plates are used, leading to a sinusoidally varying intensity profile instead of a polarization modulation. The gratings are tilted with respect to the film plane, allowing the application of an additional electric field that has a component in the direction of the grating vector for the enhancement of the process (Fig. 3.39).

Photoconductivity gives rise to the generation of charge carriers at the bright areas with constructive interference. The carriers diffuse or are shifted by the externally applied electric field, respectively. Because of the different mobilities of positive and negative charge carriers, space charges are formed. The space-charge modulation creates an electric field that is phase shifted by half a period. This internally generated modulated field leads to a refractive index grating, either by induced electrooptic polarization or, more effectively and stable, by the reorientation of dipole molecules. The effectivity of the latter process depends on the dipole moment of the molecules as well as the anisotropy of the *linear* polarizability [309]. Photorefractive processes can be distinguished from photochromic processes by the phase shift of the refractive index grating, which is commonly detected by energy coupling from one writing beam to the other (two-beam coupling).

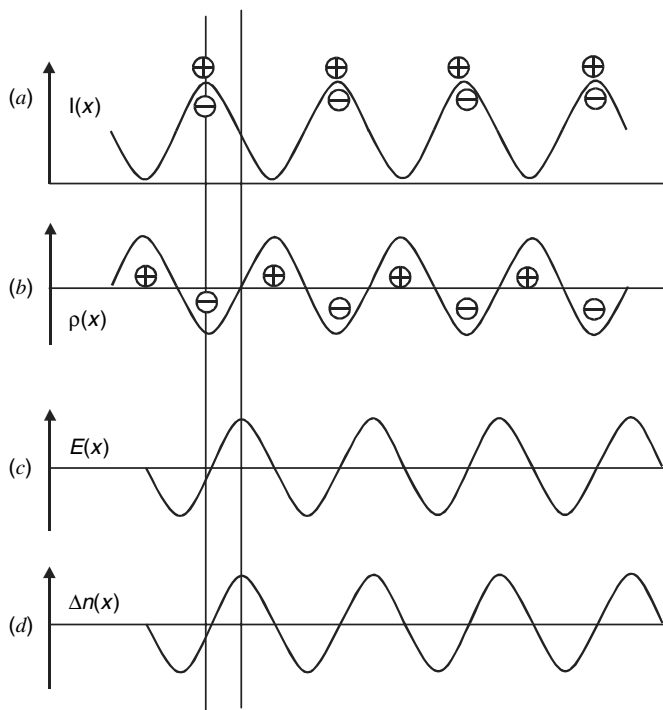


Figure 3.38. Principle of the photorefractive effect: By photoexcitation, charges are generated that have different mobilities. **(a)** The holographic irradiation intensity profile. Due to the different diffusion and migration velocity of negative and positive charge carriers, a space-charge modulation is formed. **(b)** The charge density profile. The space-charge modulation creates an electric field that is phase shifted by $\pi/2$. **(c)** The electric field profile. The refractive index modulation follows the electric field by electrooptic response. **(d)** The refractive index profile.

In order to maintain sufficient mobility for the reorientation process, T_g should not be too high. Thus, with respect to T_g , this application differs from the other applications treated in this chapter, generally requiring a high T_g . However, for high T_g materials, lowering the T_g can be achieved relatively easily by using blend systems. Typical composites consist of a photorefractive glass, a dipolar chromophore, and a plasticizer.

Materials that exhibit photoconductivity and/or electrooptical response can be found in large numbers among molecular glasses (Fig. 3.40). Dihydropyridines with $T_g \sim 25^\circ\text{C}$ and low tendency of crystallization have been used (e.g., 2BNCM, **73**), adding only a small fraction of a binding polymer (<10%), and 2,4,7-trinitro-9-fluorenone (TNF) as a sensitizer [310]. A common strategy is

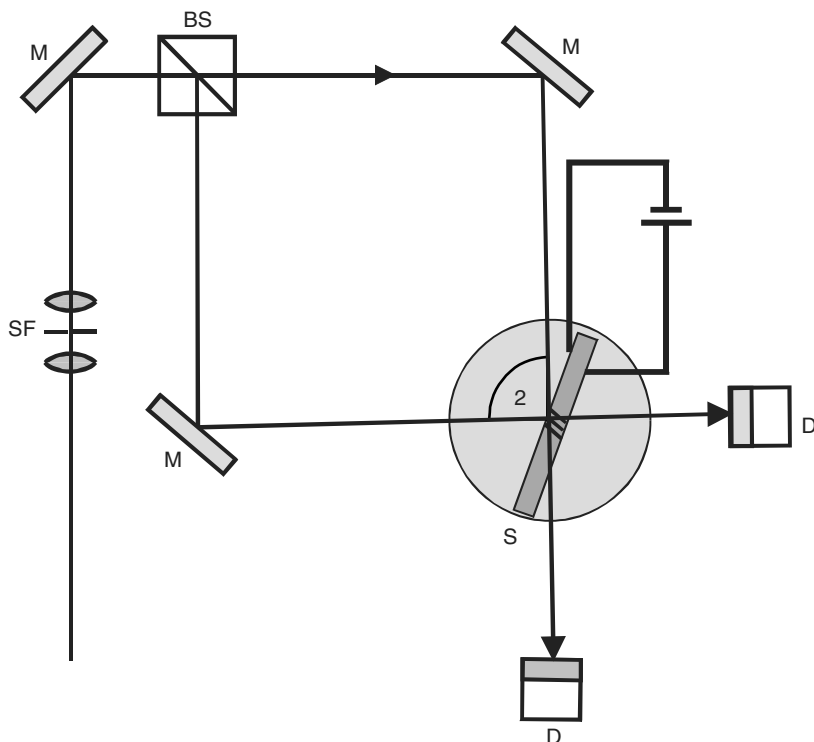


Figure 3.39. Holographic setup for photorefractive molecular glasses. The sample is tilted toward the grating, allowing an applied external field to support the motion of the mobile charges. The phase shift of the refractive index grating can be determined by measuring the transmitted writing beam intensities (two-beam coupling).

the combination of a photorefractive moiety and an electrooptic chromophore by a semiflexible spacer, adjusting T_g around room temperature. Based on this principle, carbazole- or diphenylamine-substituted triphenylamines have been coupled with azo dyes and stilbenes (e.g., **74**) [311–314], and unsubstituted triphenylamine with 4-dicyanovinylaniline (**75**) [315]. Fullerene (C_{60}) was used as sensitizer in this case, and diisooctyl phthalate as plasticizer for the high T_g glasses. The succinate spacer in the triphenylamine-4-dicyanovinylaniline system has enough flexibility to make the addition of a plasticizer unnecessary ($T_g = 34^\circ\text{C}$). Another material is based on the combination of oligo(3-alkylthiophene) with a nonlinear optical chromophore [316]. One conjugate structure having both photoconductive and electrooptic properties can be found in carbazole trimers that are coupled by ethynylene bridges **76** [317, 318].

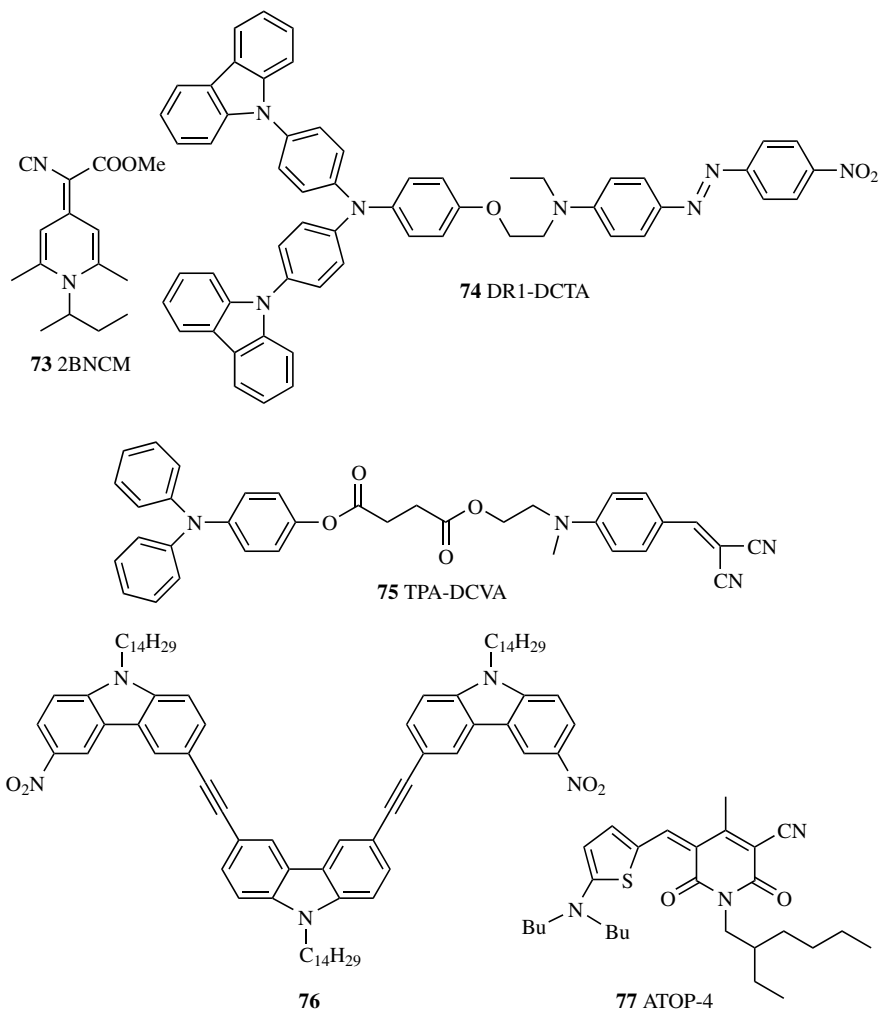


Figure 3.40. Some photorefractive molecular glasses.

Chromophores with a rather high optical anisotropy are the merocyanines (**77**), especially in the cyanine limit with equal contributions of the apolar and zwitterionic resonance structures [319]. Thus, they also have been proposed as promising candidates for photorefractive systems based on molecular glasses. For **77**, doped with a photosensitizer, a refractive index modulation of 0.01 at an electrical field of 22 V/ μm was reported.

D. Lithographic Resist Materials

The photoresponsive properties of molecular glasses also have been applied in the design of resists for semiconductor lithography. In a resist, irradiation changes the solubility of the materials, making it more or less soluble (positive or negative resist, respectively). The search for new resist materials follows the development of lithographic techniques toward deep-UV and electron beam

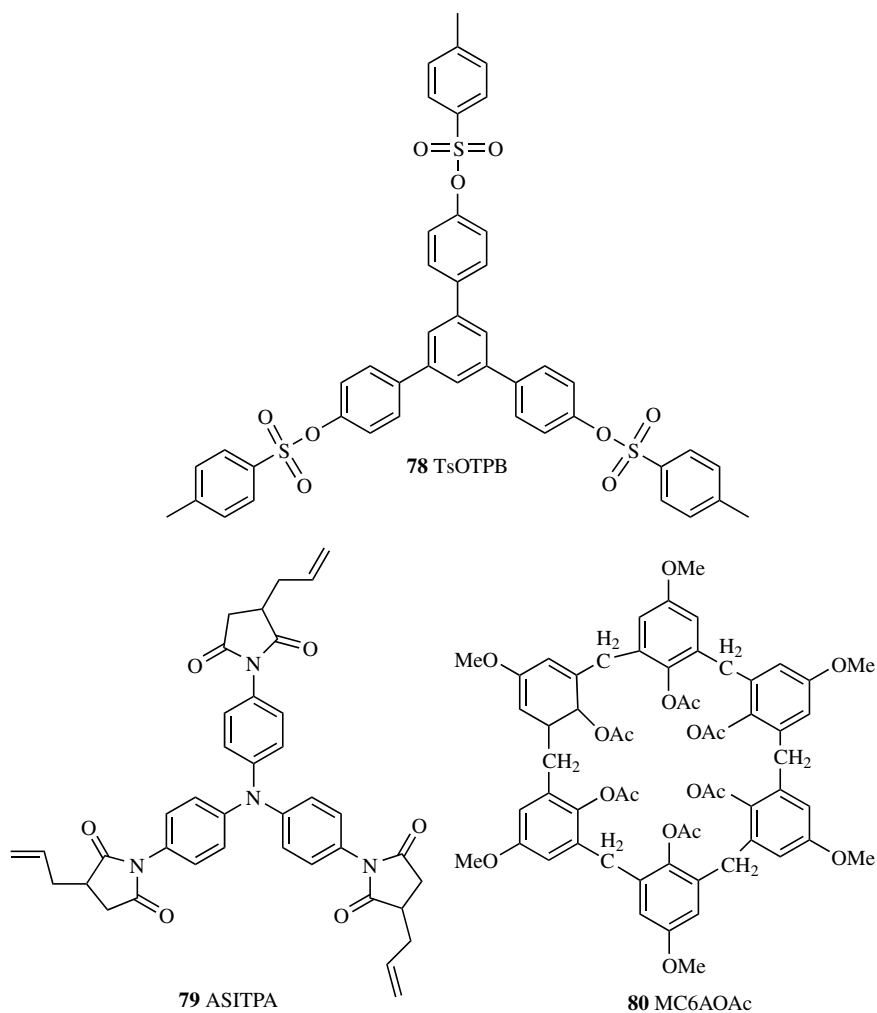


Figure 3.41. Some low molecular resist materials.

lithography. The feature sizes are as small as 100 nm, which approaches the radius of gyration of large polymers used in conventional photoresists. Thus, molecular glasses are promising candidates for the next resist generation due to their small molecular size. Some materials that have been developed for electron beam lithography are displayed in Figure 3.41 [320]. 1,3,5-tris-[4-(4-toluenesulfonyloxy)phenyl]benzene (TsOTPB, **78**) is a positive resist, which is cleaved under electron beam exposure at the sulfur–oxygen bond, yielding products that are soluble in tetramethylammonium hydroxide and isopropyl alcohol. 4,4',4''-tris(allylsuccinimido)triphenylamine (ASITPA, **79**) is a negative resist that undergoes cross-linking at the allyl groups under exposure. The unexposed areas can be removed with 2-methoxyethyl acetate. Other low molecular resists are 1,3,5-tris(*tert*-butoxycarbonyloxy)phenylbenzenes (*o*- and *p*-BCOTPB) [321] as positive resists, *p*-methylcalix[6]arene hexaacetate (MC6AOAc, **80**) [322] and 1,3,5-tris[4-(4-vinylphenylcarbonyloxy)phenyl]benzene (VCTPB) [323] as negative resists, respectively. Resolutions of down to 10 nm may be achieved with these low molecular glasses.

IX. CONCLUSION

In this chapter, we have shown that a lot of synthetic concepts emerged in the past years for glass-forming molecular materials that offer advantages over polymers due to their easier purification and better vacuum processing capabilities. There is a wide range of applications for thin-film devices based on these materials. Here, we focused mainly on the applications based on the interaction with light and electricity, from the emission of light in lasers and light emitting diodes up to the response to light in photovoltaics and photochromic systems. This does not limit the range of applications, however. A huge potential lies in the application of the electrical properties (e.g., for organic transistors [241, 324]) or in the incorporation of magnetic centers into the molecular structure [325]. We expect that in the future the number of molecular glasses and their applications will keep growing.

REFERENCES

1. R. A. Wessling, *J. Polym. Sci., Polym. Symp.* **1985**, 72, 55.
2. M. S. Bayerl, T. Braig, O. Nuyken, D. C. Müller, M. Groß, and K. Meerholz, *Macromol. Rapid Commun.* **1999**, 20, 224.
3. B. Jerome, E. Cecchetto, N. R. de Souza, and A. L. Demirel, *J. Phys. IV* **2000**, 10, 227.

4. A. Huwe, F. Kremer, L. Hartmann, T. Kratzmüller, H. G. Braun, J. Karger, P. Behrens, W. Schwieger, G. Ihlein, O. Weiss, and F. Schuth, *J. Phys. IV* **2000**, 10, 59.
5. M. T. Cohen and D. Turnbull, *J. Chem. Phys.* **1959**, 31, 1164.
6. K. Moriwaki, H. Kusumoto, K. Akamatsu, H. Nakano, and Y. Shiota, *J. Mater. Chem.* **1998**, 8, 2671.
7. J. W. Gibbs and E. A. DiMarzio, *J. Chem. Phys.* **1958**, 28, 373.
8. G. Adam and J. H. Gibbs, *J. Chem. Phys.* **1965**, 43, 139.
9. L.-M. Martinez and C. A. Angell, *Nature (London)* **2001**, 410, 663.
10. S. Sastry, *Nature (London)* **2001**, 409, 164.
11. E. Leutheusser, *Phys. Rev. A* **1984**, 29, 2765.
12. G. P. Johari and M. Goldstein, *J. Chem. Phys.* **1971**, 55, 4245.
13. D. J. Plazek and J. H. Macgill, *J. Chem. Phys.* **1968**, 45, 3038.
14. E. Rössler, *J. Chem. Phys.* **1990**, 92, 3725.
15. C. M. Whitaker and R. McMahon, *J. Phys. Chem.* **1996**, 100, 1081.
16. K. Naito, *Chem. Mater.* **1994**, 6, 2343.
17. E. Rössler and H. Sillescu, in *Materials Science and Technology*, Vol. 9, R. W. Cahn, P. Haasen, and E. J. Kramer, Eds., VCH, Weinheim, Germany, 1991.
18. C. A. Angell, K. L. Ngai, G. B. McKenna, P. F. McMillan, and S. W. Martin, *J. Appl. Phys.* **2000**, 88, 3113.
19. H. Sillescu and D. Ehlich, in *Lasers in Polymer Science and Technology*, Vol III, J. P. Fouassier and J. F. Rabek, Eds., 1990.
20. B. C. Hancock, S. L. Shamblin, and G. Zografis, *Pharm. Res.* **1995**, 12, 799.
21. G. Van den Mooter, P. Augustijns, and R. Kinget, *Eur. J. Pharm. Biopharm.* **1999**, 48, 43.
22. P. Di Martino, G. F. Palmieri, and S. Martelli, *Chem. Pharm. Bull.* **2000**, 48, 1105.
23. I. Alig, D. Braun, R. Langendorf, M. Voigt, and J. H. Wendorff, *J. Non-Cryst. Sol.* **1997**, 221, 261.
24. E. M. Han, L. M. Do, Y. Niidome, and M. Fujihira, *Chem. Lett.* **1994**, 5, 969.
25. C. H. Chen, J. Shi, and C. W. Tang, *Macromol. Symp.* **1997**, 125, 1.
26. F. Steuber, J. Staudigel, M. Stössel, J. Simmerer, A. Winnacker, H. Spreitzer, F. Weisörtel, and J. Salbeck, *Adv. Mater.* **2000**, 12, 130.
27. K. Naito and A. Miura, *J. Phys. Chem.* **1993**, 97, 6240.
28. H. O. Wirth, *Angew. Makromol. Chem.* **1991**, 185/186, 329.
29. D. F. O'Brian, P. E. Burrows, S. R. Forrest, B. E. Koene, D. E. Loy, and M. E. Thompson, *Adv. Mater.* **1998**, 10, 1108.
30. K. A. Higginson, X.-M. Zhang, and F. Papadimitrakopoulos, *Chem. Mater.* **1998**, 10, 1017.
31. C. H. Chen and J. Shi, *J. Coord. Chem. Rev.* **1998**, 171, 161.
32. M. Brinkmann, G. Gadret, M. Muccini, C. Taliani, N. Masciocchi, and A. Sironi, *J. Am. Chem. Soc.* **2000**, 122, 5147.

33. L. S. Sapochak, A. Padmaperuma, N. Washton, F. Endrino, G. T. Schmett, J. Marshall, D. Fogarty, P. E. Burrows, and S. R. Forrest, *J. Am. Chem. Soc.* **2001**, *123*, 6300.
34. K. A. Higginson, B. Yang, and F. Papadimitrakopoulos, *Mater. Res. Soc. Symp. Proc.* **1999**, *561*, 179.
35. J. Kido and Y. Iizumi, *Appl. Phys. Lett.* **1998**, *73*, 2721.
36. F. Toffolo, M. Brinkmann, O. Greco, F. Biscarini, C. Taliani, H. L. Gomes, I. Aiello, and M. Ghedini, *Synth. Met.* **1999**, *101*, 140.
37. Y. Hamada, H. Kanno, T. Sano, H. Fujii, Y. Nishio, H. Takahashi, T. Usuki, and K. Shibata, *Chem. Lett.* **1993**, 905.
38. M. A. Baldo, S. Lamansky, P. E. Burrows, M. E. Thompson, and S. R. Forrest, *Appl. Phys. Lett.* **1999**, *75*, 4.
39. J. Kido, H. Hayase, K. Hongawa, K. Nagai, and K. Okuyama, *Appl. Phys. Lett.* **1994**, *65*, 2124.
40. T. Sano, M. Fujita, T. Fujii, Y. Hamada, K. Shibata, and K. Kuroki, *Jpn. J. Appl. Phys.* **1995**, *34*, 1883.
41. M. R. Robinson, M. B. O'Regan, and G. Bazan, *Chem. Commun.* **2000**, 1645.
42. C. W. Tang and S. A. Van Slyke, *Appl. Phys. Lett.* **1987**, *51*, 913.
43. I. Alig, D. Braun, R. Langendorf, H. O. Wirth, M. Voigt, and J. H. Wendorff, *J. Mater. Chem.* **1998**, *8*, 847.
44. D. Braun and R. Langendorf, *J. Prakt. Chem. Chem. Z.* **1999**, *341*, 128.
45. R. Fink, Y. Heischkel, M. Thelakkat, H.-W. Schmidt, C. Jonda, and M. Hüppauff, *Chem. Mater.* **1998**, *10*, 3620.
46. M. Stolka, J. F. Yanus, and D. M. Pai, *J. Phys. Chem.* **1984**, *88*, 4707.
47. S. A. Van Slyke, C. H. Chen, and C. W. Tang, *Appl. Phys. Lett.* **1996**, *69*, 2160.
48. Y. Shirota, K. Okumoto, and H. Inada, *Synth. Met.* **2000**, *111–112*, 387.
49. H. Tanaka, S. Tokito, Y. Taga, and A. Okada, *J. Chem. Soc., Chem. Commun.* **1996**, *29*, 2175.
50. H. Kanai, S. Ichinosawa, and Y. Sato, *Synth. Met.* **1997**, *91*, 195.
51. J. A. Sinicropi, J. R. Cowdery-Corvan, E. H. Magin, and P. M. Borsenberger, *Proc. SPIE* **1996**, *2850*, 192, 202.
52. T. Fuhrmann and T. Tsutsui, *Chem. Mater.* **1999**, *11*, 2226.
53. T. Noda, I. Imae, N. Noma, and Y. Shirota, *Adv. Mater.* **1997**, *9*, 239.
54. T. Noda, H. Ogawa, N. Noma, and Y. Shirota, *Adv. Mater.* **1997**, *9*, 720.
55. T. Noda, H. Ogawa, N. Noma, and Y. Shirota, *J. Mater. Chem.* **1999**, *9*, 2177.
56. T. Noda and Y. Shirota, *J. Am. Chem. Soc.* **1998**, *120*, 9714.
57. Y. Aso, T. Okai, Y. Kawaguchi, and T. Otsubo, *Chem. Lett.* **2001**, *2001*, 420.
58. G. Barbarella, L. Favaretto, M. Zambianchi, O. Pudova, C. Arbizzani, A. Bongini, and M. Mastragostino, *Adv. Mater.* **1998**, *10*, 551.
59. Y. Hamada, C. Adachi, T. Tsutsui, and S. Saito, *Jpn. J. Appl. Phys.* **1992**, *31*, 1812.
60. J. Bettenhausen, M. Grezcmiel, M. Jandke, and P. Strohriegl, *Synth. Met.* **1997**, *91*, 223.

61. S. Tokito, H. Tanaka, N. Koda, A. Okada, and Y. Taga, *Macromol. Symp.* **1997**, *125*, 181.
62. Y. Sakamoto, T. Suzuki, A. Miura, H. Fujikawa, S. Tokito, and Y. Taga, *J. Am. Chem. Soc.* **2000**, *122*, 1832.
63. S. Heidenhain, Y. Sakamoto, T. Suzuki, A. Miura, H. Fujikawa, T. Mori, S. Tokito, and Y. Taga, *J. Am. Chem. Soc.* **2000**, *122*, 10240.
64. E. Aminaka, T. Tsutsui, and S. Saito, *Jpn. J. Appl. Phys.* **1994**, *33*, 1061.
65. H. Tokailin, H. Higashi, C. Hosokawa, and T. Kusumoto, *Proc. SPIE* **1993**, *1910*, 38.
66. B. E. Koene, D. E. Loy, and M. E. Thompson, *Chem. Mater.* **1998**, *10*, 2235.
67. Y. Shirota, T. Kobata, and N. Noma, *Chem. Lett.* **1989**, 1145.
68. Y. Kuwabara, H. Ogawa, H. Inada, N. Noma, and Y. Shirota, *Adv. Mater.* **1994**, *6*, 677.
69. A. Higuchi, H. Inada, T. Kobata, and Y. Shirota, *Adv. Mater.* **1991**, *3*, 549.
70. J. Bettenhausen and P. Strohhriegl, *Adv. Mater.* **1996**, *8*, 507.
71. H. Kageyama, K. Ohnishi, S. Nomura, and Y. Shirota, *Chem. Phys. Lett.* **1997**, *277*, 137.
72. W. Ishikawa, H. Inada, H. Nakano, and Y. Shirota, *Chem. Lett.* **1991**, 1731.
73. M. Thelakkat and H.-W. Schmidt, *Adv. Mater.* **1998**, *10*, 219.
74. H. Kageyama, K. Itano, W. Ishikawa, and Y. Shirota, *J. Mater. Chem.* **1996**, *6*, 675.
75. T. Ohara, N. Fujii, and Y. Shirota, 76th Annual Meeting of the Chemical Society of Japan, Kanagawa, 1999, prepr. no. 1, p. 372.
76. J. Bettenhausen and P. Strohhriegl, *Macromol. Rapid. Commun.* **1996**, *17*, 623.
77. T. M. Miller, T. X. Neenan, R. Zayas, and H. E. Bair, *J. Am. Chem. Soc.* **1992**, *114*, 1018.
78. H. Inada and Y. Shirota, *J. Mater. Chem.* **1993**, *3*, 319.
79. J. Bettenhausen and P. Strohhriegl, *Adv. Mater.* **1996**, *8*, 507.
80. M. Kinoshita and Y. Shirota, *Chem. Lett.* **2001**, *2001*, 614.
81. K. Kreger, M. Jandke, and P. Strohhriegl, *Synth. Met.* **2001**, *119*, 163.
82. J. Salbeck, N. Yu, J. Bauer, F. Weissörtel, and H. Bestgen, *Synth. Met.* **1997**, *91*, 209.
83. H. Spreitzer, H. Schenk, J. Salbeck, F. Weissörtel, H. Riel, and W. Riess, *Proc. SPIE* **1999**, *3797*, 316.
84. P. Bäuerle, U. Mitschke, E. Mena-Osteritz, M. Sokolowski, D. Müller, M. Groß, and K. Meerholz, *Proc. SPIE* **1998**, *3476*, 32.
85. U. Mitschke and P. Bäuerle, *J. Chem. Soc., Perkin Trans. 1* **2001**, *2001*, 740.
86. F. Wu, E. C. Riesgo, R. Thummel, A. Juris, M. Hissler, A. El-ghayoury, and R. Ziesel, *Tetrahedron Lett.* **1999**, *40*, 7311.
87. J. Salbeck, F. Weissörtel, and J. Bauer, *Macromol. Symp.* **1997**, *125*, 121.
88. J. Salbeck, J. Bauer, and F. Weissörtel, *Polymer Preprints* **1997**, *38*, 349.
89. K.-J. Weinfurter, F. Weissörtel, G. Harmgarth, and J. Salbeck, *Proc. SPIE* **1998**, *3476*, 40.
90. M. R. Shortreed, S. F. Swallen, Z. Y. Shi, W. H. Tan, Z. F. Xu, C. Devadoss, J. S. Moore, and R. Kopelman, *J. Phys. Chem. B* **1997**, *101*, 6318.

91. J. Salbeck, in *Inorganic and Organic Electroluminescence EL96*, R. H. Mauch, H.-E. Gumlich, Eds., Berlin, 1996.
92. D. Braun, C.-C. Keller, M. D. Roth, B. Schartel, M. Voigt, and J. H. Wendorff, *J. Prakt. Chem.* **1997**, 339, 708.
93. S. Wang, W. J. Oldham, Jr., R. A. Hudack, Jr., and G. C. Bazan, *J. Am. Chem. Soc.* **2000** 122, 5695.
94. J. Kido, C. Ontaki, K. Hongawa, K. Okayama, and K. Nagai, *Jpn. J. Appl. Phys.* **1993**, 32, L917.
95. A. Dodabalapur, *Solid State Commun.* **1997**, 102, 259.
96. D. Braun and R. Langendorf, *J. Prakt. Chem.* **2000**, 342, 80.
97. K. Nishimura, T. Kobota, H. Inada, and Y. Shirota, *J. Mater. Chem.* **1991**, 1, 897.
98. N.-X. Hu, S. Xie, Z. D. Popovic, B. Ong, and A.-M. Hor, *Synth. Met.* **2000**, 111–112, 421.
99. F. Würthner, R. Wortmann, R. Matschiner, K. Lukaszuk, K. Meerholz, Y. DeNardin, R. Bittner, C. Bräuchle, and R. Sens, *Angew. Chem. Int. Ed. Engl.* **1997**, 36, 2765.
100. F. Würthner, R. Sens, K.-H. Etzbach, and G. Seybold, *Angew. Chem. Int. Ed. Engl.* **1999**, 38, 1649.
101. F. Würthner, S. Yao, and R. Wortmann, *J. Inf. Recording*, **2000**, 25, 69.
102. Y. Shirota, *J. Mater. Chem.* **2000**, 10, 1.
103. U. Mitschke and P. Bäuerle, *J. Mater. Chem.* **2000**, 10, 1471.
104. J. V. Grazulevicius and P. Strohrriegl, in *Handbook of Advanced Electronic and Photonic Materials*, Vol. 10, H. S. Nalwa, Ed., Academic Press, San Diego, 2000, p. 233.
105. C. Adachi, T. Tsutsui, and S. Saito, *Appl. Phys. Lett.* **1989**, 55, 1489.
106. C. Adachi, T. Tsutsui, and S. Saito, *Appl. Phys. Lett.* **1990**, 56, 799.
107. T. Tsutsui, E. Mainaka, C. P. Lin, and D.-U. Kim, *Philos. Trans. R. Soc. London A* **1997**, 355, 801.
108. N. Johansson, D. A. dos Santos, S. Guo, J. Cornil, M. Fahlman, J. Salbeck, H. Schenk, H. Arwin, J. L. Bredas, and W. R. Salaneck, *J. Chem. Phys.* **1997**, 107, 2542.
109. K. Naito, Y. Watanabe, and S. Egusa, *Jpn. J. Appl. Phys.* **1999**, 38, 2792.
110. A. S. Davydov, *Zh. Eksp. Teor. Fiz.* **1948**, 18, 515.
111. I. B. Berلمان, *Mol. Cryst.* **1968**, 4, 157.
112. U. Brackmann, *Lambdachrome Laser Dyes*, Lambda Physik, Goettingen, 1986.
113. W. Kern, M. Seibel, and H.-O. Wirth, *Makromol. Chem.* **1959**, 29, 164.
114. W. Heitz and R. Ulrich, *Makromol. Chem.* **1966**, 98, 29.
115. P. Galda and M. Rehahn, *Synthesis* **1996**, **1996**, 614.
116. J. Grimme and U. Scherf, *Macromol. Chem. Phys.* **1996**, 197, 2297.
117. K. Müllen and G. Wegner, *Electronic Materials: The Oligomer Approach*, Wiley-VCH, New York, 1998, p. 31.
118. F. Milota, Master Thesis, Wien University, Wien, Austria, 1999.

119. F. Milota, C. Warmuth, A. Tortschanoff, J. Sperling, T. Fuhrmann, J. Salbeck, and H. F. Kauffmann, *Synth. Met.* **2001**, *121*, 1497.
120. J. B. Birks, *Photophysics of Aromatic Molecules*, Wiley-Interscience, London 1970.
121. I. A. Berlman, *Handbook of Fluorescence Spectra of Aromatic Molecules*, Academic Press, New York, 1971.
122. B. Schartel, T. Damerau, and M. Hennecke, *Phys. Chem. Chem. Phys.* **2000**, *2*, 4690.
123. M. Schörner, Master Thesis, Kassel University, Kassel, Germany, 2000.
124. D. Z. Garbuzov, S. R. Forrest, A. G. Tsekoun, P. E. Burrows, V. Bulovic, and M. E. Thompson, *J. Appl. Phys.* **1996**, *80*, 4644.
125. H. Matoussi, H. Murata, C. D. Merritt, Y. Iizumi, J. Kido, and Z. H. Kafafi, *J. Appl. Phys.* **1999**, *86*, 2642.
126. J. Kalinowski, C. Giro, M. Cocchi, V. Fattori, and P. DiMarco, *Appl. Phys. Lett.* **2000**, *76*, 2352.
127. W. Stampor, *Chem. Phys.* **2000**, *256*, 351.
128. H. Ogawa, K. Ohnishi, and Y. Shirota, *Synth. Met.* **1997**, *91*, 243.
129. N. Tamoto, C. Adachi, and K. Nagai, *Chem. Mater.* **1997**, *9*, 1077.
130. C. Hosokawa, H. Higashi, H. Nakamura, and T. Kusumoto, *Appl. Phys. Lett.* **1995**, *67*, 3853.
131. N. J. Turro, *Modern Molecular Photochemistry*, University Science Books, Sausalito, CA, 1991, p. 170.
132. J. H. Burroughes, D. D. C. Bradley, A. R. Brown, R. N. Marks, K. MacKay, R. H. Friend, P. L. Burn, and A. B. Holmes, *Nature (London)* **1990**, *347*, 539.
133. A. Schmidt, M. L. Anderson, D. Dunphy, T. Wehrmeister, K. Müllen, and N. R. Armstrong, *Adv. Mater.* **1995**, *7*, 722.
134. H. Bässler, in: K. Müllen, and G. Wegner, *Electronic Materials: The Oligomer Approach*, Wiley-VCH, New York, 1998, p. 416.
135. V. Choong, Y. Park, Y. Gao, T. Wehrmeister, K. Müllen, B. R. Hsieh, and C. W. Tang, *Appl. Phys. Lett.* **1996**, *69*, 1492.
136. M. Brinkmann, G. Gadret, M. Muccini, C. Taliani, N. Masciocchi, and A. Sironi, *J. Am. Chem. Soc.* **2000**, *122*, 5147.
137. G. P. Kushto, Y. Iizumi, J. Kido, and Z. H. Kafafi, *J. Phys. Chem.* **2000**, *104*, 3670.
138. D. Z. Garbuzov, V. Bulovic, P. E. Burrows, and S. R. Forrest, *Chem. Phys. Lett.* **1996**, *249*, 433.
139. H. Murata, C. D. Merritt, H. Matoussi, and Z. H. Kafafi, *Proc. SPIE* **1998**, *3476*, 88.
140. Y. Hamada, T. Sano, M. Fujita, T. Fujii, Y. Nishio, and K. Shibata, *Chem. Lett.* **1993**, 905.
141. Y. Sakon and M. Ohta, *IEICE Tech. Rep. OME92*, Tokyo 1992.
142. J. M. Lupton, I. D. W. Samuel, R. Bevington, P. L. Burn, and H. Bässler, *Adv. Mater.* **2001**, *13*, 258.

143. C. van Pham, A. Burckhardt, R. Shabana, D. D. Cunningham, H. B. Mark., Jr., and H. Zimmer, *Phosphorus Sulfur Silicon Relat. Elem.* **1989**, *46*, 153.
144. R. S. Becker, J. S. de Melo, A. L. Macanita, and F. Elisei, *Pure Appl. Chem.* **1995**, *67*, 9.
145. Y. Shirota, M. Kinoshita, T. Noda, K. Okumoto, and T. Ohara, *J. Am. Chem. Soc.* **2000**, *122*, 11021.
146. Y. Aso, T. Okai, Y. Kawaguchi, and T. Otsubo, *Proceedings of the 10th International Workshop on Inorganic and Organic Electroluminescence*, Hamamatsu, Japan, 2000, p. 269.
147. G. Barbarella, L. Favaretto, G. Sotgiu, M. Zambianchi, A. Bongini, C. Arbizzani, M. Mastragostino, M. Anni, G. Gigli, and R. Cingolani, *J. Am. Chem. Soc.* **2000**, *122*, 11971.
148. T. Wakimoto, Y. Yonemoto, J. Futaki, M. Tsuchida, R. Murayama, H. Nakada, H. Matsumoto, S. Yamamura, and M. Nomura, *Synth. Met.* **1997**, *91*, 15.
149. C. H. Chen, C. W. Tang, J. Shi, and K. P. Klubek, *Thin Solid Films* **2000**, *363*, 327.
150. Y. Hamada, H. Kanno, T. Tsujioka, and H. Takahashi, *Appl. Phys. Lett.* **1999**, *75*, 1682.
151. T. Virgilli, D. G. Lidzey, and D. D. C. Bradley, *Adv. Mater.* **2000**, *12*, 58.
152. Z. Y. Lu, M. G. Xie, N. Liu, Q. Jiang, L. Z. Li, L. Liu, and W. L. Li, *Synth. Met.* **1997**, *91*, 233.
153. X. T. Tao, S. Miyata, H. Sasabe, G. J. Zhang, T. Wada, and M. H. Jiang, *Appl. Phys. Lett.* **2001**, *78*, 279.
154. M. Mitsuya, T. Suzuki, T. Koyama, H. Shirai, Y. Taniguchi, M. Satsuki, and S. Suga, *Appl. Phys. Lett.* **2000**, *77*, 3272.
155. Y. Sakakibara, S. Okutsu, T. Enokida, and T. Tani, *Thin Solid Films* **2000**, *363*, 29.
156. L. C. Picciolo, H. Murata, and Z. H. Kafafi, *Appl. Phys. Lett.* **2001**, *78*, 2378.
157. H. Suzuki, *Appl. Phys. Lett.* **2000**, *76*, 1543.
158. L. H. Sloof, A. Polman, F. Cacialli, R. H. Friend, G. A. Hebbink, F. C. J. M. van Veggel, and D. N. Reinhoudt, *Appl. Phys. Lett.* **2001**, *78*, 2122.
159. M. Wohlgenannt, K. Tandon, S. Mazumdar, S. Ramasesha, and Z. V. Vardeny, *Nature (London)* **2001**, *409*, 494.
160. M. A. Baldo, D. F. O'Brien, M. E. Thompson, and S. R. Forrest, *Phys. Rev. B*, **1999**, *14422*.
161. M. A. Baldo, M. E. Thompson, and S. R. Forrest, *Pure Appl. Chem.* **1999**, *71*, 2095.
162. J. Kido, K. Nagai, Y. Okamoto, and T. Skotheim, *Chem. Lett.* **1991**, *1991*, 1267.
163. G. A. Crosby, R. E. Whan, and R. M. Alire, *J. Chem. Phys.* **1961**, *34*, 743.
164. M. A. Baldo, D. F. O'Brien, Y. You, A. Shoustikov, S. Sibley, M. E. Thompson, and S. R. Forrest, *Nature (London)* **1998**, *395*, 151.
165. C. Adachi, M. A. Baldo, S. R. Forrest, S. Lamansky, M. E. Thompson, and R. C. Kwong, *Appl. Phys. Lett.* **2001**, *78*, 1622.
166. A. Higuchi and Y. Shirota, *Mol. Cryst. Liq. Cryst. Sect. A* **1994**, *242*, 127.
167. S. Blumstengel, F. Meinardi, R. Tubino, M. Gurioli, M. Jandke, and P. Strohriegel, *J. Chem. Phys.* **2001**, *115*, 3249.

168. S. Blumstengel, E. Colabella, A. Borghesi, R. Tubino, M. Jandke, and P. Strohriegl, *Synth. Met.* **2001**, *121*, 1711.
169. J. Kido, M. Kimura, and K. Nagai, *Science* **1995**, *267*, 1332.
170. J. Kido, W. Ikeda, M. Kimura, and K. Nagai, *Jpn. J. Appl. Phys. Part 2*, **1996**, *35*, L394.
171. R. S. Deshpande, V. Bulovic, and S. R. Forrest, *Appl. Phys. Lett.* **1999**, *75*, 888.
172. Z. Y. Xie, J. S. Huang, C. N. Li, S. Y. Liu, Y. Wang, Y. Q. Li, and J. C. Shen, *Appl. Phys. Lett.* **1999**, *74*, 641.
173. J. Thompson, R. I. Blyth, M. Mazzeo, M. Anni, G. Gigli, and R. Cingolani, *Appl. Phys. Lett.* **2001**, *79*, 560.
174. J. Feng, F. Li, W. Gao, S. Liu, Y. Liu, and Y. Wang, *Appl. Phys. Lett.* **2001**, *78*, 3947.
175. Y. Hamada, T. Sano, H. Fujii, Y. Nishio, H. Takahashi, and K. Shibata, *Jpn. J. Appl. Phys. Part 2*, **1996**, *35*, L1339.
176. S. H. Chen, D. Katsis, A. W. Schmid, J. C. Mastrangelo, T. Tsutsui, and T. N. Blanton, *Nature (London)* **1999**, *397*, 506.
177. F. Hide, M. Diaz-Garcia, B. Schwartz, M. Andersson, Q. Pei, and A. Heeger, *Science* **1996**, *273*, 1833.
178. N. Tessler, D. J. Denton, and R. H. Friend, *Nature (London)* **1996**, *382*, 695.
179. J. H. Schön, C. Kloc, A. Dodabalapur, and B. Batlogg, *Science* **2000**, *289*, 599.
180. See, for example, P. Yeh, *Optical Waves in Layered Media*, John Wiley & Sons, Inc., New York, 1988.
181. See, for example, A. Yariv, *Quantum electronics*, John Wiley & Sons, Inc., New York, 1988.
182. N. Johansson, J. Salbeck, J. Bauer, F. Weissörtel, P. Broems, A. Andersson, and W. R. Salaneck, *Adv. Mater.* **1998**, *10*, 1136.
183. M. D. McGehee, R. Gupta, S. Veenstra, E. K. Miller, M. A. Diaz-Garcia, and A. J. Heeger, *Phys. Rev. B*, **1998**, *58*, 7035.
184. J. Salbeck, M. Schörner, and T. Fuhrmann, *Thin Solid Films*, in press.
185. W. Holzer, A. Penzkofer, and H. H. Hörhold, *Synthetic Metals* **2000**, *113*, 281.
186. M. Anni, G. Gigli, R. Cingolani, M. Zavelani-Rossi, C. Gadermaier, G. Lanzani, G. Barbarella, and L. Favaretto, *Appl. Phys. Lett.* **2001**, *78*, 2679.
187. K. P. Kretsch, C. Belton, S. Lipson, W. J. Blau, F. Z. Henari, H. Rost, S. Pfeiffer, A. Teuschel, H. Tillmann, and H.-H. Hörhold, *J. Appl. Phys.* **1999**, *86*, 6155.
188. M. Berggren, A. Dodabalapur, R. E. Slusher, and Z. Bao, *Nature (London)* **1997**, *389*, 466.
189. M. Berggren, A. Dodabalapur, and R. E. Slusher, *Appl. Phys. Lett.* **1997**, *2230*.
190. V. G. Kozlov, V. Bulovic, P. E. Burrows, and S. R. Forrest, *Nature (London)* **1997**, *389*, 362.
191. M. Berggren, A. Dodabalapur, R. E. Slusher, and Z. Bao, *Synth. Met.* **1997**, *91*, 65.
192. H. Kogelnik and C. V. Shank, *J. Appl. Phys.* **1972**, *43*, 2327.
193. H. Kogelnik and C. V. Shank, *Appl. Phys. Lett.* **1971**, *18*, 152.

194. M. Berggren, A. Dodabalapur, R. E. Slusher, A. Timko, and O. Nalamasu, *Appl. Phys. Lett.* **1998**, *72*, 410.
195. S. Riechel, U. Lemmer, T. Benstem, W. Kowalsky, U. Scherf, A. Gombert, and V. Wittwer, *Appl. Phys. B.* **2000**, *71*, 897.
196. S. Riechel, U. Lemmer, J. Feldmann, S. Berleb, A. G. Muckl, W. Brütting, A. Gombert, and V. Wittwer, *Opt. Lett.* **2001**, *26*, 595.
197. K. P. Kretsch, W. J. Blau, V. Dumarcher, L. Rocha, C. Fiorini, J.-M. Nunzi, S. Pfeiffer, H. Tillmann, and H.-H. Hörhold, *Appl. Phys. Lett.* **2000**, *76*, 2149.
198. M. Meier, A. Mekis, A. Dodabalapur, A. Timko, R. E. Slusher, J. D. Joannopoulos, and O. Nalamasu, *Appl. Phys. Lett.* **1999**, *74*, 7.
199. M. Meier, A. Dodabalapur, J. A. Rogers, R. E. Slusher, A. Mekis, A. Timko, C. A. Murray, R. Ruel, and O. Nalamasu, *J. Appl. Phys.* **1999**, *86*, 3502.
200. T. Tsutsui, C. Adachi, S. Saito, M. Watanabe, and M. Koishi, *Chem. Phys. Lett.* **1991**, *182*, 143.
201. N. Takada, T. Tsutsui, and S. Saito, *Appl. Phys. Lett.* **1993**, *63*, 2032.
202. T. Tsutsui, N. Takada, and S. Saito, *Appl. Phys. Lett.* **1994**, *65*, 1868.
203. T. Nakayama, Y. Itoh, and A. Kakuta, *Appl. Phys. Lett.* **1993**, *63*, 594.
204. A. Dodabalapur, L. J. Rothberg, and T. M. Miller, *Appl. Phys. Lett.* **1994**, *65*, 2308.
205. N. C. Greenham, R. H. Friend, and D. D. C. Bradley, *Adv. Mater.* **1994**, *6*, 491.
206. S. Tokito, K. Noda, and Y. Taga, *Appl. Phys. Lett.* **1996**, *68*, 2633.
207. S. Tokito, Y. Taga, and T. Tsutsui, *Synth. Met.* **1997**, *91*, 49.
208. S. Dirr, S. Wiese, H.-H. Johannes, D. Ammermann, A. Böhler, W. Grahn, and W. Kowalsky, *Synth. Met.* **1997**, *91*, 53.
209. S. Tokito, T. Tsutsui, and Y. Taga, *J. Appl. Phys.* **1999**, *86*, 2407.
210. V. G. Kozlov, V. Bulovic, P. E. Burrows, M. Baldo, V. B. Khalfin, G. Parthasarathy, S. R. Forrest, Y. You, and M. E. Thompson, *J. Appl. Phys.* **1998**, *84*, 4096.
211. D. G. Lidzey, D. D. C. Bradley, M. S. Skolnick, T. Virgill, S. Walker, and D. M. Whittaker, *Nature (London)* **1998**, *395*, 53.
212. N. M. Lawandy, R. M. Balachandran, A. S. L. Gomes, and E. Sauvain, *Nature (London)* **1994**, *368*, 436.
213. S. V. Frolov, Z. V. Vardeny, K. Yoshino, A. Zahidov, and R. H. Baughman, *Phys. Rev. B* **1999**, *59*, R5284.
214. U. Lemmer, A. Haugeneder, C. Kallinger, and J. Feldmann, in *Semiconducting Polymers. Chemistry, Physics and Engineering*, G. Hadziioannou and P. F. van Hutten, Eds., Wiley-VCH, Weinheim, Germany, 2000, pp. 309–332.
215. G. Kranzelbinder and G. Leising, *Rep. Prog. Phys.* **2000**, *63*, 729.
216. N. Tessler, *Adv. Mater.* **1999**, *11*, 363.
217. See, for example, J. Salbeck, *Ber. Bunsenges. Phys. Chem.* **1996**, *100*, 1667.
218. See, for example, J. C. Scott and G. C. Malliaras, in *Semiconducting Polymers*, G. Hadziioannou and P. F. van Hutten, Eds., Wiley-VCH, Weinheim, Germany, 2000, pp. 411–462.

219. L. S. Hung, C. W. Tang, and M. G. Mason, *Appl. Phys. Lett.* **1997**, *71*, 1762.
220. S. E. Shaheen, G. E. Jabbour, M. M. Morrell, Y. Kawabe, B. Kippelen, N. Peyghambarian, M. F. Nabor, R. Schlaf, E. A. Mash, and N. R. Armstrong, *J. Appl. Phys.* **1998**, *84*, 2324.
221. T. M. Brown, R. H. Friend, I. S. Millard, D. J. Lacey, J. H. Burroughes, and F. Cacialli, *Appl. Phys. Lett.* **2000**, *77*, 3096.
222. K. Furukawa, Y. Terasaka, H. Ueda, and M. Matsumura, *Synth. Met.* **1997**, *91*, 99.
223. F. Nuesch, E. W. Forsythe, Q. T. Lee, Y. Gao, and L. J. Rothberg, *J. Appl. Phys.* **2000**, *87*, 7973.
224. S. A. Carter and M. Angelopoulos, *Appl. Phys. Lett.* **1997**, *70*, 2067.
225. E. Aminaka, T. Tsutsui, and S. Saito, *J. Appl. Phys.* **1996**, *79*, 8808.
226. J. Heinze, *Angew. Chem.* **1984**, *96*, 823.
227. H. Ishii, K. Sugiyama, E. Ito, and K. Seki, *Adv. Mater.* **1999**, *11*, 605.
228. A. J. Bard and L. R. Faulkner, *Electrochemical Methods, Fundamentals and Applications*, 2nd ed., John Wiley & Sons, Inc., New York, 2001.
229. J. Pommerehne, H. Westweber, W. Guss, R. F. Mahrt, H. Bässler, M. Porsch, J. Daub, *Adv. Mater.* **1995**, *7*, 551.
230. H. Fujikawa and S. Tokito, Y. Taga, *Synth. Met.* **1997**, *91*, 161.
231. J. D. Anderson, E. M. McDonald, P. A. Lee, M. L. Anderson, E. L. Ritchie, H. K. Hall, T. Hopkins, E. A. Mash, J. Wang, A. Padias, S. Thayumanavan, S. Barlow, S. R. Marder, G. E. Jabbour, S. Shaheen, B. Kippelen, N. Peyghambarian, R. M. Whightman, and N. R. Armstrong, *J. Am. Chem. Soc.* **1998**, *120*, 9646.
232. J. Uebe and J. Salbeck, unpublished.
233. H. Ishii, T. Imai, E. Morikawa, E. Ito, S. Hasegawa, K. Okudaira, N. Ueno, Y. Shirota, and K. Seki, *Proc. SPIE* **1999**, *3797*, 375.
234. F. Weissörtel, Ph.D. Thesis, Regensburg University, Regensburg, Germany, 1999.
235. S. T. Lee, X. Y. Hou, M. G. Mason, and C. W. Tang, *Appl. Phys. Lett.* **1998**, *72*, 1593.
236. Y. Hamada, T. Sano, M. Fujita, T. Fujii, Y. Nishio, and K. Shibata, *Jpn. J. Appl. Phys. Part 1* **1993**, *32*, 2514.
237. H. Aziz, Z. D. Popovic, N. X. Hu, A. M. Hor, and G. Xu, *Science* **1999**, *283*, 1900.
238. J. Uebe and J. Salbeck, unpublished.
239. K. Naito, M. Sakurai, and S. Egusa, *J. Phys. Chem. A* **1997**, *101*, 2350.
240. K. Meerholz, H. Gregorius, K. Müllen, and J. Heinze, *Adv. Mater.* **1994**, *6*, 671.
241. G. Horowitz, in *Semiconducting Polymers. Chemistry, Physics and Engineering*, G. Hadziioannou and P. F. van Hutten, Eds., Wiley-VCH, Weinheim, Germany, 2000, pp. 463–514.
242. S. F. Nelson, Y.-Y. Lin, J. Gundlach, and T. N. Jackson, *Appl. Phys. Lett.* **1998**, *72*, 1854.
243. J. H. Schön, S. Berg, C. Kloc, and B. Batlogg, *Science* **2000**, *287*, 1022.
244. H. E. Katz, A. J. Lovinger, J. Johnson, C. Kloc, T. Siegrist, W. Li, Y.-Y. Lin, and A. Dodabalapur, *Nature (London)* **2000**, *404*, 478.

245. D. Adam, P. Schumacher, J. Simmerer, L. Häußling, K. Siemensmeyer, K.-H. Etzbach, H. Ringsdorf, and D. Haarer, *Nature (London)* **1994**, 371, 141.
246. H. Bässler, *Phys. Stat. Sol. B* **1993**, 175, 15.
247. J. S. Facci and M. Stolka, *Philos. Mag. B* **1986**, 54, 1.
248. J. Stephan, S. Schrader, and L. Brehmer, *Synth. Met.* **2000**, 111, 353.
249. A. R. Brown, C. P. Jarrett, D. M. de Leeuw, and M. Matters, *Synth. Met.* **1997**, 88, 37.
250. P. M. Borsenberger and D. S. Weiss, *Organic Photoreceptors for Imaging Systems*, Marcel Dekker, New York, 1993.
251. S. Heun and P. M. Borsenberger, *Chem. Phys.* **1995**, 200, 245.
252. P. M. Borsenberger, E. H. Magin, and J. Shi, *Physica B* **1996**, 217, 212.
253. Z. B. Deng, S. T. Lee, D. P. Webb, Y. C. Chan, and W. A. Gambling, *Synth. Met.* **1999**, 107, 107.
254. S. Naka, H. Okada, H. Onnagawa, Y. Yamaguchi, and T. Tsutsui, *Synth. Met.* **2000**, 111, 331.
255. U. Bach, K. De Cloedt, H. Spreitzer, and M. Grätzel, *Adv. Mater.* **2000**, 12, 1060.
256. P. M. Borsenberger, W. T. Grünbaum, and E. H. Magin, *Physica B*, **1996**, 226.
257. K. Okumoto, K. Wayaku, T. Noda, H. Kageyama, and Y. Shirota, *Synth. Met.* **2000**, 111, 473.
258. J. A. Sinicropi, J. R. Cowdery-Corvan, E. H. Magin, and P. M. Borsenberger, *Chem. Phys.* **1997**, 218, 331.
259. S. Nomura, K. Nishimura, and Y. Shirota, *Thin Solid Films* **1996**, 273, 27.
260. R. H. Young and J. J. Fitzgerald, *J. Phys. Chem.* **1995**, 99, 4230.
261. R. G. Kepler, P. M. Beeson, S. J. Jacobs, R. A. Anderson, M. B. Sinclair, V. S. Valencia, and P. A. Cahill, *Appl. Phys. Lett.* **1995**, 66, 3618.
262. H. Tokuhisa, M. Era, T. Tsutsui, and S. Saito, *Appl. Phys. Lett.* **1995**, 66, 3433.
263. J. Bettenhausen, P. Strohrriegl, W. Bruetting, H. Tokuhisa, and T. Tsutsui, *J. Appl. Phys.* **1997**, 82, 4957.
264. M. Redecker, D. D. C. Bradley, M. Jandke, and P. Strohrriegl, *Appl. Phys. Lett.* **1999**, 75, 109.
265. E. H. Magin and P. M. Borsenberger, *J. Appl. Phys.* **1993**, 73, 787.
266. S. Naka, H. Okada, and H. Onnagawa, *Appl. Phys. Lett.* **2000**, 76, 197.
267. B. J. Murray, J. E. Kaeding, W. T. Gruenbaum, and P. M. Borsenberger, *Jpn. J. Appl. Phys. Part 1* **1996**, 35, 5384.
268. V. Choong, S. Shi, J. Curless, C. Shieh, H.-C. Lee, J. Shen, and J. Yang, *Appl. Phys. Lett.* **1999**, 75, 172.
269. X. Zhou, J. Blochwitz, M. Pfeiffer, A. Nollau, T. Fritz, and K. Leo, *Adv. Funct. Mater.* **2001**, 11, 310.
270. B. O'Regan and M. Grätzel, *Nature (London)* **1991**, 353, 737.
271. J. Hagen, W. Schaffrath, P. Otschik, R. Fink, A. Bacher, H. W. Schmidt, and D. Haarer, *Synth. Met.* **1997**, 89, 215.

272. U. Bach, D. Lupo, J. E. Moser, F. Weissörtel, J. Salbeck, H. Spreitzer, and M. Grätzel, *Nature (London)* **1998**, *393*, 583.
273. M. Thelakkat, J. Hagen, D. Haarer, and H.-W. Schmidt, *Synth. Met.* **1999**, *102*, 1125.
274. C. W. Tang, *Appl. Phys. Lett.* **1986**, *48*, 183.
275. H. R. Kerp and E. E. van Faassen, *Phys. Chem. Chem. Phys.* **1999**, *1*, 1761.
276. P. Peumans, V. Bulovic, and S. R. Forrest, *Appl. Phys. Lett.* **2000**, *76*, 2650.
277. K. Takahashi, N. Kuraya, T. Yamaguchi, T. Komura, and K. Murata, *Solar Energy Materials Solar Cells* **2000**, *61*, 403.
278. K. Petritsch, R. H. Friend, A. Lux, G. Rozenberg, S. C. Moratti, and A. B. Holmes, *Synth. Met.* **1999**, *102*, 1776.
279. L. Schmidt-Mende, A. Fechtenkotter, K. Müllen, E. Moons, R. H. Friend, and J. D. MacKenzie, *Science* **2001**, *293*, 1119.
280. M. Kinoshita, N. Fujii, T. Tsuzuki, and Y. Shirota, *Synth. Met.* **2001**, *121*, 1571.
281. J.-F. Nierengarten, J.-F. Eckert, J.-F. Nicoud, L. Ouali, V. Krasnikov, and G. Hadziioannou, *Chem. Commun.* **1999**, *1999*, 617.
282. J.-F. Eckert, J.-F. Nicoud, J.-F. Nierengarten, S.-G. Liu, L. Echegoyen, F. Barigelletti, N. Armadori, L. Ouali, V. Krasnikov, and G. Hadziioannou, *J. Am. Chem. Soc.* **2000**, *122*, 7467.
283. B. L. Feringa, W. F. Jager, and B. de Lange, *Tetrahedron* **1993**, *49*, 8267.
284. H. Rau in *Photochemistry and Photophysics*, Vol. 2, J. F. Rabek, Ed., CRC press, Boca Raton, FL, 1988, pp. 119–141.
285. H. Meier, *Angew. Chem.* **1992**, *104*, 1425.
286. M. Irie, *Chem. Rev.* **2000**, *100*, 1685.
287. G. Berkovic, V. Krongauz, and V. Weiss, *Chem. Rev.* **2000**, *100*, 1741.
288. Y. Yokoyama, *Chem. Rev.* **2000**, *100*, 1717.
289. J. Achatz, C. Fischer, J. Salbeck, and J. Daub, *J. Chem. Soc. Chem. Commun.* **1991**, *1991*, 504.
290. H. Dürr, *Angew. Chem.* *101*, 427 (1989).
291. J. Salbeck, V. N. Komissarov, V. I. Minkin, and J. Daub, *Angew. Chem.* **1992**, *104*, 1498.
292. T. Kawai, N. Fukuda, D. Groeschl, S. Kobatake, and M. Irie, *Jpn. J. Appl. Phys.* **1999**, *38*, L1194.
293. H. Utsumi, D. Nagahama, H. Nakano, and Y. Shirota, *J. Mater. Chem.* **2000**, *10*, 2436.
294. M. Fukudome, K. Kamiyama, T. Kawai, and M. Irie, *Chem. Lett.* **2001**, *2001*, 70.
295. Y. Shirota, K. Moriwaki, S. Yoshikawa, T. Ujike, and H. Nakano, *J. Mater. Chem.* **1998**, *8*, 2579.
296. T. Ujike, K. Moriwaki, H. Nakano, and Y. Shirota, *J. Photopolym. Sci. Technol.* **1998**, *11*, 33.
297. A. Honma, T. Kanbara, and K. Hasegawa, *Mol. Cryst. Liq. Cryst. Sci. Technol. Sect. A* **2000**, *345*, 449.

298. J. Michl and E. W. Thulstrup, *Spectroscopy with Polarized Light*, VCH, New York, 1986.
299. T. Fuhrmann, M. Kunze, and J. H. Wendorff, *Macromol. Theory Simul.* **1998**, 7, 421.
300. L. Nikolova and T. Todorov, *Opt. Acta* **1984**, 31, 579.
301. P. Rochon, E. Batalla, and A. Natansohn, *Appl. Phys. Lett.* **1995**, 66, 136.
302. D. Y. Kim, L. Li, J. Kumar, and S. K. Tripathy, *Appl. Phys. Lett.* **1995**, 66, 1166.
303. P. S. Ramanujam, N. C. R. Holme, and S. Hvilsted, *Appl. Phys. Lett.* **1996**, 68, 1329.
304. M. Eich, J. H. Wendorff, B. Reck, and H. Ringsdorf, *Macromol. Chem. Rapid. Commun.* **1987**, 8, 59.
305. A. Natansohn, P. Rochon, J. Gosselin, and S. Xie, *Macromolecules* **1992**, 25, 2268.
306. Courtesy of A. Perschke, Duisburg University.
307. A. Perschke and T. Fuhrmann, *Adv. Mater.* **2002**, 14, 841.
308. K. Naito, *Mol. Cryst. Liq. Cryst.* **1996**, 276, A113.
309. K. Meerholz, *Angew. Chem.* **1997**, 109, 981.
310. P. M. Lundquist, R. Wortmann, C. Geletneky, R. J. Twieg, M. Jurich, V. Y. Lee, C. R. Moylan, and D. M. Burland, *Science* **1996**, 274, 1182.
311. C. Hohle, U. Hofmann, S. Schloter, M. Thelakkat, P. Strohrig, D. Haarer, and S. J. Zilker, *J. Mater. Chem.* **1999**, 9, 2205.
312. C. Hohle, M. Jandke, S. Schloter, N. Koch, R. Resel, D. Haarer, and P. Strohrig, *Synth. Met.* **1999**, 102, 1535.
313. M. Thelakkat, C. Schmitz, C. Hohle, P. Strohrig, H.-W. Schmidt, U. Hofmann, S. Schloter, and D. Haarer, *Phys. Chem. Chem. Phys.* **1999**, 1, 1693.
314. S. Schloter, A. Schreiber, M. Grasmuck, A. Leopold, M. Kol'chenko, J. Pan, C. Hohle, P. Strohrig, S. J. Zilker, and D. Haarer, *Appl. Phys. B.* **1999**, 68, 899.
315. K. Ogino, S.-H. Park, and H. Sato, *Appl. Phys. Lett.* **1999**, 74, 3936.
316. W. J. Li, A. Gharavi, Q. Wang, and L. P. Yu, *Adv. Mater.* **1998**, 10, 927.
317. L. Wang, Y. Zhang, T. Wada, and H. Sasabe, *Appl. Phys. Lett.* **1996**, 69, 728.
318. Y. Zhang, L. Wang, T. Wada, and H. Sasabe, *Appl. Phys. Lett.* **1997**, 70, 2949.
319. F. Würthner, S. Yao, J. Schilling, R. Wortmann, M. Redi-Abshiro, E. Mecher, F. Gallego-Gomez, and K. Meerholz, *J. Am. Chem. Soc.* **2001**, 123, 2810.
320. M. Yotoshiiwa, H. Kageyama, Y. Shirota, F. Wakaya, K. Gamo, and M. Takai, *Appl. Phys. Lett.* **1996**, 69, 2605.
321. T. Kadota, H. Kageyama, F. Wakaya, K. Gamo, and Y. Shirota, *J. Photopolym. Sci. Technol.* **1999**, 12, 375.
322. J. Fujita, Y. Ohnishi, Y. Ochiai, and S. Matsui, *Appl. Phys. Lett.* **1996**, 68, 1297.
323. T. Kadota, H. Kageyama, F. Wakaya, K. Gamo, and Y. Shirota, *J. Photopolym. Sci. Technol.* **1998**, 11, 147.
324. Z. Bao, *Adv. Mater.* **2000**, 12, 227.
325. O. Kahn, *Molecular Magnetism*, VCH, New York, 1993.

INDEX

- Absorption properties, molecular glasses,
112–123
doped systems, color conversion, 117–120
fluorescent emitters, blue to red, 112–117
phosphorescent emitters, 120–121
polarized light creation, 123
white light creation, 121–123
- Acceptor-heads, molecular dyes in zeolite L
channels, 24–26
- Alkyl bridges, molecular glass structure, twin
molecules, 94–99
- Alq₃ (tris(i-quinolinolato)aluminium)
amplified spontaneous emission and lasing
gain narrowing and organic waveguides,
125–126
laser resonators, 126–131
charge transport of molecular glasses, electron
mobilities, 141
color conversion, molecular glasses, yellow/
red dopants, 118–120
molecular glasses, fluorescence quantum
yield, 116
molecular glass structure, chelate complexes,
93–94
organic light emitting diode (OLED) structure,
electron injection, 136–138
- Amplified spontaneous emission (ASE),
molecular glasses, 123–131
gain narrowing, organic waveguides,
123–126
laser resonators, 126–131
- Antenna systems
supramolecularly organized luminescent dye
molecules, energy transfer mechanisms,
3–4
three-dye antenna, 18–24
- Arrhenius behavior
benzophenone-*N,N*-dimethylaniline proton-
transfer reactions (Bp::DMA),
semiclassical/quantum model
comparisons, 68–71
molecular glass structure, 90–93
- Arylaldehyde, molecular glasses, 109, 111
- Arylamines
charge transport of molecular glasses, hole
mobilities, 140–141
molecular glasses, fluorescence quantum
yield, 115
- Arylketone hydrazone, molecular glasses, 109,
111
- Avogadro's number
Förster electronic excitation energy transfer,
dye molecules in zeolite L channels, 28–36
radiationless energy transfer, visual
experiments, 40–42
- Axial trapping, molecular dyes in zeolite L
channels, Förster electronic excitation
energy transfer, 35–36
- Azo dyes
molecular glass structure, free volume theory,
89–93
photochromic properties, molecular glasses,
optoelectronic applications, reorientation
and surface gratings, 146–148

- Benzene centers, starburst glass molecule structure, 100–104
- Benzophenone-*N,N*-dimethylaniline proton-transfer reactions (Bp::DMA)
- Borgis–Hynes (BH) model, 65–66
 - transfer kinetics, 72–74
 - classical model, 59–60
 - N,N*-dimethylaniline photoreduction of benzophenone, 53–58
 - Dogonadze, Kuznetsov, and Levich (DKL) model, 62–65
 - energetics, 71
 - kinetics, 71–72
 - Lee–Hynes model, 66–67
 - transfer kinetics, 74–78
 - research background, 52–53
 - semiclassical model, 61
 - semiclassical/quantum model comparisons, 67–71
 - tunneling mechanisms, 61–62
- Biphenyl bonds, molecular glass structure, twin molecules, 95–99
- Bipolar molecular glasses, organic light emitting diode (OLED) structure, 138–139
- Blue/green dopants, color conversion, molecular glasses, 118
- Boltzmann constant, benzophenone-*N,N*-dimethylaniline proton-transfer reactions (Bp::DMA), Dogonadze, Kuznetsov, and Levich (DKL) model, 65
- Bond stretching, benzophenone-*N,N*-dimethylaniline proton-transfer reactions (Bp::DMA), Lee–Hynes (LH) model kinetics, 74–78
- Borgis–Hynes (BH) model, benzophenone-*N,N*-dimethylaniline proton-transfer reactions (Bp::DMA), 65–66
 - kinetics, 72–74
 - semiclassical/quantum model comparisons, 69–71
- Bravais lattice, molecular dyes in zeolite L channels, 10–12
- Calorimetric curves, low-molecular glass, 87–93
- C axis alignment, molecular dyes, 7
- CBP, phosphorescent emission, molecular glasses, 121
- Channel distances, molecular dyes in zeolite L channels, 11–12
- Channel-to-site ratio, molecular dyes in zeolite L channels, 14
- Charge injection properties, organic light emitting diode (OLED) structure, 133–138
- Charge transfer donor-acceptor sites, molecular glasses, light to current applications, heterojunction solar cells, 144
- Charge transport, molecular glasses, 138, 140–141
- Chelate complexes, molecular glass structure, 93–94
- Chromophores
 - molecular glasses, optoelectronic applications, photorefractivity, 151–152
 - spiro molecules, 103–106
- Coat trapping, molecular dyes in zeolite L channels, Förster electronic excitation energy transfer, 35–36
- Color conversion, doped systems, molecular glasses, 117–120
 - blue/green dopants, 118
 - yellow/red dopants, 118–120
- Contact radical ion pair (CRIP), benzophenone-*N,N*-dimethylaniline proton-transfer reactions (Bp::DMA), 55–58
- Coulombic interaction, dye molecules in zeolite L channels, radiationless energy transfer, 27–28
- Coumarines, color conversion, molecular glasses, 118
- C_3 symmetry, starburst glass molecule structure, 100–103
- Cyanine dyes, color conversion, molecular glasses, 120
- Cyclovoltammetric measurements, organic light emitting diode (OLED) structure, redox potential and charge injection properties, 134–138
- Cylinder morphology, molecular dyes in zeolite L channels, 8–12
 - Förster electronic excitation energy transfer, 31–32
- Davydov rule, molecular glasses, fluorescence quantum yield, oligophenyls, 113–115
- DCM (4-dicyanomethylene-2-methyl-6-(*p*-dimethylaminostyryl)-4*H*-pyran)

- amplified spontaneous emission and lasing
 - gain narrowing and organic waveguides, 125–126
 - laser resonators, 126–131
 - color conversion, molecular glasses, 118–120
- Decay pathways, benzophenone-*N,N*-dimethylaniline proton-transfer reactions (Bp::DMA), 57–58
- Dendrimer-like molecules, spiro structure, 106
- Densely packed molecules, dye molecules in zeolite L channels, Förster electronic excitation energy transfer, 30–32
- Dicyanomethylene dyes, color conversion, molecular glasses, 118–120
- Dihydropyridines, molecular glasses, optoelectronic applications, photorefractivity, 150–152
- Dimeric twin molecules, molecular glass structure, 94–99
- N,N*-Dimethylaniline (DMA), benzophenone proton-transfer reactions (Bp::DMA)
 - Borgis–Hynes (BH) model, 65–66
 - transfer kinetics, 72–74
 - classical model, 59–60
 - N,N*-dimethylaniline photoreduction of benzophenone, 53–58
 - Dogonadze, Kuznetsov, and Levich (DKL) model, 62–65
 - energetics, 71
 - kinetics, 71–72
 - Lee–Hynes model, 66–67
 - transfer kinetics, 74–78
 - research background, 52–53
 - semiclassical model, 61
 - semiclassical/quantum model comparisons, 67–71
 - tunneling mechanisms, 61–62
- Dirac pulse, molecular dyes in zeolite L channels, 10–12
- Distributed bragg reflector (DBR), amplified spontaneous emission and lasing, laser resonators, 129–131
- Distributed feedback (DFB) lasers, amplified spontaneous emission and lasing, laser resonators, 129–131
- Dithienylethene, photochromic properties, molecular glasses, optoelectronic applications, 145–146
- DMPOPOP molecular dye, size and properties, 16–18
- Dogonadze, Kuznetsov, and Levich (DKL) model, benzophenone-*N,N*-dimethylaniline proton-transfer reactions (Bp::DMA), basic properties, 62–65
- Donor fluorescence rate, Förster electronic excitation energy transfer, molecular dyes in zeolite L channels, 36
- Donor-to-acceptor distances, dye molecules in zeolite L channels, intrazeolite diffusion, 43–44
- Doped systems, molecular glasses, color conversion, 117–120
 - blue/green dopants, 118
 - yellow/red dopants, 118–120
- DPH molecule, size and properties, 17–18
- DPVBi (4,4'-bis(2,2'-diphenylethenyl)-biphenyl), molecular glasses, fluorescence quantum yield, 115
- Dye molecules, zeolite L channels
 - categories and abbreviations, 15–18
 - electronic excitation energy transfer, 26–38
 - Förster energy transfer, 28–36
 - radiationless energy transfer, 27–28
 - spectral overlap, 36–38
 - energy transfer and migration, visual experiments, 38–47
 - intrazeolite diffusion, 42–44
 - migration experiments, 45–47
 - transfer experiments, 39–42
 - geometrical constraints, 8–12
 - lattice constants, 5–6
 - nanocrystals, inner- and outer-surfaces, 12–14
 - research background, 2–4
 - size categories, 5–8
 - stopcock principle, 24–26
 - structural properties, 5–8
 - three-dye antenna, 18–24
- Dye-sensitized solar cells, molecular glasses, light to current applications, 142–143
- Electrical excitation
 - energy transfer, dye molecules in zeolite L channels, 26–38
 - Förster energy transfer, 28–36
 - radiationless energy transfer, 27–28
 - spectral overlap, 36–38
 - multilayer organic electroluminescent devices (OLEDs), molecular glasses, 131–141
 - charge transport mechanisms, 138–141

- Electrical excitation (*Continued*)
 redox potential and charge injection properties, 133–138
 structural properties, 131–133
- Electronic coupling, benzophenone-*N,N*-dimethylaniline proton-transfer reactions (Bp::DMA), semiclassical/quantum model comparisons, 70–71
- Electronic transition dipole moment
 molecular dyes in zeolite L channels, 9–12
 spectral overlap, 37–38
- Electron injection
 charge transport of molecular glasses, 141
 organic light emitting diode (OLED) structure, 136–138
- Electron transfer, benzophenone-*N,N*-dimethylaniline proton-transfer reactions (Bp::DMA)
 Borgis–Hynes (BH) model, 65–66
 transfer kinetics, 72–74
 classical model, 59–60
N,N-dimethylaniline photoreduction of benzophenone, 53–58
 Dogonadze, Kuznetsov, and Levich (DKL) model, 62–65
 energetics, 71
 kinetics, 71–72
 Lee–Hynes model, 66–67
 transfer kinetics, 74–78
 research background, 52–53
 semiclassical model, 61
 semiclassical/quantum model comparisons, 67–71
 tunneling mechanisms, 61–62
- Emission properties, molecular glasses, 112–123
 doped systems, color conversion, 117–120
 fluorescent emitters, blue to red, 112–117
 phosphorescent emitters, 120–121
 polarized light creation, 123
 white light creation, 121–123
- Energetics, benzophenone-*N,N*-dimethylaniline proton-transfer reactions (Bp::DMA), 71
- Energy transfer, molecular dyes in zeolite L channels
 electronic excitation energy transfer, 26–38
 Förster energy transfer, 26–36, 28–36
 radiationless energy transfer, 27–28
 spectral overlap, 36–38
 probability calculations, 12
 visual transfer and migration experiments, 38–47
 intrazeolite diffusion, 42–44
 migration experiments, 45–47
 transfer experiments, 39–42
- Enthalpy changes, benzophenone-*N,N*-dimethylaniline proton-transfer reactions (Bp::DMA), 71
 Lee–Hynes (LH) model kinetics, 74–78
- Europium complexes, phosphorescent emission, molecular glasses, 120–121
- Excitation probability, molecular dyes in zeolite L channels, Förster electronic excitation energy transfer, 32–36
- Excited vibrations, benzophenone-*N,N*-dimethylaniline proton-transfer reactions (Bp::DMA), Lee–Hynes (LH) model kinetics, 76–78
- Fermi's Golden rule
 amplified spontaneous emission and lasing, gain narrowing and organic waveguides, 124–126
 dye molecules in zeolite L channels, radiationless energy transfer, 27–28
- Field-effect transistors, charge transport of molecular glasses, 140–141
- Fluorescence quantum yield
 molecular dyes in zeolite L channels, 7
 visual energy transfer experiments, 41–42
 molecular glasses, 112–117
 Alq₃, 116
 arylamines, 115
 DBVBi and derivatives, 115
 oligophenylenevinylenes, 115–116
 oligophenyls, 113–115
 oligothiophenes, 117
 oxadiazoles, 112–113
 stilbeneamines, 117
- Förster energy transfer
 amplified spontaneous emission and lasing, 123
 laser resonators, 126–131
 dye molecules in zeolite L channels, 28–36
 visual experiments, 39–42
 molecular glasses, absorption and emission, white light creation, 122–123
- Franck–Condon factor, amplified spontaneous emission and lasing, 123

- Free volume theory, molecular glass structure, 89–93
- Front-back trapping, molecular dyes in zeolite L channels, Förster electronic excitation energy transfer, 34–36
- Front trapping, molecular dyes in zeolite L channels, Förster electronic excitation energy transfer, 34–36
- Fullerenes, molecular glasses, optoelectronic applications, photorefractivity, 151–152
- Gain narrowing, amplified spontaneous emission and lasing, organic waveguides, 123–126
- Gaussian distribution, charge transport of molecular glasses, 138, 140–141
- Geometrical constraints, molecular dyes in zeolite L channels, 8–12
- Grain boundaries, low-molecular glass, 87–93
- Grätzel cell, molecular glasses, light to current applications, 142–143
- Hammond postulate, benzophenone-*N,N*-dimethylaniline proton-transfer reactions (Bp::DMA), semiclassical/quantum model comparisons, 68–71
- Heterojunction solar cells, molecular glasses, light to current applications, 143–144
- Highest occupied molecular orbital (HOMO), organic light emitting diode (OLED) structure, 131–133
- bipolar molecular glasses, 138
 - electron injection, 136–138
 - hole injection energy levels, 135–136
 - redox potential and charge injection properties, 133–138
- Hole injection
- charge transport of molecular glasses, 140–141
 - organic light emitting diode (OLED) structure, redox potential and charge injection properties, 135–136
- 3-Hydroxyflavone, proton-transfer reactions, 78–79
- Indoline-dimethine-dioxypyridine (IDOP), molecular glasses, 111
- Indolocarbazoles, molecular glasses, 109, 111
- Integrated fluorescence, molecular dyes in zeolite L channels, Förster electronic excitation energy transfer, 34–36
- Internal photon-to-electron-conversion efficiency (IPCE), molecular glasses, light to current applications, dye-sensitized solar cells, 142–143
- Intrazeolite diffusion, dye molecules in zeolite L channels, energy transfer monitoring, 42–44
- Ion pairing, benzophenone-*N,N*-dimethylaniline proton-transfer reactions (Bp::DMA), 55–58
- energetics, 71
- Ir(ppy)₃ (*fac*-tris(2-phenylpyridine)iridium), phosphorescent emission, molecular glasses, 121
- ITO (indium titanium oxide), organic light emitting diode (OLED) structure, 132–133
- Kinetic isotope effects, benzophenone-*N,N*-dimethylaniline proton-transfer reactions (Bp::DMA)
- classical model, 59–60
 - semiclassical/quantum model comparisons, 68–71
- Kinetics, benzophenone-*N,N*-dimethylaniline proton-transfer reactions (Bp::DMA), 71–72
- Lambert's law, amplified spontaneous emission and lasing, laser resonators, 130–131
- Landau–Zener crossing formalism, benzophenone-*N,N*-dimethylaniline proton-transfer reactions (Bp::DMA), Borgis–Hynes (BH) model, 66
- Lanthanide complexes, phosphorescent emission, molecular glasses, 120–121
- Laser resonators, amplified spontaneous emission and lasing, 126–131
- Lasing techniques, molecular glasses, 123–131
- gain narrowing, organic waveguides, 123–126
 - laser resonators, 126–131
- Lee–Hynes (LH) model, benzophenone-*N,N*-dimethylaniline proton-transfer reactions (Bp::DMA), 66–67
- kinetics, 74–78
 - semiclassical/quantum model comparisons, 70–71
- Ligand structures, molecular glass structure, chelate complexes, 94

- Linear channel structures, molecular dyes in zeolite L channels, 9–12
- Linear polarizability, molecular glasses, optoelectronic applications, photorefractive materials, 149–152
- Lithium fluoride, organic light emitting diode (OLED) structure, 132–133
- Lithographic resist materials, molecular glasses, optoelectronic applications, 153–154
- Lowest unoccupied molecular orbital (LUMO) molecular glasses, light to current applications, dye-sensitized solar cells, 142–143
- organic light emitting diode (OLED) structure, 131–133
- bipolar molecular glasses, 138
- electron injection, 136–138
- hole injection energy levels, 135–136
- redox potential and charge injection properties, 133–138
- Low-molecular glass, structure and applications, 87–93
- Marcus theory of charge transfer, charge transport of molecular glasses, 140
- Markoff chain, molecular dyes in zeolite L channels, Förster electronic excitation energy transfer, 33–36
- MBOXE molecule, size and properties, 17–18
- Merocyanines
- molecular glasses, 109, 111
- molecular glasses, optoelectronic applications, photorefractivity, 152
- Methylviologen
- size and properties, 16–18
- zeolite L channels, 7
- Migration experiments, dye molecules in zeolite L channels, 45–47
- Mode coupling theory, molecular glass structure, 90–93
- Molar decadic extinction coefficient, dye molecules in zeolite L channels, radiationless energy transfer, spectral overlap, 37–38
- Molecular alignment, zeolite L channels, 7
- Molecular glasses, optoelectronic applications
- absorption and emission properties, 112–123
- doped systems, color conversion, 117–120
- fluorescent emitters, blue to red, 112–117
- phosphorescent emitters, 120–121
- polarized light creation, 123
- white light creation, 121–123
- amplified spontaneous emission and lasing, 123–131
- gain narrowing, organic waveguides, 123–126
- laser resonators, 126–131
- azo reorientation and surface gratings, 146–148
- chelate complexes, 93–94
- electrical excitation, multilayer organic electroluminescent devices (OLEDs), 131–141
- charge transport mechanisms, 138–141
- redox potential and charge injection properties, 133–138
- structural properties, 131–133
- lithographic resist materials, 153–154
- low-molecular glass, 87–93
- photochromic materials, 144–146
- photorefractive materials, 148–152
- research background, 85–87
- ring structures, 109–111
- solar cell light to current applications, 142–144
- dye-sensitized solar cells, 142–143
- heterojunction solar cells, 143–144
- spiro molecules, 103–106
- starburst molecules, C₃ symmetry, 100–103
- tetrahedral molecules, 107–109
- twin molecules, 94–99
- Morphological stability, molecular glasses, 86–87
- Multilayer organic electroluminescent devices (OLEDs), electrical excitation, molecular glasses, 131–141
- charge transport mechanisms, 138–141
- redox potential and charge injection properties, 133–138
- structural properties, 131–133
- Nanocrystal structures, molecular dyes in zeolite L channels, inner- and outer-surfaces, 12–14
- Naphthol photoacids-carboxylic base pairs, proton-transfer reactions, 79
- Nonadiabatic proton transfer, benzophenone-*N,N*-dimethylaniline proton-transfer reactions (Bp::DMA)
- Borgis-Hynes (BH) model, 65–66

- Dogonadze, Kuznetsov, and Levich (DKL) model, 63–65
- Lee–Hynes (LH) model, 66–67
- Occupation probability, molecular dyes in zeolite L channels, 9–12
- Oligophenylenevinylene, molecular glasses, fluorescence quantum yield, 115–116
- Oligophenyls, molecular glasses, fluorescence quantum yield, 113–115
- Oligothiophenes, molecular glasses, fluorescence quantum yield, 117
- Optical fluorescence microscopy
molecular dye size and properties, 16–18
three-dye antenna systems, 21–24
- Optoelectronics, molecular glasses
absorption and emission properties, 112–123
doped systems, color conversion, 117–120
fluorescent emitters, blue to red, 112–117
phosphorescent emitters, 120–121
polarized light creation, 123
white light creation, 121–123
amplified spontaneous emission and lasing, 123–131
gain narrowing, organic waveguides, 123–126
laser resonators, 126–131
- azo reorientation and surface gratings, 146–148
- chelate complexes, 93–94
- electrical excitation, multilayer organic electroluminescent devices (OLEDs), 131–141
charge transport mechanisms, 138–141
redox potential and charge injection properties, 133–138
structural properties, 131–133
- lithographic resist materials, 153–154
- low-molecular glass, 87–93
- photochromic materials, 144–146
- photorefractive materials, 148–152
- research background, 85–87
- ring structures, 109–111
- solar cell light to current applications, 142–144
dye-sensitized solar cells, 142–143
heterojunction solar cells, 143–144
- spiro molecules, 103–106
- starburst molecules, C_3 symmetry, 100–103
- tetrahedral molecules, 107–109
- twin molecules, 94–99
- Organic light emitting diode (OLED)
electrical excitation, multilayer structures, molecular glasses, 131–141
charge transport mechanisms, 138–141
redox potential and charge injection properties, 133–138
structural properties, 131–133
fluorescence emission
oxadiazoles, 112–113
stilbeneamines, 117
structural properties, 85–86
- Organic waveguides, amplified spontaneous emission and lasing, gain narrowing, 123–126
- Oscillator strength, dye molecules in zeolite L channels, radiationless energy transfer, spectral overlap, 37–38
- Oxadiazoles
charge transport of molecular glasses, electron mobilities, 141
fluorescence emission, 112–113
molecular glass structure, twin molecules, 97–99
organic light emitting diode (OLED) structure, electron injection, 137–138
- Ox^+ molecule, 22–24
dye molecules in zeolite L channels
energy migration experiments, 45–47
intrazeolite diffusion, 42–44
radiationless energy transfer
spectral overlap, 37–38
visual experiments, 39–42
- Parallel channel structure, molecular dyes in zeolite L channels, 9–12
- PEDOT (polyethylenedioxythiophene), organic light emitting diode (OLED) structure, 133
- Pentaphenylcyclopentadiene, color conversion, molecular glasses, 118
- Perylene, color conversion, molecular glasses, 118
- Phenoxazine, phosphorescent emission, molecular glasses, 121
- Phenylquinoxalines
organic light emitting diode (OLED) structure, electron injection, 137–138
phosphorescent emission, molecular glasses, 121

- Phosphorescent emitters, molecular glasses, 120–121
- Photochromic materials, molecular glasses, optoelectronic applications, 144–146
azo reorientation and surface gratings, 146–148
- Photoconductivity, molecular glasses, optoelectronic applications, photorefractive materials, 149–152
- Photoinduced birefringence, molecular glasses, optoelectronic applications, azo reorientation and surface gratings, 146–148
- “Photonic funnels,” spiro molecules, 106
- Photorefractive materials, molecular glasses, optoelectronic applications, 148–152
- Platinum complexes, phosphorescent emission, molecular glasses, 120–121
- pn*-heterojunction devices, molecular glasses, light to current applications, 143–144
- Point trapping, molecular dyes in zeolite L channels, Förster electronic excitation energy transfer, 35–36
- Polarized light, molecular glasses, absorption and emission, white light creation, 123
- Polystyrenesulfonic acid (PSS), organic light emitting diode (OLED) structure, 133
- POPOP molecule
size and properties, 17–18
three-dye antenna systems, 20–24
zeolite L channels, alignment in, 7
- Proton-transfer reactions
benzophenone/*N,N*-dimethylaniline photochemistry
Borgis–Hynes (BH) model, 65–66
transfer kinetics, 72–74
classical model, 59–60
N,N-dimethylaniline photoreduction of benzophenone, 53–58
Dogonadze, Kuznetsov, and Levich (DKL) model, 62–65
energetics, 71
kinetics, 71–72
Lee–Hynes model, 66–67
transfer kinetics, 74–78
research background, 52–53
semiclassical model, 61
semiclassical/quantum model comparisons, 67–71
tunneling mechanisms, 61–62
3-hydroxyflavone, 78–79
solvent dynamics, 78–79
- Py⁺ molecule
dye molecules in zeolite L channels:
energy migration experiments, 45–47
intrazeolite diffusion, 42–44
radiationless energy transfer
spectral overlap, 37–38
visual experiments, 39–42
three-dye antenna systems, 20–24
- Q bands, color conversion, molecular glasses, 120
- Quantum models, benzophenone-*N,N*-dimethylaniline proton-transfer reactions (Bp::DMA), semiclassical model comparisons, 67–71
- Quenching mechanisms, benzophenone-*N,N*-dimethylaniline proton-transfer reactions (Bp::DMA), 55–58
- Quinacridones, color conversion, molecular glasses, 118
- Radiationless energy transfer, dye molecules in zeolite L channels, 26–28
spectral overlap, 36–38
- Raman spectrum, oligophenyls, fluorescence quantum yield, 114
- “Random” laser, amplified spontaneous emission and lasing, 130–131
- Rayleigh scattering, molecular glass structure, 91–93
- Reaction potentials, benzophenone-*N,N*-dimethylaniline proton-transfer reactions (Bp::DMA), Dogonadze, Kuznetsov, and Levich (DKL) model, 63–65
- Redox potential, organic light emitting diode (OLED) structure, 133–138
- Resorfin anionic organic dye, in zeolite L channels, 7–8
- Ring structures
amplified spontaneous emission and lasing, laser resonators, 128–131
molecular dyes in zeolite L channels, 12
molecular glasses, 109, 111
- Rubrene, color conversion, molecular glasses, 118–120
- Ruthenium dyes, molecular glasses, light to current applications, dye-sensitized solar cells, 142–143
- Sandwich materials, synthesis, three-dye antenna, 20–24

- Semiclassical model, benzophenone-*N,N*-dimethylaniline proton-transfer reactions (Bp::DMA), 60
quantum model comparisons, 67–71
- Single-photon processes, dye molecules in zeolite L channels, 26
visual energy transfer experiments, 41–42
- Single unit cells, dye molecules in, 5–7
- Solar cells, molecular glasses, light to current applications, 142–144
dye-sensitized solar cells, 142–143
heterojunction solar cells, 143–144
- Solubility, spiro molecules, 106
- Solvent dynamics, benzophenone-*N,N*-dimethylaniline proton-transfer reactions (Bp::DMA)
Dogonadze, Kuznetsov, and Levich (DKL) model, 63–65
kinetics, 71–72
Lee–Hynes (LH) model kinetics, 74–78
semiclassical/quantum model comparisons, 69–71
- Solvent separated radical ion pair (SSRIP), benzophenone-*N,N*-dimethylaniline proton-transfer reactions (Bp::DMA), 55–58
- “Soret” bands, color conversion, molecular glasses, 120
- Spectral overlap
molecular dyes in zeolite L channels, 36–38
molecular glasses, optoelectronic applications, azo reorientation and surface gratings, 146–148
- Spiro molecules
amplified spontaneous emission and lasing, 126–131
oligophenyls, fluorescence quantum yield, 113–115
organic light emitting diode (OLED) structure, hole injection energy levels, 135–136
structure and properties, 103–108
- Starburst molecules
charge transport of molecular glasses, hole mobilities, 140–141
molecular glass structure, 100–103
organic light emitting diode (OLED) structure, hole injection energy levels, 135–136
- Stilbenamines, molecular glasses, fluorescence quantum yield, 117
- Stilbene-like molecules
molecular glass structure, twin molecules, 97–99
tetrahedral structure, 109–110
- Stokes-Einstein relation, molecular glass structure, 90–93
- Stokes shift
amplified spontaneous emission and lasing, 123
DPVBi (4,4'-bis(2,2'-diphenylethynyl)-biphenyl), fluorescence quantum yield, 115
dye molecules in zeolite L channels, radiationless energy transfer, spectral overlap, 37–38
oligophenyls, fluorescence quantum yield, 113–115
- Stopcock principle, molecular dyes in zeolite L channels, 24–26
- Supramolecularly organized luminescent dye molecules, zeolite L channels
dye molecules and abbreviations, 15–18
electronic excitation energy transfer, 26–38
Förster energy transfer, 26–36, 28–36
radiationless energy transfer, 27–28
spectral overlap, 36–38
energy transfer and migration, visual experiments, 38–47
intrazeolite diffusion, 42–44
migration experiments, 45–47
transfer experiments, 39–42
geometrical constraints, 8–12
lattice constants, 5–6
nanocrystals, inner- and outer-surfaces, 12–14
research background, 2–4
size categories, 5–8
stopcock principle, 24–26
structural properties, 5–8
three-dye antenna, 18–24
- Tail moiety, molecular dyes in zeolite L channels, stopcock principle, 24–26
- Tetrahedral molecules, structure and properties, 107, 109–110
- Tetraphenylporphyrins, color conversion, molecular glasses, 120
- Thermodynamics
benzophenone-*N,N*-dimethylaniline proton-transfer reactions (Bp::DMA), 78–79
molecular glass structure, 89–93

- Thiophene compounds
 molecular glasses, fluorescence quantum yield, oligothiophenes, 117
 organic light emitting diode (OLED) structure, hole injection energy levels, 135–136
 spiro molecules, 104–106
- Three-dye antenna, structure and properties, 18–24
- Time scales, low-molecular glass, 87–93
- Titanium oxide compounds, molecular glasses, light to current applications, dye-sensitized solar cells, 142–143
- TNF (2,4,7-trinitro-9-fluorenone), molecular glasses, optoelectronic applications, photorefractivity, 150–152
- TPD complexes
 amplified spontaneous emission and lasing, gain narrowing and organic waveguides, 125–126
 charge transport of molecular glasses, hole mobilities, 140–141
 molecular glasses, absorption and emission, white light creation, 122–123
 organic light emitting diode (OLED) structure, hole injection energy levels, 135–136
- Transition state theory, benzophenone-*N,N*-dimethylaniline proton-transfer reactions (Bp::DMA), 52–53
 classical model, 59–60
- Transversal electric (TE) field, amplified spontaneous emission and lasing, gain narrowing and organic waveguides, 124–126
- Transversal magnetic (TM) field, amplified spontaneous emission and lasing, gain narrowing and organic waveguides, 124–126
- Trap fluorescence, molecular dyes in zeolite L channels, Förster electronic excitation energy transfer, 34–36
- Trapping rate
 dye molecules in zeolite L channels, energy migration experiments, 45–47
 Förster electronic excitation energy transfer, molecular dyes in zeolite L channels, 36
- Triarylamine centers, starburst glass molecule structure, 100–103
- Trivial transfer mechanisms, dye molecules in zeolite L channels, 26
- Tryptycenes, molecular glasses, 111
- Tunneling mechanisms, benzophenone-*N,N*-dimethylaniline proton-transfer reactions (Bp::DMA), 52–53
 classical model, 59–60
 proton tunneling, 61–62
 semiclassical model, 61
- Twin molecules
 molecular glass structure, 94–99
 organic light emitting diode (OLED) structure, electron injection, 137–138
- Viscosity, molecular glass structure, 90–93
- Vogel–Fulcher–Tamman relation, molecular glass structure, 90–93
- White light, molecular glasses, absorption and emission, 121–123
- WKB approximation, benzophenone-*N,N*-dimethylaniline proton-transfer reactions (Bp::DMA)
 Lee–Hynes (LH) model, 67
 proton tunneling, 62
- Yellow/red dopants, color conversion, molecular glasses, 118–120
- Zeolite L channels, supramolecularly organized luminescent dye molecules
 dye molecules and abbreviations, 15–18
 electronic excitation energy transfer, 26–38
 Förster energy transfer, 28–36
 radiationless energy transfer, 27–28
 spectral overlap, 36–38
 energy transfer and migration, visual experiments, 38–47
 intrazeolite diffusion, 42–44
 migration experiments, 45–47
 transfer experiments, 39–42
 geometrical constraints, 8–12
 lattice constants, 5–6
 nanocrystals, inner- and outer-surfaces, 12–14
 research background, 2–4
 size categories, 5–8
 stopcock principle, 24–26
 structural properties, 5–8
 three-dye antenna, 18–24
- Zero-point energies, benzophenone-*N,N*-dimethylaniline proton-transfer reactions (Bp::DMA), classical model, 60
- ZSM-12, supramolecularly organized dye molecules, 4

CUMULATIVE INDEX VOLUMES 1-27

| | VOL. | PAGE |
|--|------|------|
| Addition of Atoms to Olefins, in Gas Phase (Cvetanovic) | 1 | 115 |
| Advances in the Measurement of Correlation in Photoproduct Motion (Morgan, Drabbels, and Wodtke) | 23 | 279 |
| AFM and STM in Photochemistry Including Photon Tunneling (Kaupp) | 19 | 119 |
| Alcohols, Ethers, and Amines, Photolysis of Saturated (von Sonntag and Schuchmann) | 10 | 59 |
| Alkanes and Alkyl Radicals, Unimolecular Decomposition and Isotope Effects of (Rabinovitch and Setser) | 3 | 1 |
| Alkyl Nitrites, Decomposition of and the Reactions of Alkoxy Radicals (Heicklen) | 14 | 177 |
| Alternative Halocarbons, Atmospheric Photochemistry of (Francisco and Maricq) | 20 | 79 |
| Anthracenes, Excited State Reactivity and Molecular Topology Relation- ships in Chromophorically Substituted (Becker) | 15 | 139 |
| Anti-Stokes Fluorescence, Cooling of a Dye Solution by (Zander and Drexhage) | 20 | 59 |
| Aromatic Hydrocarbon Solutions, Photochemistry of (Bower) | 1 | 23 |
| Asymmetric Photoreactions of Conjugated Enones and Esters (Pete) . . . | 21 | 135 |
| Atmospheric Reactions Involving Hydrocarbons, FTIR Studies of (Niki and Maker) | 15 | 69 |
| | | |
| Benzene, Excitation and Deexcitation of (Cundall, Robinson, and Pereira) | 10 | 147 |
| Biocatalysis and Biomimetic Systems, Artificial Photosynthetic Trans- formations Through (Willner and Willner) | 20 | 217 |
| Biochromophoric Systems, Excited State Behavior of Some (De Schryver, Boens, and Put) | 10 | 359 |

| | VOL. | PAGE |
|---|------|------|
| Cancer Treatment, Photochemistry in (Dougherty) | 17 | 275 |
| Carbonyl Compounds, The Photocycloaddition of, to Unsaturated Systems: The Syntheses of Oxetanes (Arnold). | 6 | 301 |
| Catalysis of Photoinduced Electron Transfer Reactions (Fukuzumi and Itoh). | 25 | 107 |
| Cobalt (III) and Chromium (III) Complexes, the Photochemistry of, in Solution (Valentine, Jr.). | 6 | 123 |
| Complexes, Photoinitiated Reactions in Weakly Bonded (Shin, Chen, Nickolaisen, Sharpe, Beaudet, and Wittig) | 16 | 249 |
| Cyclic Ketones, Photochemistry of (Srinivasan) | 1 | 83 |
| Cyclobutanones, Solution Phase Photochemistry of (Morton and Turro). | 9 | 197 |
| Cyclometallated Complexes, Photochemistry and Luminescence of (Maestri, Balzani, Deuschel-Cornioley, and von Zelewsky). | 17 | 1 |
| α -Dicarbonyl Compounds, The Photochemistry of (Monroe) | 8 | 77 |
| Diffusion-Controlled Reactions, Spin-Statistical Factors in (Saltiel and Atwater). | 14 | 1 |
| Electron and Energy Transfer, Mimicking of Photosynthetic (Gust and Moore). | 16 | 1 |
| Electron Energy Transfer between Organic Molecules in Solution (Wilkinson) | 3 | 241 |
| Electronically Excited Halogen Atoms (Hussain and Donovan) | 8 | 1 |
| Electron Spin Resonance Spectroscopy. Application of to Photochemistry (Wan). | 9 | 1 |
| Electron Transfer, Photoinduced in Organic Systems, Control of Back Electron Transfer of (Fox). | 13 | 237 |
| Electron Transfer Luminescence in Solution (Zweig) | 6 | 425 |
| Elementary Photoprocesses in Designed Chromophore Sequence on α -Helical Polypeptides (Sisido). | 22 | 197 |
| Ethylene Bonds, Present Status of the Photoisomerization Abut (Arai and Tokumaru) | 20 | 1 |
| Excimers, What's New in (Yakhot, Cohen, and Ludmer) | 11 | 489 |
| Excited Electronic States, Electronic and Resonance Raman Spectroscopy Determination of Molecular Distortions in (Zink and Shin). | 16 | 119 |
| Flash Photolysis with Time-Resolved Mass Spectrometry (Carr) | 25 | 1 |
| Free Radical and Molecule Reaction in Gas Phase, Problems of Structure and Reactivity (Benson) | 2 | 1 |
| FTIR Emission Studies, Time Resolved, of Photochemical Reactions (Hancock and Heard) | 18 | 1 |
| Functional Molecular Glasses: Building Blocks for Future Optoelectronics (Fuhrmann and Salbeck) | 27 | 83 |
| Gas Phase, Addition of Atoms of Olefins in (Cvetanovic) | 1 | 115 |
| Gas Phase Reaction, Photochemical, in Hydrogen-Oxygen System (Volman) | 1 | 43 |
| Gas Phase Reactions, Involving Hydroxyl and Oxygen Atoms, Mechanisms and Rate Constants of (Avramenko and Kolesnika). | 2 | 25 |
| Halogenated Compounds, Photochemical Processes in (Major and Simons) | 2 | 137 |

| | VOL. | PAGE |
|---|------|------|
| Heterogeneous Catalysts, the Question of Artificial Photosynthesis of Ammonia on (Davies, Boucher, and Edwards) | 19 | 235 |
| Hydrogen-Oxygen Systems, Photochemical Gas Phase Reactions in (Volman) | 1 | 43 |
| Hydroxyl and Oxygen Atoms, Mechanisms and Rate Constants of Elementary Gas Phase Reactions Involving (Avramenko and Kolesnikova) | 2 | 25 |
| Hydroxyl Radical with Organic Compounds in the Gas Phase, Kinetics and Mechanisms of the Reactions of (Atkinson, Darnall, Winter, Lloyd, and Pitts) | 11 | 375 |
| Hypophalites, Developments in Photochemistry of (Akhtar) | 2 | 263 |
| Imaging Systems, Organic Photochemical (Delzenne) | 11 | 1 |
| Intramolecular Proton Transfer in Electronically Excited Molecules (Klöpffer) | 10 | 311 |
| Ionic States, in Solid Saturated Hydrocarbons, Chemistry of (Kevan and Libby) | 2 | 183 |
| Isotopic Effects in Mercury Photosensitization (Gunning and Strausz) . . | 1 | 209 |
| Ketone Photochemistry, a Unified View of (Formosinho and Arnaut) . . . | 16 | 67 |
| Lanthanide Complexes of Encapsulating Ligands at Luminescent Devices (Sabbatini, Guardigli, and Manet) | 23 | 213 |
| Laser Trapping-Spectroscopy-Electrochemistry of Individual Microdroplets in Solution (Nakatani, Chikami, and Kitamura) | 25 | 173 |
| Mechanism of Energy Transfer, in Mercury Photosensitization (Gunning and Strausz) | 1 | 209 |
| Mechanistic Organic Photochemistry, A New Approach to (Zimmerman) | 1 | 183 |
| Mercury Photosensitization, Isotopic Effects and the Mechanism of Energy Transfer in (Gunning and Strausz) | 1 | 209 |
| Metallocenes, Photochemistry in the (Bozak) | 8 | 227 |
| Methylene, Preparation, Properties, and Reactivities of (De More and Benson) | 2 | 219 |
| Molecular Distortions in Excited Electronic States, Electronic and Resonance Raman Spectroscopy Determination of (Zink and Shin) | 16 | 119 |
| Neutral Oxides and Sulfides of Carbon, Vapor Phase Photochemistry of the (Fileeth) | 10 | 1 |
| Nitric Oxide, Role in Photochemistry (Heicklen and Cohen) | 5 | 157 |
| Noyes, W., A., Jr., a Tribute (Heicklen) | 13 | vii |
| Nucleic Acid Derivatives, Advances in the Photochemistry of (Burr) . . . | 6 | 193 |
| Olefins, Photolysis of Simple, Chemistry of Electronic Excited States or Hot Ground States? (Colling) | 14 | 135 |
| Onium Salts, Photochemistry and Photophysics of (DeVoe, Olofson, and Sahyun) | 17 | 313 |
| Optical Single-Molecule Detection at Room Temperature (Meixner) . . . | 24 | 1 |
| Organic Molecules, Photochemical Rearrangements of (Chapman) | 1 | 323 |

| | VOL. | PAGE |
|--|------|------|
| Organic Molecules in Adsorbed or Other Perturbing Polar Environments, Photochemical and Spectroscopic Properties of (Nichollas and Leermakers) | 8 | 315 |
| Organic Molecules in their Triplet States, Properties and Reactions of (Wagner and Hammond) | 5 | 21 |
| Organic Nitrites, Developments in Photochemistry of (Akhtar) | 2 | 263 |
| Organic Photochemical Refractive-Index Image Recording Systems (Tomlinson and Chandross) | 12 | 201 |
| Organized Media on Photochemical Reactions, A Model for the Influence of (Ramamurthy, Weiss, and Hammond) | 18 | 67 |
| Organo-Transition Metal Compounds, Primary Photoprocesses of (Bock and von Gustorf) | 10 | 221 |
| Perhalocarbons, Gas Phase Oxidation of (Heicklen) | 7 | 57 |
| Phenyl Azide, Photochemistry of (Schuster and Platz) | 17 | 69 |
| Phosphorescence and Delayed Fluorescence from Solutions (Parker) | 2 | 305 |
| Phosphorescence-Microwave Multiple Resonance Spectroscopy (El-Sayed) | 9 | 311 |
| Photoassociation in Aromatic Systems (Stevens) | 8 | 161 |
| Photochemical Mechanisms, Highly Complex (Johnston and Cramarossa) | 4 | 1 |
| Photochemical Oxidation of Aldehydes by Molecular Oxygen, Kinetics and Mechanism of (Niclause, Lemaire, and Letort) | 4 | 25 |
| Photochemical Reactivity, Reflections on (Hammond) | 7 | 373 |
| Photochemical Rearrangements of Conjugated Cyclic Ketones: The Present State of Investigations (Schaffner) | 4 | 81 |
| Photochemical Transformations of Polyenic Compounds (Mousseron) | 4 | 195 |
| Photochemically Induced Dynamic Nuclear Polarization (Goez) | 23 | 63 |
| Photochemistry in Cyclodextrin Cavities (Bortolus and Monti) | 21 | 1 |
| Photochemistry of Triarylmethane Dye Leuconitriles (Jarikov and Neckers) | 26 | 1 |
| Photochemistry of Conjugated Dienes and Trienes (Srinivasan) | 4 | 113 |
| Photochemistry of Rhodopsins, The (Ottolenghi) | 12 | 97 |
| Photochemistry of Simple Aldehydes and Ketones in the Gas Phase (Lee and Lewis) | 12 | 1 |
| Photochemistry of the Troposphere (Levy) | 9 | 369 |
| Photochemistry of Vitamin D and Its Isomers and of Simple Trienes (Jacobs and Havinga) | 11 | 305 |
| Photochemistry, Vocabulary of (Pitts, Wilkinson, Hammond) | 1 | 1 |
| Photochromism (Dessauer and Paris) | 1 | 275 |
| Photodissociation Dynamics of Hydride Molecules: H Atom Photofragment Translational Spectroscopy (Ashfold, Mordaunt, and Wilson) | 21 | 217 |
| Photo-Fries Rearrangement and Related Photochemical (1,j) Shifts of (j=3,5,7) of Carbonyl and Sulfonyl Groups (Bellus) | 8 | 109 |
| Photography, Silver Halide, Chemical Sensitization, Spectral Sensitization, Latent Image Formation (James) | 13 | 329 |
| Photo-Induced and Spontaneous Proton Tunneling in Molecular Solids (Trommsdorff) | 24 | 147 |
| Photoionization and Photodissociation of Aromatic Molecules, by Ultra violet Radiation (Terenin and Vilesov) | 2 | 385 |

| | VOL. | PAGE |
|---|------|------|
| Photoluminescence Methods in Polymer Science (Beavan, Hargreaves, and Phillips) | 11 | 207 |
| Photolysis of the Diazirines (Frey) | 4 | 225 |
| Photooxidation Reactions, Gaseous (Hoare and Pearson) | 3 | 83 |
| Photooxygenation Reactions, Type II, in Solution (Gollnick) | 6 | 1 |
| Photophysical Probes of DNA Sequence-Directed Structure and Dynamics (Murphy) | 26 | 145 |
| Photophysics of Gaseous Aromatic Molecules: Excess Vibrational Energy Dependence of Radiationless Processes (Lim) | 23 | 165 |
| Photopolymerization, Dye Sensitized (Eaton) | 13 | 427 |
| Photoreactive Organic Thin Films in the Light of Bound Electromagnetic Waves (Sekkat and Knoll) | 22 | 117 |
| Photosensitized Reactions, Complications in (Engel and Monroe) | 8 | 245 |
| Photosynthetic Electron and Energy Transfer, Mimicking of (Gust and Moore) | 16 | 1 |
| Photothermal Studies of Photophysical and Photochemical Processes by the Transient Grating Method (Terazima) | 24 | 255 |
| Phytochrome, Photophysics and Photochemistry of (Schaffner, Branslavsky, and Holzwarth) | 15 | 229 |
| Polymers, Photochemistry and Molecular Motion in Solid Amorphous (Guillet) | 14 | 91 |
| Pressure-Tuning Photochemistry of Metal Complexes in Solution (Eldik and Ford) | 24 | 61 |
| Proton-Transfer Reactions in Benzophenone/ <i>N,N</i> -Dimethylaniline Photochemistry (Peters) | 27 | 51 |
| Primary Processes and Energy Transfer: Consistent Terms and Definitions (Porter, Balzani and Moggi) | 9 | 147 |
| Quantized Matter, Photochemistry and Photoelectrochemistry of: Properties of Semiconductor Nanoparticles in Solution and Thin-Film Electrodes (Weller and Eychmüller) | 20 | 165 |
| Quantum Theory of Polyatomic Photodissociation (Kreslin and Lester) | 13 | 95 |
| Radiationless Transitions, Isomerization as a Route for (Phillips, Lamaire, Burton, and Noyes, Jr.) | 5 | 329 |
| Radiationless Transitions in Photochemistry (Jortner and Rice) | 7 | 149 |
| Semiconductor Nanoclusters, Photophysical and Photochemical Processes of (Wang) | 19 | 179 |
| Semiconductor Photocatalysis for Organic Synthesis (Kisch) | 26 | 93 |
| Silver Halides, Photochemistry and Photophysics of (Marchetti and Eachus) | 17 | 145 |
| Single Crystals, Photochemical Mechanism in: FTIR Studies of Diacyl Peroxides (Hollingsworth and McBride) | 15 | 279 |
| Singlet Molecular Oxygen (Wayne) | 7 | 311 |
| Singlet Molecular Oxygen, Bimolecular Reactivity of (Gorman) | 17 | 217 |
| Singlet Molecular Oxygen, Physical Quenchers of (Bellus) | 11 | 105 |
| Singlet and Triple States: Benzene and Simple Aromatic Compounds (Noyes and Unger) | 4 | 49 |

| | VOL. | PAGE |
|--|------|------|
| Small Molecules, Photodissociation of (Jackson and Okabe) | 13 | 1 |
| Solid Saturated Hydrocarbons, Chemistry of Ionic States in (Kevan and Libby) | 2 | 183 |
| Solvation, Ultrafast Photochemical Intramolecular Charge Transfer and Excited State (Barbara and Jarzeba). | 15 | 1 |
| Spectroscopy and (Photochemistry of Polyatomic Alkaline Earth Containing Molecules (Bernath) | 23 | 1 |
| Spin Conservation (Matsen and Klein) | 7 | 1 |
| Stilbenes, Bimolecular Photochemical Reactions of (Lewis) | 13 | 165 |
| Stilbenes and Stilbene-Like Molecules, <i>Cis-Trans</i> Photoisomerization of (Görner and Kuhn) | 19 | 1 |
| Structure and Reactivity of Organic Intermediates as Revealed by Time-Resolved Infrared Spectroscopy (Toscano). | 26 | 41 |
| Sulfur Atoms, Reactions of (Gunning and Strausz) | 4 | 143 |
| Sulfur and Nitrogen Heteroatomic Organic Compounds, Photochemical Reaction of (Mustafa). | 2 | 63 |
| Supramolecularly Organized Luminescent Dye Molecules in the Channels of Zeolite L (Calzaferri, Maas, Pauchard, Pfenniger, Megelski, Devaux) | 27 | 1 |
| Surfactant Solutions, Photochemistry in (von Büнау and Wolff) | 14 | 273 |
| | | |
| The EPR Spectroscopic <i>D</i> Parameter of Localized Triplet Diradicals as Probe for Electronic Effects in Benzyl-type Monoradicals (Adam, Harrer, Kita, and Nau) | 24 | 205 |
| The Photochemistry of Indoles (Weedon) | 22 | 229 |
| Theory and Applications of Chemically Induced Magnetic Polarization in Photochemistry (Wan). | 12 | 283 |
| Transition Metal Complexes, Primary Processes in (Forster) | 16 | 215 |
| Triatomic Free Radicals, Spectra and Structures of (Herzberg). | 5 | 1 |
| | | |
| Ultraviolet Photochemistry, Vacuum (McNesby and Okabe) | 3 | 157 |
| Ultraviolet Photodissociation Studies of Organosulfur Molecules and Radicals: Energetics, Structure Identification, and Internal State Distribution (Cheuk-Yiu Ng) | 22 | 1 |
| Ultraviolet Radiation, Photoionizational and Photodissociation of Aromatic Molecules by (Terenin and Vilessov) | 2 | 385 |
| Up-Scaling Photochemical Reactions (Braun, Jakob, Oliveros, Oller do Nascimento). | 18 | 235 |
| | | |
| Velocity Mapping of UV Multiphoton Excited Molecules (Chandler and Parker). | 25 | 59 |
| | | |
| Weakly Bonded Complexes, Photoinitiated Reactions in (Shin, Chen, Nickolaisen, Sharpe, Beaudet, and Wittig) | 16 | 249 |
| | | |
| Xanthine Dyes, Photochemistry of the (Neckers and Valdes-Aguilera) . . | 18 | 315 |